Frontier Materials & Technologies

Founded in 2008
№ 2
2023
16+
Quarterly
Scientific Journal

The Founder is
Togliatti State University

Editor-in-Chief
Mikhail M. Krishtal, DSc (Physics and Mathematics), Professor

Deputy Editor-in-Chief
for Metallurgy and Materials Science
Dmitry L. Merson, DSc (Physics and Mathematics), Professor

Deputy Editor-in-Chief
for Mechanical Engineering and Machine Science
Aleksandr P. Shaikin, DSc (Engineering), Professor

Deputy Editor-in-Chief
for Welding and Allied Processes and Technologies
Aleksandr I. Kovtunov, DSc (Engineering), Associate Professor

Editors:
Petr Yu. Bochkarev, DSc (Engineering), Professor
Boris M. Brzhozovskiy, DSc (Engineering), Professor
Aleksandr F. Denisenko, DSc (Engineering), Professor
Yuri Z. Estrin, DSc (Physics and Mathematics), Professor
Sergey S. Gavryushin, DSc (Engineering), Professor
Gregory Gerstein, DSc (Engineering)
Fedor V. Grechnikov, Academician of the Russian Academy of Sciences, DSc (Engineering), Professor
Mikhail I. Karpov, Corresponding Member of the Russian Academy of Sciences, DSc (Engineering), Professor
Aleksandr V. Katsman, PhD (Physics and Mathematics)
Aleksandr A. Kazakov, DSc (Engineering), Professor
Leonid V. Khudobin, DSc (Engineering), Professor
Aleksandr V. Kudrya, DSc (Engineering), Professor
Sergey V. Kuzmin, Corresponding Member of the Russian Academy of Sciences, DSc (Engineering), Professor
Vasily P. Larshin, DSc (Engineering), Professor
Aleksey V. Makarov, Corresponding Member of the Russian Academy of Sciences, DSc (Engineering)
Svetlana V. Maksimova, DSc (Engineering)
Radik R. Mulyukov, Corresponding Member of the Russian Academy of Sciences, DSc (Physics and Mathematics), Professor
Oleg B. Naimark, DSc (Physics and Mathematics), Professor
Nikolay V. Nosov, DSc (Engineering), Professor
Aleksandr V. **Pilinsky**, PhD (Engineering), Associate Professor
Aleksey E. Romanov, DSc (Physics and Mathematics), Professor
Vasili V. Rubanik, Corresponding Member of the National Academy of Sciences of Belarus, DSc (Engineering)
Vladimir A. Shishkov, DSc (Engineering)
Rudolf N. Starobinski, DSc (Engineering), Professor
Ramasubbu Sunder, Fellow of the Indian Academy of Sciences, PhD (Engineering)
Vladimir P. Tabakov, DSc (Engineering), Professor
Alexey Yu. Vinogradov, DSc (Engineering), PhD (Physics and Mathematics), Professor

Until December 2021,
the journal was published
under the title
**"Science Vector
of Togliatti State
University".**

Indexed in Scopus.
Included in the List of HAC,
RSCI core, DOAJ, CNKI,
"White List".
Available in Crossref,
Google Scholar

Registered by the Federal
Service for Supervision
of Communications,
Information Technology
and Mass Media
(Registration Certificate
ПИ No. ФС77-83040
dated March 31, 2022).

Desktop publishing:
Natalya A. Nikitenko

*Responsible/technical
editor:*
Natalya A. Nikitenko

Mailing Address:
14, Belorusskaya St.,
Togliatti,
Russia, 445020
Phone: **(8482) 44-91-74**
E-mail:
vektornaukitgu@yandex.ru

Website:
https://vektornaukitech.ru

Passed for printing
30.06.2023.
Published 06.09.2023.
Format 60×84 1/8.
Digital printing.
Conventional printed sheets 17.2.
Circulation is 30 copies.
Order 3-399-23
The price is free.

Togliatti State University
Publishing
14, Belorusskaya St.,
Togliatti, Russia, 445020

© Togliatti State University, 2023

EDITORIAL BOARD INFORMATION

Editor-in-Chief
Mikhail M. Krishtal, Doctor of Sciences (Physics and Mathematics), Professor, Rector (Togliatti State University, Togliatti, Russia).
Scopus AuthorID: 14634063100
ResearcherID: AAD-7707-2019
ORCID: https://orcid.org/0000-0001-7189-0002

Deputy Editor-in-Chief for Metallurgy and Materials Science
Dmitry L. Merson, Doctor of Sciences (Physics and Mathematics), Professor, Director of the Research and Development Institute of Advanced Technologies (Togliatti State University, Togliatti, Russia).
Scopus AuthorID: 6603449333
ResearcherID: M-7210-2016
ORCID: https://orcid.org/0000-0001-5006-4115

Deputy Editor-in-Chief for Mechanical Engineering and Machine Science
Aleksandr P. Shaikin, Doctor of Sciences (Engineering), Professor, Professor at the Department of the Energy-Converting Machines and Control Systems (Togliatti State University, Togliatti, Russia).
Scopus AuthorID: 6602779899
ORCID: https://orcid.org/0000-0002-9832-4753

Deputy Editor-in-Chief for Welding and Allied Processes and Technologies
Aleksandr I. Kovtunov, Doctor of Sciences (Engineering), Associate Professor, Professor at the Department of Welding, Pressure Treatment of Materials and Allied Processes (Togliatti State University, Togliatti, Russia).
Scopus AuthorID: 36761987000
ResearcherID: B-4545-2016
ORCID: https://orcid.org/0000-0002-7705-7377

Editorial board:
Petr Yu. Bochkarev, Doctor of Sciences (Engineering), Professor, Professor of Chair “Mechanical Engineering Technology and Applied Mechanics” (Kamyshin Technological Institute (Branch) of Volgograd State Technical University, Kamyshin, Russia), Professor of Chair “Technical Support of Agro-Industrial Complex” (Saratov State Vavilov Agrarian University, Saratov, Russia).
Scopus AuthorID: 57189893110
Boris M. Brzhozovskiy, Doctor of Sciences (Engineering), Professor, chief researcher of Laboratory of Theory of Mechanisms and Machine Structure (Institute of Machines Science named after A.A. Blagonravov of the Russian Academy of Sciences, Moscow, Russia).
Scopus AuthorID: 55683317200
Alexander F. Denisenko, Doctor of Sciences (Engineering), Professor, Professor of Chair “Technology of Mechanical Engineering, Machines and Tools” (Samara State Technical University, Samara, Russia).
Scopus AuthorID: 36131150100
Yuri Z. Estrin, Doctor of Sciences (Physics and Mathematics), Professor, Professor of Chair of Engineering Materials (Monash University, Melbourne, Australia).
Scopus AuthorID: 7005031984
Sergey S. Gavryushin, Doctor of Sciences (Engineering), Professor, Head of the Department of Computer Systems of Production Automation (Bauman Moscow State Technical University, Moscow, Russia).
Scopus AuthorID: 6507067486
ResearcherID: AAT-8610-2020
ORCID: https://orcid.org/0000-0002-6547-1351
Gregory Gerstein, DSc (Engineering), Laboratory Head (Leibniz University Hannover, Hanover, Germany).
Scopus AuthorID: 55001912200
Fedor V. Grechnikov, Academician of the Russian Academy of Sciences, Doctor of Sciences (Engineering), Professor, Head of the Department of Forming Processes (Samara National Research University, Samara, Russia).
Scopus AuthorID: 6506174877
ResearcherID: P-2319-2016
ORCID: https://orcid.org/0000-0002-3767-4004
Mikhail I. Karpov, Corresponding Member of the Russian Academy of Sciences, Doctor of Sciences (Engineering), Professor, Head of the Laboratory of Materials Science (Institute of Solid State Physics RAS, Chernogolovka, Russia).
Scopus AuthorID: 7004130343
ResearcherID: Q-9288-2016
Aleksandr V. Katsman, PhD (Physics and Mathematics), Senior Research Associate (Technion – Israel Institute of Technology, Haifa, Israel).
Scopus AuthorID: 7004225554
Aleksandr A. Kazakov, Doctor of Sciences (Engineering), Professor, Professor at the Department of Metallurgy and Casting Technologies, Head of the Metallurgy Expertise Laboratory (Peter the Great Saint-Petersburg Polytechnic University, St. Petersburg, Russia).
Scopus AuthorID: 56037035400
ResearcherID: E-6090-2014
ORCID: https://orcid.org/0000-0001-6511-1228

Leonid V. Khudobin, Doctor of Sciences (Engineering), Professor, Professor of Chair “Innovative Technologies in Mechanical Engineering” (Ulyanovsk State Technical University, Ulyanovsk, Russia).
Scopus AuthorID: 6701859584
Aleksandr V. Kudrya, Doctor of Sciences (Engineering), Professor, Professor at the Department of Physical Metallurgy and Physics of Strength (National University of Science and Technology MISiS, Moscow, Russia).
Scopus AuthorID: 6603628218
Sergey V. Kuzmin, Corresponding Member of the Russian Academy of Sciences, Doctor of Sciences (Engineering), Professor, First Prorector, Professor of Chair “Equipment and Technology of Welding Production” (Volgograd State Technical University, Volgograd, Russia).
Scopus AuthorID: 57217278342
ResearcherID: I-7424-2012
ORCID: https://orcid.org/0000-0003-2802-8497
Vasily P. Larshin, Doctor of Sciences (Engineering), Professor, Professor at the Department of Technology of Mechanical Engineering (Odessa National Polytechnic University, Odessa, Ukraine).
Scopus AuthorID: 7801669969
ORCID: https://orcid.org/0000-0001-7536-3859
Vasily P. Larshin, Doctor of Sciences (Engineering), Professor, Professor at the Department of Technology of Mechanical Engineering (Odessa National Polytechnic University, Odessa, Ukraine).
Scopus AuthorID: 7801669969
ORCID: https://orcid.org/0000-0001-7536-3859
Aleksey V. Makarov, Corresponding Member of the Russian Academy of Sciences, Doctor of Sciences (Engineering), Chief Research Associate, Head of the Department of Materials Science, Head of the Laboratory of Mechanical Properties (M.N. Mikheev Institute of Metal Physics of Ural Branch of Russian Academy of Sciences, Ekaterinburg, Russia).
Scopus AuthorID: 36889178900
Scopus AuthorID: 57195590138
ResearcherID: D-5663-2016
ORCID: https://orcid.org/0000-0002-2228-0643
Svetlana V. Maksimova, Doctor of Sciences (Engineering), Head of the Department of Physical and Chemical Processes of Brazing (E.O. Paton Institute of Electric Welding of the National Academy of Sciences of Ukraine, Kyiv, Ukraine).
Scopus AuthorID: 6701488549
ORCID: https://orcid.org/0000-0003-0158-5760
Radik R. Mulyukov, Corresponding Member of the Russian Academy of Sciences, Doctor of Sciences (Physics and Mathematics), Professor, Director (Institute for Metals Superplasticity Problems of the Russian Academy of Sciences, Ufa, Russia).
Scopus AuthorID: 7003520439
ResearcherID: B-3800-2016
ORCID: https://orcid.org/0000-0002-0452-3816
Oleg B. Naimark, Doctor of Sciences (Physics and Mathematics), Professor, Head of the Laboratory of Physical Foundations of Strength (Institute of Continuous Media Mechanics of Ural Branch of Russian Academy of Sciences, Perm, Russia).
Scopus AuthorID: 6701720806
Nikolay V. Nosov, Doctor of Sciences (Engineering), Professor, Professor of Chair “Technology of Mechanical Engineering, Machines and Tools” (Samara State Technical University, Samara, Russia).
Scopus AuthorID: 6602506825
Aleksandr V. Pilinsky, PhD (Engineering), Associate Professor, MSME (Master of Science in Mechanical Engineering), Manager (Raymer Metals, Inc., Los Angeles, USA).
Aleksey E. Romanov, Doctor of Sciences (Physics and Mathematics), Professor, Professor of the Institute of Advanced Data Transfer Systems (ITMO University, St. Petersburg, Russia).
Scopus AuthorID: 7202768874
Vasili V. Rubanik, Corresponding Member of the National Academy of Sciences of Belarus, Doctor of Sciences (Engineering), Head of the Laboratory of Metal Physics (Institute of Technical Acoustics of the National Academy of Sciences of Belarus, Vitebsk, Belarus).
Scopus AuthorID: 57215218253
Vladimir A. Shishkov, Doctor of Sciences (Engineering), Head of the Technical Department (Palladio LLC, Togliatti, Russia).
Rudolf N. Starobinski, DSc (Engineering), Professor, Scientific Consultant (Silencers. Consulting and Engineering, Hamburg, Germany).
Scopus AuthorID: 6602638504
Ramasubbu Sunder, Fellow of the Indian Academy of Sciences, PhD (Engineering), Director (BISS (P) Ltd, Bangalore, India).
Scopus AuthorID: 7003530245
ResearcherID: H-6740-2016
ORCID: https://orcid.org/0000-0001-6143-0723
Vladimir P. Tabakov, Doctor of Sciences (Engineering), Professor, Head of Chair “Innovative Technologies in Mechanical Engineering” (Ulyanovsk State Technical University, Ulyanovsk, Russia).
Scopus AuthorID: 6701501345
ResearcherID: E-1832-2017
ORCID: https://orcid.org/0000-0002-2568-9401
Alexey Yu. Vinogradov, Doctor of Sciences (Engineering), PhD (Physics and Mathematics), Professor, Professor of Faculty of Mechanical and Industrial Engineering (Norwegian University of Science and Technology, Trondheim, Norway).
Scopus AuthorID: 7402889776
ResearcherID: A-7175-2009
ORCID: https://orcid.org/0000-0001-9585-2801

From the 11th till 15th of September Togliatti will host the XI International School "Physical Materials Science" (hereinafter – PMS-2023) which will focus on the issues of fundamental materials science, analysis of micro- and macrostructure, response of materials under the influence of various fields, cyclically changing loads, hydrogen embrittlement, corrosion damage and other important issues of materials science.

Following its long tradition, PMS-2023 launches a competition for the best scientific work among young scientists who will not be older than 35 by the start of PMS-2023. This competition is held in two stages. At the first stage, all the works written in the form of a research article with a thorough review are recognized as the winners and are recommended for publication in the scientific journal '**Frontier Materials & Technologies**'. At the second stage, the contestants present their reports at the PMS-2023 where they will be rated by a board of jury made up of leading scientists. The winners of the second stage are awarded with valuable prizes.

This issue of the journal contains the first three works of the winners of the first stage; the rest of the works will be published in the subsequent issues.

Chairperson of the School Organizing Committee, Professor Dmitry L. Merson

CONTENT

doi: 10.18323/2782-4039-2023-2-64-2

The formation of highly dispersed zinc oxide powder during combustion of zinc nitrate with glycine mixture and its application for photocatalytic phenol decomposition

Aleksandr P. Amosov*[1,3], Doctor of Sciences (Physics and Mathematics), Professor,
Head of Chair "Metals Science, Powder Metallurgy, Nanomaterials"
Vladislav A. Novikov[1,4], PhD (Engineering),
assistant professor of Chair "Metals Science, Powder Metallurgy, Nanomaterials"
Egor M. Kachkin[1,5], student
Nikita A. Kryukov[1,6], student
Aleksandr A. Titov[1,7], student
Ilya M. Sosnin[2,8], junior researcher at the Research
Institute of Advanced Technologies
[1]*Samara State Technical University, Samara (Russia)*
[2]*Togliatti State University, Togliatti (Russia)*

***E-mail: mvm@samgtu.ru**
egundor@yandex.ru

[3]ORCID: https://orcid.org/0000-0003-1994-5672
[4]ORCID: https://orcid.org/0000-0002-8052-305X
[5]ORCID: https://orcid.org/0000-0002-4745-2237
[6]ORCID: https://orcid.org/0000-0001-6900-4278
[7]ORCID: https://orcid.org/0000-0001-8707-6523
[8]ORCID: https://orcid.org/0000-0002-5302-3260

Received 13.07.2022 *Accepted 02.05.2023*

Abstract: The paper presents the results of a detailed study of the process and products of combustion during self-propagating high-temperature synthesis (SHS) of ZnO zinc oxide powder from mixtures of such common reagents as oxidizer zinc nitrate and reducing agent (fuel) glycine, as well as the application of synthesized highly dispersed submicron and nanosized ZnO powder for the phenol photocatalytic decomposition under the action of ultraviolet irradiation. An aqueous solution of a mixture of reagents (the SHS-S process or Solution Combustion Synthesis – SCS) and the gel from a mixture of initial dry reagents formed when they were moistened due to hygroscopicity (the SHS-G process or Gel Combustion Synthesis – GCS) were combusted. The authors studied the phase and chemical compositions, the structure of the combustion product, and the effect of calcination in an oxidizing air medium and grinding in drum ball and planetary-centrifugal mills, as well as in mortar, on them and their photocatalythic activity. The study showed that calcination considerably increases the photocatalytic activity of combustion products due to a significant decrease in carbon impurity in the unburned fuel remains, and grinding in mills reduces the photocatalytic activity due to iron contamination and coarsening of ZnO particle agglomerates. The difference between the photocatalytic activity of the SHS-G and SHS-S products in the phenol decomposition is evident only at the initial stage of ultraviolet irradiation, after which this difference disappears. The authors discuss the direction of further research to increase significantly the photocatalytic activity of zinc oxide synthesized during combustion to use it effectively for the phenol decomposition under the action of visible light.

Keywords: highly dispersed zinc oxide powder; zinc oxide; zinc nitrate and glycine mixture; photocatalytic phenol decomposition; combustion; self-propagating high-temperature synthesis; ZnO.

Acknowledgments: The work was carried out under the financial support of the Russian Science Foundation within the project No. 22-29-00287.

For citation: Amosov A.P., Novikov V.A., Kachkin E.M., Kryukov N.A., Titov A.A., Sosnin I.M. The formation of highly dispersed zinc oxide powder during combustion of zinc nitrate with glycine mixture and its application for photocatalytic phenol decomposition. *Frontier Materials & Technologies*, 2023, no. 2. DOI: 10.18323/2782-4039-2023-2-64-2.

INTRODUCTION

Recently, the problem of wastewater pollution and purification from such a highly toxic organic compound as phenol C_6H_5OH and its derivatives has become particularly acute [1]. Among various methods of water purification from this pollutant, the most effective and environmentally friendly is the use of photocatalysts – materials decomposing organic pollutants under the action of electromagnetic radiation (visible or ultraviolet light), without the formation of residual toxic compounds. Highly dispersed nanosized and submicron powder of zinc oxide ZnO is considered one of the most promising, in application, as a heterogeneous photocatalytic material for the degradation of organic pollutants [2–4].

There are quite a few methods for synthesis of ZnO-based nanomaterials, which can be divided into two groups: solution and gas-phase [3; 4]. Gas-phase methods are complex, implemented on expensive equipment, energy-intensive, and inefficient. Simpler and less energy intensive solution methods make it possible to effectively control the composition, morphology, and size of synthesized ZnO nanopowders using such factors as the type of solvent, composition of re-agents, and synthesis conditions. However, both types of methods are characterized by low productivity, which prevents the organization on their basis of industrial production of nanostructured ZnO photocatalysts for wastewater purification.

The method of solution self-propagating high-temperature synthesis (SHS) of oxides in the combustion mode differs noticeably from the methods listed above, in its simplicity, energy saving, and high productivity, which makes it attractive for creating technologies, for the industrial production of various low-budget oxide nanomaterials for manifold uses [5–7]. The method of solution SHS (SHS-S) is based on the combustion of a mixture of dissolved, most often in water, re-agents of exothermic redox reactions or on the combustion of a gel from a mixture of dry re-agents (SHS-G), therefore it is also called synthesis during solution combustion (Solution Combustion Synthesis – SCS) or synthesis during gel combustion (Gel Combustion Synthesis – GCS).

A gel from a mixture of re-agents is formed, both in the SHS-S process from a mixture of aqueous solutions of re-agents after solvent evaporation, and in the SHS-G process when mixing dry re-agents, which is accompanied by their spontaneous moistening from the ambient air due to hygroscopicity. Thus, in both cases, the oxide nanopowder synthesis occurs during gel combustion. There are studies on the possibility of obtaining ZnO during the combustion of gels, but they do not describe the process and combustion products in sufficient detail, which makes it difficult to choose them for reasonable practical application [8–10].

This work [11] presents the results of a detailed study of the SHS-S process of zinc oxide ZnO nanopowder from a solution of a mixture of such common re-agents as the oxidizing agent zinc nitrate $Zn(NO_3)_2$ and the reducing agent (fuel) glycine $C_2H_5NO_2$, as well as the use of synthesized ZnO for the phenol photocatalytic decomposition. Let us present the results of this study in more detail, since this work is a continuation of [11].

The results of these experimental studies [11] demonstrate that when heating a vessel with an aqueous solution of zinc nitrate and glycine re-agents at h=6.5 mm and T_S=460 °C, after water evaporation and gel formation (on average for 8 min at $0.5 \leq \varphi \leq 1.5$), the reaction proceeds in the mode of rapid (≤3 s), overall combustion with a yellow flame and a sudden, almost complete release of the reaction mixture and milky reaction products in the form of thick white smoke (pure ZnO is white) from the vessel. This is clearly illustrated in Fig. 1 by the close to zero values of the product mass conservation coefficient $K_M(\varphi)$ in the range of $0.5 \leq \varphi \leq 1.5$ obtained as a result of three experiments for each value of the criterion φ.

Fig. 1 shows that the combustion characteristic values obtained in three experiments for the same criterion φ value can differ significantly from each other, that is, they have a large spread. With a reduced fuel content φ=0.25, the reaction proceeds in a flameless mode with a rapid release of red smoke for 2–5 s and a partial emission of a light-green product. When φ>1.5, the combustion and product appearance change. When increasing φ, a transition to synthesis in the mode of progressively slower smoldering (up to 3 min in average) occurs, the color of the loose product changes from grey with an admixture of white to black, with an admixture of white. At φ=2.5 and more, the color becomes completely black, and the product mass conservation coefficient K_M at φ>2 becomes even greater than one.

According to [11], at $0.5 \leq \varphi \leq 1.5$, the SHS-S reaction proceeds in the most intense explosive mode, due to the closeness to the optimal ratio of fuel and oxidizer at φ=1

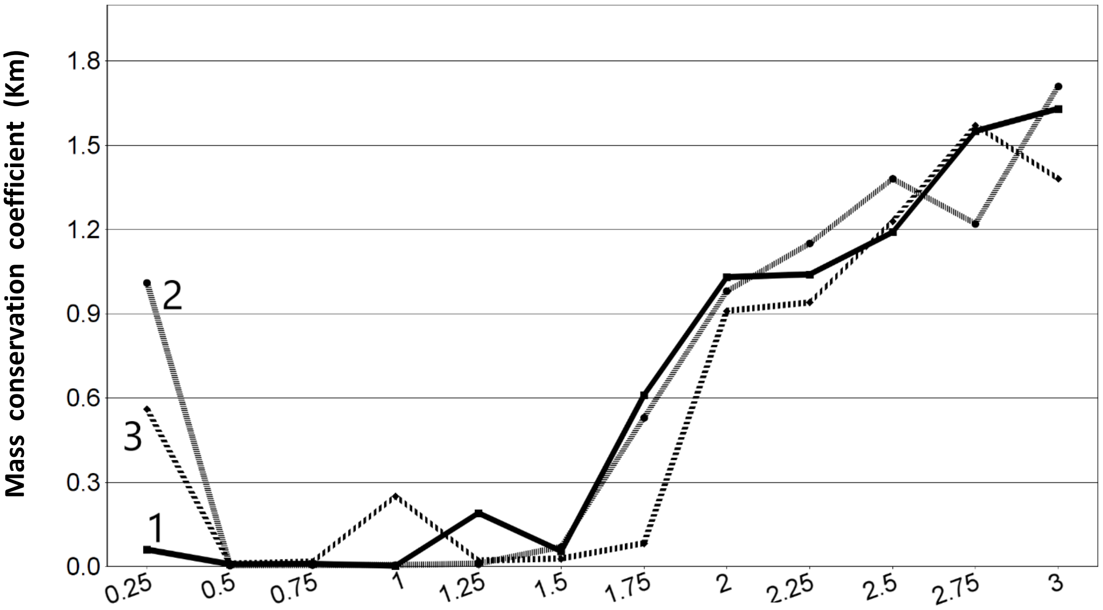

Fig. 1. *The dependence of the product mass conservation coefficient K_m on the value of the criterion φ at the combustion of the solution of re-agents [11, p. 932]. The numbers on the lines indicate the numbers of experiments*

with a sudden, almost complete release of the product from the reaction vessel. At φ<0.5 and at φ>1.5, the initial mixture of re-agents in the solution contains an excess of oxidizer or fuel, respectively, and the reaction of solution SHS of zinc oxide proceeds in a quieter mode without a sudden release of the product from the vessel, especially at φ≥2.

In this range of φ values, changes in the product colour and mass are explained by the fact that at φ>1.5, the mixture of re-agents becomes fuel-rich, it lacks internal oxygen in the mixture of re-agents and external oxygen from the ambient air for complete oxidizing of carbon in the fuel, and its removal from the combustion product in the form of CO_2. The combustion product, along with pure white ZnO, contains an increasing amount of black free carbon and unburned fuel residues; at φ>2, its color is completely black, and the mass exceeds the theoretical yield of ZnO, and therefore the K_M coefficient becomes greater than one [11]. In this case, for the reaction to proceed throughout the entire volume of the mixture of re-agents, it is necessary to stir constantly this mixture during smoldering. Following these results, one can conclude that the value φ=2 is the most suitable for practical use; with this value, there is no explosive combustion with the release of the product from the vessel, observed at lower φ, and intense smoldering in about 8 s leads to the formation of an easily destructible powder with its retention in a vessel without the need for constant stirring to complete the synthesis reaction, which is required when φ>2.

Fig. 2 shows the combustion product microstructure for φ=2 in the form of a frozen foamy mass with a large number of pores of various diameters and agglomerates of small nanosized and submicron ZnO particles [11].

In Fig. 2, an amorphous component is represented by foam due to the solidification of the gel-like residue in the combustion product. Such a residue is present as a consequence of the formation of free carbon in amorphous form, and carbon bound with oxygen and hydrogen in unburned fuel residues, as shown in [12; 13].

The carbon content in the SHS-S product at φ=2 reaches almost 10 % in average [11]. When performing oxidative annealing (calcination) of the combustion product for 1 h at 650 °C in a muffle furnace with an air atmosphere, the carbon content decreases to an average of 1 %, and the calcined synthesis product acquires a uniform structure of powder body of porous agglomerates up to 100 µm in size sintered from well-defined crystalline nanosized, and submicron ZnO particles with an average crystallite size of 40 nm. In the paper [11], nanostructured ZnO obtained for the first time by the solution SHS method was used as a photocatalyst for the phenol decomposition, in an aqueous solution under the action of electromagnetic radiation (ultraviolet and visible). In the calcined state, it showed high photocatalytic activity leading to near-complete phenol decomposition in 3.5–4.5 h of ultraviolet irradiation. However, under the action of visible light, the photocatalytic activity turned out to be significantly lower than under ultraviolet irradiation: after 5 h of irradiation with visible light, the phenol concentration decreased by only 10 % [11].

The work [11] did not study the grinding of the synthesized zinc oxide (SHS-S product), and the effect of grinding on the photocatalytic activity in the phenol decomposition. Such a study is of definite interest because an increase in the specific surface area of a heterogeneous catalyst during its grinding usually improves the catalysis efficiency; therefore, much attention is paid to increasing the zinc oxide dispersion and the use of ZnO nanoparticles in photocatalysis [2–4]. Another type of the SHS process for zinc oxide has not been studied either, when burning not a solution of the initial re-agents (SHS-S), but a gel from the initial dry mixture of the same re-agents (SHS-G). This process is implemented simpler and quicker and can lead to the ZnO synthesis with a higher photocatalytic activity in the phenol decomposition.

The aim of this study is to increase the photocatalytic activity of zinc oxide synthesized both by the SHS-S method when burning a solution of re-agents by grinding the combustion product in various ways, and by the SHS-G method by burning the gel from the initial dry mixture of the same re-agents.

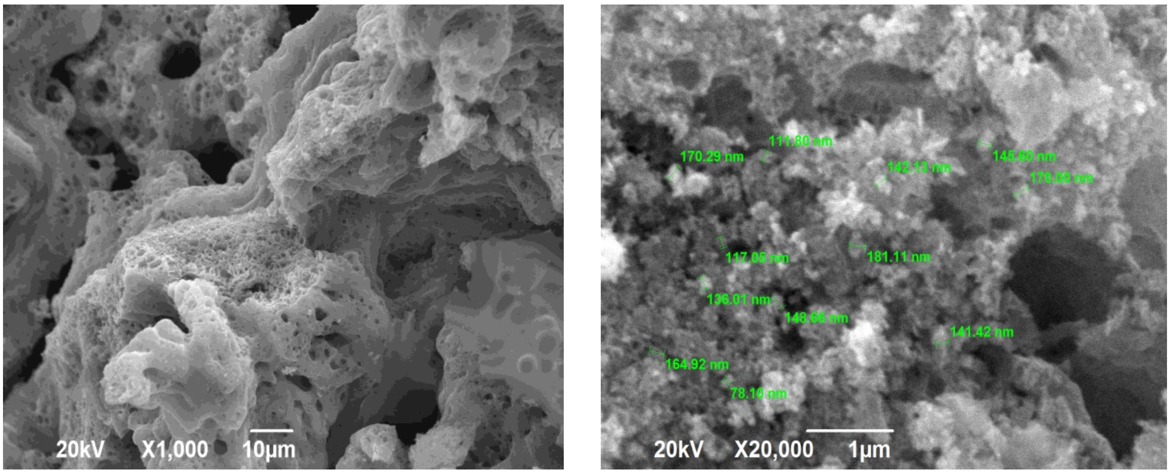

***Fig. 2.** Microstructure of the solution combustion product at different magnifications at φ=2 [11, p. 936]*

METHODS

For the experimental studies, the following re-agents were used: zinc nitrate 6-aqueous $Zn(NO_3)_2 \cdot 6H_2O$ produced according to GOST 5106-77, of analytical grade; glycine $C_2H_5NO_2$ (GOST 5860-75, analytical grade); distilled water (GOST 6709-72); technical synthetic phenol (GOST 23519-93, high grade).

The equation for the ZnO synthesis reaction using the selected re-agents is written as [11]:

$$\begin{aligned} & Zn(NO_3)_2 + \frac{10}{9}\varphi C_2H_5NO_2 + \frac{5}{2}(\varphi - 1)O_2 = \\ & = ZnO + \frac{25}{9}\varphi H_2O + \frac{20}{9}\varphi CO_2 + \left(\frac{5}{9}\varphi + 1\right)N_2 \end{aligned}, \quad (1)$$

where the dimensionless φ criterion characterizes the molar ratio of fuel and oxidizer.

At $\varphi<1$, the excess oxygen is released from the mixture of re-agents, and at $\varphi>1$, the oxygen required for the complete oxidation of elements is consumed from the surrounding gaseous medium. (Note that anhydrous zinc nitrate appears in equation (1), since when the mixture of re-agents is heated, almost all free and bound water evaporates, and the synthesis reaction proceeds during the combustion of an almost anhydrous gel [7].) The φ value largely determines a combustion mode, as well as the combustion product composition and structure. The experimental study of the combustion process and the combustion products was carried out with changing the values of the criterion φ in the range of $0.25 \leq \varphi \leq 3$ with a step of 0.25.

Mixtures of re-agents were heated in a flat-bottomed metal vessel on an electric heater with a power of 1 kW. The average temperature of the contact metal surface of the electric heater was T_S=460 °C. When studying the SHS-S method, the volume of saturated aqueous solutions of mixtures of re-agents with V=25 ml and a height thickness of h=6.5 mm was used for heating.

The solution heating led to the spontaneous onset of a chemical reaction with intense heat and gas evolution (self-ignition), culminating in combustion of various types: 1) flameless combustion without the formation of luminous zones; 2) smoldering with the formation of focal and frontal luminous zones; 3) overall combustion with the formation of a flame. After the end of combustion, a loose or dense sinter of solid combustion products remained in the vessel, the mass of which depended on the combustion type. Intense combustion could lead to the release of a part of the reacting mixture and combustion products from the vessel, so that only a part of the combustion products remained in the vessel. In this regard, the authors calculated the product mass conservation coefficient K_M as the ratio of the mass of the combustion product remained in the reaction vessel after the experiment, to the theoretical product mass calculated according to the reaction equation. Along with determining the combustion type and calculating the K_M coefficient, the combustion time characteristics were determined: 1) the delay time for the onset of combustion (ignition) from the start of heating; 2) the combustion duration. One should note that the specified time characteristics of combustion and the product mass conservation coefficient K_M were first introduced when considering the solution SHS process and studied in our work [11].

When studying the SHS-G process, the authors used the masses of mixtures of dry re-agents corresponding to the mass of mixtures of re-agents in a saturated aqueous solution with a volume of V=25 ml at the corresponding φ value. Dry powders of the components – zinc nitrate and glycine – were weighed and mixed manually in a mortar until visually homogeneous. During mixing, the mixture of powders was saturated with moisture from the air due to hygroscopicity to form a gel, which was placed in a metal flat-bottomed vessel for heating on an electric heater with a surface temperature of T_S=460 °C. Heating led to spontaneous gel ignition, the occurrence of the SHS-G process in the form of combustion, and the formation of a combustion product – zinc oxide with impurities of products of incomplete combustion, mainly in the form of free and combined carbon.

To remove impurities of free carbon and carbon bound with oxygen and hydrogen in the unburned fuel residues, the combustion product was subjected to calcination (oxidizing burning) in the NAKAL PL 5/12.5 muffle furnace with an air atmosphere at a temperature of 500, 650, and 750 °C during 1 h.

X-ray diffraction (XRD) phase analysis of combustion products was carried out on an ARL X'TRA Thermo Fisher Scientific X-ray diffractometer. The microstructure and elemental chemical composition were studied using a JSM-6390A scanning electron microscope (Jeol) with a JSM-2200 energy dispersive spectroscopy (EDS) device. The size of coherent scattering regions (CSRs) was estimated using the Scherrer formula.

Grinding of the solution SHS powdered product (SHS-S product) was carried out in three ways. The first method – in a drum ball mill (DBM) with a volume of 1 l and a drum rotation speed of 120 rpm, 1 kg of milling agents in the form of rollers with a diameter of 5 mm made of ШХ15 steel and up to 7 g of grindable powder were loaded. The grinding time was 15, 30, and 60 min. The second method is grinding in an Activator-2SL planetary-centrifugal mill (PCM). Grinding balls with a diameter of 5 mm and a mass of 375 g made of ШХ15 steel and up to 7 g of grindable powder were loaded into two drums with a volume of 270 ml each with an inner radius of 35 mm. The drums were mounted on a planetary disk with a ratio of the radii of rotation of the disk and drums equal to 1.5, and ensured grinding at a centrifugal acceleration of 20 g. The powder grinding time in the PCM was 15, 30, and 45 s. The third way – the synthesized powder was manually ground with a pestle in a ceramic mortar with a grinding time of 5, 10, and 15 min.

The synthesized ZnO photocatalytic activity was studied by decomposition of phenol dissolved in 100 ml of water at a concentration of 1 mg/l. ZnO particles were dispersed in the solution in an amount of 1 g/l using a Sapphire UZV-2.8 ultrasonic bath. The photocatalytic decomposition process proceeded with constant stirring of the solution under the action of ultraviolet radiation with a wavelength of 365 nm on a Lab 365 nm TL-D 18W BLB device from Philips. The concentration of phenol dissolved in water was determined by registering a characteristic fluorescent peak by the spectrofluorimetry method using a Shimadzu RF-6000 device. (SHS-G and SHS-S products for comparative studies of their photocatalytic activity after synthesis or calcination were subjected to grinding during 10 min in a ceramic mortar.)

RESULTS

SHS-S product grinding

Fig. 3 shows the appearance of the ground non-calcined combustion product synthesized from a solution of zinc nitrate with glycine at φ=2 after grinding in a drum ball mill (60 min) and a mortar (15 min).

Fig. 3 demonstrates that the appearance of the synthesized combustion product at the end of grinding in a DBM and in a mortar vary notably. If in a ball mill the ground product sticks by a continuous layer on the grinding agents (steel rollers), and on the steel wall of the drum (Fig. 3 a), then in a ceramic mortar the sticking of the product is much less (Fig. 3 b). Significant sticking of the ground product was also noted during intensive grinding in a planetary mill. Such ground product sticking in the DBM and PCM takes a significant part of the product. After each grinding session, it is necessary to clean and wash the drums and grinding agents (rollers and balls) from sticky product, to dry them, which leads to great inconvenience. Moreover, when grinding in a DBM and PCM, the powder darkens, which indicates its possible contamination with the material of the grinding agents. With much simpler grinding in a mortar, there is practically no sticking of the powder, and it does not darken during grinding.

The microstructure of the non-calcined combustion product ground by all three methods is represented in Fig. 4. The time of grinding in a mortar was 10 min, in DBM – 60 min, in PCM – 45 s.

The microstructure of the powder ground by different ways also varies markedly (Fig. 4). After grinding in a mortar (Fig. 4 a), the powder structure is quite homogeneous and consists of submicron agglomerates of smaller particles with a visually observed minimum size of 60 to 90 nm. After grinding in a ball mill (Fig. 4 b), the structure of the ground material is heterogeneous and consists of a mixture of individual small particles with a visually observed minimum size of 70 to 140 nm and agglomerates, the size of which reaches 3 μm.

Increasing the time of grinding in the DBM leads to a decrease in the number of individual small particles, and an increase in the number and size of particle agglomerates with an amorphous component between them. In a planetary mill, the ground material acquires a more heterogeneous structure (Fig. 4 c). There are practically no individual small particles with a minimum size of 150 to 250 nm, the powder consists of a pasty mass of micron-sized agglomerates with an amorphous component. Increasing the grinding time also leads to coarsening of the agglomerates.

The phase composition of the non-calcined synthesis product ground by all three methods is shown in Fig. 5 and in Table 1.

A quantitative X-ray diffraction analysis, according to X-ray diffraction patterns (Fig. 5 and Table 1) of the ground non-calcined combustion product, shows the content of both carbon impurity from 2 to 10 % and a significant content of Fe_2O_3 iron oxide impurity: 30 % after grinding in the DBM and 36 % after grinding in the PCM, and the absence of this impurity after grinding in a mortar. Thus, intensive milling of ZnO powder in the DBM and PCM actually leads to powder contamination with an admixture of iron oxide from steel drums and grinding agents, but in the case of grinding in a ceramic mortar, there is no such contamination.

The product synthesized from a solution of zinc nitrate with glycine at φ=2 was also ground after oxidative roasting (calcination) at 650 °C during 1 h. Fig. 6 presents the results of grinding the calcined product in various ways. The time of grinding in the mortar was 15 min, in the DBM – 60 min, and in the PCM – 45 s.

a ***b***

Fig. 3. *The appearance of the non-calcined solution combustion (SHS-S) product after grinding:*
a *– in the drum ball mill;* ***b*** *– in the mortar*

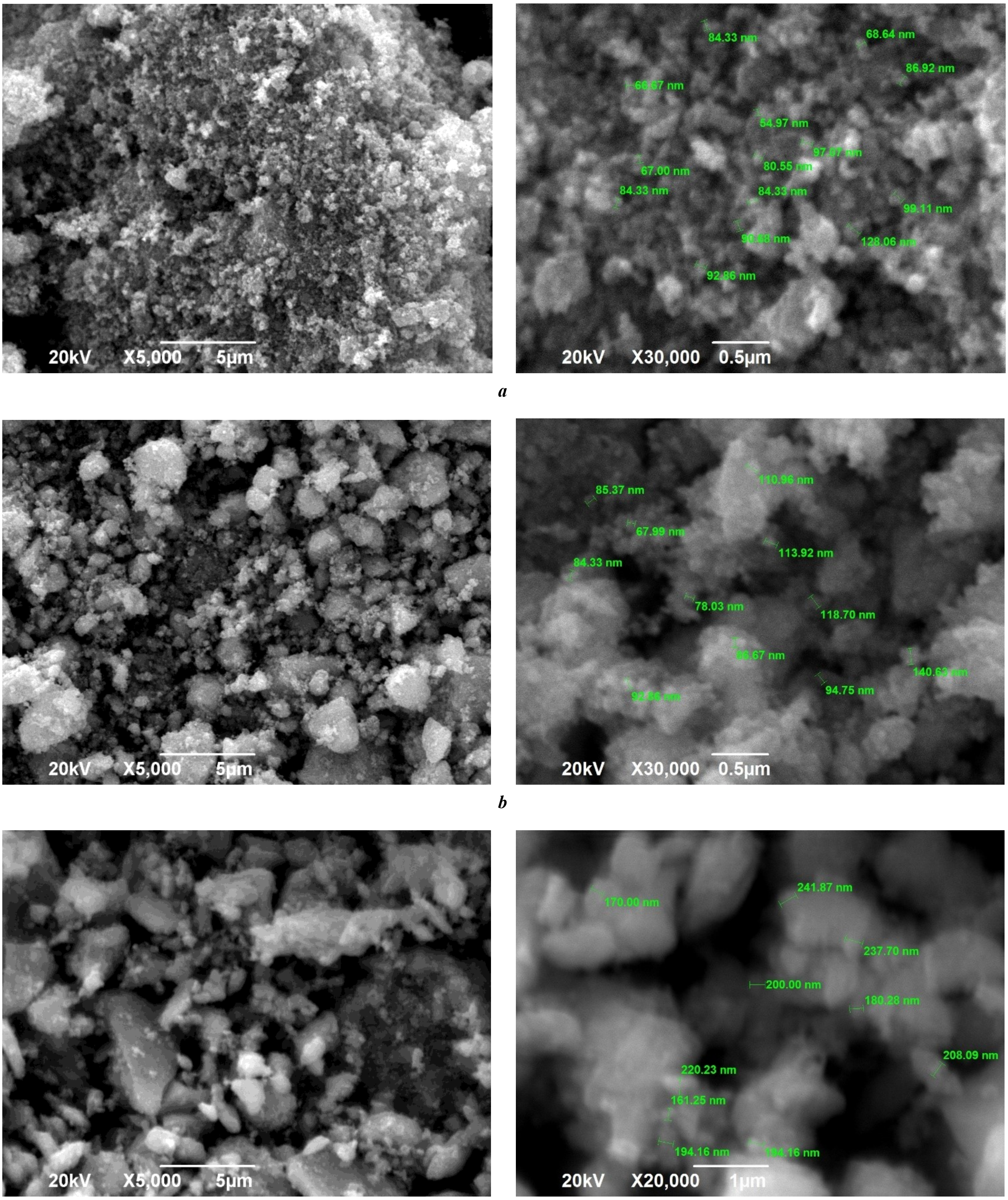

a

b

c

Fig. 4. *Microstructure of the non-calcined solution combustion (SHS-S) product after grinding:*
a *– in the mortar;* ***b*** *– in the drum ball mill;* ***c*** *– in the planetary-centrifugal mill*

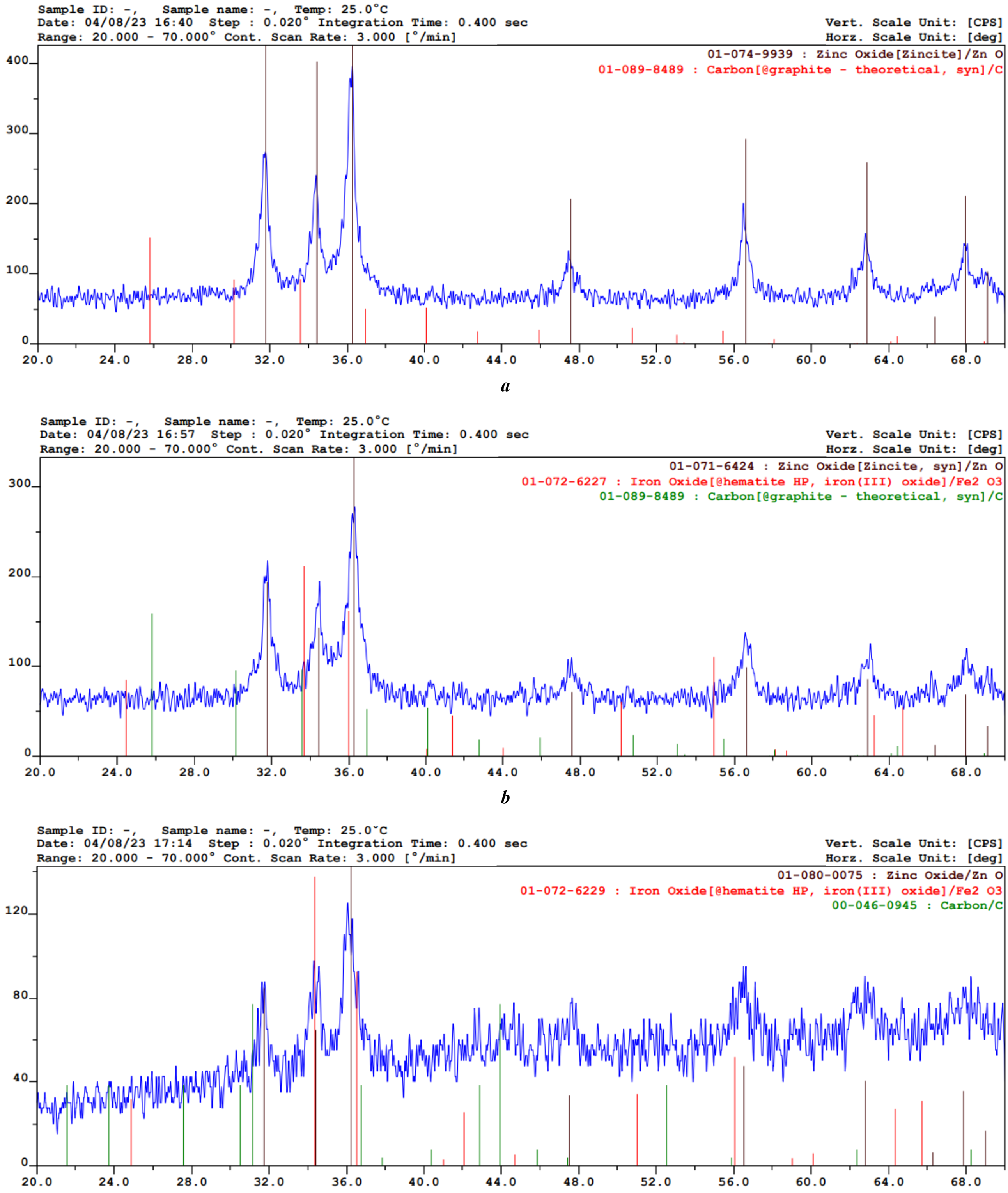

Fig. 5. *XRD pattern of the non-calcined solution combustion (SHS-S) product after grinding:*
a *– in the mortar;* ***b*** *– in the drum ball mill;* ***c*** *– in the planetary-centrifugal mill*

Table 1. *Phase composition of the non-calcined solution combustion (SHS-S) product at different grinding methods*

Type of grinding	Content, %		
	ZnO	C	Fe_2O_3
A mortar, 15 min	93	7	0
A drum ball mill, 60 min	60	10	30
A planetary-centrifugal mill, 45 s	62	2	36

Fig. 6 demonstrates that the amorphous component from the residues of unburned fuel in the structure is absent. The most uniform and fine powder structure is observed after grinding in a mortar. This is confirmed by the results of determining the particle-size distribution of the combustion product calcined at 650 °C during 1 h after grinding in a mortar and PCM (Fig. 7) with an average particle size of D_{50}=0.90 and 8.27 µm, respectively.

Fig. 7 clearly shows that after grinding in a mortar, the particle size is in the range from 0.18 to 8.3 µm, and after grinding in a planetary mill – from 0.18 to 130 µm. The lower limits and submicron sizes here refer to individual small particles, and micron sizes up to the upper limits refer to strong sintered porous agglomerates of submicron ZnO particles that are not separated by ultrasonic treatment in water [11].

Fig. 8 presents the elemental chemical composition of the calcined combustion product determined by the EDS method after milling by various methods. The time of grinding in a mortar was 10 min, in a DBM – 60 min, in a PCM – 45 s.

The local elemental composition of the calcined combustion product after grinding (Fig. 8) shows the presence of carbon residues ranging from 0.83 to 2.01 % after grinding by all methods, but the presence of iron impurities was found only after grinding in mills: 2.07–6.38 % (DBM) and 0.8–2.4 % (PCM).

Based on the results obtained, one can conclude that simple grinding in a mortar gives the purest and finest ZnO powder obtained by the SHS-S method.

SHS-S product photocatalytic activity

Fig. 9 presents the results of the application of the non-calcined SHS-S product ground in a drum ball mill and a mortar for the phenol photocatalytic decomposition in an aqueous solution under the action of ultraviolet irradiation.

Fig. 9 shows that, regardless of the duration of grinding in a DBM, the phenol concentration behaves much the same – during the entire 5.5 h of irradiation, it fluctuates around the initial relative value of 100 % without a noticeable decrease, and even vice versa, with an increase of up to 20 % against the initial value.

The results of studying the phenol photocatalytic decomposition using the combustion product ground by different methods and calcined for 1 h at different temperatures (500, 650, and 750 °C) are shown in Fig. 10.

It is obvious that the selected calcination temperatures give similar results, while different grinding methods lead to significantly different results. Calcined ZnO powder ground in a mortar has a much higher photocatalytic activity than one ground in ball and planetary mills. Judging by the data in Fig. 8 about the local content of elements in ZnO powder, all these three powders have approximately the same small carbon impurities (in the range of 1–2 %), but the powder after grinding in a mortar does not have iron Fe impurities and, after grinding in mills, iron contamination is more noticeable: from 2.07 to 6.38 % in a DBM and from 0.8 to 2.4 % in a PCM. Moreover, Fig. 6 and 7 show that when grinding in a mortar, the powder is much finer than when grinding in mills, in particular, the average particle size D_{50}=0.90 µm when grinding in a mortar and D_{50}=8.27 µm after a PCM. Thus, when grinding the calcined solution SHS product in a mortar, the obtained ZnO powder is much purer and finer than when grinding in ball and planetary mills. This explains the highest photocatalytic activity of ZnO powder ground in a mortar in the reaction of phenol decomposition in an aqueous solution under the action of ultraviolet irradiation (Fig. 10).

Obtaining SHS-G product

During heating, convective mixing of the viscous gel was observed, and after some time a combustion reaction spontaneously began, the duration of which determined the combustion time. Fig. 11 demonstrates the dependence of the mass conservation coefficient of the product of the combustion in the K_M vessel on the φ criterion in the range of $0.25 \leq \varphi \leq 3$ for this SHS-G process obtained as a result of three experiments for each value of the φ criterion.

When comparing Fig. 11 (for the SHS-G process with gel combustion) with a similar Fig. 1 (for the SHS-S process with solution combustion), one can observe that they are close and indicate the existence of an explosive combustion mode with an almost complete release of the combustion product from the reaction vessel in the range of molar ratios of glycine with zinc nitrate in the initial mixture of re-agents of $0.5 \leq \varphi \leq 1.5$. In the range of $\varphi > 1.5$, the K_M mass conservation coefficient of the SHS-G product tends to the K_M=1 value with an increase in the φ criterion up to the value of φ=3. By comparison, in the case of the SHS-S product, the K_M coefficient tended to the K_M=1.5 value, which is an indication of greater contamination of the SHS-S product with the unburned glycine fuel residues. For both the SHS-G and SHS-S processes, the ignition delay time differs significantly. In the case of using dry mixtures of re-agents, combustion begins much faster (1.5 min on average) than in the case of dissolved

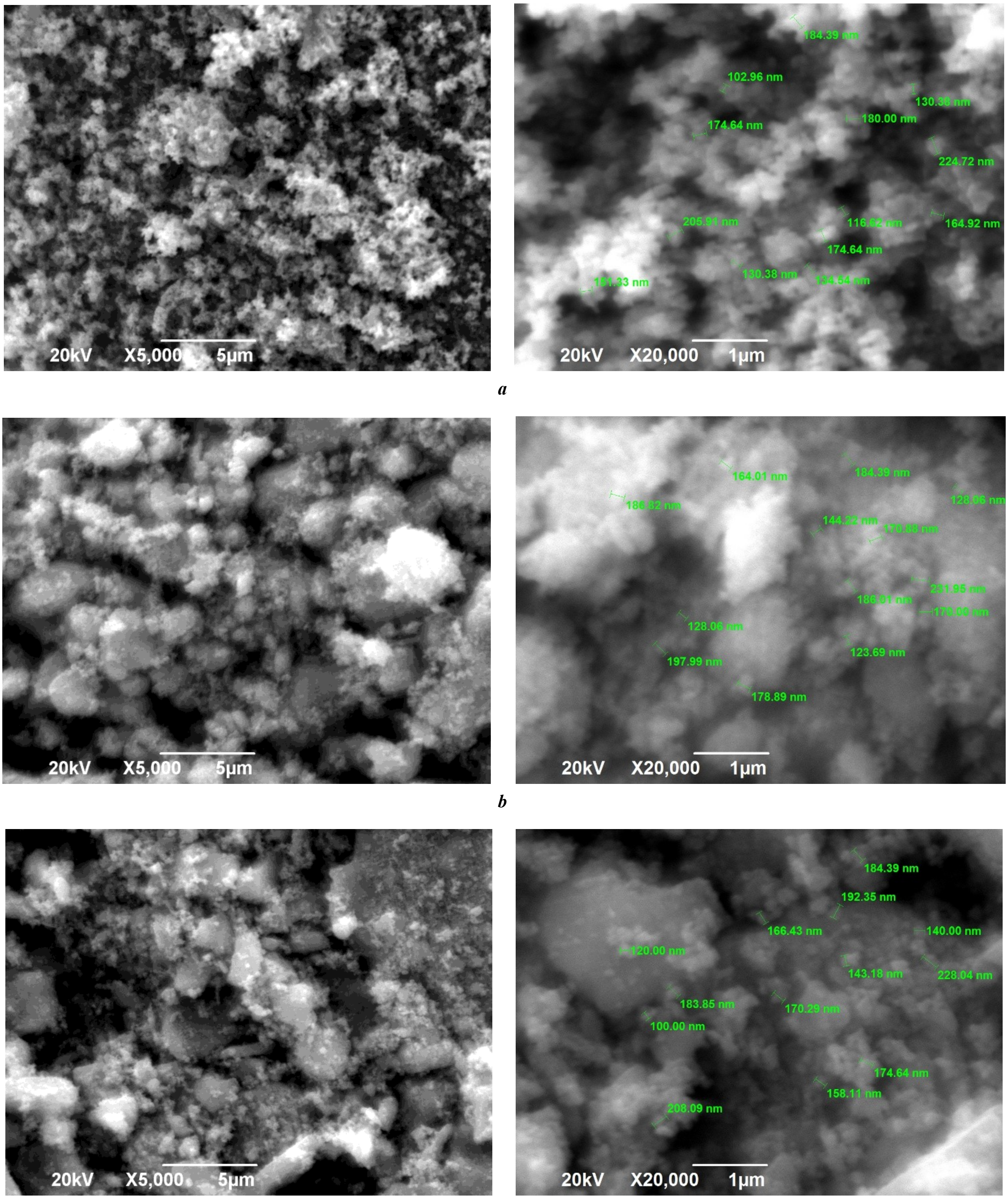

Fig. 6. *Microstructure of the calcined solution combustion (SHS-S) product after grinding:*
a *– in the mortar;* ***b*** *– in the drum ball mill;* ***c*** *– in the planetary-centrifugal mill*

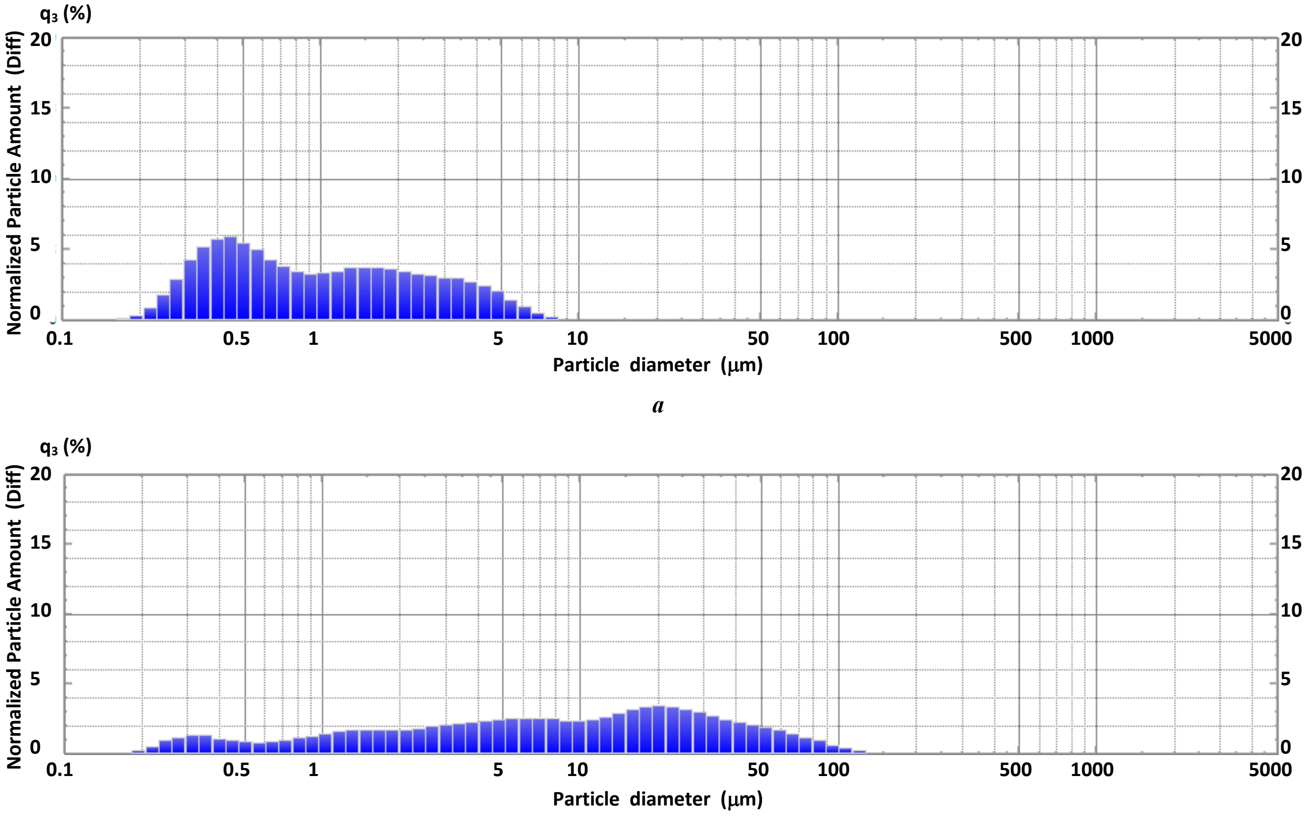

a

b

Fig. 7. *The particle-size distribution (the dependence of the normalized particle amount q_3 (%) on the particle diameter) of the powdered calcined solution combustion (SHS-S) product after grinding:*
***a** – in the mortar, D_{50} = 0.90 μm; **b** – in the planetary-centrifugal mill, D_{50} = 8.27 μm*

re-agents (8 min on average), since in the latter case a lot of time is spent for heating the solution to boiling water and evaporating water before gel formation. The time and type of combustion, color and consistency of the synthesized ZnO combustion product in the SHS-G process remain close to those of the process and product of SHS-S[1].

Composition and structure of the SHS-G products

Fig. 12 and 13 show the results of determining the phase composition and microstructure of non-calcined SHS-G products for three different values of φ criterion: 0.25, 1, and 2.

Fig. 14 shows an example of determining the local content of elements at various points of the synthesized product by the EDS method.

The results of the XRD analysis of the SHS-G product at a minimum value of φ=0.25 show (Fig. 12 a) that the synthesis product consists of two phases: crystalline zinc oxide ZnO and free X-ray contrast carbon C with a graphite crystal lattice. The presence of free carbon indicates that the reaction temperature was not high enough to complete the chemical reaction of glycine oxidation. High peaks relative to the main background of the diffraction pattern indicate the presence of a formed crystal structure of wurtzite in zinc oxide obtained as a result of synthesis. The crystallite size obtained by the CSR assessment according to the Scherrer formula is 48, 41, and 40 nm on three peaks with the highest intensity, and the average crystallite size is 43 nm. Fig. 13 a demonstrates that the resulting powder has a homogeneous structure with non-agglomerated, clearly defined particles of equiaxial submicron crystals. It can be concluded that a highly dispersed powder with a particle size of less than 1 μm consisting of a mixture of nanosized and submicron particles with an average crystallite size of 43 nm has been synthesized.

Fig. 14 shows the results of the EDS analysis of the local elemental composition of this powder at three points. The results show a content of 0.83 to 1.77 wt. % of carbon in the combustion product, on average 1.18 %, which corresponds to the XRD results (Fig. 12 a) on the presence of free carbon in the product. The average values of carbon impurity in the non-calcined SHS-G product determined by the EDS method are equal to 1.45 and 1.9 % for the values of φ=1 and 2, respectively.

At φ=1, the synthesis product consists of two phases as well: crystalline ZnO and X-ray contrast carbon C. The average size of ZnO crystallites according to the Scherrer formula is 21 nm. A smoother transition of the diffraction pattern (Fig. 12 b) from the main background level to the peak level may indicate the appearance of an amorphous component in the synthesis products.

---

[1] *Novikov V.A., Titov A.A., Kryukov N.A., Kachkin E.M. Combustion modes of gel of zinc nitrate with various fuels in the synthesis of zinc oxide nanopowders. Sovremennye materialy, tekhnika i tekhnologii, 2022, no. 2, pp. 17–39. EDN: LFWVFA.*

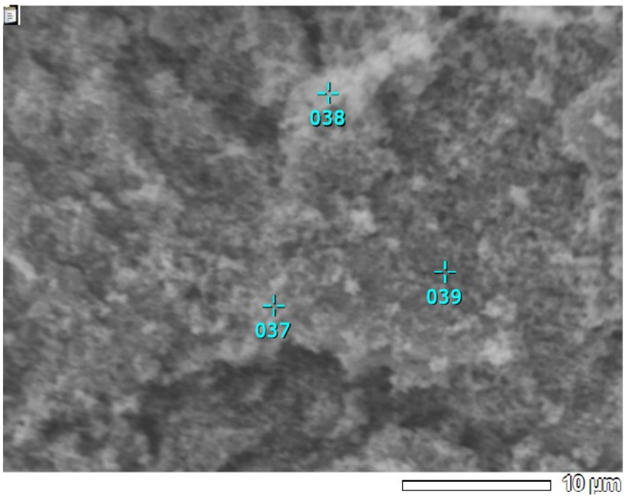

Element	Mass content, %, at the points		
	037	038	039
C	0.83	1.14	0.86
O	6.63	7.77	6.43
Zn	92.54	91.09	92.71

a

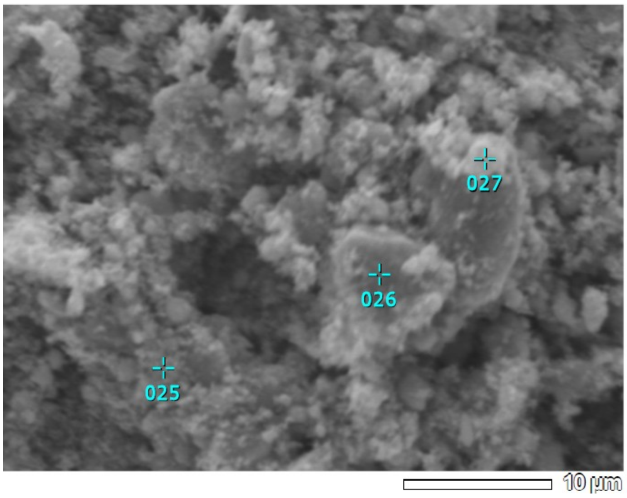

Element	Mass content, %, at the points		
	25	26	27
C	0.76	1.07	2.01
O	5.83	9.32	15.20
Fe	6.38	2.07	4.01
Zn	87.03	87.54	78.78

b

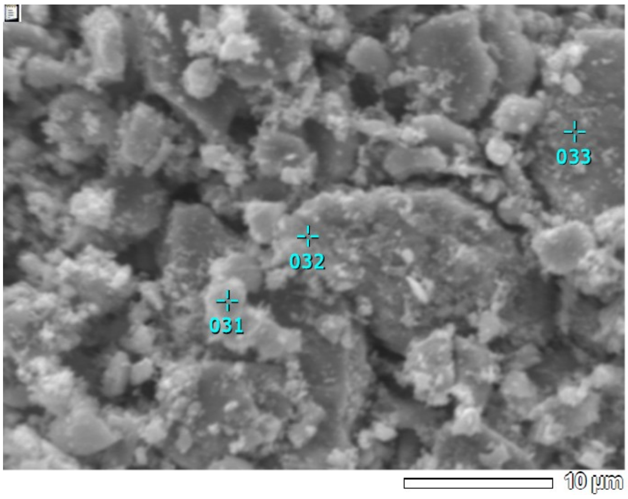

Element	Mass content, %, at the points		
	31	32	33
C	1.7	1.99	0.66
O	10.86	13.13	5.57
Fe	2.40	0.80	1.22
Zn	85.05	84.08	92.54

c

Fig. 8. *The local elemental composition of the calcined solution combustion (SHS-S) product after grinding:*
a *– in the mortar;* ***b*** *– in the drum ball mill;* ***c*** *– in the planetary-centrifugal mill*

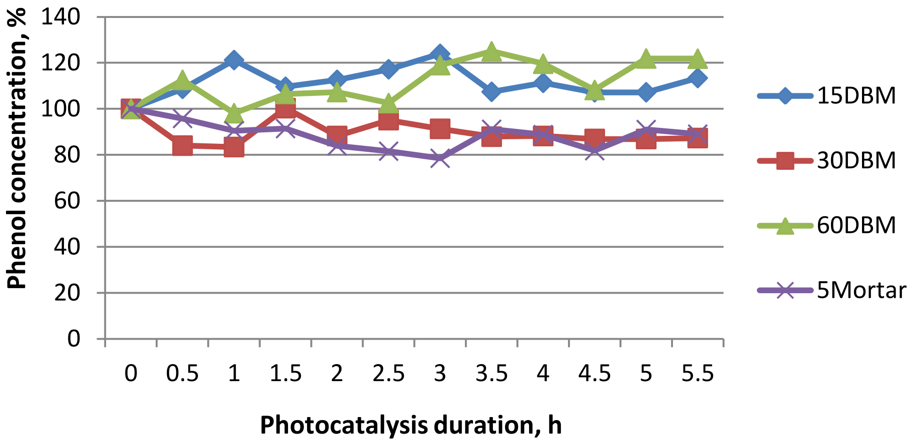

Fig. 9. *Change in time under the action of ultraviolet irradiation of the phenol relative concentration in an aqueous solution with a suspension of particles of the non-calcined solution combustion (SHS-S) product ground in the drum ball mill (15, 30, and 60 min) and in the mortar (5 min)*

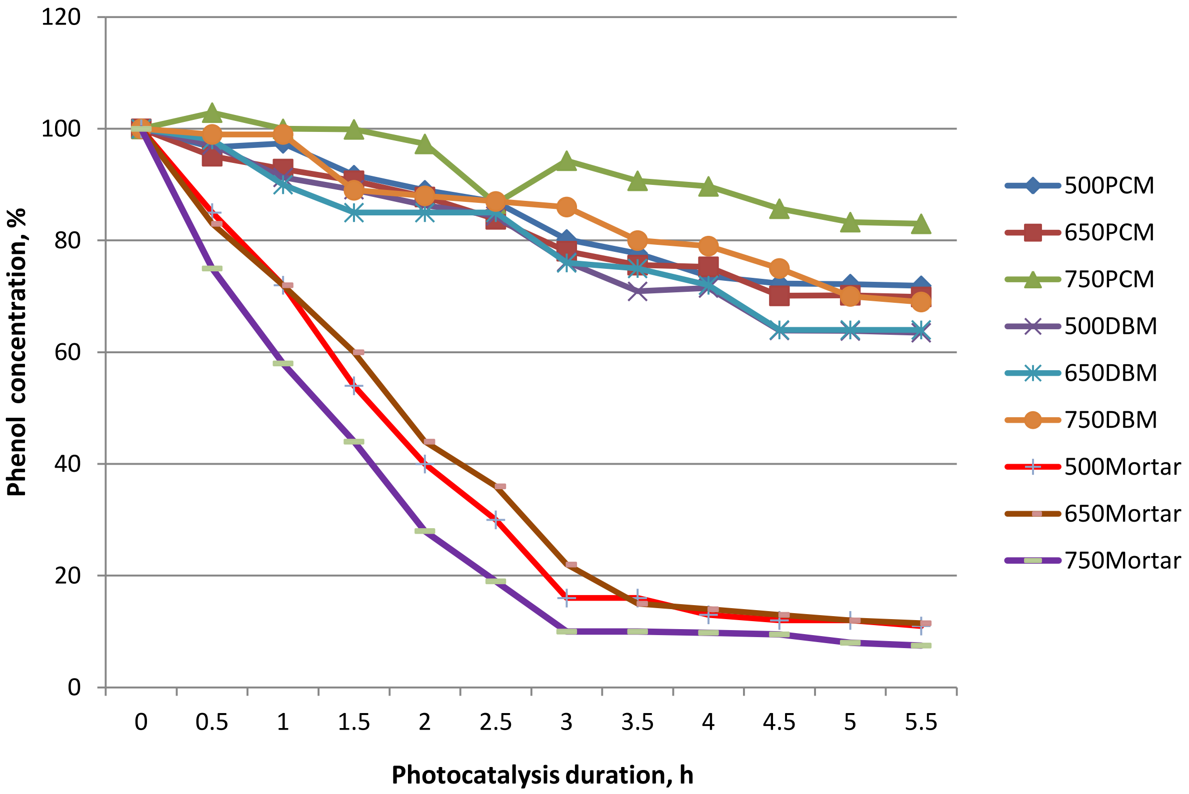

Fig. 10. *Change in time under the action of ultraviolet irradiation of the phenol relative concentration in an aqueous solution with a suspension of particles of the solution combustion (SHS-S) product calcined at different temperatures (figures for lines, °C) and ground in the mortar (10 min), in the drum ball mill (DBM) (30 min); and in the planetary-centrifugal mill (PCM) (45 s)*

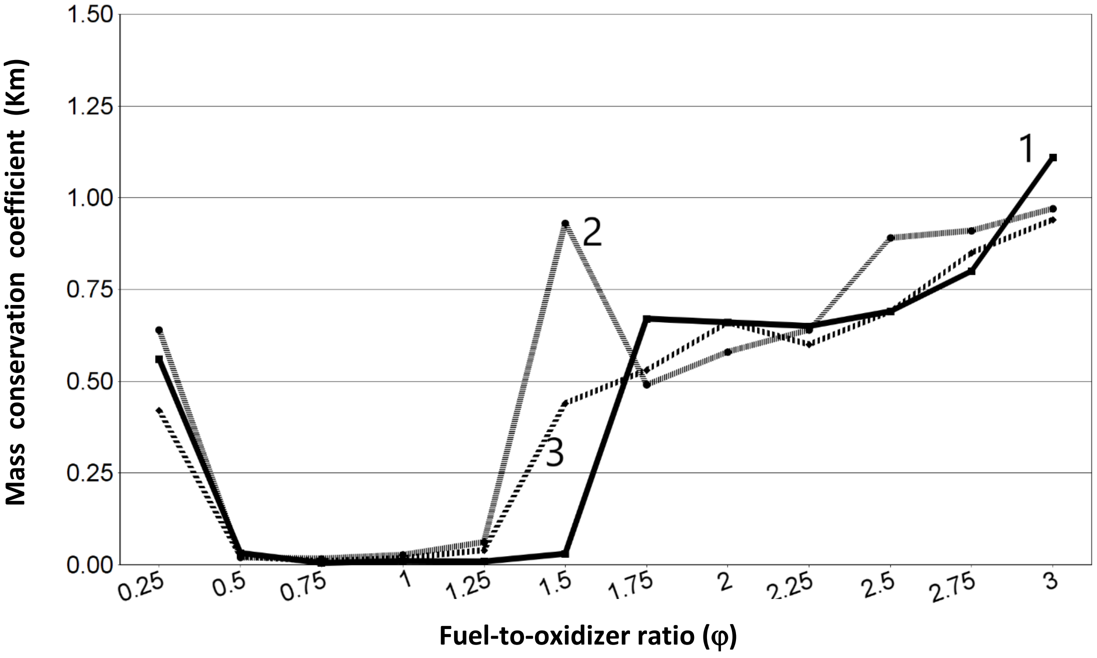

Fig. 11. *The dependence of the product mass conservation coefficient* K_M *on the value of the criterion φ at the combustion of gel from dry reagents (SHS-G). The numbers on the lines indicate the numbers of experiments*

This is confirmed by the structure of the synthesized product in the form of a frozen foamy mass with many pores of various diameters and agglomerates of small submicron oval particles (Fig. 13 b). Local elemental analysis of the combustion product gives an average carbon content of 1.45 wt. %.

With a further increase in φ, the microstructure of the combustion product remains similar – in the form of a frozen melted amorphous foam with many pores of various diameters and agglomerates of small nanosized and submicron particles (Fig. 13 c). The diffraction pattern (Fig. 12 c) for φ=2 shows the presence of only the ZnO crystalline phase with an average crystallite size of 34 nm. At the same time, from the results of the EDS analysis of this SHS-G product, it follows that the content of carbon impurities in it is on average 1.9 %, which indicates the presence of carbon in the form of an impurity of free carbon in amorphous form and in the form of combined carbon in the unburned fuel residues. The EDS analysis of a similar SHS-S product synthesized at φ=2 showed a significantly higher average carbon content – about 10 % [11]. From the comparison of carbon content in the SHS-G and SHS-S products synthesized at other φ values, the general conclusion follows that the carbon impurity content in the non-calcined SHS-G products is significantly lower in comparison with the non-calcined SHS-S products synthesized at the same values of φ criterion.

The results of determining the carbon impurity in the SHS-G product after calcination (oxidative annealing) at a temperature of 650 °C during 1 h (φ=2) are shown in Fig. 15 and equal on average to 0.94 %.

Thus, calcination noticeably reduces the carbon impurity content in the SHS-G product from 1.9 % for the non-calcined product at φ=2 to 0.94 % (Fig. 15).

Photocatalytic activity of the synthesized products

Fig. 16 presents the results of comparing the photocatalytic activity for non-calcined synthesis products obtained in the SHS-S and SHS-G modes with different fuel/oxidizer ratios in the composition of the initial reaction mixture, i.e., with different φ criterion values: 0.25, 1, and 2.

Fig. 16 shows that for all φ values, in the first hours of ultraviolet irradiation, the SHS-G products exhibit slightly higher catalytic activity, which is close to the activity of the SHS-S products for the same φ value, but after 5 h of irradiation, their activity practically coincides. In general, the photocatalytic activity of non-calcined products is low, especially at φ=2, and leads to a decrease in the phenol concentration in an aqueous solution by 40–60 % over 5 h of irradiation. These results can be explained by the fact that non-calcined SHS-G products are slightly purer in terms of the carbon impurity content than non-calcined SHS-S products. At φ=2, the carbon impurity content is the highest compared to φ=0.25 and 1, and the smallest ZnO crystallite size of 21 nm (Fig. 12) is observed at φ=1 with the highest photocatalytic activity.

Fig. 17 shows the results of the same comparison for the SHS-S and SHS-G products calcined for 1 h at 650 °C.

The authors also determined the particle-size composition of these calcined and ground in a mortar (10 min) SHS-G products synthesized at various φ values (Fig. 18).

As one can see from Fig. 17, calcination (650 °C, 1 h) of the synthesized SHS-S and SHS-G products significantly increases their photocatalytic activity, especially of the SHS-G products, which contribute to the almost complete phenol decomposition in 3.5–4.5 h of ultraviolet irradiation. Such activity of the products is explained both by their significant purification from carbon impurities during calcination to a level of 1 % ([11] and Fig. 15) and by

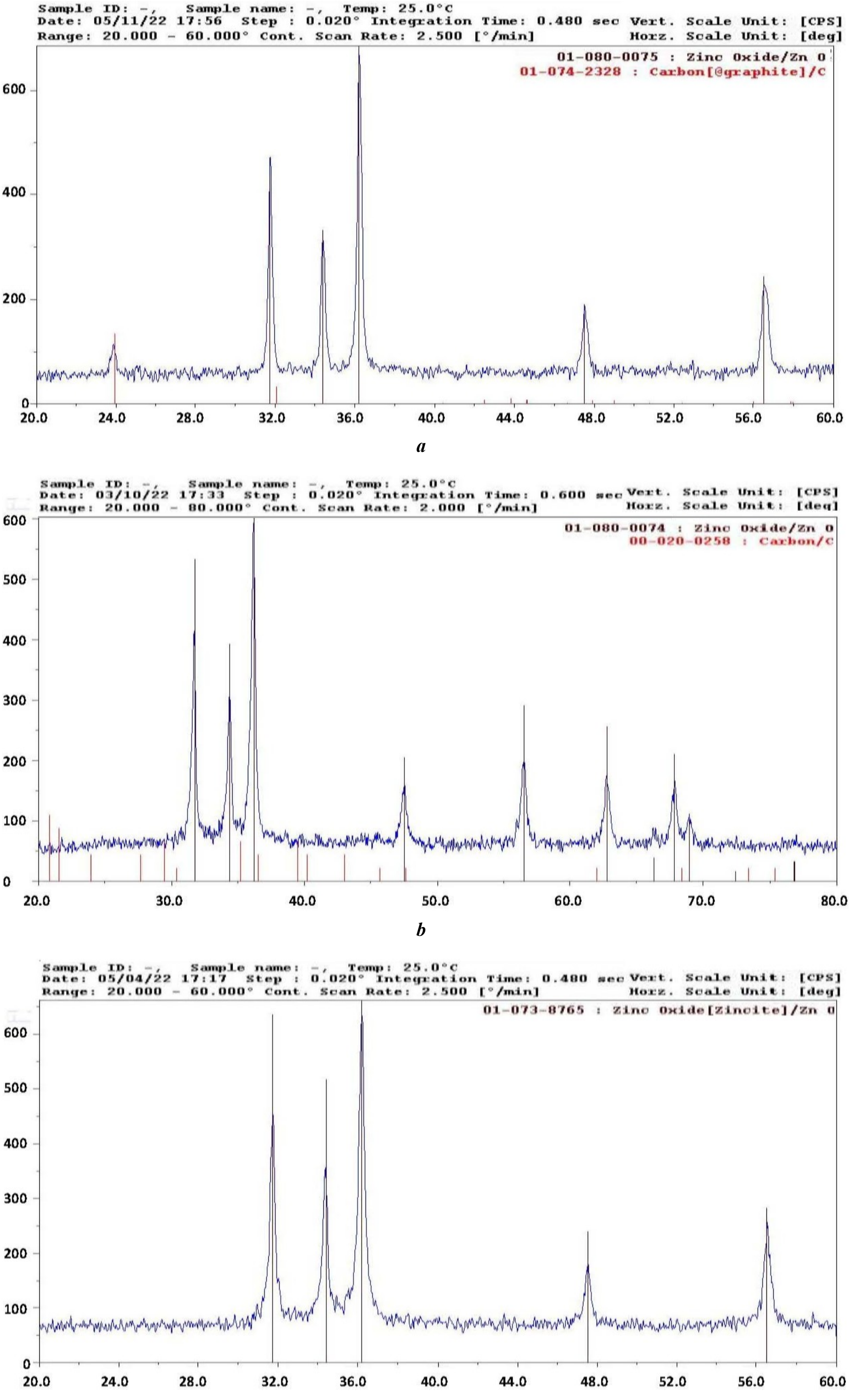

a

b

c

Fig. 12. *XRD patterns of the non-calcined gel combustion (SHS-G) product at various φ:*
***a** – φ=0.25; **b** – φ=1; **c** – φ=2*

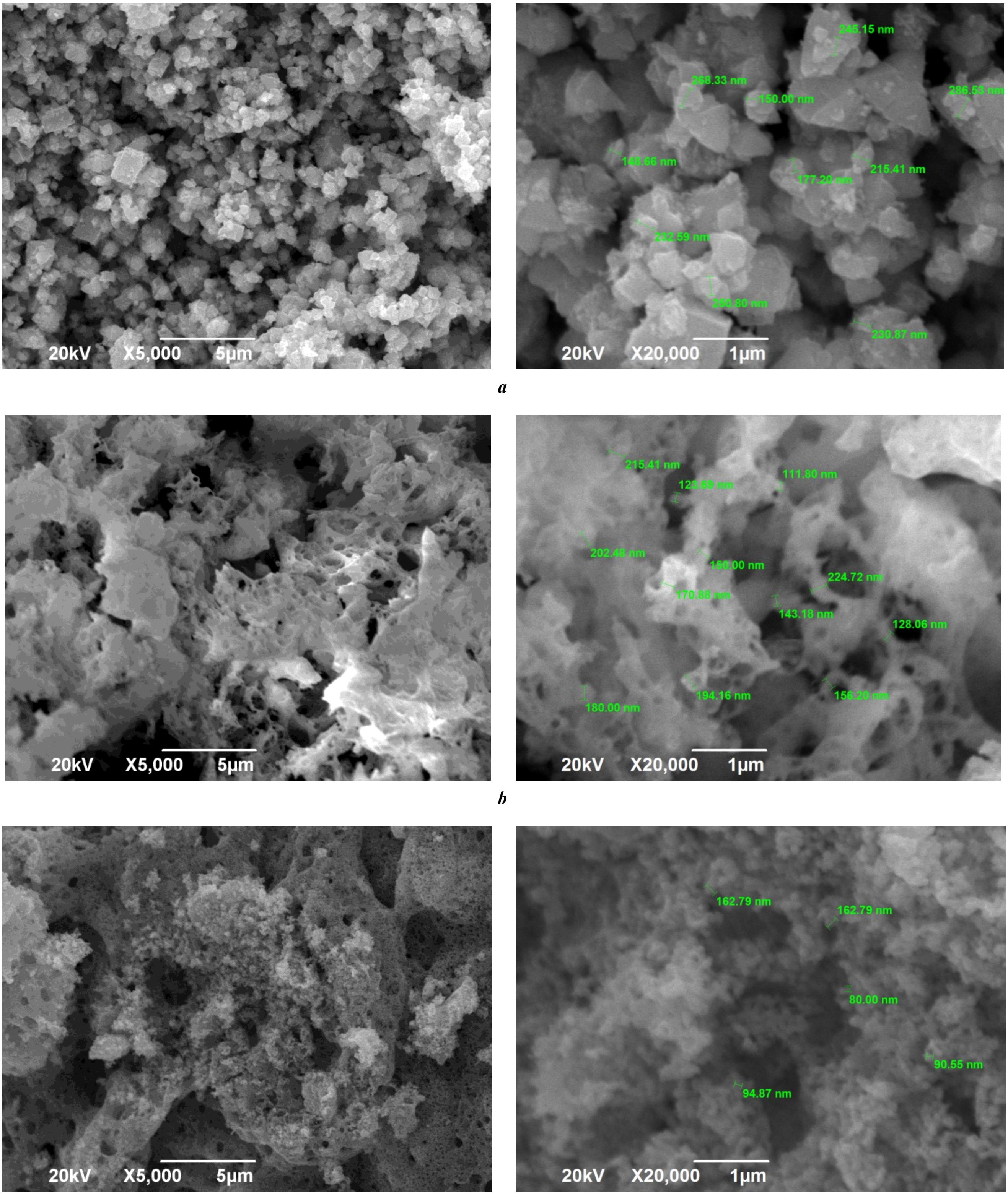

a

b

c

Fig. 13. *Microstructure of the non-calcined gel combustion (SHS-G) product at various φ:*
a *– φ=0.25;* ***b*** *– φ=1;* ***c*** *– φ=2*

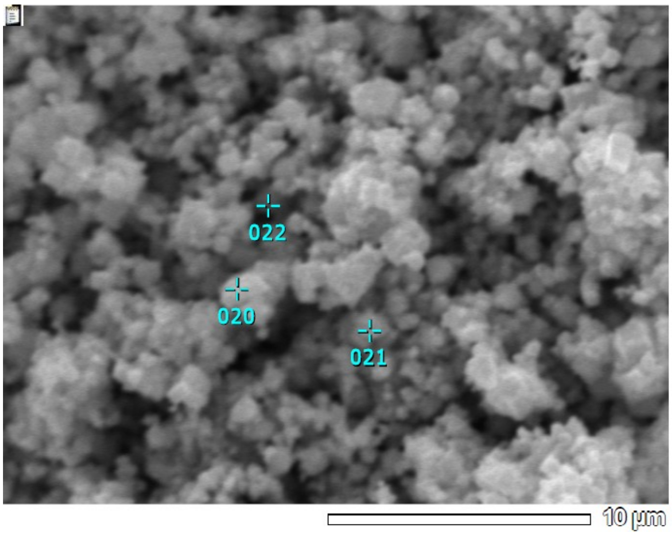

Element	Mass content, %, at the points		
	20	21	22
C	1.77	0.95	0.83
O	13.95	6.02	6.73
Zn	84.29	93.03	92.44

Fig. 14. *The local elemental composition of the non-calcined gel combustion (SHS-G) product at φ=0.25*

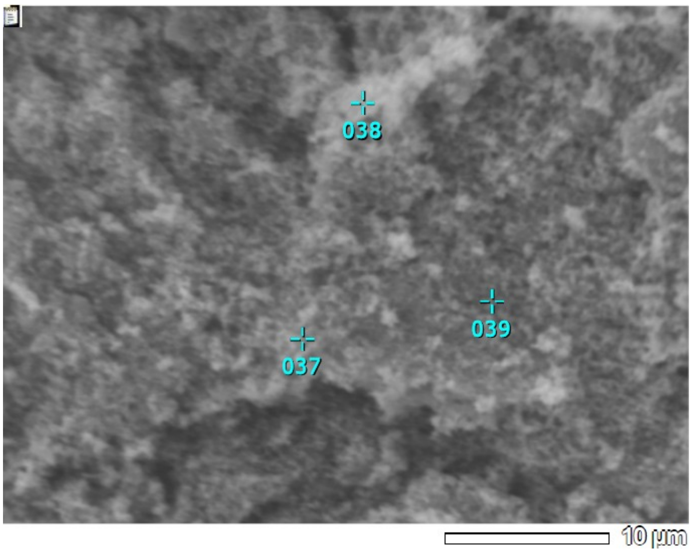

Element	Mass content, %, at the points		
	037	038	039
C	0.83	1.14	0.86
O	6.63	7.77	6.43
Zn	92.54	91.09	92.71

Fig. 15. *The local elemental composition of the calcined gel combustion (SHS-G) product at φ=2*

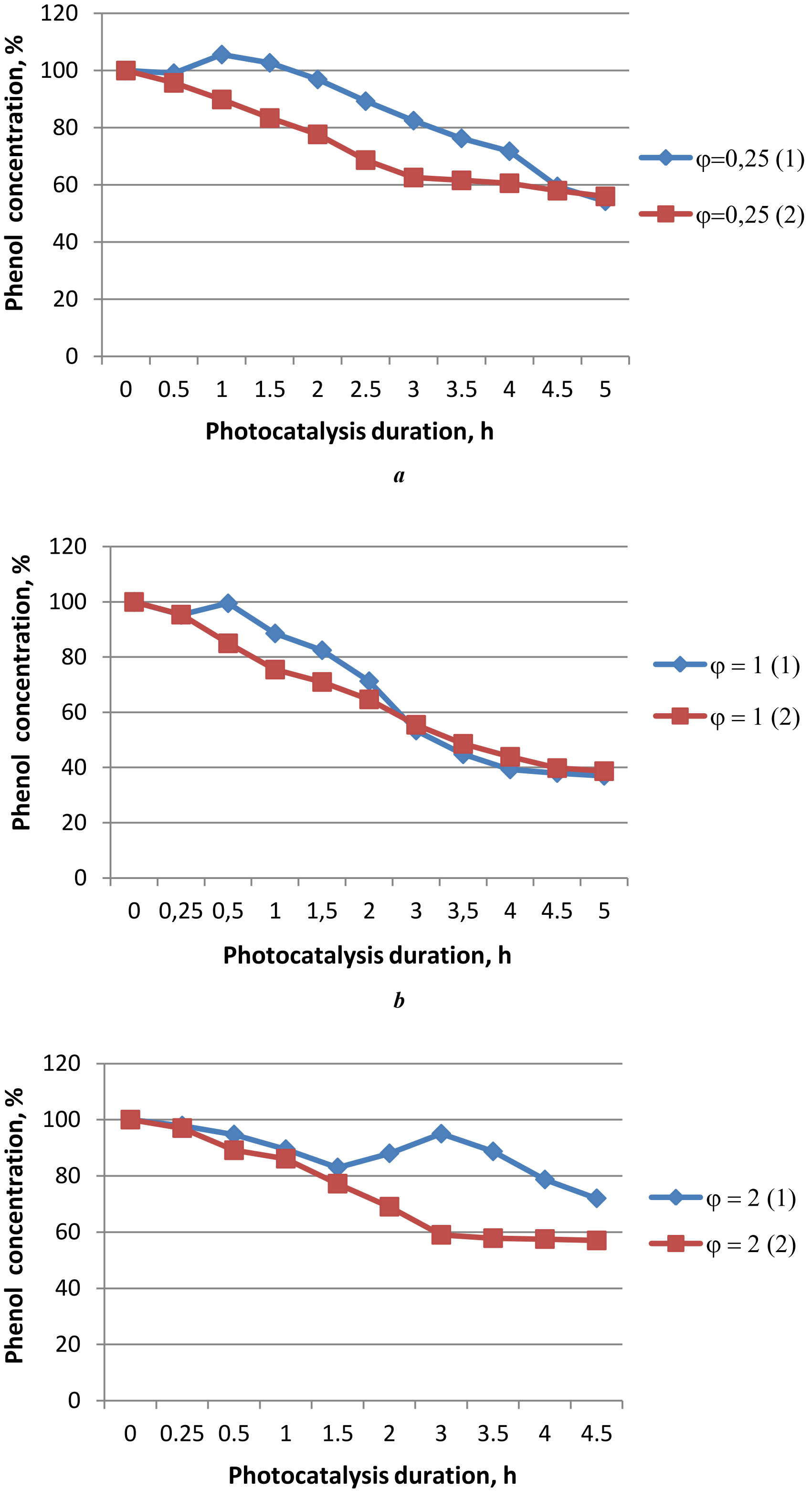

a

b

c

Fig. 16. *Change in time under the action of ultraviolet irradiation of the phenol relative concentration in an aqueous solution with a suspension of particles of non-calcined products of solution combustion (SHS-S) (1) and gel combustion (SHS-G) (2) synthesized at:*
a *– φ=0.25;* ***b*** *– φ=1;* ***c*** *– φ=2*

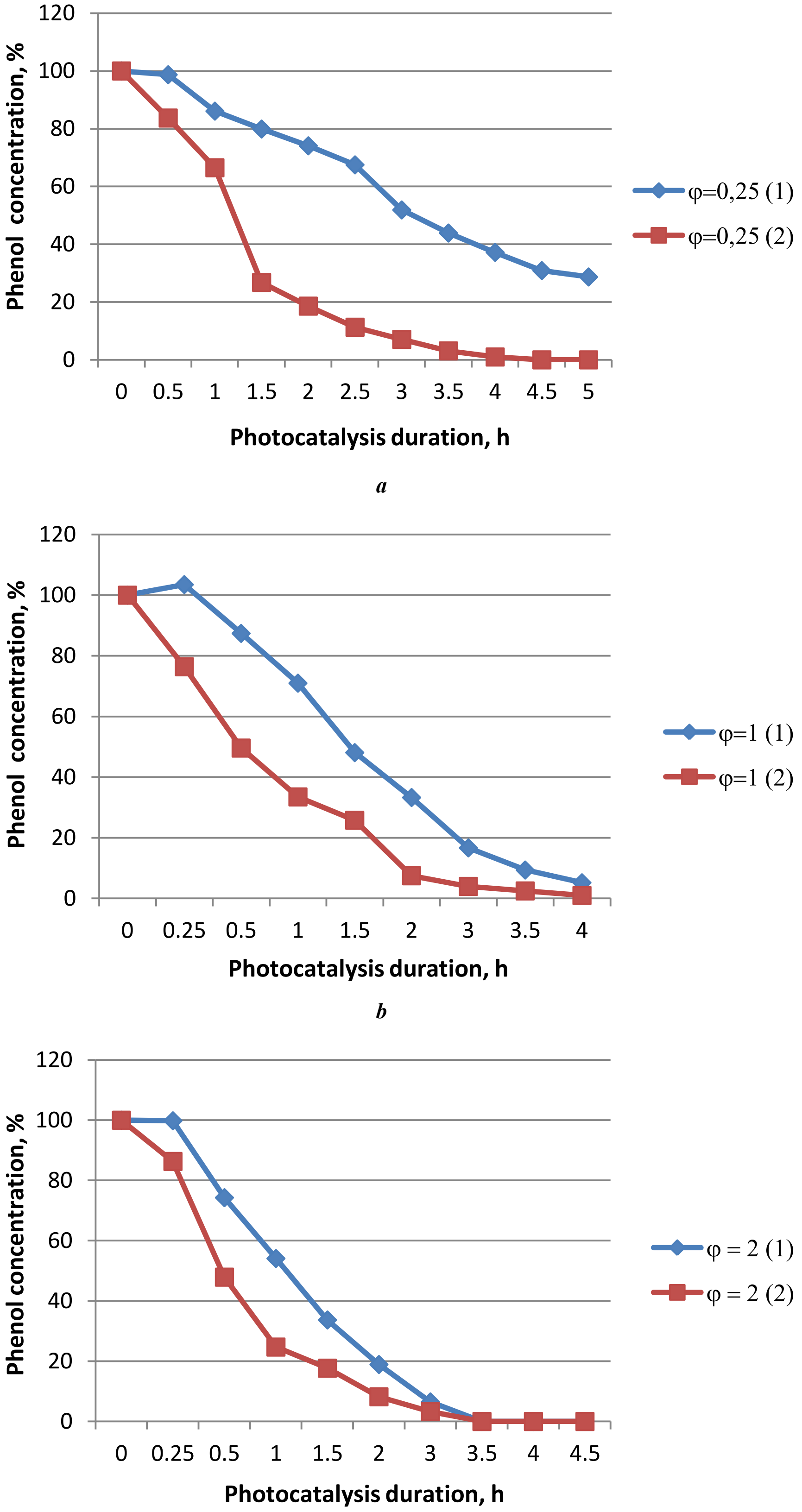

a

b

c

Fig. 17. *Change in time under the action of ultraviolet irradiation of the phenol relative concentration in an aqueous solution with a suspension of particles of calcined products of solution combustion (SHS-S) (1) and gel combustion (SHS-G) (2) synthesized at:* ***a*** *– φ=0.25;* ***b*** *– φ=1;* ***c*** *– φ=2*

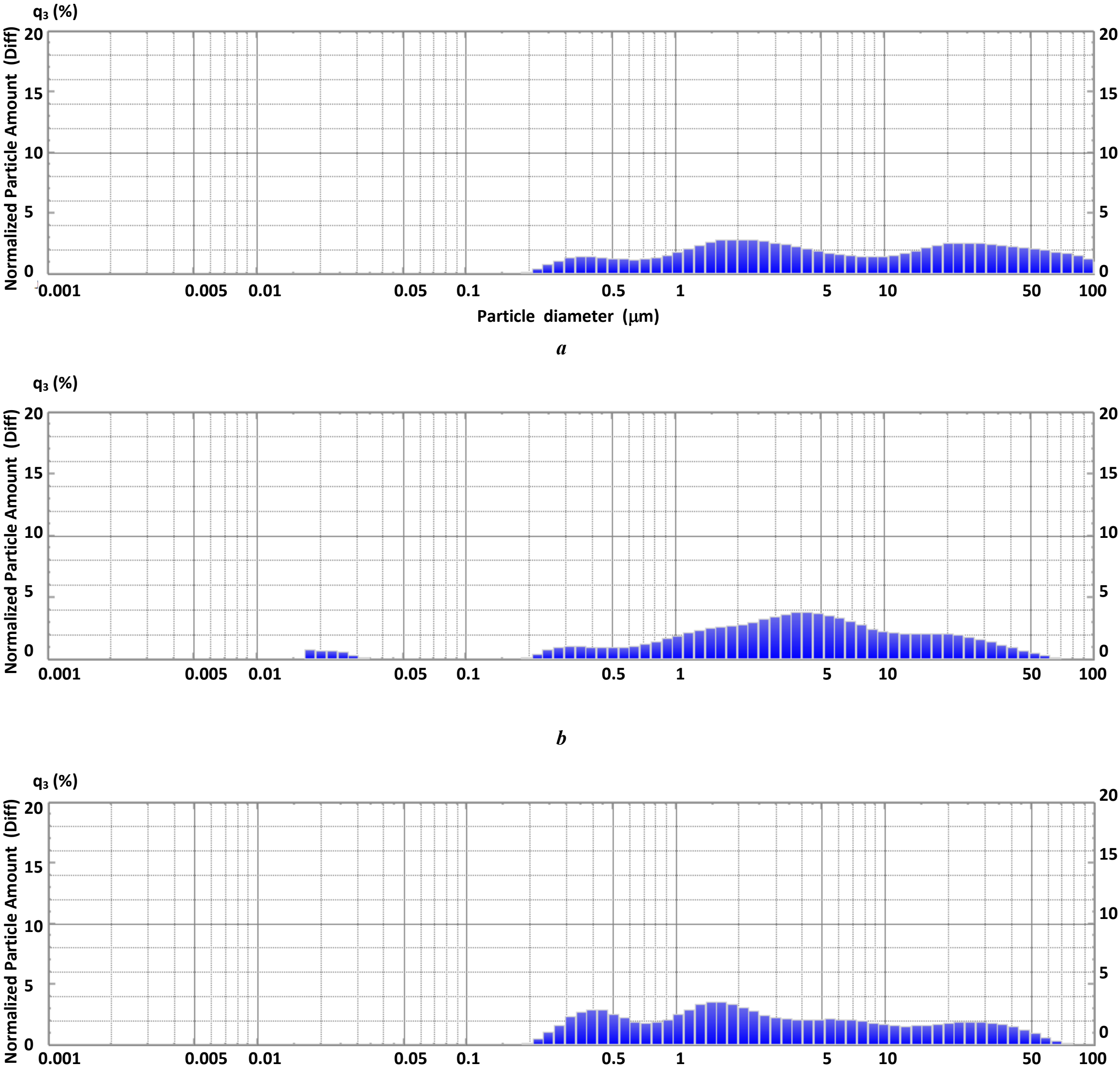

a

b

c

Fig. 18. *The particle-size distribution (the dependence of the normalized particle amount q_3 (%) on the particle diameter) of the calcined and ground in the mortar (10 minutes) SHS-G product synthesized at:*
a *– φ=0.25, D_{50}=5.4 µm;* ***b*** *– φ=1, D_{50}=3.81 µm;* ***c*** *– φ=2, D_{50}=2.37 µm*

the smallest sizes of ZnO particles (Fig. 18). The most active SHS-G product at φ=2 has the smallest average particle size D_{50}=2.37 µm and 90 % of the particles are smaller than 27 µm. In the SHS-G product at φ=1 with an average particle size D_{50}=3.81 µm, even the presence of 4 % of nanoparticles with a size of less than 0.035 µm is observed, and 90 % of the particles have a size of less than 22 µm. The largest particles are at φ=0.25: the average size D_{50}=5.4 µm, 90 % of particles are smaller than 55 µm. However, in some time after the start of ultraviolet irradiation, the photocatalytic activity of the SHS-G and SHS-S products becomes the same, for example, after 3.5 h at φ=2.

DISCUSSION

To increase the photocatalytic activity of zinc oxide synthesized by the solution SHS method, the authors carried out a detailed study of grinding the SHS-S product in a drum ball mill, a planetary centrifugal mill, and a mortar. Intensive grinding in a DBM and PCM leads to a strong sticking of the ground material on the grinding agents and the walls of the mill drums (Fig. 3), which creates great inconvenience due to the necessity of cleaning them; to the darkening of the ground product due to high contamination with iron oxide (30 % after grinding in the DBM and 36 % after grinding in the PCM according to Fig. 5) due to the milling of iron from steel grinding agents and drums; to the formation of large dense agglomerates from the initial small nanosized and submicron ZnO particles of the synthesized product (Fig. 4). The purest (without iron impurity) and finest ZnO powder is produced by simply grinding the synthesis product in a ceramic mortar.

Non-calcined ZnO powders ground by any method exhibit weak photocatalytic properties during the phenol decomposition (Fig. 9) due to their contamination with up to 10 % carbon (Fig. 5, Table 1). An increase in the phenol concentration by 20 % over 100 % observed in Fig. 9 can be explained by the release of unburned organic fuel residues from porous agglomerates of non-calcined ZnO particles into the solution. These residues have fluorescent properties similar to phenol, and the total concentration of these residues and phenol is reflected in the graph and can exceed 100 % [11]. (Calcination at 650 °C for 1 h and more leads to a significant decrease in the unburned organic fuel residues in the porous agglomerates of ZnO particles. The exceeding of 100 % of the relative phenol concentration in the experiments on the photocatalytic phenol decomposition under the action of ultraviolet irradiation is not observed [11].)

Calcination (oxidative annealing) at 650 °C for 1 h significantly reduces the carbon impurity content in the SHS-S product to a level of 1–2 %, but does not free the product ground in a DBM and PCM from the iron impurity (Fig. 8). The amorphous component from the unburned fuel residues is absent in the structure of calcined products (Fig. 6). The most homogeneous and fine powder structure is obtained after grinding in a mortar (Fig. 7). As a result, the highest photocatalytic activity in the reaction of phenol decomposition in an aqueous solution under the action of ultraviolet irradiation is observed in the calcined ZnO powder ground in a ceramic mortar (Fig. 10). However, this photocatalytic activity does not exceed the photocatalytic activity of the calcined ZnO powder without any grinding given in the work [11].

In such manner, through grinding the nanostructured product of the solution SHS, it was not possible to increase its photocatalytic activity in the phenol decomposition. Firstly, grinding in a ceramic mortar slightly reduces the photocatalytic activity due to an increase in the size of agglomerates of nano- and submicron particles of the ZnO powder. Secondly, grinding in drum ball and planetary centrifugal mills even significantly impairs the photocatalytic activity both due to a greater increase in the size and density of agglomerates of the ZnO powder particle and due to contamination with iron impurities from steel grinding agents and mill drums.

The study of another SHS process variant, when synthesizing ZnO nanopowder from a gel formed from moistened initial dry mixtures of zinc nitrate and glycine (SHS-G process), showed that its characteristics and product, although similar (as can be seen from the comparison of Fig. 1 and Fig. 11, as well as from the description of the products), in some positions they compare favorably with the solution SHS process (SHS-S). Firstly, the SHS-G process is easier and faster to implement, since there is no need to prepare saturated solutions of re-agents, combustion begins much faster (1.5 min on average) than in the case of dissolved re-agents (8 min on average), since in the case of the SHS-S process, a lot of time is spent for heating the solution to boiling water and evaporating water before gel formation. Secondly, the synthesized SHS-G product is finer and cleaner in terms of the content of carbon impurities (Fig. 11–14). The average carbon content in the non-calcined SHS-G product is 1–2 % for different φ criterion values, while in the non-calcined SHS-S product the average carbon content is about 10 % [11]. Calcination at a temperature of 650 °C for 1 h significantly reduces the average content of carbon impurity in the SHS-G product from 2 % for the non-calcined product to 1 % (Fig. 15). On average, about 1 % of carbon is also contained in the SHS-S product after calcinations at 650 °C [11].

Non-calcined SHS-G and SHS-S products have a low photocatalytic activity in the phenol decomposition (Fig. 16), which is slightly higher for the SHS-G product due to the higher purity in terms of the carbon impurity content. The calcinations of the synthesized SHS-G and SHS-S products significantly increases their photocatalytic activity (Fig. 17), especially of the SHS-G products, which contribute to the almost complete phenol decomposition within 3.5–4.5 h of ultraviolet irradiation. Such activity of the products is explained both by their significant purification from carbon impurities during calcinations to a level of 1 % ([11] and Fig. 15) and by the smallest sizes of ZnO particles (Fig. 18). However, the difference between the photocatalytic activity of the SHS-G and SHS-S products, both non-calcined (Fig. 16) and calcined (Fig. 17), in the phenol decomposition, is noticeable only within the first few hours (3.5–5 h in most cases) of ultraviolet irradiation. Then this difference disappears, i.e., the SHS-G and SHS-S products have almost the same photocatalytic activity in the phenol decomposition under the action of ultraviolet irradiation.

Such a result can be explained by the fact that both related processes – the combustion of a solution of an exothermic mixture of initial re-agents of zinc nitrate oxidizer and glycine organic fuel (SHS-S) and the combustion of a gel from a moistened mixture of dry initial re-agents (SHS-G) – lead to the synthesis of almost one and the same product: highly dispersed crystalline powder of zinc oxide ZnO with an admixture of amorphous unburned organic fuel residues in the form of free and combined carbon (Fig. 2 and 13). After the combustion product is calcined in a muffle furnace with an air atmosphere during 1 h at 650 °C, the carbon content decreases to 1 % in average and the calcined synthesis product acquires a uniform powder body structure from the porous agglomerates up to 100 μm in size, sintered from crystalline nanosized and submicron ZnO particles with an average crystallite size of 10 to 50 nm. Such nanostructured zinc oxide demonstrates high photocatalytic activity in the phenol decomposition in an aqueous solution with a suspension of ZnO particles under the action of ultraviolet irradiation leading to almost complete phenol decomposition in less than 4.5 h. This photocatalytic activity is comparable to the activity in the phenol photocatalytic decomposition of ZnO powders with a nanosized substructure obtained by the hydrothermal method after annealing at 650 °C for 3–5 h [14]. At the same time, the SHS-S and SHS-G methods are much more productive than the hydrothermal method, and the synthesized photocatalyst particles are much larger.

The positive aspects of these SHS methods should also include the presence of carbon impurities in their products (up to 1 % in calcined products), which can increase the photocatalytic activity of synthesized ZnO, as shown in the works [15–17]. Moreover, SHS processes are characterized by an increased defectiveness of synthesized powders due to very high rates of heating and cooling of combustion products, which can also increase their photocatalytic activity [18; 19]. One more advantage of the synthesized ZnO powders is that sufficiently large sintered porous agglomerates up to 100 μm in size from the high-dispersed ZnO particles, with their high photocatalytic activity, can significantly simplify the possibility of their application in the suspension state in a membrane photocatalytic plant for fine water purification. In this case, the separation of the photocatalyst after water purification can be carried out by simple filtration instead of a much more complex and inefficient separation through a ceramic ultrafiltration membrane with a pore size of 100 nm [14].

Consequently, the authors failed to increase the photocatalytic activity in the phenol decomposition of a fine zinc oxide ZnO powder obtained by burning a solution of the zinc nitrate and glycine mixture (the solution SHS method) either by grinding a product of the solution combustion of an exothermic mixture of initial zinc nitrate and glycine re-agents, or by using a combustion product of a gel from a moistened mixture of dry re-agents. The authors of this paper continue to study the possibility of increasing the photocatalytic activity of this powder by doping it with various metal elements (Fe, Mg, Ni, Co), since it is known that such doping can significantly increase the photocatalytic activity of zinc oxide and make it effective in the decomposition of organic water pollutants when irradiated both with visible light and with ultraviolet radiation, which is very important for the practical application of a photocatalyst for the industrial wastewater treatment [20; 21]. Therefore, a simple energy-efficient method of burning mixtures of zinc nitrate with glycine will allow obtaining an inexpensive nanostructured catalyst based on doped zinc oxide with high photocatalytic activity in the phenol decomposition under the action of visible light.

CONCLUSIONS

1. Nanostructured zinc oxide ZnO produced by the method of the solution self-propagating high-temperature synthesis through the combustion of a solution of a mixture of zinc nitrate re-agents, with glycine and subsequent calcination in an oxidizing air atmosphere, has a high photocatalytic activity in the phenol decomposition in an aqueous solution under the action of ultraviolet irradiation, but is ineffective when irradiated with visible light.

2. Grinding of this SHS-S product in a drum ball mill, planetary centrifugal mill, and in a mortar to increase its photocatalytic activity did not lead to a desired result. Intensive grinding in a DBM and PCM is accompanied by a large contamination of the product with iron oxide due to the milling of iron from steel grinding agents and drums, as well as by the formation of large dense agglomerates from the initial small nanosized and submicron ZnO particles, which significantly reduces the photocatalytic activity of the ground product. The purest (without iron impurity) and fine ZnO powder is produced by simply grinding the synthesis product in a ceramic mortar, but its photocatalytic activity does not increase from this.

3. The study of another version of the SHS process, when synthesizing ZnO from a gel formed from the moistened initial dry mixtures of zinc nitrate and glycine (SHS-G process), showed that its characteristics and product, although similar, differ from the SHS-S process. Firstly, it is implemented easier and faster. Secondly, the SHS-G product is smaller and cleaner in terms of the content of carbon impurities. However, the difference between the photocatalytic activity of the SHS-G and SHS-S products in the phenol decomposition is noticeable only at the initial stage of ultraviolet irradiation, after which this difference disappears. The calcined SHS-G and SHS-S products have practically the same high photocatalytic activity in the phenol decomposition under the action of ultraviolet irradiation causing almost complete phenol decomposition in 3.5–4.5 h of ultraviolet irradiation.

4. Neither by grinding the SHS-S product, nor by using the SHS-G method, it was possible to increase the photocatalytic activity in the phenol decomposition of the highly dispersed zinc oxide powder produced by these SHS methods. Probably, the continuation of these studies concerning the use of doping of zinc oxide synthesized by the combustion of mixtures of re-agents with various metal elements (Fe, Mg, Ni, Co) will help to significantly increase its photocatalytic activity and make it effective in the phenol decomposition upon irradiation with visible light.

REFERENCES

1. Anku W.W., Mamo M.A., Govender P.P. Phenolic compounds in water: sources, reactivity, toxicity and treatment methods. *Phenolic Compounds – Natural Sources, Importance and Applications*. Croatia, InTechOpen Publ., 2017, pp. 419–443. DOI: 10.5772/66927.
2. Alberti S., Basciu I., Vocciante M., Ferretti M. Experimental and physico-chemical comparison of ZnO nanoparticles' activity for photocatalytic applications in wastewater treatment. *Catalysts*, 2021, vol. 11, no. 6, pp. 678–691. DOI: 10.3390/catal11060678.
3. Ong C.B., Ng L.Y., Mohammad A.W. A review of ZnO nanoparticles as solar photocatalysts: Synthesis, mechanisms and applications. *Renewable and Sustainable Energy Reviews*, 2018, vol. 81, part 1, pp. 536–551. DOI: 10.1016/j.rser.2017.08.020.
4. Kumar N., Yadav S., Mittal A., Kumari K. Photocatalysis by zinc oxide-based nanomaterials. *Nanostructured Zinc Oxide. Synthesis, Properties and Applications*. The Netherlands, Elsevier Publ., 2021, pp. 393–457. DOI: 10.1016/B978-0-12-818900-9.00005-X.
5. Patil K.C., Hedge M.S., Rattan T., Aruna S.T. *Chemistry of nanocrystalline oxide materials: combustion synthesis, properties and applications*. New Jersey, World Scientific Publ., 2008. 362 p. DOI: 10.1142/6754.
6. González-Cortés L.S., Imbert F.E. Fundamentals, properties and applications of solid catalysts prepared by solution combustion synthesis (SCS). *Applied Catalysis A: General*, 2013, vol. 452, pp. 117–131. DOI: 10.1016/J.APCATA.2012.11.024.
7. Varma A., Mukasyan A.S., Rogachev A.S., Manukyan K.V. Solution combustion synthesis of nanoscale

materials. *Chemical Reviews*, 2016, vol. 116, no. 23, pp. 14493–14586. DOI: 10.1021/acs.chemrev.6b00279.

8. Hwang C.-C., Wu T.-Yu. Synthesis and characterization of nanocrystalline ZnO powders by a novel combustion synthesis method. *Materials Science and Engineering B*, 2004, vol. 111, no. 2-3, pp. 197–206. DOI: 10.1016/j.mseb.2004.04.021.
9. Riahi-Noori N., Sarraf-Mamoory R., Alizadeh P., Mehdikhani A. Synthesis of ZnO nano powder by a gel combustion method. *Journal of Ceramic Processing Research*, 2008, vol. 9, no. 3, pp. 246–249.
10. Zak A.K., Abrishami M.E., Majid W.H.A., Yousefi R., Hosseini S.M. Effects of annealing temperature on some structural and optical properties of ZnO nanoparticles prepared by a modified sol–gel combustion method. *Ceramics International*, 2011, vol. 37, no. 1, pp. 393–398. DOI: 10.1016/j.ceramint.2010.08.017.
11. Amosov A.P., Novikov V.A., Kachkin E.M., Kryukov N.A., Titov A.A., Sosnin I.M., Merson D.L. The solution combustion synthesis of ZnO powder for the photodegradation of phenol. *Ceramics*, 2022, vol. 5, no. 4, pp. 928–946. DOI: 10.3390/ceramics5040067.
12. Khaliullin S.M., Zhuravlev V.D., Ermakova L.V., Buldakova L.Y., Yanchenko M.Y., Porotnikova N.M. Solution combustion synthesis of ZnO using binary fuel (glycine + citric acid). *International Journal of Self-Propagating High-Temperature Synthesis*, 2019, vol. 28, no. 4, pp. 226–232. DOI: 10.3103/S1061386219040058.
13. Ermakova L.V., Zhuravlev V.D., Khaliullin Sh.M., Vovkotrub E.G. Thermal analysis of the products of SCS of zinc nitrate with glycine and citric acid. *Thermochimica Acta*, 2020, vol. 695, article number 178809. DOI: 10.1016/j.tca.2020.178809.
14. Vikarchuk A.A., Sosnin I.M., Stepanov S.V., Stepanov A.S. Nanotechnology for deep sewage treatment of airports from toxic pollution, materials and equipment for its implementation. *Vodoochistka. Vodopodgotovka. Vodosnabzhenie*, 2018, no. 12, pp. 18–23. EDN: YPXEFV.
15. Haibo O., Feng H.J.F., Cuiyan Li., Liyun C., Jie F. Synthesis of carbon doped ZnO with a porous structure and its solar-light photocatalytic properties. *Materials Letters*, 2013, vol. 111, pp. 217–220. DOI: 10.1016/j.matlet.2013.08.081.
16. Bechambi O., Sayadi S., Najjar W. Photocatalytic degradation of bisphenol A in the presence of C-doped ZnO: effect of operational parameters and photodegradation mechanism. *Journal of Industrial and Engineering Chemistry*, 2015, vol. 32, pp. 201–210. DOI: 10.1016/j.jiec.2015.08.017.
17. Pan L., Muhammad T., Ma L., Huang Z.-F., Wang S., Wang L., Zou J.-J., Zhang X. MOF-derived C-doped ZnO prepared via a two-step calcination for efficient photocatalysis. *Applied Catalysis B: Environmental*, 2016, vol. 189, pp. 181–191. DOI: 10.1016/j.apcatb.2016.02.066.
18. Xanthopoulou G. Catalytic properties of the SHS products. Review. *Advances in Science and Technology*, 2010, vol. 63, pp. 287–296. DOI: 10.4028/www.scientific.net/AST.63.287.
19. Al-Sabahi J., Bora T., Al-Abri M., Dutta J. Controlled defects of zinc oxide nanorods for efficient visible light photocatalytic degradation of phenol. *Materials*, 2016, vol. 9, no. 4, article number 238. DOI: 10.3390/ma9040238.
20. Reddy I.N., Reddy C.V., Shim J., Akkinepally B., Cho M., Yoo K., Kim D. Excellent visible-light driven photocatalyst of (Al, Ni) co-doped ZnO structures for organic dye degradation. *Catalysis Today*, 2020, vol. 340, pp. 277–285. DOI: 10.1016/j.cattod.2018.07.030.
21. Nadeem M.S., Munawar T., Mukhtar F., Rahman M.N., Riaz M., Iqbal F. Enhancement in the photocatalytic and antimicrobial properties of ZnO nanoparticles by structural variations and energy bandgap tuning through Fe and Co co-doping. *Ceramics International*, 2021, vol. 47, no. 8, pp. 11109–11121. DOI: 10.1016/j.ceramint.2020.12.234.

doi: 10.18323/2782-4039-2023-2-64-9

Irregularity of microhardness and microstructure of low-carbon steel rolled in a two-stand rolling-leveling mill

Vladimir P. Ivanov[1], Doctor of Sciences (Engineering), Professor
Stanislav V. Pilipenko*[2], PhD (Engineering), Associate Professor
Oleg P. Shtempel[3], PhD (Engineering), Associate Professor
Tatyana V. Vigerina[4], PhD (Engineering), Associate Professor
Euphrosyne Polotskaya State University of Polotsk, Novopolotsk (Republic of Belarus)

***E-mail: s.pilipenko@psu.by,**
44-08@mail.ru

[1]ORCID: https://orcid.org/0000-0002-4621-7155
[2]ORCID: https://orcid.org/0000-0002-1110-2016
[3]ORCID: https://orcid.org/0000-0001-7247-0798
[4]ORCID: https://orcid.org/0000-0002-8862-5456

Received 07.04.2023 *Accepted 16.06.2023*

Abstract: The relevance of the study is proved by two factors. One of them is the necessity to study the nature of the change in the microstructure of the cross-section of extra-thin tinplate made of TS 435 steel (analogue of 08ps steel) skin-passed in a new DSR-1250 mill of the Miory Metal Rolling Plant. The second factor is the need to develop an effective method for obtaining accurate geometry characteristics of an oblique cut of tinplate 0.19 mm or less thick. The purpose of the work is to determine the changes in microhardness and microstructure over the thickness of tinplate samples and identify the existence of a layer microstructure necessary for this type of flat-rolled products. The study was carried out on the selected samples of tinplate of TS 435 steel 0.19 mm thick. This tinplate was rolled from an annealed strip, 0.224 mm thick. The total magnitude of reduction in the mill was 15 %, and the reduction in the skin-pass stand was at least 3 %. The authors carried out measurements of microhardness at different points over the thickness of the selected tinplate samples. The microhardness values over the strip thickness were averaged using 6th degree polynomial interpolation. To study the grain dimension, a number of microstructure images were taken in various areas over the sheet thickness with ×500 magnification. The microstructure studies showed a pronounced strain microstructure with grains elongated in the direction of rolling. At the very boundary of metal contacting the rolls, the grains received the greatest deformation. The highest values of microhardness were identified in two zones adjacent to both strip surfaces and in the central layers along the strip thickness. The change in the microhardness values along the sheet thickness has a wave-like character with three pronounced zones of increase in hardness and two zones of a decrease in its values. The zones with the lowest microhardness values are located between the zones with the maximum values.

Keywords: tinplate; low-carbon steel TS 435; microhardness irregularity; microstructure irregularity; strip section; oblique cut; grain dimension ratio; rolling-leveling mill.

Acknowledgements: The authors express their sincere gratitude to the management of OOO Metal-Rolling Company (Miory, the Republic of Belarus) for the provision of samples for the research and participation in the discussion of the results.

For citation: Ivanov V.P., Pilipenko S.V., Shtempel O.P., Vigerina T.V. Irregularity of microhardness and microstructure of low-carbon steel rolled in a two-stand rolling-leveling mill. *Frontier Materials & Technologies*, 2023, no. 2. DOI: 10.18323/2782-4039-2023-2-64-9.

INTRODUCTION

Cold-rolled sheets are one of the most commonly used types of rolled products. Many scientific papers cover the study of the development of the theory and technology of cold sheet rolling. The necessary final properties of such sheet-rolled products as tinplate are provided by skin-pass rolling, the technology of which largely determines the quality of tinplate [1–3]. In most cases, tinplate itself is a blank for cold stamping [4]. It is very important that during such processing, no destruction of the sheet integrity occur, and no shear lines form on its surface [5; 6]. Skin pass ensures good formability, good sheet flatness, and the required surface roughness [5]. The latter is especially important when applying coatings to the sheet surface (tinning, etc.). Tensile diagrams of tempered sheets does not show a yield plateau or its length is significantly reduced [6–8]. This allows increasing the stamping process accuracy and prevents distortion of stamped parts [6; 9; 10].

When tempering mild-carbon steel sheets with a percentage reduction of up to 1.2 %, the yield strength of the material decreases. This is explained by the processes of the nucleation of new dislocations. At percentage reductions of more than 1.2 %, the yield strength begins to increase [5]. As a rule, when tempering mild-carbon steel sheets, the percentage reduction is in the range from 0.5 to 3 %. Skin pass is performed after cold-rolled sheets are annealed (as a rule, in a shielding atmosphere) [11–13].

In 2020, a tinplate production line was put into operation at the Miory Metal Rolling Plant [14]. According to the technical characteristics, the installed equipment allows rolling sheet metal with a minimum thickness of 0.15 mm.

Two rolling mills are installed within the production line: RCM-1250 – a six-roll reversing mill for cold thin-sheet rolling, and DSR-1250 – a continuous rolling-leveling mill consisting of one reduction stand (quarto) and one skin-pass stand (quarto).

The plant receives rolls of pickled annealed sheet of 2 mm in thickness. The technological process of cold rolling of sheets at this plant consists of the following main operations (Fig. 1). After the preparation process, the coils (1) are rolled in several passes to the desired thickness (2) on a RCM-1250 reversing mill (3). Next, the rolls (4) after electrolytic cleaning (5) are fed for annealing. Annealing is carried out in bell-type furnaces with a shielding atmosphere (6). Annealed coils are transferred for rolling in a DSR-1250 two-stand rolling-leveling mill (7 and 8).

After rolling the strips in the DSR-1250 mill, the coils are transferred for tinning, cutting, reeling, and packaging (9, 10).

At the DSR-1250 mill, the process of reduction of the sheet annealed in a shielding atmosphere and the process of its tempering are carried out sequentially. It is obvious that rolling is carried out with tension. The study of special aspects of such process, including changes in the microhardness and microstructure of the metal along the tin strip thickness is of interest.

In the process of skin pass, with an increase in the degree of deformation, the tensile strength and hardness of the metal increase, and the yield strength, up to the limit of the deformation degree determined for each metal, first decreases and then increases. Thus, it is convenient to judge the degree of deformation of a given metal during skin pass by the change in its microhardness, since this value continuously increases.

The aim of the research is to study the microstructure, and the nature of the change in microhardness along the thickness of a sheet of tempered tinplate strips made of TS 435 steel (manufactured in accordance with the EN 10202:2001 requirements).

METHODS

The study was carried out on a tinplate strip made of TS 435 steel (a 08ps grade analogue according to the GOST 1050 standard) 0.19 mm thick. This tinplate is rolled from an annealed strip 0.224 mm thick in a DSR-1250 mill. The total value of the percentage reduction in the mill was 15 %, the value of the percentage reduction in the skin-pass mill was 3 %.

To study microhardness and microstructure, the following technique was developed.

Samples were cut out from areas in the middle of the width of the rolled tinplate strip along and across the rolling direction.

To ensure the possibility of performing multiple measurements of microhardness over the thickness of a tin strip (0.19 mm), the authors used the technology of grinding the surface at an angle of 3°. This gives the possibility of performing microhardness measurements at a large number of points over the thickness of the strip on an oblique ground cut. The sample preparation technology for oblique grinding of a tin strip is shown in Fig. 2.

As is seen from Fig. 2 a sample prepared for studying, an oblique cut in the form of a tinplate strip was glued onto a base strip (Fig. 2 a) ground at an angle of 3° to the horizontal line. The curing of the adhesive on specimens prepared in this way must take place under load. In this case, the specimen strips were pressed with a rubber-sealed clamp (the sample strip is pressed against the base by a surface with an inclination of 3°). It is possible to use a press, (with the same sealing parts and a container

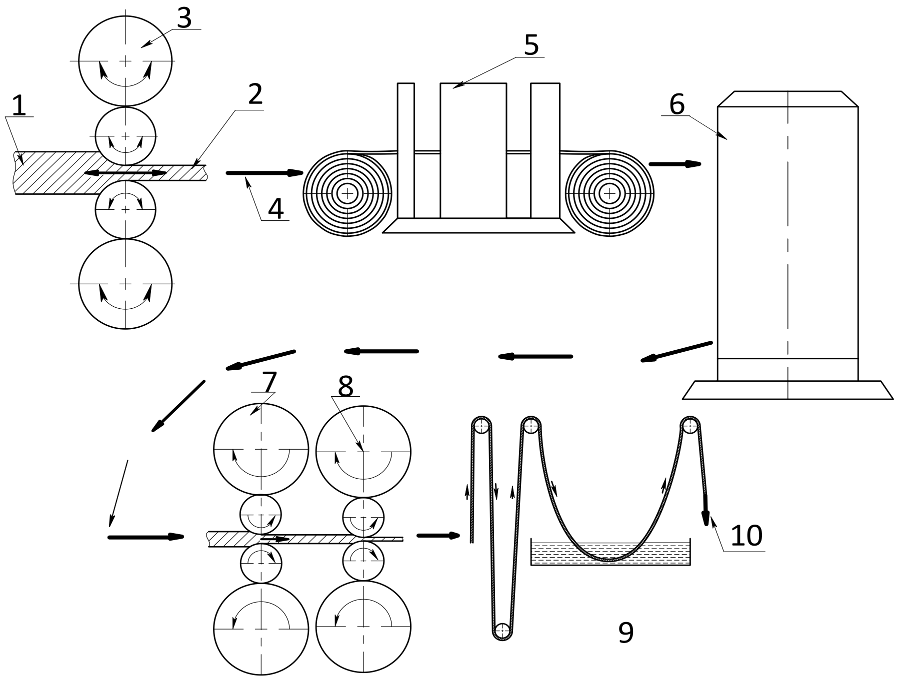

Fig. 1. Tinplate production at Miory Metal Rolling Plant:
1 – coils of etched annealed sheet 2 mm thick; 2 – a strip leaving the RCM-1250 mill; 3 – RCM-1250 reversing mill;
4 – movement of coils along the technological line of the workshop; 5 – electrolytic cleaning plant; 6 – bell-type furnaces;
7 – cogging stand of the DSR-1250 mill; 8 – pinch-pass stand of the DSR-1250 mill; 9 – tinning stack;
10 – cutting, coiling, packing, and sales

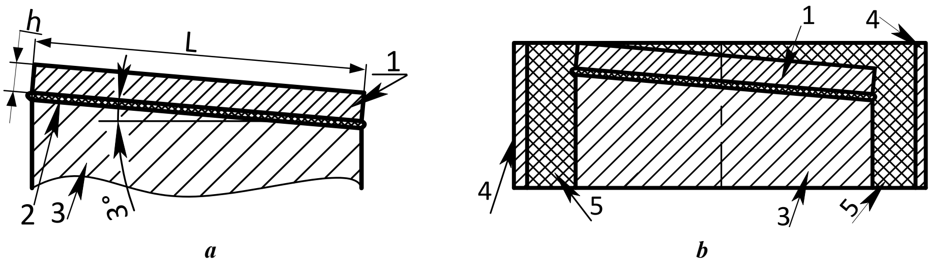

Fig. 2. *The technology of preparing a specimen for an oblique cut to study tinplate microstructure:*
a *– sticking tinplate strips on the base metal;* ***b*** *– pouring the specimen with epoxy resin.*
1 – test tinplate strip with the corresponding length of the platform to measure microhardness along the tin strip thickness; 2 – fast-setting glue layer; 3 – base strip; 4 – cylindrical container; 5 – epoxy resin; h – tinplate strip thickness

providing the desired position of the sample strip, the base, and the surface pressing the strip against it). After the adhesive has hardened (Fig. 2 b), the sample is placed in a container and poured with epoxy resin. After the resin hardens, the unnecessary part of the tin strip under study is ground off.

Fig. 3 shows the container with the samples after grinding. It is evident that on the samples prepared by the above-described method (Fig. 2), in the process of flat grinding of the container with the samples, an oblique cut angle of 3° is formed spontaneously.

The samples were prepared on a Presi Mecapol P262 polishing station. The microstructure was studied using a Nikon Epiphot 200 microscope, with a magnification up to 1000 times. Vickers hardness was determined on a Buehler Model No 1105D microhardness tester. The etchant is Rzheshotarsky's solution (5 % solution of nitric acid in alcohol).

Surface microhardness measurements were carried out using the Vickers method with a small load on a Buehler Model No 1105D microhardness tester. The force was 0.9807 N, which corresponds to the HV 0.1 hardness scale. The load application time is 10 s. A diamond tip was used with the working part in the form of a tetrahedral pyramid with a rhombic base.

During the study of rolled steel samples, the following operations were carried out:

– multiple microhardness measurements on the tin strip surfaces followed by deriving the average values for certain samples;

– multiple microhardness measurements for the end sections with microhardness measurements at three points: 40 μm from the edge of the strip surface of each end section, and in the middle of the section. Average values were derived (separately for each edge and middle of a particular end section);

– multiple microhardness measurements on the oblique cuts with a step of 50–100 μm along the oblique cut. Up to 25 measurements were made at each coordinate. Average values were derived according to the technique described in [15; 16].

The hardness measuring uncertainty was leveled by measuring a number of hardness reference gages (the spread of hardness values is within the range of ±12.5 %) [17].

The grain size, in the middle regions of the strip cross section was calculated by counting the intersections of grain boundaries [18; 19]. Based on the sheet thickness, a segment with a length of 0.08 mm was chosen to count the intersections along the *X* and *Y* axes. To count the number of grain intersections along the diagonal line (against the *X* and *Y* axes), a segment length of 0.113 mm was chosen. The segments were located on each image at random. One should note that the *X*-axis always coincided with the sheet thickness.

The grain size, in near-surface regions, was determined by counting the intersections of grain boundaries [20]. The counting was carried out along the *Y* axis on a number of segments 0.09 mm in length. The segments were located on each image at random.

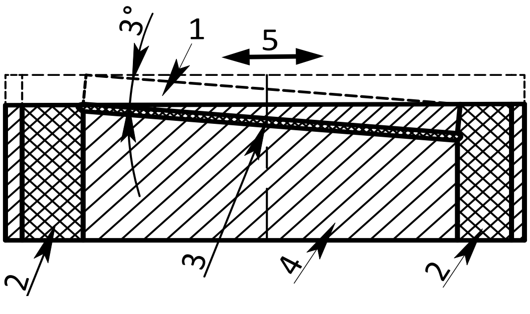

Fig. 3. *A container with tinplate specimens after flat grinding machine:*
1 – ground part of a specimen; 2 – epoxy resin; 3 – fast-setting glue layer; 4 – metal base with a glued specimen; 5 – movement direction of a grinding tool

RESULTS

Fig. 4 demonstrates the metal microstructure of the strip fed for skin pass to the DSR-1250 mill and pre-annealed in a bell-type furnace with a shielding atmosphere (Fig. 1, position 6).

Fig. 4 shows that the microstructure of samples from annealed TS 435 steel is a generally homogeneous ferritic structure, with pronounced equilibrium grains. Finely dispersed inclusions, probably of a carbide nature, are distributed over the body of the ferrite grains relatively evenly. The microhardness in the near-surface zone of the strip is 79.71 HV±7 %, in the middle regions – 78.89 HV±5.5 %.

As one can see from the analysis of the measurement results (Fig. 5 and 6), three zones of the highest hardness values are observed in the samples:

– on both surfaces of the strip;

– in the central layers of the strip thickness.

At a depth of 0.04 to 0.05 mm from the strip surface on the end cut, and of 0.01 to 0.015 mm on oblique cuts, zones of the lowest hardness values are observed. Thus, the averaged microhardness values (obtained by interpolation with a 6-th degree polynomial) show a wavelike change in the hardness values, over the sheet depth with three pronounced zones of increasing hardness, and two zones of decreasing hardness values. In other words, different layers over the sheet depth received different degrees of deformation.

Fig. 7 shows photographs of the microstructures of the cross sections of the investigated tinplate strips. The microstructure study on a thin section of the tin strip thickness located along the rolling direction (Fig. 7 a)

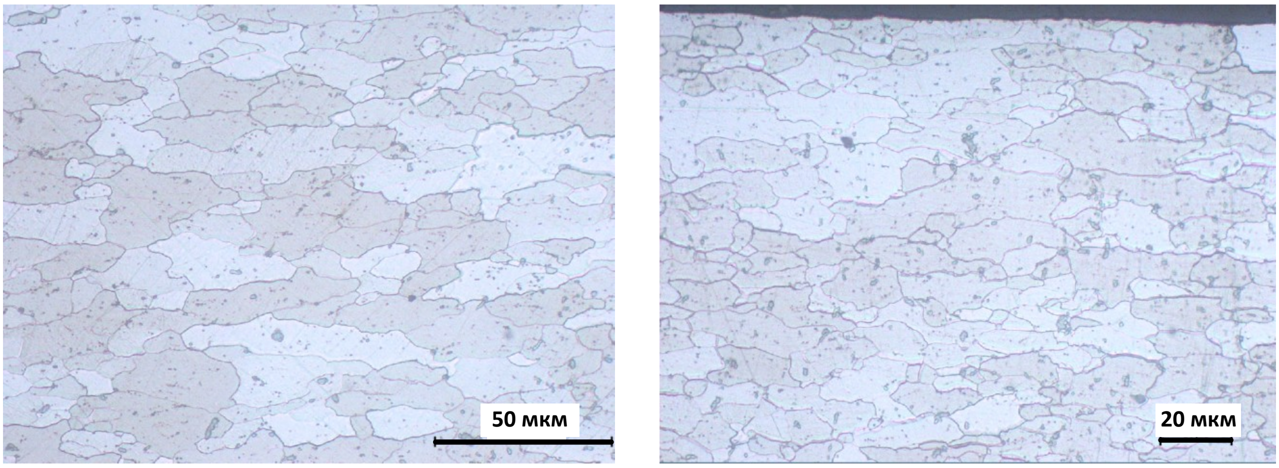

a *b*

Fig. 4. *Metal microstructure of an annealed TS 435 steel strip 0.224 mm thick, which is fed to the DSR-1250 mill for skin pass (×500):*
a *– central part of the strip cross section;* ***b*** *– surface part of the strip cross section*

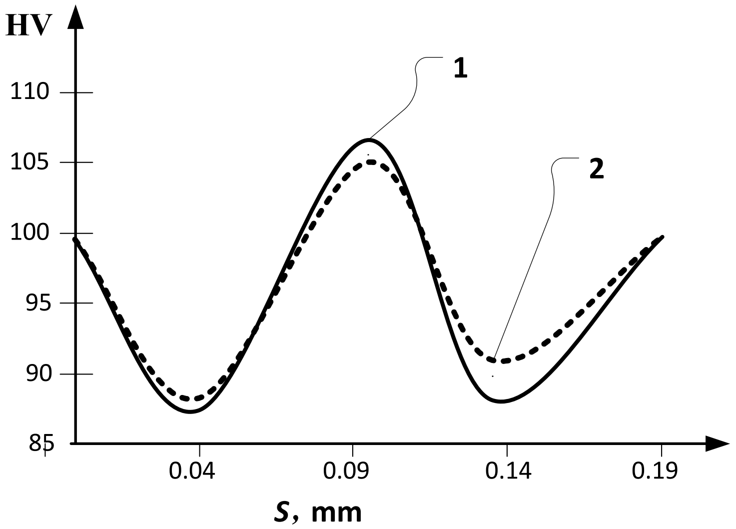

Fig. 5. *Microhardness distribution along the thickness of the TS 435 steel sheet 0.19 mm thick subjected to skin pass in the DSR-1250 mill, according to the results of measurements from the sheet end face:*
S – depth (measurement coordinate) along the sheet thickness; HV – microhardness on the oblique cut surface;
1 – cross cut measurements; 2 – along cut measurements

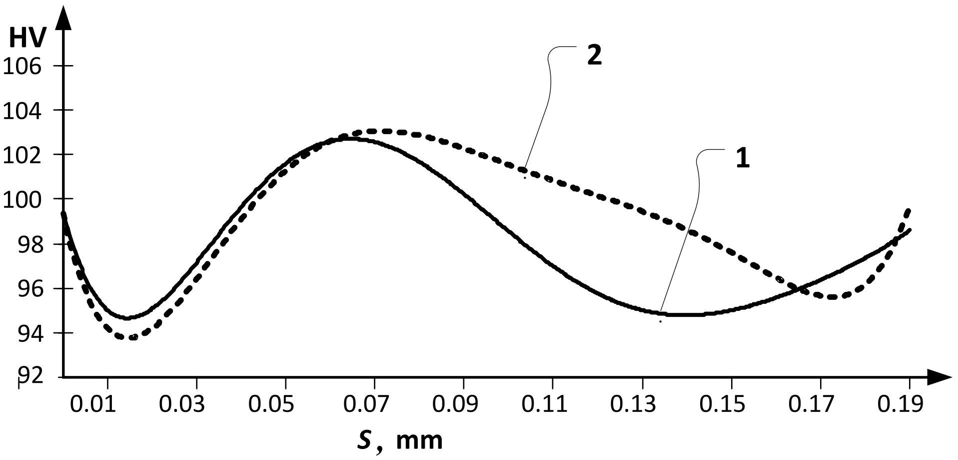

Fig. 6. *Microhardness distribution along the thickness of the TS 435 steel sheet 0.19 mm thick subjected to skin pass in the DSR-1250 mill, according to the results of measurements on the oblique cut surface: HV – microhardness on the oblique cut surface; S – depth (measurement coordinate) along the sheet thickness; 1 – cross cut measurements; 2 – along cut measurements*

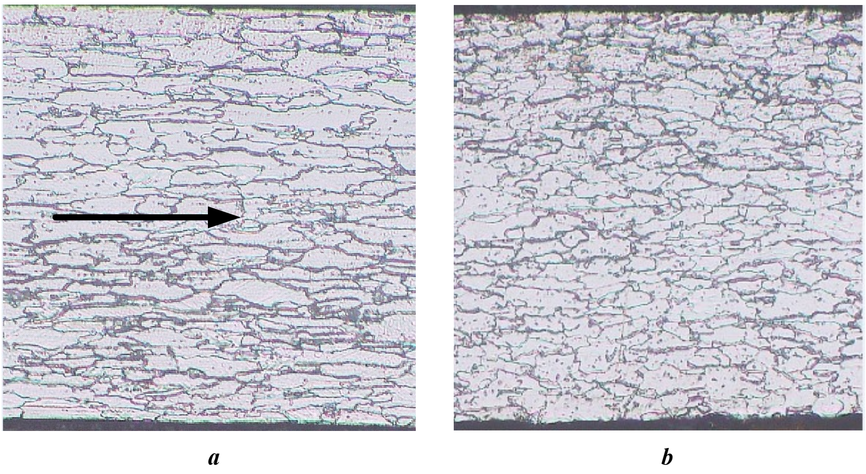

Fig. 7. *Microstructure of the TS 435 steel tinplate sheet 0.19 mm thick:*
a *– microstructure in the strip thickness section (×200) along the rolling line (an arrow – the rolling direction);*
b *– microstructure in the strip thickness section (×200) across the rolling line (the rolling direction – toward us)*

showed the presence of a clearly pronounced banded (fibrous, elongated) microstructure along the rolling direction. The grains are elongated in the direction of longitudinal deformation (along the rolling line).

On the section, where the tin strip thickness is located in the plane across the rolling line (Fig. 7 b), the width of the grains is less than their length on the section made along the rolling direction.

To study the grain size, a number of microstructure photographs were taken in the regions bordering the tin strip surface (Fig. 8 a and 9 a) and in the middle regions of the strip (Fig. 8 b and 9 b). The photographs were taken with a magnification of 500 times. From the photographs, one can judge the change in the microstructure along the cross section of the strip.

The calculation gave the following results:

– in the sheet thickness area bordering the surface, in the section along the rolling line, along the *X* axis – 305 grains (1.6 mm), along the *Y* axis – 119 grains (2.4 mm), along the diagonal line – 322 grains (2.263 mm);

– in the sheet thickness middle area, in the section along the rolling line, along the *X* axis – 567 grains (3.28 mm), along the *Y* axis – 98 grains (2.56 mm), along the diagonal line – 357 grains (2.828 mm);

– in the sheet thickness border area, in the section across the rolling line, along the *X* axis – 273 grains (1.6 mm), along the *Z* axis – 181 grains (2.4 mm), along the diagonal line – 296 grains (2.263 mm);

– in the strip thickness middle region, in the section across the rolling line, along the *X* axis – 289 grains (2.08 mm), along the *Z* axis – 152 grains (2.32 mm), along the diagonal line – 256 grains (2.263 mm).

The calculation data were processed according to the standard procedure [16; 18]. Tables 1 and 2 provide data on the average grain size in the directions described above.

In addition to grain sizes, data on the average ratio of the grain length along the *Z* axis to the length along the *X* axis both across the rolling line (grain width coefficient), and along the rolling line (grain length coefficient) were obtained.

When determining the grain size in the area of contact between the metal and the rolls, 103 grains were counted across the rolling line (1.44 mm) and 56 grains (1.8 mm) along the rolling line. The results of grain size calculations along the rolling line (grain length) and across it (grain width) are summarized in Table 3.

DISCUSSION

It is determined that the microstructure of the studied samples is a ferrite with different degrees of plastic deformation over the sheet thickness.

There are obvious differences in the microstructure on sections made along and across the rolling line (Fig. 7–9), since this factor was mainly influenced by the schemes of plastic deformation during preliminary cold rolling in the first stand and skin pass in the second stand of a DSR-1250 continuous 2-roll rolling-leveling mill.

Tables 1 and 2, show that the grain length coefficient is always greater than the grain width coefficient, both in the border and in the central regions over the strip width. This is quite natural for sheet rolling [15; 20]. One can conclude that the broadening of the grains in the central regions is somewhat less than the broadening of the grains in the regions bordering the strip surface (width coefficient 2.311 versus 2.208). This can be caused by the action of friction forces acting along the rolling line on the contact surface of the rolls and metal.

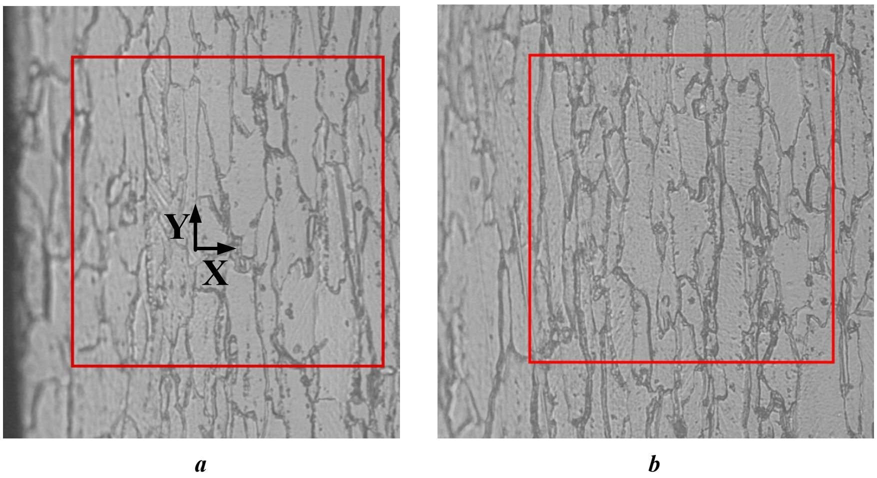

Fig. 8. *Tinplate microstructure in the thickness sections of the TS 435 steel sheet 0.19 mm thick in the plane along the rolling direction line (×500):*
a *– sheet end face area adjacent to the surface;* ***b*** *– sheet end face middle area (a square 0.08×0.08 mm).*
X-axis is oriented along the sheet thickness, Y-axis – along the rolling axis

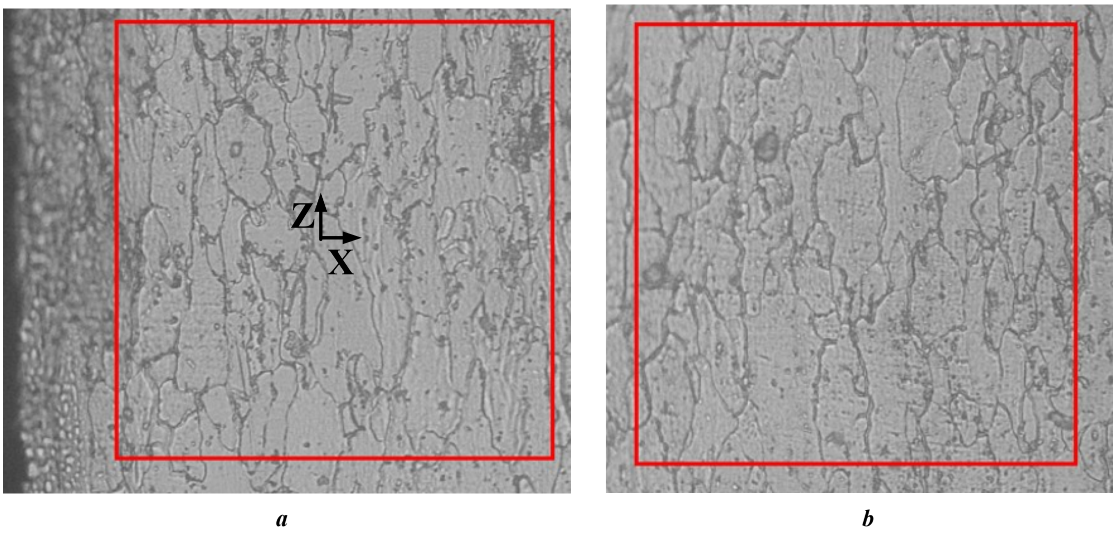

Fig. 9. *Microstructure of the TS 435 steel tinplate sheet 0.19 mm thick in the plane across the rolling direction line (×500):*
a *– sheet end face area adjacent to the surface;* ***b*** *– sheet end face middle area (a square 0.08×0.08 mm).*
X-axis is oriented along the sheet thickness, Z-axis – across the rolling axis (along the sheet width)

Table 1. *The average grain size in the section across the rolling line*

Measurement point	**A cut across the rolling line**		
	Measurement axis	**Average grain size, mm**	**The average ratio of grain length along the *Z* axis (over the strip width) to the length along the *X* axis (over the strip thickness)**
Edge of sheet thickness	*X*	0.00594±12.5 %	2.311
	Z	0.01374±15.0 %	
	along the diagonal	$0{,}00767\,^{+12.0\%}_{-7.5\%}$	
Middle of sheet thickness	*X*	0.00728±12.5 %	2.208
	Z	0.01608±16.0 %	
	along the diagonal	0.00908±10.5 %	

Table 2. *The average grain size in the section along the rolling line*

Measurement point	**A cut along the rolling line**		
	Measurement axis	**Average grain size, mm**	**The average ratio of grain length along the *Y* axis (along the rolling line) to the length along the *X* axis (over the strip thickness)**
Edge of sheet thickness	*X*	0.00534±14.5 %	4.017
	Y	0.02145±12.0 %	
	along the diagonal	0.00714±12.5 %	
Middle of sheet thickness	*X*	0.00589±14.5 %	4.716
	Y	0.02779±12.5 %	
	along the diagonal	0.00808±12.0 %	

Table 3. *The average grain size in the metal-to-roll contact area*

Measurement point	**Measurement axis**	**Average grain size, mm**	**The average ratio of grain length along the *Y* axis to the length along the *X* axis**
In the contact area of the metal and a roll	A cut – across the rolling line		2.299
	X	0.01398±11.5 %	
	A cut – along the rolling line		
	Y	0.03214±12 %	

Considering the grain length factor, one can conclude that the grains in the border areas received less elongation than the grains in the middle regions of the sheet thickness (grain length factor 4.017 versus 4.716).

The smallest grain size in all cases, was identified when counting the number of grains along the diagonal lines, and along the X axis. From a visual analysis of the microstructure photographs of the near-border areas, it can be noticed that the grains at the very border of the contact of the metal, with the rolls receive the greatest deformation.

In the middle areas, where deformation occurs under a significant action of tensile stresses, grain fragments, and even single destroyed grains are encountered, which is natural and acceptable.

Tables 1 and 2 show, that the average ratio of the grain length to its width is 1.561 in the extreme region of the tin strip end and 1.729 in its middle parts.

As one can see from Table 3, the ratio of grain length to width is 2.299. Thus, in two areas, the grains received a large elongation – in the area of direct contact of the metal with the roll (sheet surface), and in the middle regions relative to the sheet thickness. It is these areas where the increased values of microhardness are observed.

Therefore, during the study of the changes in the microstructure and microhardness of ultra-thin tinplate made of TS 435 steel rolled in a DSR-1250 mill, the expected existence of a layered structure of strips, which is typical for tempered sheet material, was confirmed. According to the work [1; 2; 6; 10], the formation of such a layered microstructure prevents the Chernov–Luders lines from coming to the surface of the stamped sheet, and helps to improve sheet formability. As practice shows, when tinning strips with a similar structure, the adhesion of the tinned layer to the surface improves.

The nature of the change in microhardness over the thickness of the strips is confirmed by the corresponding nature of the change in the microstructure. It was identified that the near-surface layers, as well as the middle ones, receive a greater degree of deformation than the metal layers between them. Probably, such behaviour of mechanical characteristics over the sheet thickness is associated with the presence of a significant degree of metal tension between the stands of the DSR-1250 two-stand mill. It is known that during the rolling of the strips on such mill, sometimes even their tightening was observed, which is definitely caused by the influence of the strip tension.

CONCLUSIONS

During skin-pass carried out on a DSR-1250 continuous rolling-leveling mill produced by SMS group, the necessary multilayer structure occurs in pre-annealed cold-rolled thin sheets made of TS 435 steel, in which different layers have individual microstructure combinations (grain elongation degree, grain size, etc.) and mechanical properties.

In the areas of metal adjacent to the tin surfaces, the layers were subjected to the deforming effect of the rolls to a greater extent than the subsurface layers. As a result, surface zones were formed, characterised by higher hardness and strength. In the surface zones, a greater degree of grain elongation is observed than in the subsurface ones.

In the subsurface layers, lower hardness values are observed. The grains of these layers received lower strain values. The highest hardness values are noted in the central regions of the sheet cross section. Separate destroyed grains are observed here. It is possible that the higher hardness of the central layers is associated with a significant degree of strip tension between the stands of the DSR-1250 two-stand mill. These findings require further, broader research.

REFERENCES

1. Mazur V.L., Nogovitsyn O.V. *Theory and Technology of Sheet Rolling: Numerical Analysis and Applications*. London, CRS Press Publ., 2019. 477 p.
2. Mazur V.L. Preventing surface defects in the uncoiling of thin steel sheet. *Steel in Translation*, 2015, no. 45, pp. 959–966. DOI: 10.3103/S0967091215120062.
3. Wang D.-C., Liu H.-M., Liu J. Research and Development Trend of Shape Control for Cold Rolling Strip. *Chinese Journal of Mechanical Engineering*, 2017, no. 30, pp. 1248–1261. DOI: 10.1007/s10033-017-0163-8.
4. Kozhevnikov A.V. The Development and Application of Methodologies for the Design of Technological Modes of Cold Rolling. *IOP Conference Series: Materials Science and Engineering*, 2020, vol. 718, article number 012007. DOI: 10.1088/1757-899X/718/1/012007.
5. Pimenov A.F., Soskovets O.N., Trayno A.I., Mazur V.L., Chernov P.P., Dobronravov A.I. *Kholodnaya prokatka i otdelka zhesti* [Cold rolling and finishing of tinplate]. Moscow, Metallurgiya Publ., 1990. 206 p.
6. Timofeeva M.A., Garber E.A. *Protsess dressirovki kholodnokatanykh stalnykh polos (teoriya, tekhnologiya, oborudovanie, tendentsii ikh razvitiya i sovershenstvovaniya)* [The process of training cold-rolled steel strips (theory, technology, equipment, trends in their development and improvement)]. Cherepovets, ChGU Publ., 2017. 155 p.
7. Ogarkov N.N., Zvyagina E.Y., Ismagilov R.R. Theoretical analysis of formation of automobile sheet roughness during temper rolling in shot-blasted rolls. *Steel in Translation*, 2019, vol. 49, no. 8, pp. 499–503. DOI: 10.3103/S0967091219080138.
8. Cui H., Chen H., Lu L., He Z. Determinant parameters of surface morphology to corrosion behaviour of cold-rolled auto sheet steel. *Journal of Materials Science*, 2021, no. 56, pp. 8297–8308. DOI: 10.10078/s10853-021-05812-6.
9. Poddar V.S., Rathod M.J. Evaluation of mechanical properties of cold roll bonded mild steel and aluminum. *Materials Today: Proceedings*, 2021, vol. 43-5, pp. 3014–3022. DOI: 10.1016/j.matpr.2021.01.363.
10. Li T., Yan S., Liu X. Enhancement austenite content in medium-Mn steel by introducing cold-rolled deformation and inhibiting subsequent recrystallization. *Materials Letters*, 2021, vol. 301, article number 130249. DOI: 10.1016/j.matlet.2021.130249.
11. Mazur V.L., Nogovitsyn O.V. *Theory and Technology of Sheet Rolling. Numerical Analysis and Applications*. New York, CRC Press Publ., 2018. 500 p.
12. Zakarlyuka S.V., Yurchenko Yu.I., Goncharov V.E., Budakva S.A. Non-flatness parameters variation in case of elastic stretching of strips Non-flatness parameters variation in case of elastic stretching of strips.

Modelirovanie i razvitie protsessov OMD, 2018, no. 24, pp. 3–12. EDN: UQLSOA.

13. Zaytsev A.I., Rodionova I.G., Koldaev A.V., Arutyunyan N.A., Aleksandrova N.M. Effect of composition and processing parameters on microstructure and mechanical properties of cold-rolled and galvanized roll products from IF-steels. *Metallurg*, 2020, no. 6, pp. 41–47. EDN: URLJOH.
14. Dyakonov V.A., Pilipenko S.V., Shtempel O.P. Influence of deformation on the mechanical properties of tinplated tin. *Vestnik Polotskogo gosudarstvennogo universiteta. Seriya B. Promyshlennost. Prikladnye nauki*, 2022, no. 10, pp. 18–24. EDN: YFNRXI.
15. Li L., Matsumoto R., Utsunomiya H. Experimental Study of Roll Flattening in Cold Rolling Process. *ISIJ International*, 2018, vol. 58, no. 4, pp. 714–720. DOI: 10.2355/isijinternational.ISIJINT-2017-623.
16. Bogush R.P., Adamovskiy E.R., Denisenok S.F. Processing and analysis of images of microstructure metals for determining the grain point. *Doklady Belorusskogo gosudarstvennogo universiteta informatiki i radioelektroniki*, 2021, vol. 19, no. 4, pp. 70–79. DOI: 10.35596/1729-7648-2012-19-4-70-79.
17. Anisovich A.G. Problems of application of standards in evaluation of microstructure of metals and alloys. *Izvestiya Natsionalnoy akademii nauk Belarusi. Seriya Fiziko-tekhnicheskikh nauk*, 2021, vol. 66, no. 1, pp. 12–19. DOI: 10.29235/1561-8358-2021-66-1-12-19.
18. Anisovich A.G., Rumyantseva I.N., Bislyuk L.V. Determination of steel grain grade by computer methods. *Lite i metallurgiya*, 2010, no. 3S, pp. 100–104. EDN: UINMCT.
19. Anisovich A.G., Andrushevich A.A. *Mikrostruktury chernykh i tsvetnykh metallov* [Microstructures of ferrous and non-ferrous metals]. Minsk, Belaruskaya navuka Publ., 2015. 131 p.
20. Li S., Wang Z., Guo Y. A novel analytical model for prediction of rolling force in hot strip rolling based on tangent velocity field and MY criterion. *Journal of Manufacturing Processes*, 2019, vol. 47, pp. 202–210. DOI: 10.1016/j.jmapro.2019.09.037.

doi: 10.18323/2782-4039-2023-2-64-1

Simulation of the processes of drilling polymer composite blanks using digital twins

Maksim V. Ilyushkin[1,3], PhD (Engineering), Deputy Director
Evgeny S. Kiselev*[2,4], Doctor of Sciences (Engineering), Professor
[1]*Ulyanovsk Research Institute of Aviation Technology and Production Organization, Ulyanovsk (Russia)*
[2]*Ulyanovsk State Technical University, Ulyanovsk (Russia)*

***E-mail: kec.ulstu@mail.ru**

[3]ORCID: https://orcid.org/0000-0002-3335-728X
[4]ORCID: https://orcid.org/0000-0002-1745-9016

Received 08.02.2023 *Accepted 28.04.2023*

Abstract: Polycrystalline composite materials made of carbon fibre reinforced plastics have more and more widespread application in mechanical engineering and become the main material for the production of modern types of high-speed transport. Thus, their share has already reached 35–45 % in the structural design of passenger aircrafts. However, the technology of machining surfaces of parts made of these materials, in particular, holes, is characterized by insufficient knowledge, the absence of regulatory standards for cutting modes, and is most often based on the production experience of enterprises. When changing the processing conditions and the material, the pre-production engineering duration causes a significant increase in the cost of manufacturing parts due to the need for experimental selection of the cutting mode rational elements. To exclude the empirical selection of rational elements of the machining equipment cutting mode, the authors considered the possibility of using digital twins, for studying the processes of drilling holes in the blanks made of composite materials. The authors included those with the ultrasonic field energy introduction into the new surface shaping zone (to improve the processing quality and productivity). When modelling, the LS-DYNA program was used. The authors prepared the models and processed the results using the LS-PrePost 4.8 program. During the study, an explicit modelling method was used with preliminary validation and calibration of the results of tests of composites. The authors carried out calibration on test operations of tension, three-point bending, and interlaminar shear of the ВКУ-39 polymer composite material based on carbon fibres (carbon fibre reinforced plastic) widely used in domestic engineering. The developed finite element computer models allow simulating drilling procedures without carrying out rather complicated and expensive field tests. As a result of modelling, a simulation file was obtained, which reflects the process of drilling holes in a polymer composite material blank, as close as possible to the real-life situation with chip removal.

Keywords: drilling of composite materials; ВКУ-39; ultrasonic field energy; ultrasound; drilling process simulation; digital twin.

For citation: Ilyushkin M.V., Kiselev E.S. Simulation of the processes of drilling polymer composite blanks using digital twins. *Frontier Materials & Technologies*, 2023, no. 2. DOI: 10.18323/2782-4039-2023-2-64-1.

INTRODUCTION

Numerous studies performed by some authors established a significant difference in the processes of edge cutting machining of polymer composite and metal blanks [1–3]. Drilling holes in the blanks made of carbonfibre-based polymer composite materials (PCM) is particularly difficult [4–6], which is explained, on the one hand, by the fibre-matrix system fragility and heterogeneity, and, on the other hand, by different operating conditions of various sections of the drill cutting edges, due to the cutting speed variability when removing stock (from zero to maximum values on the outer surface of a drilling tool).

When drilling holes in PCM, the material removal, in contrast to cutting metals, occurs through a series of successive ruptures, which is facilitated by the different nature and uneven distribution of the load between the matrix and fibres [7; 8]. Such chip formation is caused by the composite material brittle fracture, due to the crack initiation and propagation in the primary shear zone after the partial formation of a cleavage and forces to make appropriate adjustments to the software. Since brittle fracture is the dominant process occurring when machining a composite material, the powdery dust segment chips are formed. However, these type of chips, which are formed when drilling holes in PCM, depend largely on the properties of fibres and the matrix. In some cases, “continuous/flow” chips may form, like in metal processing [9; 10]. Moreover, with an increase in the fibre volume fraction, most of the composite materials can be removed by successive destruction due to non-uniform plastic deformation, contributing to the formation of segment chips. It is worth noting that the chip type depends on the cutting mode inputs such as cutting speed and feed. The main factor reducing the efficiency of PCM edge cutting machining is the abrasive nature of the filler [11]. The abundance of carbon or other types of fibers in the PCM structure ensures rapid tool wear (mainly along the flank surface). The listed differences in the stock removal processes are simultaneously accompanied by the almost complete absence of cutting modes when processing composite materials.

As known, the ultrasonic (US) field energy introduction into the machining zone contributes to a significant reduction in the friction force between the cutting tool and the blank [12; 13]. This both speeds up shaping and significantly improves the quality of new surfaces, primarily by reducing the probability of defects in the form of delamination, cleavages, cracking, thermal damage and polymer matrix melting, microcracks between the fibre and the binder, etc. [14; 15].

When designing new technological processes, including ones with the ultrasonic vibrations introduction into the processing zone, the selection of the hole-drilling mode elements is carried out, as a rule, empirically. Experimental selection of drilling mode elements is characterized by high labour intensity, high cost and time expenditures.

Reducing the time expenditures for designing the technological process of manufacturing any mechanical engineering products, especially products from composites, can be achieved using Computer-aided engineering (CAE) systems [16; 17]. Creating a model in CAE systems allows obtaining information about stresses, temperature, distribution of forces in the processing zone, and deformations [18; 19].

The purpose of the study is to create computer models of the processes of drilling polymer composite blanks, including those with the introduction of ultrasonic field energy into the new surfaces shaping zone.

METHODS

Tests

At the first stage, tests of the composites' mechanical characteristics were carried out. The results of these tests were required for calculations on mathematical models.

During the research, an explicit modelling method with preliminary validation and verification of test results was used. Verification was carried out on tension, three-point bending, and interlaminar shear test operations. For modelling, the authors used the LS-DYNA program. To prepare models and process the results, the LS-PrePost 4.8 program was used.

240×12×3 mm strips cut from the ВКУ-39 material were used as sample models.

In the composite, 10 layers were modelled using 8-node thick-walled shell elements with reduced integration. The size of one cell of the composite was 2×2 mm. The thickness of each layer was 0.3 mm.

The ВКУ-39 composite initial parameters were taken based on the works [19; 20]. During simulation and validation, the parameters were adjusted to match the composite used.

As a material model, a model of a composite orthotropic material with destruction was taken.

For the convenience of calculations, the authors used a system of units other than the SI system (length in millimeters, time in seconds, and mass in tons). The following parameters were set in the material model [20]:

– density – $1.525 \cdot 10^{-6}$ kg/mm^3;
– Young's modulus (EA, EB) – $6.39 \cdot 10^4$ MPa;
– Poisson's ratio PRBA – 0.3;
– shear modulus – 4080 MPa.

In the material model, the failure under the action of tensile stresses, as well as the values of failure strain, were specified. Compression and shear strains were overestimated as only tensile strains affect the fracture process.

To model an adhesive layer, the authors used an automatic “surface-to-surface” contact with the tiebreak annex (cohesive breakable contact) with a crack discrete model, power dependence, and damage models with a normal and shear stress of 80 MPa and a fracture energy of 4 mJ. These parameters were adjusted by tests when validating the process.

In addition, the authors considered the assessment of the influence on the resulting moment of the coefficient of friction between a drilling tool and a composite, which changes due to the ultrasonic field introduction into the new surface formation zone, at values equal to 0, 0.1, and 0.2.

Fig. 1, 2 present the initial test models. Fig. 3 shows the pattern for testing the ВКУ-39 composite samples.

Mathematical simulation

At the second stage of the research, the updated parameters of the composite material model and its adhesive layer were used when developing mathematical models based on digital twins.

At the second stage, the authors carried out mathematical simulation of the processes of drilling ВКУ-39 polymer composite blanks, with the ultrasonic field energy introduction into the shaping zone. The main tasks were the digital model adjustment and the assessment of the ultrasonic vibrations effect when changing the amplitude from 6 to 13 μm, and the friction coefficient in the tool-blank contact zone – from 0.1 to 0.2 (the values were taken from the data of numerous studies of the 50–60-ies of the last century). The ranges of changes in these parameters are presented in Table 1. The following cutting mode elements were chosen as constant parameters in mathematical simulation of the process of drilling holes with a diameter of 5 mm

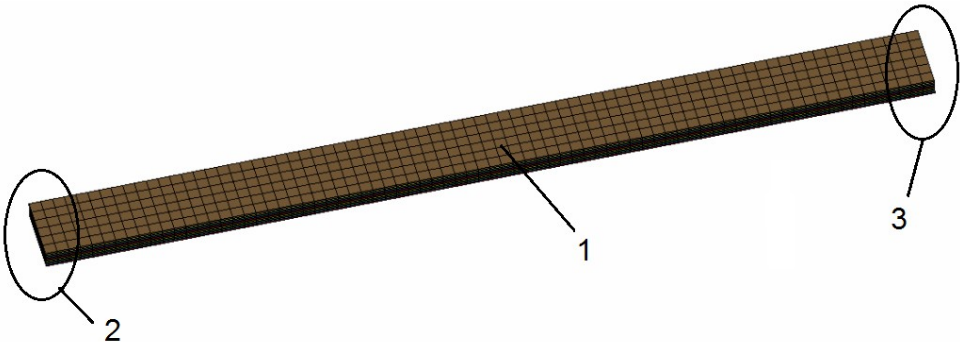

Fig. 1. A model for mathematical simulation of uniaxial tension of a composite:
1 – a composite; 2 – a gripping support; 3 – a movable support

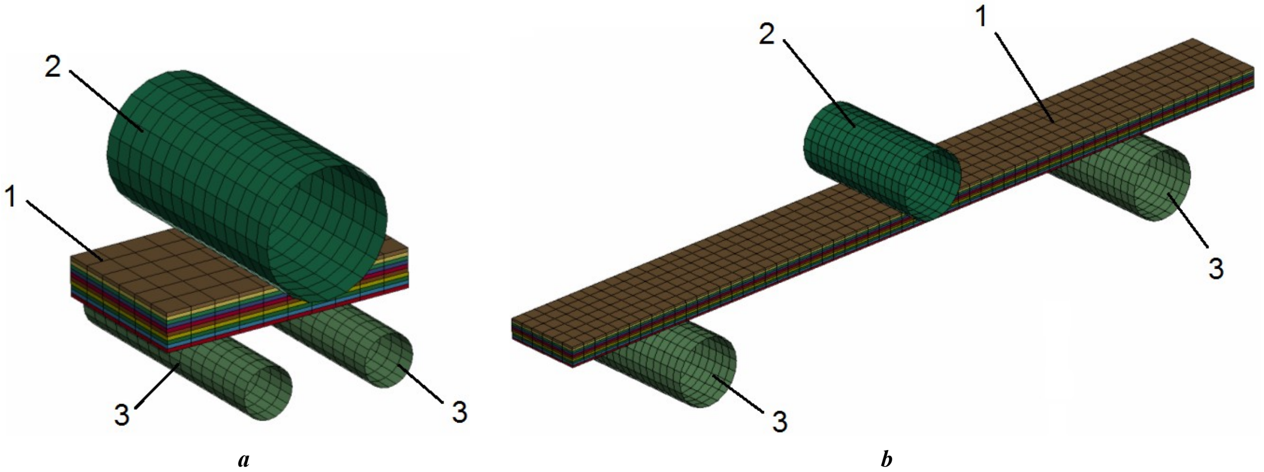

Fig. 2. *Models for mathematical simulation:* ***a*** *– for interlaminar shear;* ***b*** *– for three-point bending.*
1 – a composite, 2 – a press-on force plunger, 3 – a support

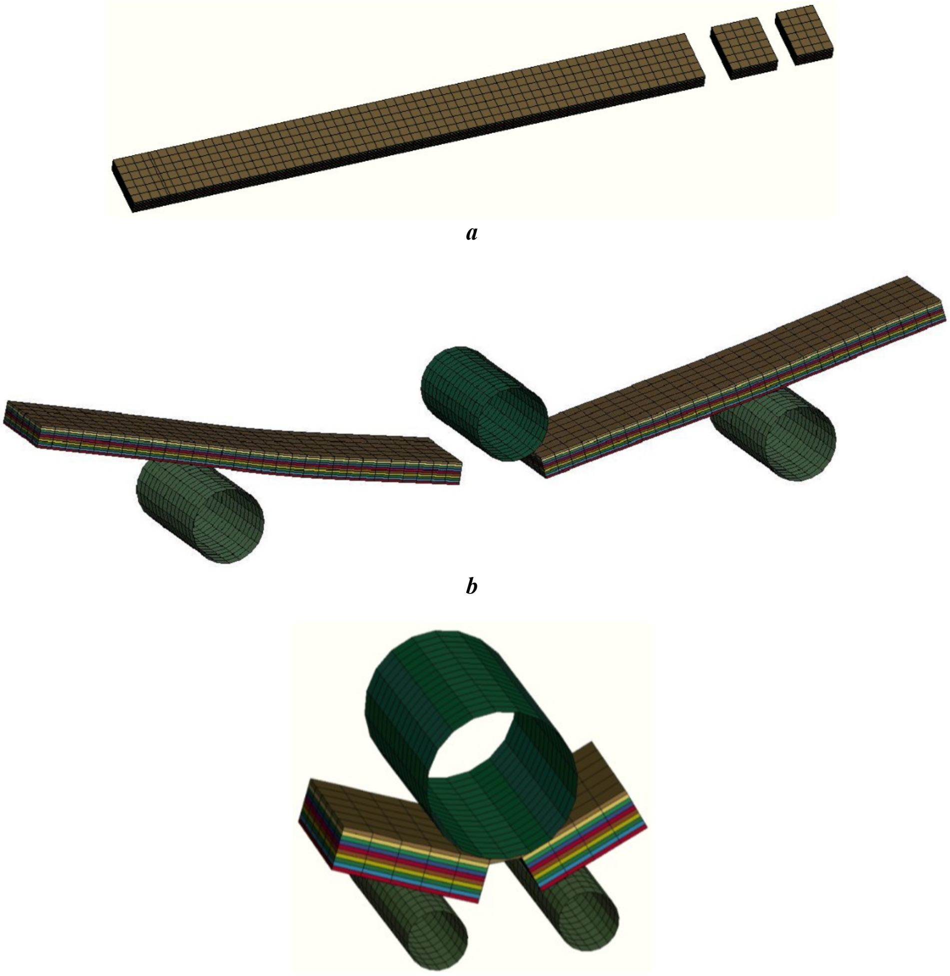

Fig. 3. *Test patterns:* ***a*** *– for uniaxial tension;* ***b*** *– for three-point bending;* ***c*** *– for interlaminar shear of a composite*

Table 1. *The range of variations of conditions of drilling holes in the ВКУ-39 polymer composite material during mathematical simulation using digital twins*

No.	The magnitude of the ultrasonic vibration amplitude, µm	Friction coefficient
1	0	0.0
2	6	0.0
3	13	0.0
4	0	0.1
5	0	0.2

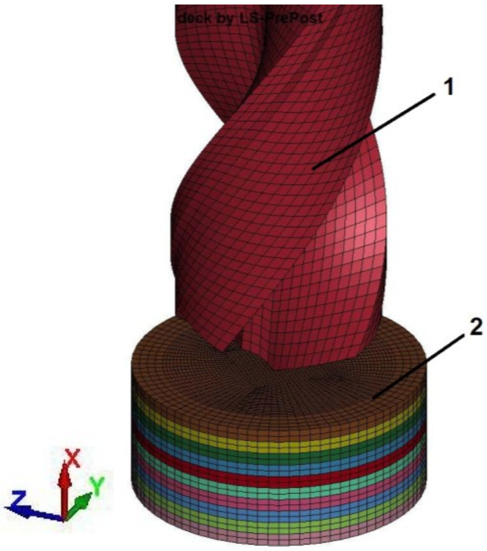

Fig. 4. *A model of a drilling tool and a composite for simulating a drilling process: 1 – a drilling tool, 2 – a composite*

using digital twins: operational cutting speed – 3.14 m/min, axial feed – 0.2 mm/rev. A drilling tool and composite model for simulating a drilling process is shown in Fig. 4.

A spiral two-blade drilling tool with a diameter of 5 mm, a length of 14 mm and an angle at the top of 2φ=140 degrees was taken as a cutting tool model. The model was represented by the solid-state elements with the sides of 0.25–0.3 mm. A cylinder 7 mm in diameter and 3 mm high was the composite blank model. In height, the composite model included 10 layers of interconnected prepregs. Each layer was a model consisting of thick-walled shell elements with dimensions of 0.1–0.15 mm.

As the main model of the material (ВКУ-39), the authors used the model of a composite orthotropic material with destruction.

After calibrating the model, the test parameters were adjusted. The failure of the material model was also set from the action of tensile stresses and amounted to 1610 MPa in the longitudinal (*XT*) and transverse (*YT*) directions of the composite. The values of breaking maximum strains of the composite and matrix layers were increased to 0.032.

The following parameters were used:

– normal stresses of the adhesive layer failure – 0.15 MPa;
– shear stresses of the adhesive layer failure – 1.5 MPa;
– failure energy (normal direction) – 0.9 mJ;
– failure energy (shear direction) – 0.9 mJ;
– rigidity (normal direction) – 6.25 MPa.

The failure parameters of the adhesive layer for bonding the layers of the composite were determined, based on the strength data of the applied adhesive compositions after carrying out tests and their validation.

To assess the conditions of the contact between the drilling tool and the composite, as well as the contacts between the layers of the composite itself (after the adhesive bond failure), a single contact taking into account the material failure was set.

To retain the force and the moments from the drilling tool impact, a penalty contact card was used.

To reduce the calculation time, the angular velocity of the drilling tool rotation was significantly increased and amounted to 628 rad/s. Such an increase is allowed in calculations in dynamic analysis programs when tracking the total energy of the process (the dynamic component should not exceed 10 % of the total energy of the process). The axial feed was 0.2 mm/rev.

The composite blank was fixed along the outer surface (Fig. 4, 5) by defining and limiting the nodal set.

After preparing the finite element model in the LS-DYNA version 971 V10.2 program, a double precision calculation was performed.

The stages of drilling a composite are shown in Fig. 6.

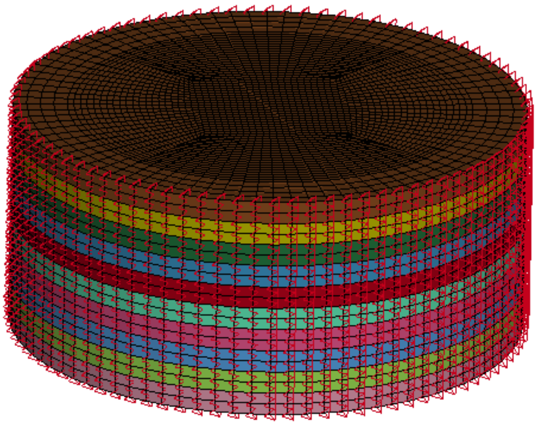

Fig. 5. *Angle restriction along the external cylindrical section of a composite blank*

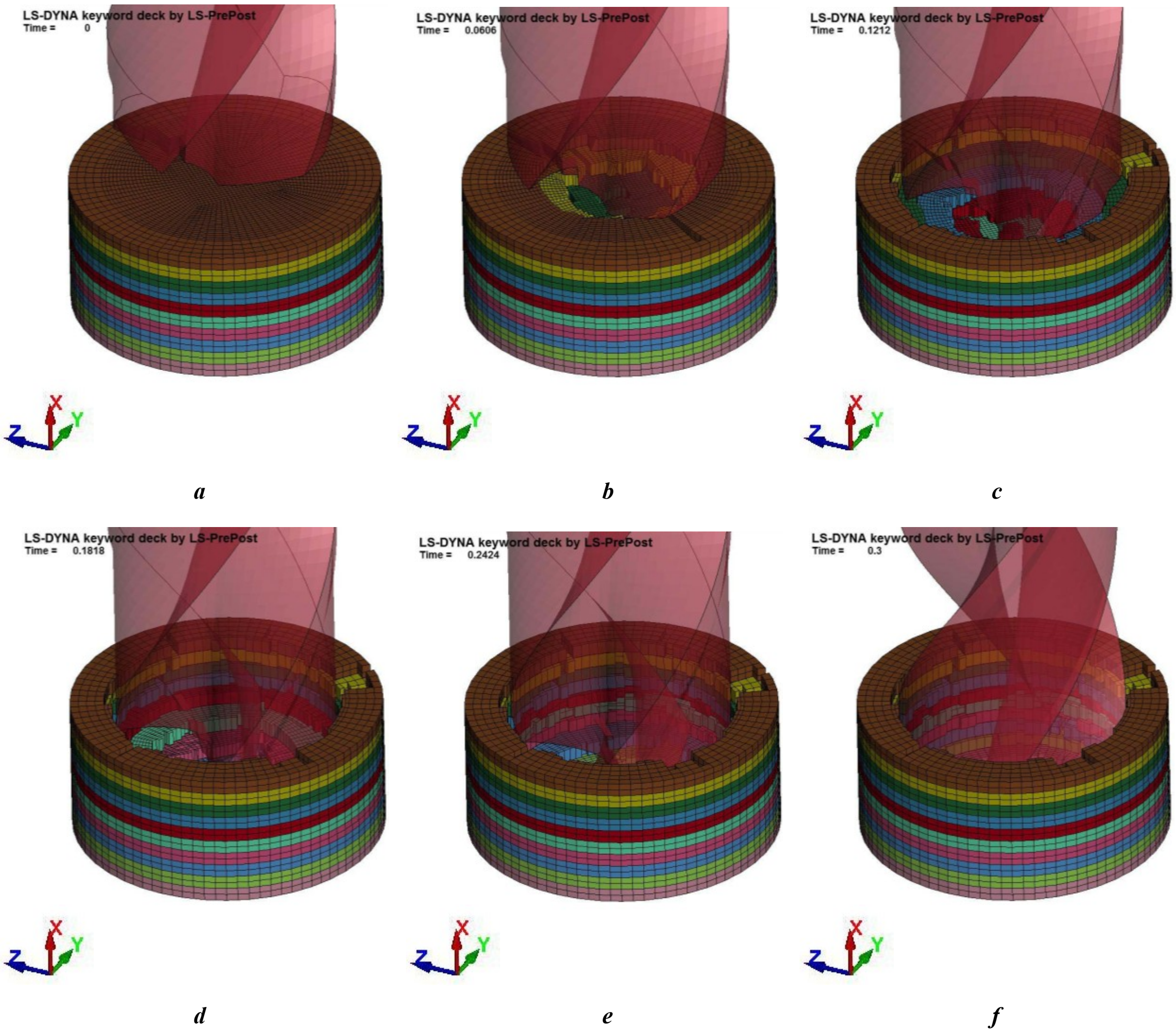

a ***b*** ***c***

d ***e*** ***f***

Fig. 6. *Composite drilling stages:* ***a*** *– 0 s;* ***b*** *– 0.06 s;* ***c*** *– 0.12 s;* ***d*** *– 0.18 s;* ***e*** *– 0.24 s;* ***f*** *– 0.3 s*

The influence of changes in the ultrasonic vibration amplitude and the ratio of friction between a rotating drilling tool and a composite blank on the efficiency of drilling composite material blanks was studied.

The ultrasonic vibrations were applied to the tool in the direction of the drill feed (along the *X*-axis). For this purpose, the motion function was specified in the initial settings. The following dependence on *time* was used as a function:

$$0.006 \cdot \sin(125600 \cdot \mathrm{time}) + 6 \cdot \mathrm{time}\ ,$$

where the parameter 0.006 is the vibration amplitude, in this case equal to 0.006 mm (6 μm);
parameter 125600 was determined from the dependence 2πω, where ω is the vibration frequency equal to 20 kHz.

The first summand of the function ensured the US vibration excitation; the second summand ensured the drilling tool feed.

RESULTS

The results of ВКУ-39 composite simulation for uniaxial tension, three-point bending, and interlaminar shear of the composite are shown in Fig. 7, 8.

The initial differences in the force of impact on the samples in some tests were in the range of 30–50 %. Additionally, varying the parameters of the material models in terms of the maximum tensile, and compressive strain of the composite layers, and the adhesive layer (in terms of normal and shear stresses and fracture energy), the authors managed to obtain a difference of no more than 10–15 %.

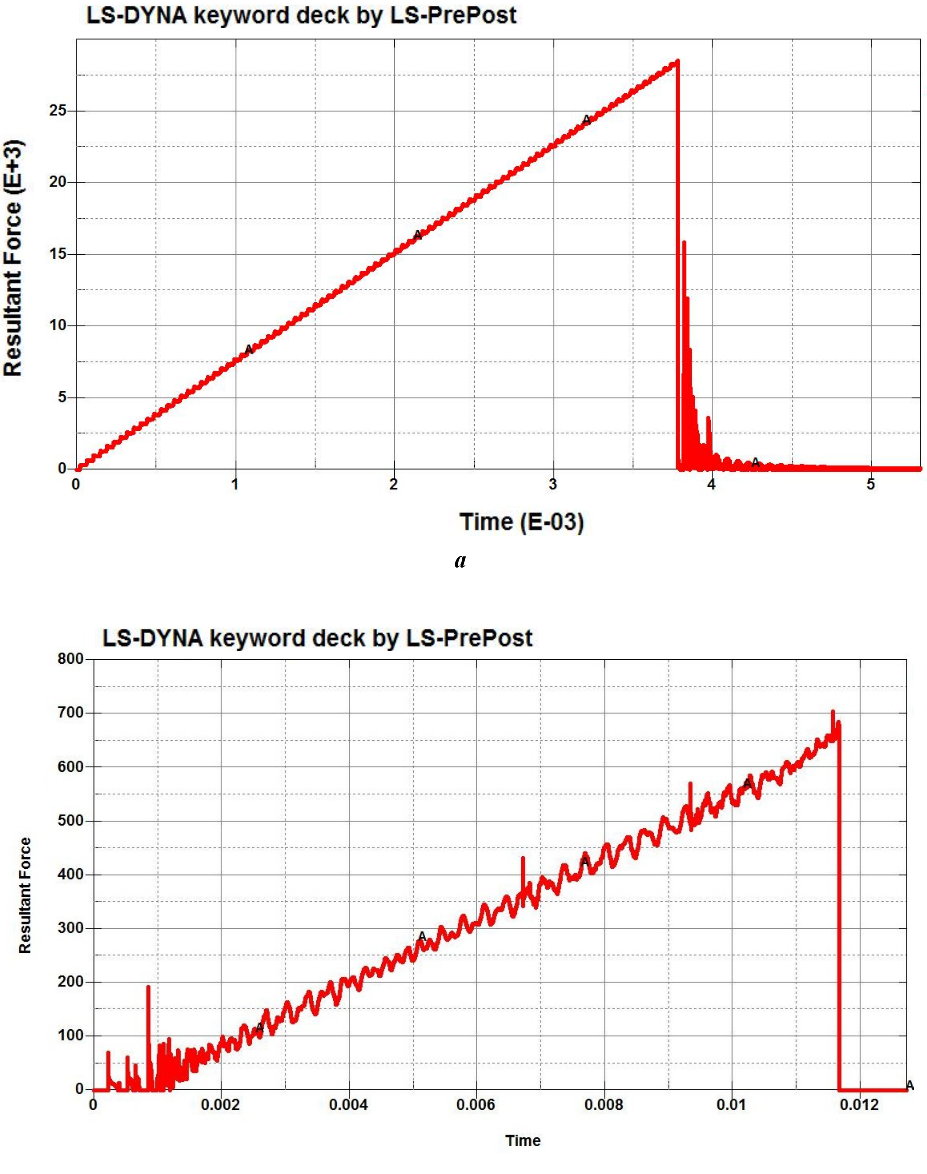

a

b

Fig. 7. *The results of simulating the ВКУ-39 composite:*
a *– for uniaxial tension;* ***b*** *– for three-point bending.*
In y-direction, a force in N is shown, in x-direction – time in s

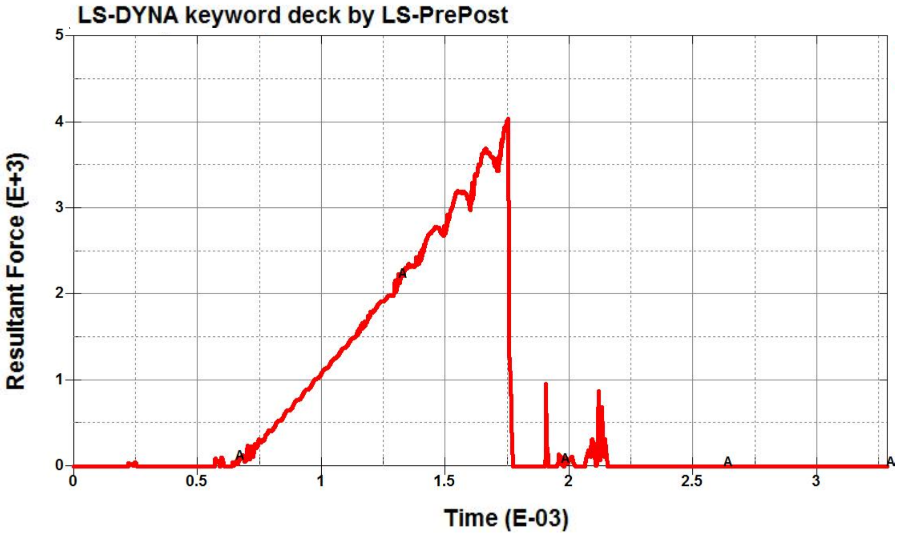

c

Fig. 8. *The results of simulating the ВКУ-39 composite for interlaminar shear of ВКУ-39 composite.*
In y-direction, a force in N is shown, in x-direction – time in s

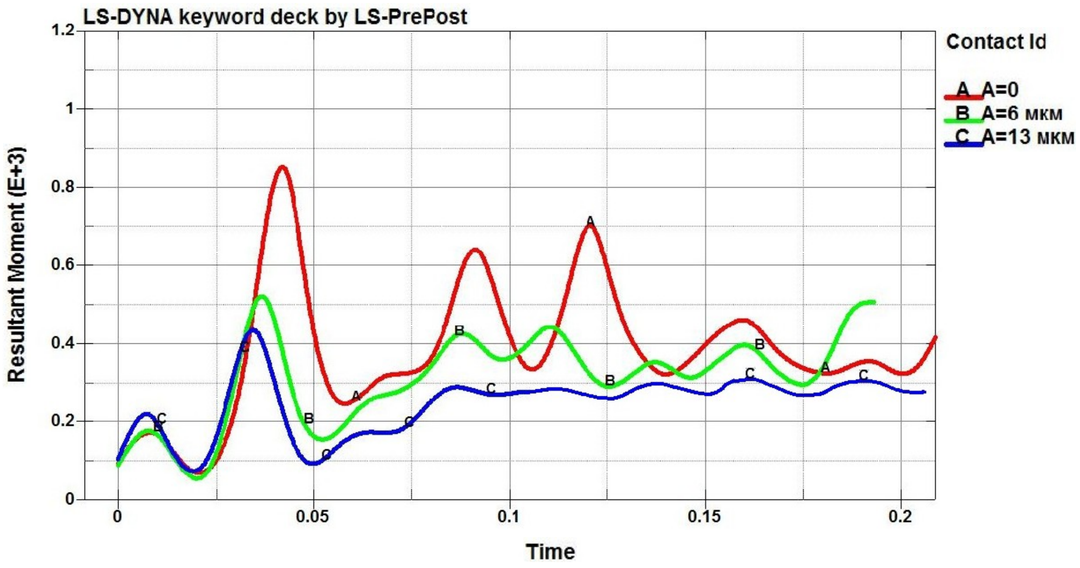

Fig. 9. *The dependence of a resultant moment on the amplitude value when applying ultrasound.*
In the graph: A – without ultrasound;
B – ultrasound with an amplitude of 6 micron;
C – ultrasound with an amplitude of 13 micron

Fig. 9 shows a diagram of the resultant moment dependence on the ultrasound amplitude magnitude. As one can see from Fig. 8, the introduction of ultrasonic vibration energy, with a frequency of 20 kHz and an amplitude of 6 µm into the treatment zone reduces the peak resultant moment from 860 to 515 N·mm. Drilling holes with the introduction of ultrasound with an amplitude of 13 µm allows reducing the peak moment to 430 N·mm.

Fig. 10 shows a diagram of the resultant moment dependence on the friction ratio. As one can see from the presented results, with a friction ratio equal to 0.2, the peak resultant moment is 1680 N·mm. The decrease in the friction ratio to 0.1 reduces the resultant moment to 1250 N·mm. With a friction ratio equal to zero (0), the resultant moment reduces to a minimum value of 810 N·mm.

DISCUSSION

According to the results of the study, one can argue that a decrease in the friction ratio under the ultrasound action, most certainly leads to a decrease in the resultant moment.

The performed computational investigations prove that the use of the obtained results can significantly reduce the duration or completely eliminate the need for experimental studies and full-scale tests to assess the influence of the cutting mode elements and the cutting tool design

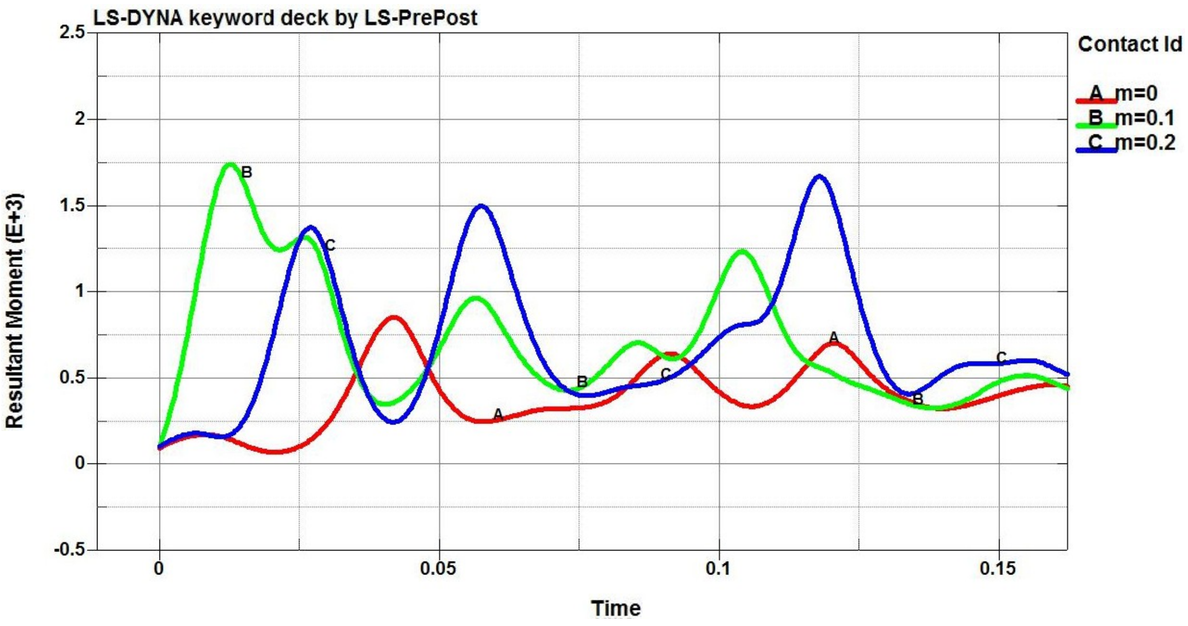

Fig. 10. *The dependence of a resultant moment on the ratio of friction (m) between a drilling tool and a composite*

parameters on the power and energy aspects of the formation of the machined surfaces of parts made of the ВКУ-39 type composite materials. In turn, this will allow significantly reducing the expenditures for technological preparation for manufacturing composite products, which means the achievement of the goal.

It is well known that the introduction of the ultrasonic vibration energy into the treatment zone leads to a decrease in the ratio of friction between the rotating tool and the metal blank being processed [12; 13].

The study visually established that the ultrasonic field energy introduction into the zone of formation of new surfaces, favorably affects the quality of the surface layer of parts made of polymer composite materials, and helps to reduce energy consumption for cutting processes and the cutting tool wear. The latter allows significantly increasing the productivity of processing blanks from such materials and reducing the cost of manufacturing parts from them.

For complete verification of computational investigations of the processes of cutting blanks from other PCMs based on carbon fibres, it is necessary to continue experimental tests on typical representatives of the existing classes of composite materials. The verification results, after making appropriate adjustments to the calculated data, will probably allow expanding the areas of using digital twins for simulating the processes of drilling blanks from other classes of polymer composite materials.

CONCLUSIONS

Thus, the research results prove that the developed computer models of the processes of drilling blanks made of laminated polymer composite materials, including with the ultrasonic field energy introduction into the zone of the new surfaces formation, are comparable to full-scale tests when testing the selected cutting mode elements, cutting tools, and other mechanical processing conditions. Considering that the use of digital twins to perform this stage of production technological preparation in the conditions of existing enterprises is not associated with expensive operation of machinery, one should expect a significant reduction in the cost of manufacturing components and parts made of similar materials in the industry, primarily in small-scale and single-item production.

REFERENCES

1. Kiselev E.S., Blagovskiy O.G. *Upravlenie formirovaniem ostatochnykh napryazheniy pri izgotovlenii otvetstvennykh detaley* [Controlling the formation of residual stresses when producing critical parts]. Sankt Petersburg, LAN Publ., 2020. 140 p.
2. Kiselev E.S., Nazarov M.V. *Osobennosti tekhnologii izgotovleniya nezhestkikh korpusnykh detaley* [Special aspects of the technology of manufacturing non-rigid body parts]. Moscow, RUSAYNS Publ., 2022. 218 p.
3. Ivanov Yu.N., Chapyshev A.P., Kaverzin E.A. Experimental study of thermal expansion effect of machined materials under dry drilling of holes in packages of “polymeric composite material–titanium alloy” structure. *Vestnik Irkutskogo gosudarstvennogo tekhnicheskogo universiteta*, 2013, no. 10, pp. 36–42. EDN: RGSXJV.
4. Ivanov Yu.N. Drilling the holes in the mixed packets. *Izvestiya Samarskogo nauchnogo tsentra Rossiyskoy akademii nauk*, 2014, vol. 16, no. 1-5, pp. 1402–1406. EDN: TJFAFL.
5. Dudarkov Yu.I., Levchenko E.A., Limonov M.V., Shevchenko A.V. Computational studies of some types of operational and technological damages impact on bearing capacity of stringer panels made of composite fiber reinforced plastic. *Trudy MAI*, 2019, no. 106, pp. 2–39. EDN: NLSATO.

6. Efremenkov I.V., Polyanskov Yu.V. Mathematical modeling of the dynamic interaction of a solid with its surrounding space in the LS-DYNA software package. *Universum: Tekhnicheskie nauki*, 2019, no. 6, pp. 6–8. EDN: JIKSOT.
7. Dudarev A.S., Dobrinskiy A.G. Efficiency of vibration drilling polymer composite materials. *Vestnik Permskogo natsionalnogo issledovatelskogo politekhnicheskogo universiteta. Mashinostroenie, materialovedenie*, 2019, vol. 21, no. 4, pp. 42–48. DOI: 10.15593/2224-9877/2019.4.05.
8. Kolesnik V.A., Krivoruchko D.V., Muzhetskiy A.I. Concerning the influence of fiber orientation on the fracture mechanism of fibrous polymer composites. *Nauchnyy Vestnik Donbasskoy gosudarstvennoy mashinostroitelnoy akademii*, 2012, no. 2, pp. 55–59.
9. Kolesnik V.A., Krivoruchko V.A., Evtukhov V.G. The microrelief formation of fibre reinforced plastic machined surface. *Tekhnologicheskie sistemy*, 2013, no. 64, pp. 60–69.
10. Vorobev Yu.A., Nikolaenko A.I., Vorobev A.Yu. Analysis of researches on drilling the mixed stacks from composite and titanium alloys. *Aviatsionno-kosmicheskaya tekhnika i tekhnologii*, 2008, no. 2, pp. 32–38.
11. Chashchin N.S., Ivanov Yu.N. Orbital drilling of holes in mixed packages. *Vestnik Irkutskogo gosudarstvennogo tekhnicheskogo universiteta*, 2015, no. 11, pp. 44–49. EDN: VAUELX.
12. Chashchin N.S., Ivanov Yu.N., Sidorova A.V., Semenov E.N., Sturov A.A. Studying the technology of small diameter hole-making in polymer composites by a robotic system. *Vestnik Irkutskogo gosudarstvennogo tekhnicheskogo universiteta*, 2017, vol. 21, no. 6, pp. 39–48. DOI: 10.21285/1814-3520-2017-6-39-48.
13. Chigrinets E.G., Rodriges S.B., Zaborotniy D.I., Chotchaeva S.K. Numerical modelling of thermal fields in a polymer composite. *Trudy MAI*, 2021, no. 116, pp. 17–48. DOI: 10.34759/trd-2021-116-17.
14. Chigrinets E.G. Titanium-reinforced glass fiber plastic main rotor blade beam drilling process optimization. *Vestnik Moskovskogo aviatsionnogo instituta*, 2016, vol. 23, no. 1, pp. 177–188. EDN: VPEKQD.
15. Hocheng H., Puw H.Y. On drilling characteristics of fiber-reinforced thermoset and thermoplastics. *International Journal of Machine Tools and Manufacture*, 1992, vol. 32, no. 4, pp. 583–592. DOI: 10.1016/0890-6955(92)90047-K.
16. Dudarev A.S., Gumarov E.K. Study of thermophysics during diamond drilling of fiberglass and carbon fibre-reinfoced polymer composites. *Proceedings of Irkutsk state technical university*, 2021, vol. 25, no. 3, pp. 290–299. DOI: 10.21285/1814-3520-2021-3-290-299.
17. Savelev K.S., Ilyushkin M.V., Kiselev E.S. Use of digital twins for mathematical modeling of ultrasonic drilling of titanium blanks. *Vektor nauki Tolyattinskogo gosudarstvennogo universiteta*, 2021, no. 1, pp. 42–54. DOI: 10.18323/2073-5073-2021-1-42-54.
18. Kiselev E.S., Ilyushkin M.V., Savelev K.S. Computer simulation of hard-to-machine billet cutting using digital twins. *Naukoemkie tekhnologii v mashinostroenii*, 2021, no. 7, pp. 29–40. DOI: 10.30987/2223-4608-2021-7-29-40.
19. Nguyen T.A., Tran T.T. Drilling Modelling Using Computer Simulation. *International Journal Of Scientific & Technology Research*, 2020, vol. 9, no. 10, pp. 171–174.
20. Vajdi M., Moghanlou F.S., Sharifianjazi F., Asl M.S., Shokouhimehr M. A review on the COMSOL Multiphysics studies of heat transfer in advanced ceramics. *Journal of Composites and Compounds*, 2020, vol. 2, no. 2, pp. 35–43. DOI: 10.29252/jcc.2.1.5.

doi: 10.18323/2782-4039-2023-2-64-3

The dependence of the biodegradable ZX10 alloy corrosion process on the structural factors and local pH level

Pavel N. Myagkikh*[1], junior researcher of the Research Institute of Advanced Technologies
Evgeny D. Merson[2], PhD (Physics and Mathematics),
senior researcher of the Research Institute of Advanced Technologies
Vitaly A. Poluyanov[3], PhD (Engineering),
junior researcher of the Research Institute of Advanced Technologies
Dmitry L. Merson[4], Doctor of Sciences (Physics and Mathematics), Professor,
Director of the Research Institute of Advanced Technologies
Togliatti State University, Togliatti (Russia)

***E-mail: feanorhao@gmail.com,
p.myagkikh@tltsu.ru**

[1]ORCID: https://orcid.org/0000-0002-7530-9518
[2]ORCID: https://orcid.org/0000-0002-7063-088X
[3]ORCID: https://orcid.org/0000-0002-0570-2584
[4]ORCID: https://orcid.org/0000-0001-5006-4115

Received 18.05.2023 *Accepted 29.05.2023*

Abstract: Magnesium biodegradable alloys are a promising material for self-dissolving surgical implants. Magnesium is known to be sensitive to electrochemical corrosion due to the galvanic effect between the matrix and particles of secondary phases and inclusions. Another important factor is the pH level. The behavior of certain chemical reactions depends on the pH level, so one can assume that the pH level of a corrosive medium at the material surface is a factor determining what chemical reactions can occur there. Finally, there is evidence that variability of the crystallographic orientation of the grains may be a cause of anisotropy of corrosion properties. The purpose of this work is to reveal the influence of the electrode potential of the microstructural elements, the crystallographic orientation of the grains, and the pH level of the near-surface volume of the corrosion solution on the corrosion process. In the study, sections of 2×1.5 mm were marked on the ZX10 alloy samples, for which maps of the distribution of crystallographic orientations and chemical composition were drawn. To assess the influence of the electrode potential of the particles, the authors carried out a Kelvin probe mapping in the 90×90 μm area. Next, corrosion tests were carried out with video filming of the surface on the marked area. To determine the pH level influence, the solution circulation in the cell was varied. Upon completion of the tests, corrosion products and corrosion damage were examined in detail. According to the results, the pH level in the liquid near-surface micro-volumes has a greater influence than the electrode potential of the particles as it provokes the formation of corrosion products of a different composition, which leads to passivation of the surface areas around the particles. The authors identified two different types of filiform corrosion. For filiform corrosion, a correlation between the corrosion direction and the crystallographic orientation of the grains was established.

Keywords: magnesium alloys; corrosion; ZX10; biodegradable materials; medical implants; electrode potential; pH level; crystallography; filiform corrosion.

Acknowledgments: The research was financially supported by the Russian Science Foundation, project No. 23-23-10041.

The paper was written on the reports of the participants of the XI International School of Physical Materials Science (SPM-2023), Togliatti, September 11–15, 2023.

For citation: Myagkikh P.N., Merson E.D., Poluyanov V.A., Merson D.L. The dependence of the biodegradable ZX10 alloy corrosion process on the structural factors and local pH level. *Frontier Materials & Technologies*, 2023, no. 2. DOI: 10.18323/2782-4039-2023-2-64-3.

INTRODUCTION

Traditionally, stainless steels and titanium-based alloys are used to produce surgical implants, such as screws for fixing bone fragments and plates for osteosynthesis. Upon completion of the healing process, in most cases, these implants are to be removed. The removal operation has a number of negative effects: risks for the patient's health, the need for post-operative recovery, an increase in the patient's disability period, etc. Therefore, one of the promising areas in this field is the creation of self-dissolving (biodegradable) metal implants. One of the most suitable metals for this purpose is magnesium: an important role in human metabolism and low cytotoxicity ensure its good biocompatibility, and mechanical characteristics close to bone tissues guarantee mechanical compatibility [1]. Since the metal dissolution in the human body is nothing but corrosion, the study of the mechanisms of corrosion processes in magnesium alloys is of great importance for both fundamental and applied science. Several factors significantly affecting the corrosion of magnesium alloys are known.

The variability of the grain crystallographic orientation can cause anisotropy of corrosion properties [2], as well as a tendency to filiform corrosion [3]. However, the experiments carried out on single crystals and polycrystals with coarse grains show contradictory results: in the work [3], it was identified that the basal plane (0001) exhibits the lowest corrosion resistance, while the works [4; 5] indicate that such an orientation of crystallites, on the contrary, provides the highest corrosion resistance. In the case of a fine-grained polycrystal, crystallographic texture has a great influence on corrosion, a phenomenon often observed after extrusion, rolling, or other thermomechanical processing of magnesium alloys, and consisting in the predominance of a certain orientation in most semi-finished product crystallites. In the work [6], when studying the anisotropy of the extruded magnesium corrosion properties, it was identified that the section plane along the bar with the predominant grain orientation (0001) is much more corrosion resistant than the plane in the section across the bar. Thus, the influence of crystallography can play an important role in the corrosion processes of magnesium alloys.

The particles of secondary phases and inclusions are equally important. Magnesium has an electrode potential of −2.375 V [7], which is significantly lower than that of most metals used as alloying elements in magnesium alloys. This causes its tendency to electrochemical corrosion manifesting itself during the interaction in a corrosive environment between two metals with different potentials. Since, under the galvanic effect, the material with a more negative potential is dissolved first, most of the particles, being positive with respect to magnesium, reduce the material corrosion resistance by provoking an intensive dissolution of the magnesium matrix.

Speaking about the particles with a more negative electron potential than magnesium, one should keep in mind several factors. First, as shown in [8], phases with a more negative potential compared to the matrix can form corrosion products, which, on the contrary, play the role of a cathode. Second, it is necessary to take into account the change in the electrode potentials of the matrix and, the secondary phase under the action of alloying elements in the form of a solid solution. It is known that many elements, such as zinc and silver [7], increase the potential of the magnesium matrix when forming a solid solution. The dissolution of such elements in secondary phases, for example, in the Mg_2Ca intermetallic compound, which has a more negative electrode potential than magnesium, leads to a shift in their potential to more positive values. The work [9] indicates that when the zinc concentration exceeds the value of 1.07 %, the Mg_2Ca phase becomes more positive than the matrix. Finally, one must take into account the fact, that the dissolution of a particle even more negative than the matrix will change the pH level in the corrosive medium microvolumes near the sample surface.

The primary reaction of magnesium in media simulating human body fluids, such as NaCl saline 0.9 %, Ringer’s solution, Hanks’ solution, etc., is as follows:

$$Mg + 2H_2O = Mg(OH)_2 + H_2\uparrow. \qquad (1)$$

The magnesium hydroxide produced during the reaction is a weak, poorly soluble base and performs two functions: to some extent passivates the material surface and, by dissociating into a magnesium cation and a hydroxyl group anion, increases the pH level. According to [8], the Mg_2Ca phase reacts with water in a similar reaction to form magnesium hydroxide and calcium hydroxide, which is a strong base. It follows from this that the corrosion of particles of such secondary phases as Mg_2Ca can lead to a significant local increase in the pH level. Based on the Pourbaix diagrams for pure magnesium in water presented in [10; 11], one can conclude that under conditions of a certain electrode potential of the surface and the pH level, various compounds can be stable: oxide, hydride, magnesium hydroxide, as well as magnesium itself, i.e., depending on the electrode potential and the pH level, the flow of well-defined reactions are thermodynamically favorable. This means that changing the pH level can significantly affect the type of corrosion products formed when reacting with water.

In solutions containing chloride ions, the reaction described by formula (1) may continue in the form of a reaction of chlorine anion with hydroxide:

$$Mg(OH)_2 + 2Cl^- \rightarrow Mg(Cl)_2 + 2OH^- \rightarrow \\ \rightarrow Mg^{2+} + 2Cl^- + 2OH^-. \qquad (2)$$

As can be seen from the reaction equation, chlorine contributes to the destruction of magnesium hydroxide, which plays the role of a weak passivating film, and then the well-soluble magnesium chloride formed can dissociate in water into magnesium and chlorine ions. However, due to the influence of various factors, such as the concentration of some ions in the solution, reactions that are more complex can occur, for example, the reaction with the formation of oxychlorides described in [8]:

$$x(Mg^{2+}) + Cl^- + y(OH^-) + z(H_2O) \rightarrow \\ \rightarrow Mg_x(OH)_yCl \cdot zH_2O. \qquad (3)$$

Detailed information on the formation of various oxychlorides in aqueous solutions at 23 °C is presented in the work [12]. The authors indicate that mainly two types of oxychlorides are formed: $5Mg(OH)_2{\cdot}MgCl_2{\cdot}8H_2O$ (shortly 5·1·8) and $3Mg(OH)_2{\cdot}MgCl_2{\cdot}8H_2O$ (shortly 3·1·8), noting that these compounds differ significantly: 5·1·8 is formed faster, and 3·1·8 tends to react with carbon dioxide and carbonate ions with the formation of chlorocarbonate. The conditions for the formation of compounds also differ from each other and depend on the concentration of chloride ions and the pH level.

Following all this, one can draw the conclusion: the electrode potential determines what will be destroyed first of all – a particle of secondary phases and inclusions or a matrix, and the pH level in the microvolumes of the corrosive medium near the metal surface, affects what chemical reactions will take place. However, it is not clear which of these factors is more important, especially against the background of the matrix crystallographic effect. Determining the influence of all three factors is important for understanding the mechanism of corrosion processes and, therefore, predicting the corrosion properties of materials and the efficiency of thermal and thermomechanical treatment modes.

The aim of this work is to study the influence of the crystallographic orientation of grains, secondary phase particles, as well as the pH level in microvolumes of the corrosive medium near the sample surface on the corrosion process of the biodegradable ZX10 alloy.

METHODS

A biodegradable as-cast ZX10 alloy of the Mg–Zn–Ca system was chosen for the study. This alloy has good cytotoxicity characteristics [13], high strength properties [14], and a relatively low corrosion rate [1; 14]. The exact chemical composition was determined using a Thermo Fisher Scientific ARL 4460 OES optical emission spectrometer.

The samples were rectangular plates of 30×15×1 mm ground on #2500 sandpaper. After grinding, in the middle of the right half of one of the sample surfaces, a 2×1.5 mm area was marked with a hard-tip chisel for precision research. Then, the surface with the marked area was polished on anhydrous diamond suspensions with an abrasive size of 3, 1, and 0.25 µm in succession. After that, the marked area was subjected to ion polishing in a Hitachi IM4000Plus device. Treatment was carried out in an ionized argon beam at an angle of 5° to the sample surface for 35 min at an accelerating voltage of 3.2 kV. From the marked area, a distribution map of crystallographic orientations was taken in the column of a Carl Zeiss SIGMA scanning electron microscope (SEM) using an EDAX module for analyzing electron back-scattered diffraction (EBSD). In the SEM column, mapping was also carried out with determining the elemental composition on the surface of the marked area using energy dispersive spectrometry (EDS). On the surface of the sample marked area intended to identify the role of the electrode potential (hereinafter, this sample is marked as EP), an area of 90×90 µm with several particles was selected, and in this area, an electrode potential distribution map was taken according to the Kelvin probe method using a NT-MDT Solver NEXT atomic force microscope. Further, all samples were subjected to corrosion tests.

The tests included holding the sample for 24 h in Ringer's solution with the composition of 8.36 g NaCl, 0.3 g KCl, 0.15 g $CaCl_2$ per 1000 ml of water. The corrosion cell volume was 5 l. The sample was fixed vertically in a silicone clamp in such a way that the clamp was as far as possible from the marked area. To monitor corrosion processes, a camera was directed to the area marked with a chisel, by analogy with our previous work [15]. Video surveillance during corrosion tests is an *in situ* method that allows tracking the staging of the corrosion damage appearance and the dynamics of their development. This method showed good results when studying the dependence of the direction of filiform corrosion propagation on the crystallographic grain orientation [16]. When testing a sample intended to determine the pH influence (hereinafter marked as PH), the corrosive medium was circulated using a peristaltic pump. The tube, through which the corrosive solution was pumped into the corrosion cell, was directed straight to the marked area from below, so that the flow was oriented diagonally from the lower right corner of the marked area tangentially to the sample surface. Thus, the corrosive medium at the sample surface, the pH level of which could be increased due to the occurrence of corrosion processes, was washed away by the solution flow.

After completion of the tests, the samples were removed, dried in a fore vacuum at room temperature for 2 h, and then loaded into a SEM to map the distribution of chemical elements in corrosion products. Then the corrosion products were removed by immersion in an aqueous solution of 20 % CrO_3+1 % $AgNO_3$ for 1 min by analogy with the work [17]. When removing corrosion products, a Sapphire ultrasonic bath was used. After the removal of corrosion products, the corrosion damage depth and morphology were assessed using an Olympus Lext OLS4000 confocal laser scanning microscope (CLSM).

RESULTS

Table 1 presents the ZX10 alloy chemical composition.

Fig. 1 shows a map of the distribution of crystallographic orientations, as well as of particles of secondary phases, and inclusions in the marked area of the EP sample. Fig. 2 shows maps of the distribution of the electrode potential and chemical elements in the area marked with a rectangle in Fig. 1. The area contains three large particles with different chemical compositions and electrode potentials. Particles No. 1 and 3 are clearly oxidized, presumably due to the air contact.

Fig. 3 presents a storyboard of the video recording of the EP sample corrosion tests. The location of corrosion centres correlates well with the distribution maps of chemical elements in Fig. 1. The structure is visible only during the first 2 h of the experiment, after which the grain boundaries become practically invisible. In 12 h, typical pale regions form around all the observed particles in the marked area due to the formation of corrosion products. No dependence of the corrosion process occurrence on grain orientation is observed. After 12 h of testing, filiform corrosion traces appear in the corner of the marked area (indicated by a red arrow), but their subsequent growth does not occur.

Fig. 4 shows a map of crystallographic orientations, and distribution of particles of secondary phases and inclusions in the marked area of the PH sample.

Fig. 5 shows a storyboard of video recording of the PH sample corrosion test. From the very beginning of the test until its completion, the structure is clearly visible, the sample remains shiny for all 24 h and is not covered with a dense layer of corrosion products, corrosion centres are clearly visible, but wide zones covered with corrosion products do not form around them. After 23 h of testing, filiform corrosion traces become visible. One should note that, as in the case of the EP sample, the initial filiform corrosion spreads along the scratches that marked the area under the study. In both cases, filiform corrosion propagates at a rate of tens or even hundreds of microns per minute.

Fig. 6 demonstrates images of the marked areas of both samples before the removal of corrosion products, as well as a height map taken using CLSM after the corrosion products were removed. Using the height map, it is possible to estimate the depth of filiform corrosion damage, it equals to 10–15 µm.

Fig. 7 shows the surface of the marked areas of both samples with a superimposed map of the distribution of crystallographic orientations. It is evidently that both samples are characterised by the presence of two types of filiform corrosion. Except for the first type damage shown by red arrows in Fig. 3 and 5, after the removal of corrosion products, the second type damage becomes visible in the form of a fine mesh and especially clearly visible on the PH sample.

Fig. 8 presents the maps of the chlorine and oxygen distribution in corrosion products. The EP sample is characterised by the formation of zones significantly depleted in these elements around corrosion centres (i.e., particles of secondary phases and inclusions). This confirms the assertion, based on the obtained height maps that there is practically no corrosion in these places. There is a lot of zinc in corrosion products, both in the form of inclusions and evenly distributed over the surface. Calcium and zirconium are present mainly in the form of inclusions; the concentration of both elements in the corrosion products is less than 0.1 %.

Table 1. *Chemical composition of the ZX10 alloy, % wt.*

Mg	Zn	Zr	Ca	Fe	Mn	Si	Al	Cu
Base	0.84	0.03	0.17	<0.004	0.007	0.008	0.01	<0.001

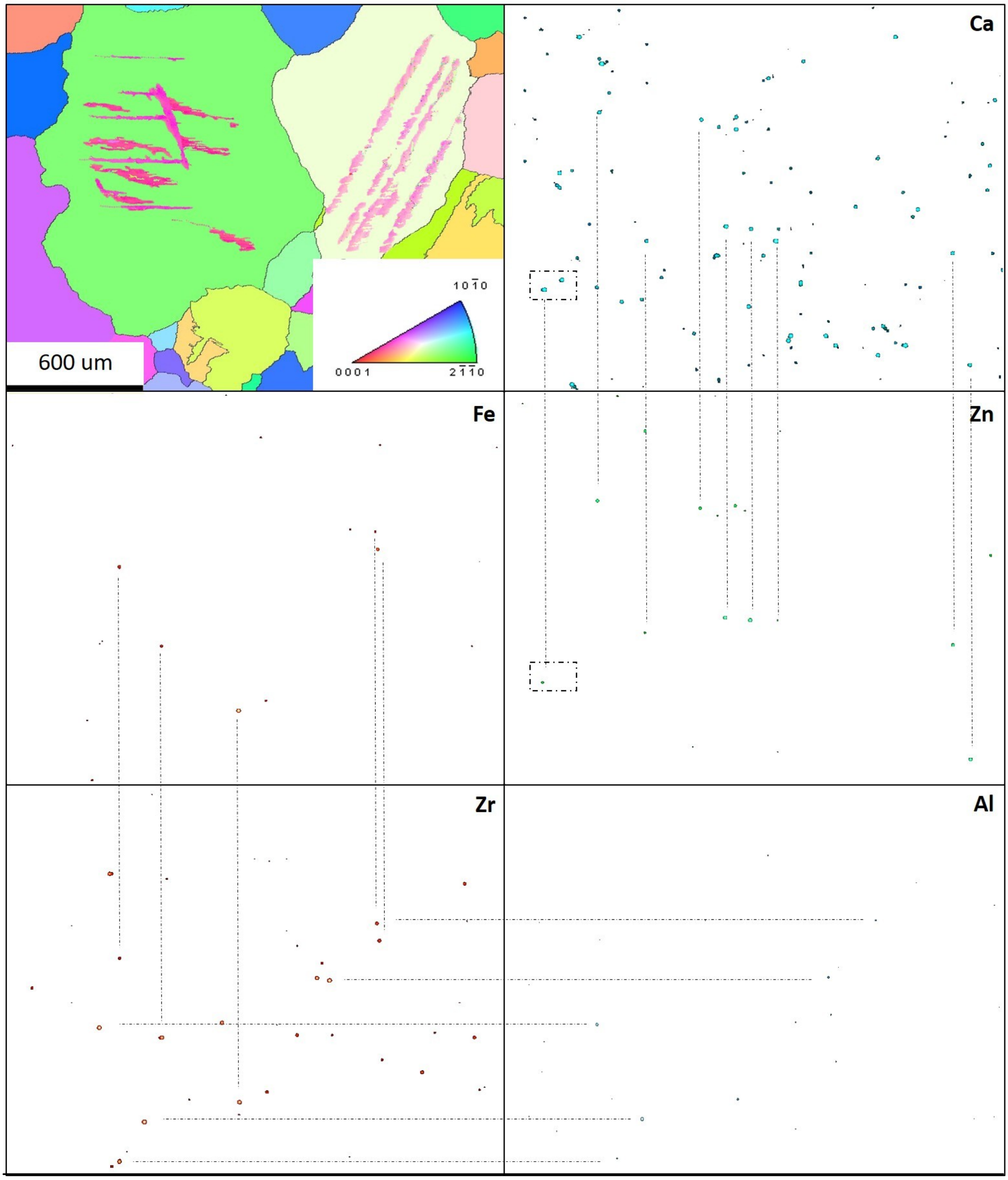

Fig. 1. *IPF-map and mapping of the particles of secondary phases and inclusions on the marked surface of EP-sample (the lines connect the same particles on the maps of different elements)*

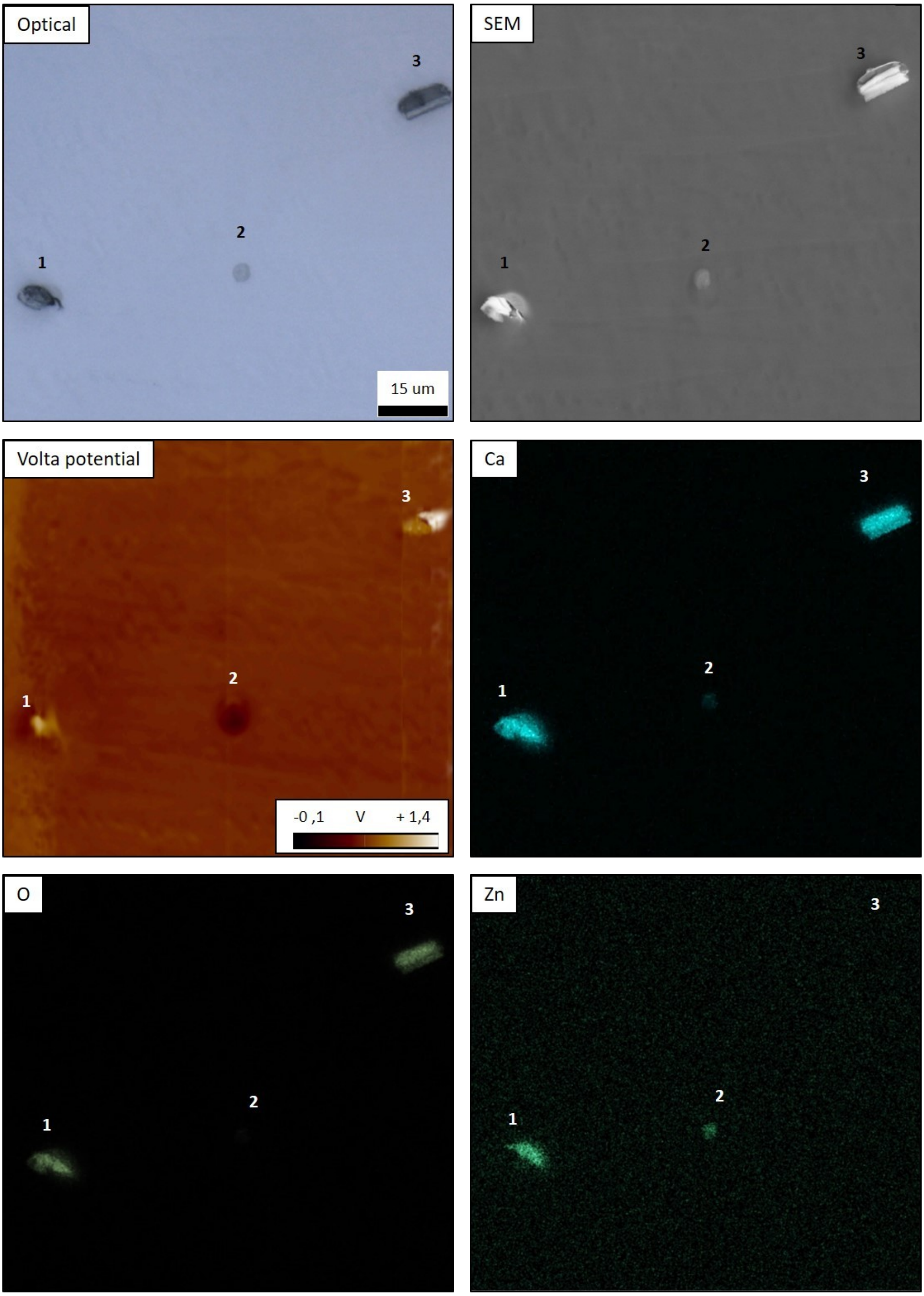

Fig. 2. *Volta potential map (by Kelvin probe method) and chemical composition of the particles in the rectangular area highlighted on the maps of zinc and calcium distribution in Fig. 1*

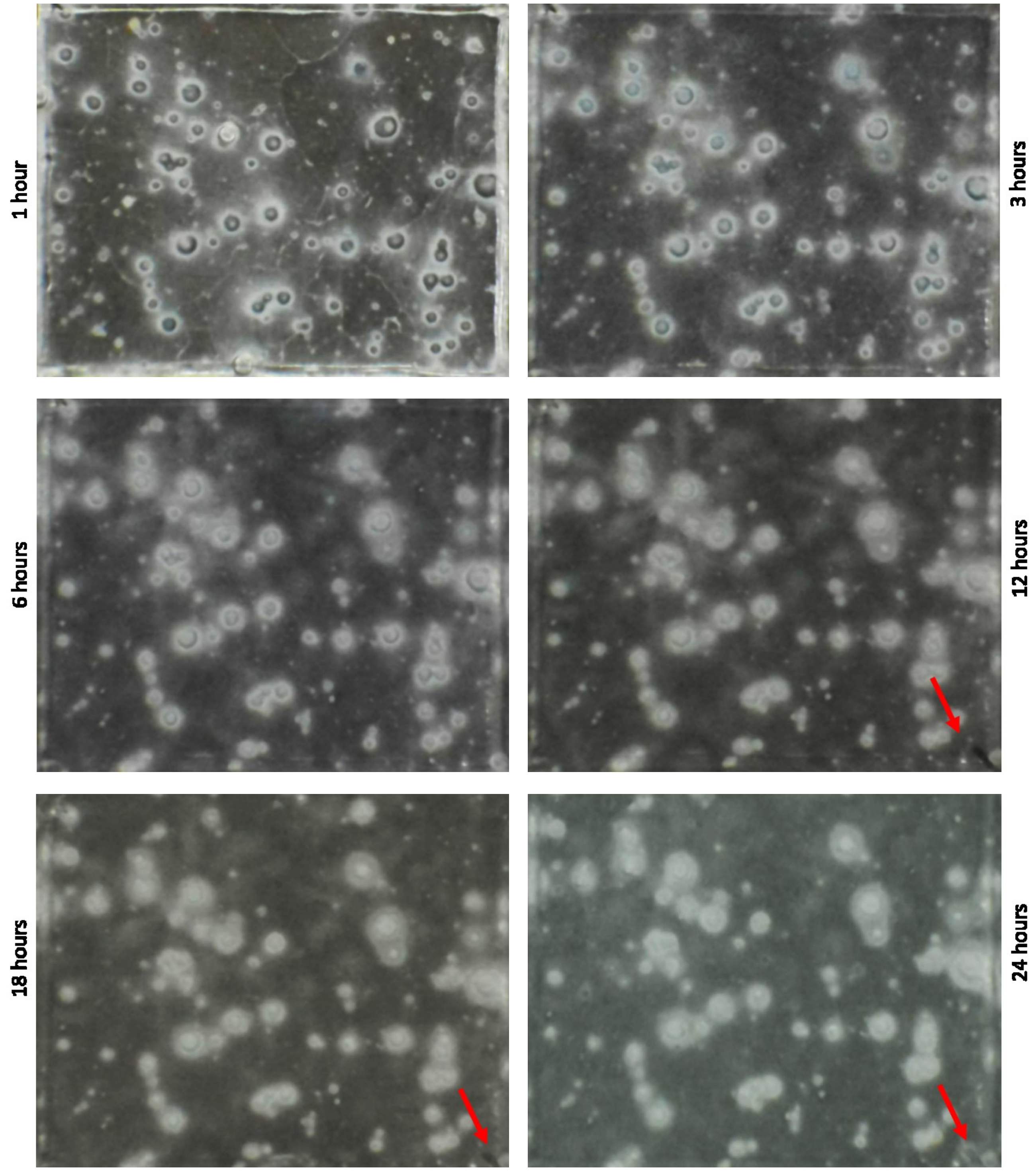

Fig. 3. *Video-monitoring results of the EP-sample marked surface during the corrosion test.
Red arrows indicate filiform corrosion*

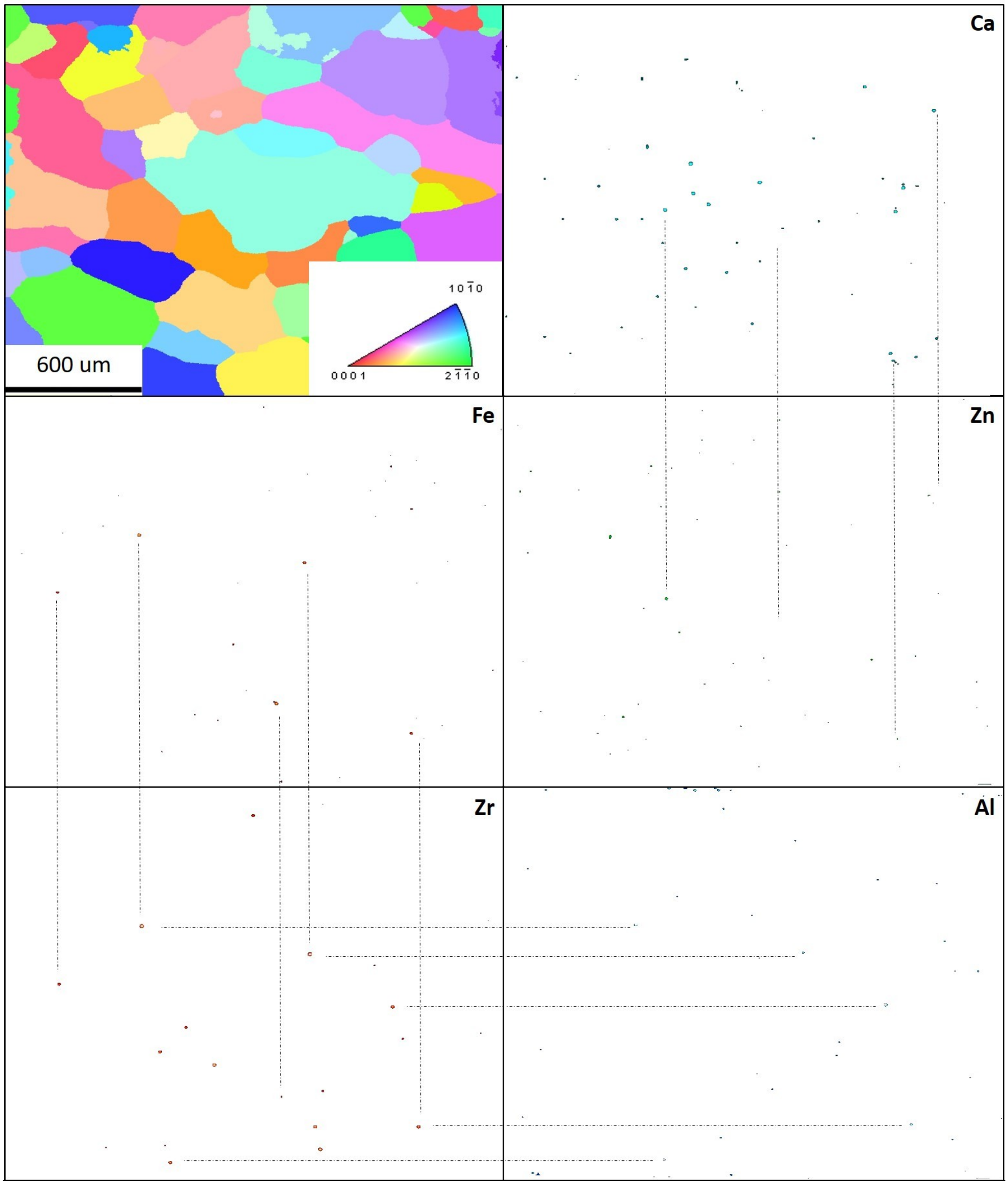

Fig. 4. *IPF-map and mapping of the particles of secondary phases and inclusions on the marked surface of the pH-sample*

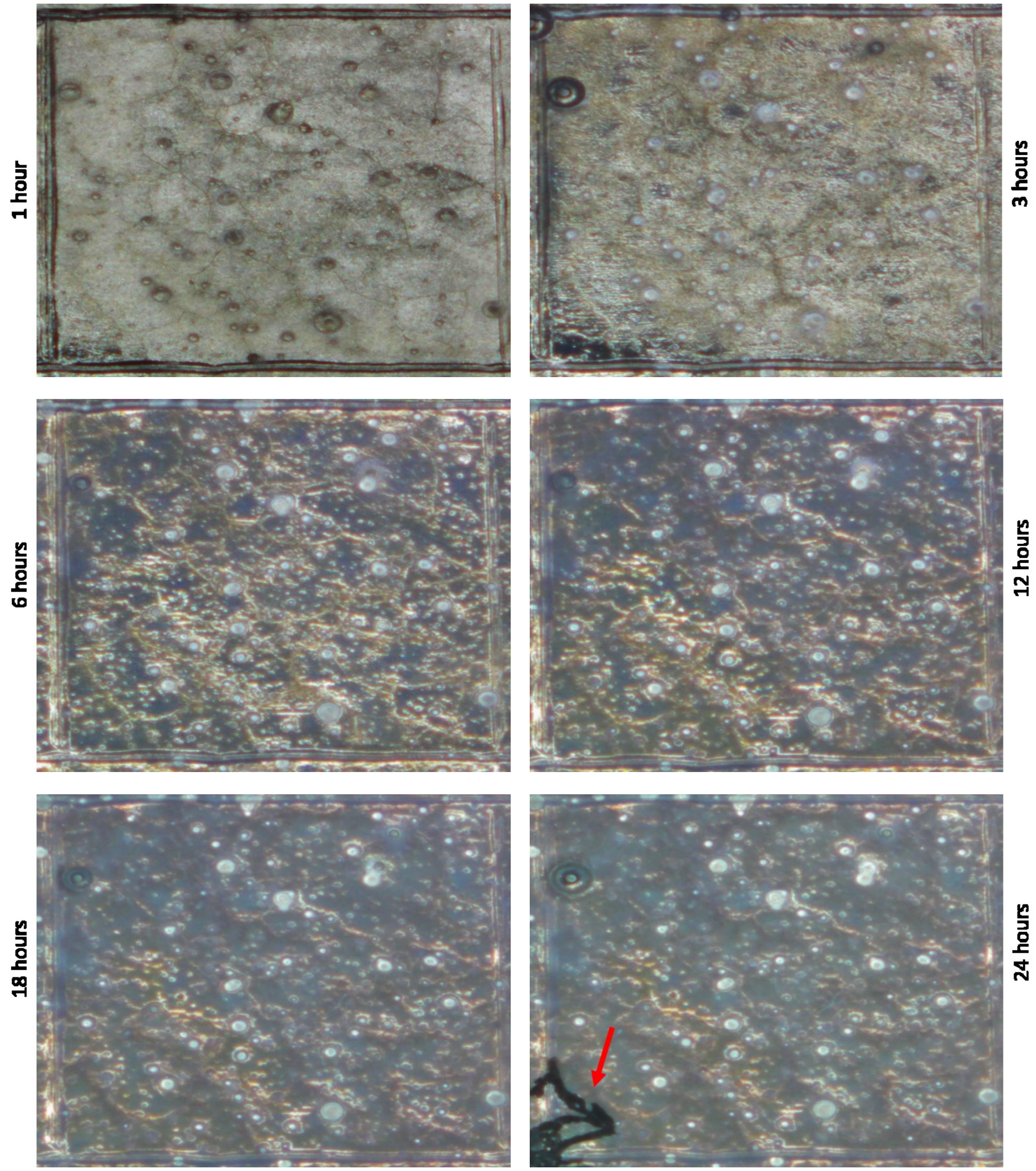

***Fig. 5.** The results of video-monitoring of the marked surface of the pH-sample during corrosion test. Red arrow indicates filiform corrosion*

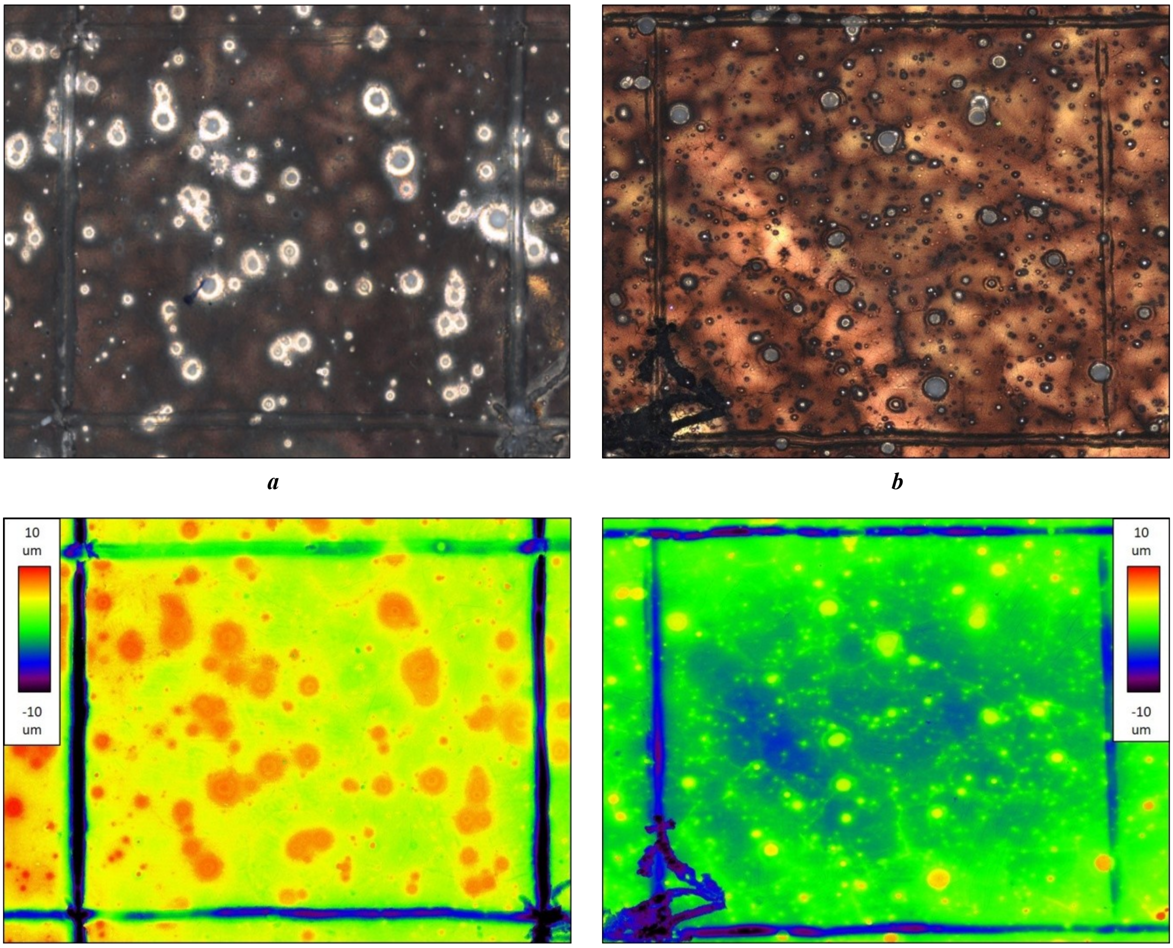

Fig. 6. *Images of marked areas of samples to reveal the role of the electrode potential (EP) (**a**, **c**) and to determine the pH (PH) effect (**b**, **d**):*
***a**, **b** – before the removal of corrosion products (optical microscopy);*
***c**, **d** – after the removal of corrosion products (height map obtained using CLSM)*

The PH sample pattern looks completely different (Fig. 9). Around the corrosion centres, there are no oxygen-depleted zones; this element is distributed evenly over the entire surface. Chlorine is distributed mainly point-wise, with most of it concentrated at the place of filiform corrosion damage of the first type. For calcium and carbon, the same patterns remain as for EP sample, but the quantity of zirconium and zinc in the corrosion products of the PH sample, are many times greater than in the EP sample corrosion products, and generally in the material. Probably, when magnesium is dissolved, these corrosion-resistant elements remain in the corrosion products.

Fig. 10 shows the maps of heights and distribution of chemical elements in corrosion products in the area shown in Fig. 2. On the height map and the oxygen and chlorine distribution maps, no differences between the particles are visible. In the region of particles No. 1 and 3, their residues in the form of calcium traces are noticeable.

Fig. 11 and 12 present the results of a detailed study of filiform corrosion damage of the first type on the PH specimen. Corrosion spread directionally; there is a large amount of chlorine at the end propagation points and places of change of its direction, although chlorine is not observed over the rest area affected by filiform corrosion. From Fig. 11 b, it is obvious that this type of corrosion strongly depends on the grain crystallographic orientation, and therefore, changes the direction of its propagation when moving from one grain to another. No correlation between the location of the most chlorine and the deepest damages is observed. The study identified an interesting honeycomb morphology of the walls of the “channel” for the filiform corrosion propagation, which is shown in Fig. 12 e, 12 f. The morphology has the form of rectangular honeycombs oriented across the direction of corrosion propagation. A fragment in Fig. 12 f is located at the boundary of two grains with different orientations. It is seen that along with the propagation direction, in this place, the orientation of the honeycombs also changes by almost 90°. This image also allows estimating the width of the channels of the second type filiform corrosion, which is about 1 μm.

DISCUSSION

Fig. 1 shows that calcium in the particles often adjoins zinc (shown by dotted lines), and there is clearly more zinc in these secondary phases. It is also obvious that there are quite a lot of particles containing calcium, but not containing zinc in the microstructure. Quite likely, these are

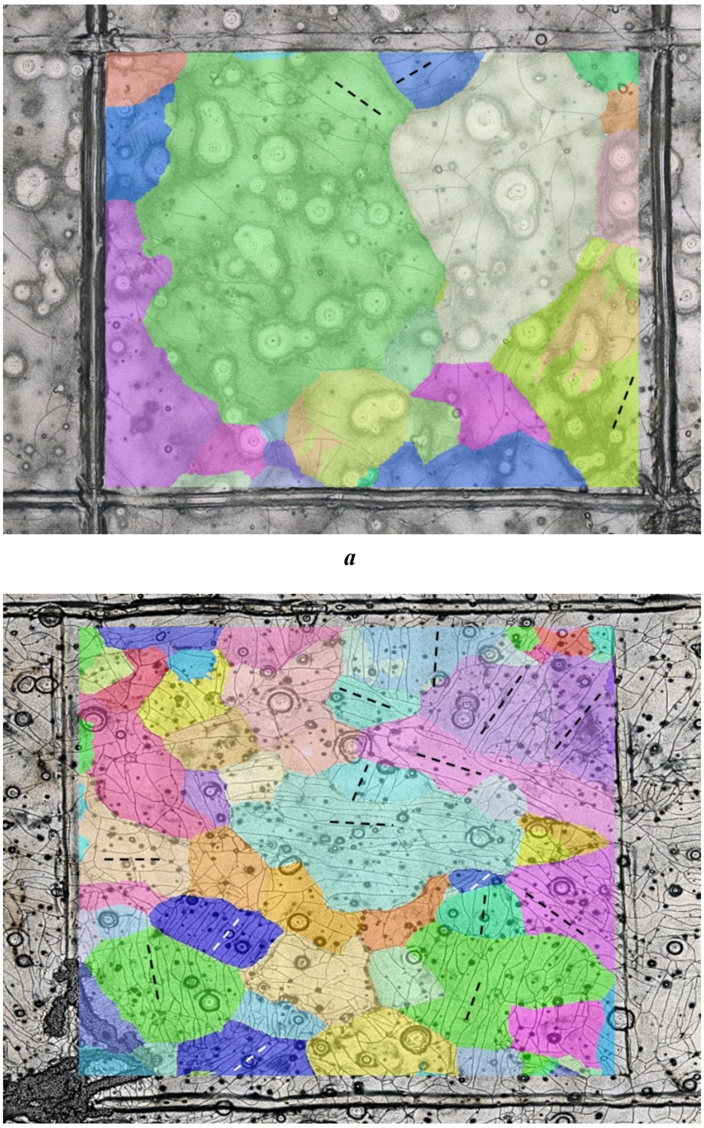

Fig. 7. *Images of marked areas of the samples to reveal the role of the electrode potential (EP) (**a**) and to determine the pH (PH) effect (**b**) after the removal of corrosion products. A map of the distribution of crystallographic orientations is superimposed on the optical image. The dotted lines show the main direction of second type filiform corrosion*

the Mg_2Ca phase particles. Zirconium is adjoins iron and aluminum, with which, as is known, it is capable of forming intermetallic compounds [18]. In the case of iron, due to the transition to the Fe_2Zr intermetallide, its negative effect on corrosion properties is reduced [19]. For the PH sample, the same features of the distribution of particles of secondary phases and inclusions of various compositions are noted as for the EP sample. In Fig. 6, it is clearly seen that a wide rounded zone is formed around the inclusions on the EP sample surface, which, judging by the height map, is subjected to the least corrosion damage. The PH sample is characterized by an elevation in the immediate proximity to a particle; large rounded zones, as in the EP sample, are not observed.

For both samples, the presence of two types of filiform corrosion is noticeable. The first type damage is characterized by a wide channel appearing in scratches and growing in one direction, which, judging by Fig. 7 and 11, has a dependence on grain orientation. The second type damage is very thin, covering the entire marked area with a fine mesh. Initially, a hypothesis arose that these damages were associated with cracking of the crust of corrosion products and the corrosion medium penetration, under the passivating layer. However, comparison with the grain orientation map clearly indicates that the direction of the filiform corrosion propagation depends on the crystallographic orientation, while, in the case of corrosion product cracking, the directions should have been chaotic. An interesting fact is that the PH sample has much more damages of this type and their correlation with crystallography can be traced significantly better than that of the EP sample. On the PH sample, it can also be observed, that on the grains with an orientation close to (0001), there is no predominant direction for filiform corrosion traces, while they are usually parallel to each other on the grains of different orientations. However, considering the small sample size, this observation needs to be clarified.

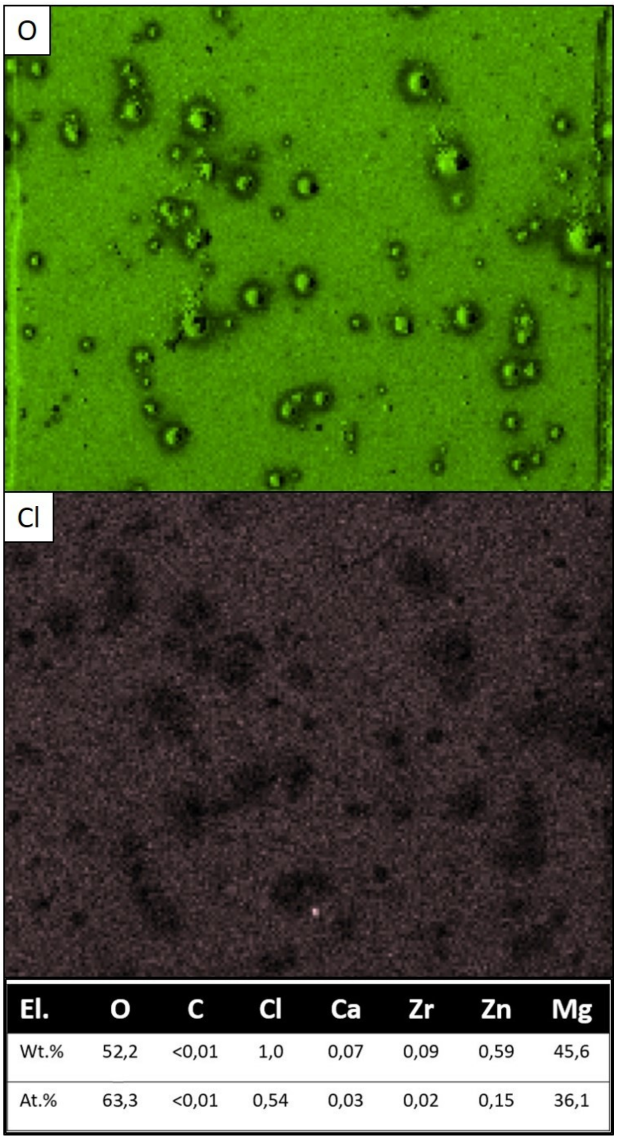

El.	O	C	Cl	Ca	Zr	Zn	Mg
Wt.%	52,2	<0,01	1,0	0,07	0,09	0,59	45,6
At.%	63,3	<0,01	0,54	0,03	0,02	0,15	36,1

Fig. 8. *Chemical composition and mapping of chlorine and oxygen in corrosion products on the marked surface of the EP-sample*

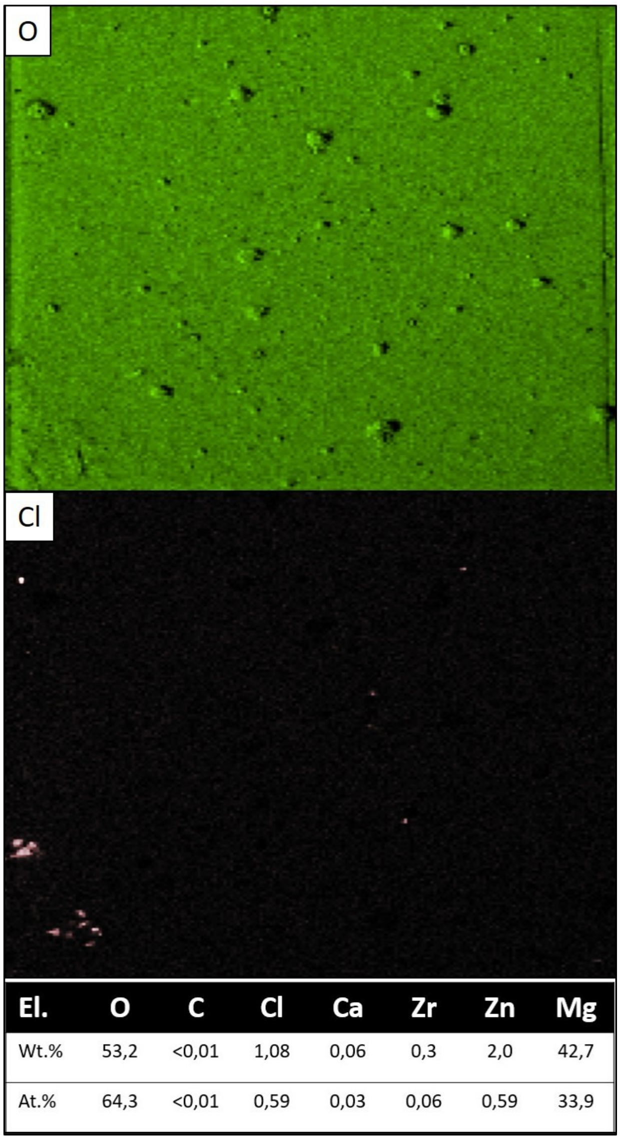

El.	O	C	Cl	Ca	Zr	Zn	Mg
Wt.%	53,2	<0,01	1,08	0,06	0,3	2,0	42,7
At.%	64,3	<0,01	0,59	0,03	0,06	0,59	33,9

Fig. 9. *Chemical composition and mapping of chlorine and oxygen in corrosion products on the marked surface of the pH-sample*

The corrosion products of both samples consist mainly of magnesium hydroxide. The chlorine concentration is many times lower than the oxygen concentration. Most likely, this is a consequence of the magnesium chloride good solubility. There is very little carbon in the corrosion products, and it is located exclusively locally, sometimes adjoining calcium. Obviously, this is a consequence of the reaction of $Mg(OH)_2$ brucite and calcium hydroxide, with carbon dioxide from the air in these areas, resulting in the formation of magnesium carbonate [9; 19] and calcium carbonate.

Comparing the distribution of chemical elements and height maps, one can see that around the particles of inclusions and secondary phases of the EP sample, a large rounded zone is formed with a fairly clear boundary, the corrosion damage of which is much less than that of the surrounding material. It can be safely said that this zone reflects the distance at which the particle has a significant effect on corrosion processes, and this distance is an order of magnitude greater than the size of the particle itself. This zone includes: a small centre, which is the particle itself and the material in the immediate proximity to it; the near halo, which is a wide rounded area with a distinct outer border in the form of a small elevation; the far halo, which is a wider rounded area between the near halo and the "outer" material, which is not affected by the processes caused by the particle in the centre. All three components of the zone of particle influence on the corrosion process are best seen in Fig. 6 and 10.

The chlorine content in corrosion products in the entire zone is many times less than in corrosion products in other places. The conclusion follows from this: the reaction described by equation (2) does not occur in this zone. This also explains its lesser damaging: chlorine does not destroy the passivating film of corrosion products. The oxygen content in the corrosion products in this zone shows its heterogeneity:

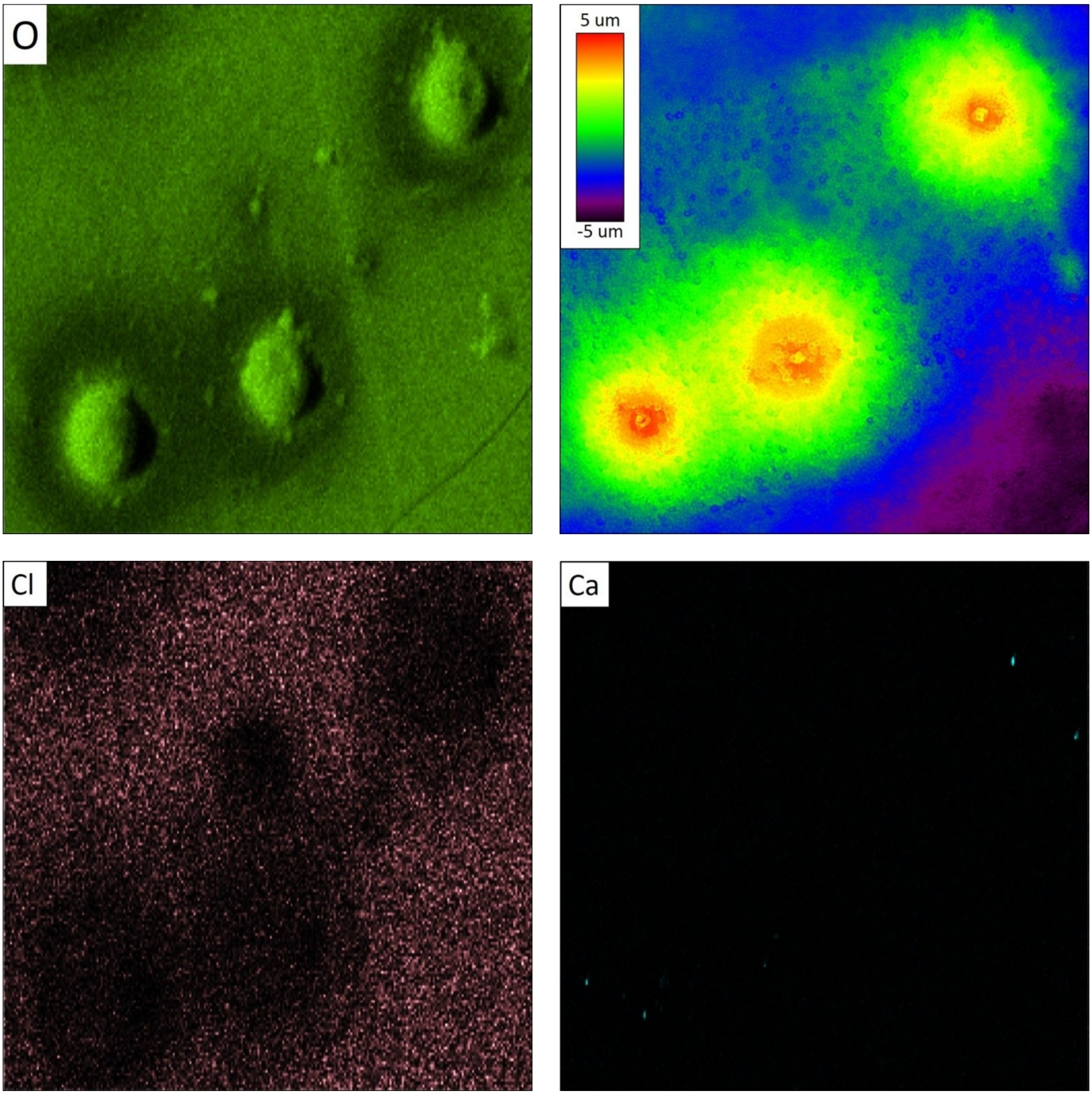

Fig. 10. *Height map (after the removal of the corrosion products) and chemical elements mapping in the corrosion products on the area shown in Fig. 2*

in the centre, and in the near halo it is approximately the same as in the corrosion products of the surrounding material, however, in the far halo, the oxygen concentration in the corrosion products drops sharply. At the same time, the height maps in Fig. 6 and 9 show that corrosion damage is present in the far halo and it is deeper than in the near halo. If the centre is the main corrosion point, then it is logically, to assume, that the pH level in the near-surface microvolumes of the corrosive medium will increase when approaching it. The Pourbaix diagram given in [10] follows that, at an electrode potential of −2.1 to −2.7 V and a high pH level, magnesium hydride and magnesium hydroxide are sTable states in the Mg–H_2O electrochemical system. Thus, one can assume that in the centre and the near halo, as well as on the surface of the “outer” material, the reaction with the formation of brucite described by equation (1) occurs, however, unlike the outer material, the resulting magnesium hydroxide is stable, and does not interact with chlorine, due to which its passivating properties are improved. In the far halo, the main corrosion product is presumably not hydroxide, but magnesium hydride, which could explain the very low oxygen concentration in the corrosion products at this location. Outside the zone of particle influence on corrosion processes, the reaction described by equation (1) is first performed, and then that described by equation (2); in this case, a uniform and continuous matrix dissolution occurs there.

In the case of the PH sample, this zone is much smaller and is limited to only ten microns around the particle, as can be seen in Fig. 6 and 9. No far halo is observed – the entire PH sample surface is uniformly covered with corrosion products containing an equal amount of oxygen.

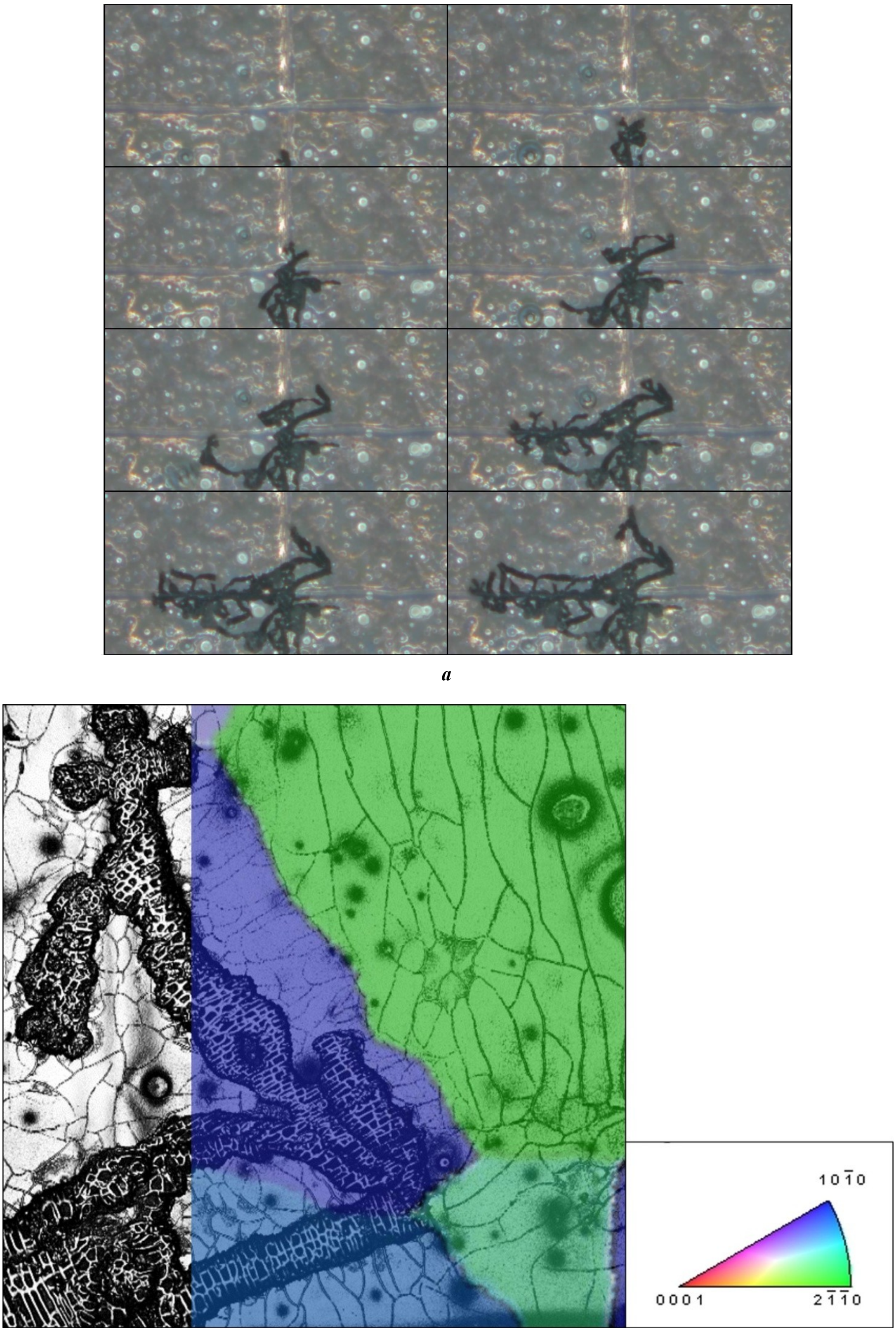

a

b

Fig. 11. *Image of first type filiform corrosion of the sample to determine the pH (PH) influence:*
a *– shooting sheet taken during corrosion tests (the period between frames is 4 minutes)*
showing the corrosion propagation speed and direction; ***b*** *– optical image with IPF-map imposed on it*

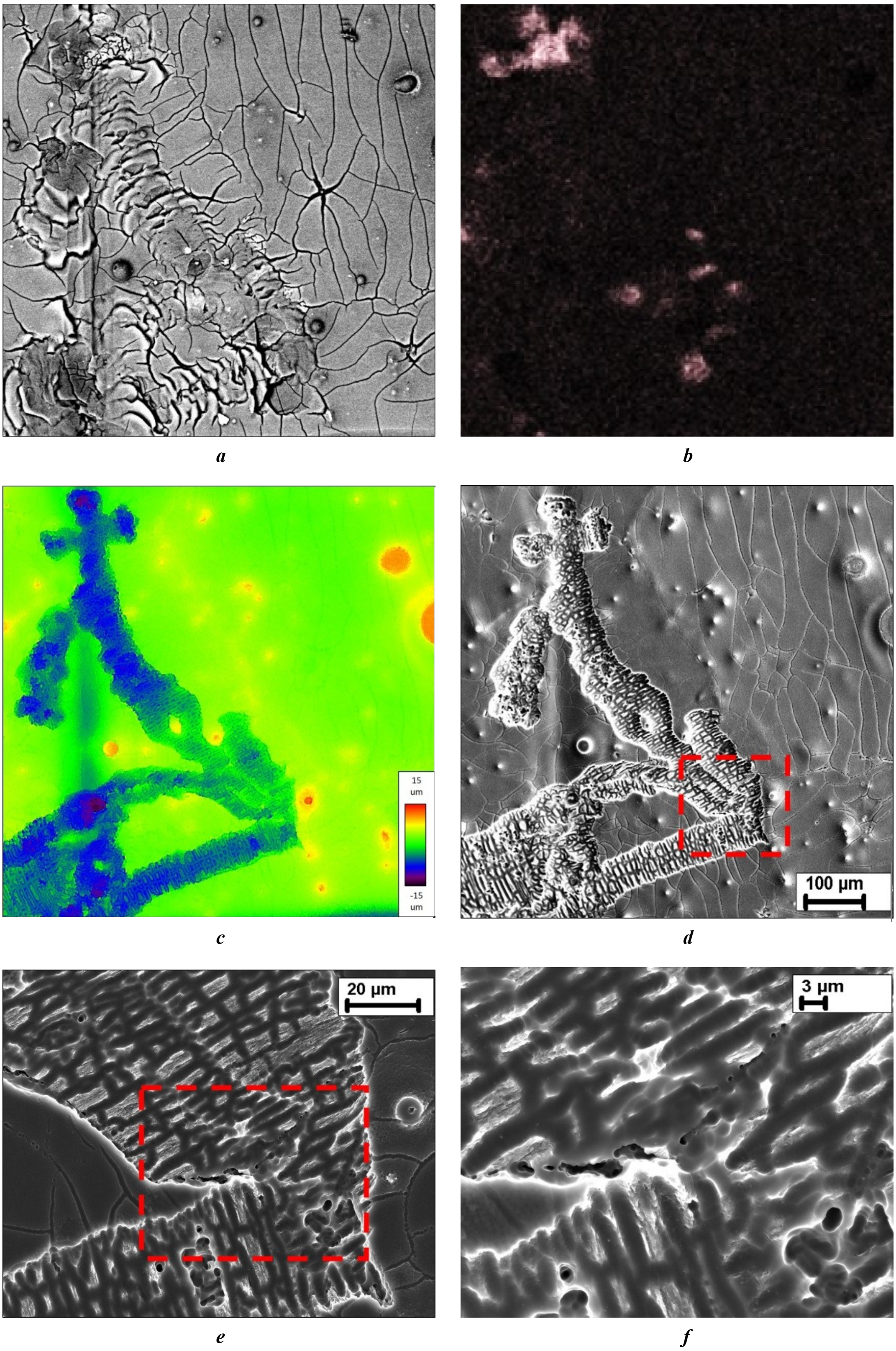

Fig. 12. *Images of the first type filiform corrosion of the sample to determine the pH (PH) influence:*
a *– SEM image (bse-detector) before the removal of corrosion products;* ***b*** *– chlorine distribution in corrosion products;*
c *– height map after the removal of corrosion products;* ***d*** *– SEM-image;* ***e*** *– a fragment highlighted with a dotted line in Fig. 12 d;*
f *– a fragment highlighted with a dotted line in Fig. 12 e*

Chlorine is evenly distributed in the corrosion products, except for several points of its increased concentration, primarily in the places of damages caused by the first type filiform corrosion. The height map shows the corrosion damage morphology, correlating with neither crystallography nor the composition of corrosion products, and therefore, is most likely determined by the trajectory of the flow washing the sample surface. Particles, and the small surface area around them, are also shown, on this map as higher and therefore less damaged areas. This may indicate that, at a small distance from the particle, the passivation effect manifests itself even under such conditions. It is curious that the corrosion damage morphology outside the marked area, to which the liquid flow was directed, is the same as in EP sample.

Fig. 2 and 10 show that the particle electrode potential had no effect on the eventual result of the corrosion process. This is easily explained by the fact that the formation of the above discussed area is conditioned by the pH level, which increases both during intense corrosion of the matrix metal, due to contact with more electropositive phases, and during the dissolution of electronegative phases, due to contact with a more positive matrix. One should note that for long-term tests, the difference might still appear, since the phases, more negative than magnesium, dissolve themselves. This means that their time of action is limited to the dissolution period – in contrast to the more noble phases, the electrochemical effect of which will remain until they will not be covered with a dense crust of corrosion products or simply will not precipitate from a corrosion-damaged surface.

Filiform corrosion traces of two types were observed on the surface of both samples. The first type is characterised by a wide (tens of microns) channel, high propagation velocity (up to hundreds of microns per minute), as well as by the fact that the channel originates in the places of scratches that marked the studied areas. Additional research showed that the scratches are free of contamination in the form of iron particles that could occur there with the chisel, their chemical composition is the same as that of the surrounding material, with the exception of the anomalous oxygen content. This indicates that the deformed scratch material is much more active than the surrounding material and is able to oxidise very quickly even upon air contact. The filiform corrosion second type is characterised by thin (1–2 μm) multiple channels over the entire sample surface. Now, nothing can be said about the places of its origin, and their propagation rate, since due to corrosion products, such light damages are invisible on video recording frames. Both types of filiform corrosion manifest themselves better on a PH sample, and both are closely related to crystallography. The first type changes the propagation direction depending on the grain crystallographic orientation, which is clearly seen in Fig. 11 b. The direction of the second type damage also depends on crystallography, as can be seen in Fig. 7 b.

The spread of the first type filiform corrosion proceeds as follows: a "corrosion front" – a corrosion centre of unknown origin, where, judging by the distribution map of chemical elements in corrosion products, there is a very high chlorine concentration, moves ahead. The "front" propagates both over scratches and over the base material, changing the movement direction depending on the crystallographic orientation of the grains. Behind the "front", deep rounded channel remains, which has a surface morphology in the form of rectangular honeycombs a few microns in size, oriented perpendicular to the main direction of the channel. In the corrosion products located in the channel, the amount of chlorine is the same as in the corrosion products of the base material, excluding some points where there was a change in the direction of filiform corrosion. Within this study, it is difficult to judge the nature of this phenomenon. Based on the fact, that chlorine practically does not remain at the points of damage, one can assume that the front is a moving centre, where the high-rate formation of chlorine-containing magnesium compounds and their prompt decay into ions that can participate in the reaction again take place. However, from the available information, it is not clear what these compounds are. Probably, this can be found out by the methods that allow determining not the elemental, but the phase composition of corrosion products, for example, infrared Fourier spectrometry.

CONCLUSIONS

1. During corrosion in an still (uncirculated) solution, a wide zone (many times larger than the particle itself) is formed around corrosion centres, which are particles of inclusions and secondary phases; this zone reflects an area, where corrosion processes depend on the particle. Corrosion damage in this zone is much less than in the rest of the material. This zone includes the centre, the near halo, and the far halo. These components have a clear boundary between themselves and with the surrounding material manifesting itself both in the difference in the damage depth and in the different composition of corrosion products. The latter means that different chemical reactions take place on the surface of the components of this zone, which is associated with the difference in the pH level.
2. The particle electrode potential does not have a visible effect on the formation of the aforementioned zone, which is probably associated as well with a stronger influence of the pH level.
3. When a sample is flowed over with a liquid removing a corrosive medium with a high pH content from the surface, the size of the round-shaped zone around the particle is many times smaller compared to the case when the sample is in a non-circulating solution.
4. Two types of filiform corrosion were identified: the first type forms damage in the form of a channel several tens of microns wide; the second type is 1–2 microns wide. The development of both types occurs in accordance with the crystallographic orientation of the grains. Corrosion of the first type originates in scratches, where the metal is more susceptible to oxidation.

REFERENCES

1. Chen J., Tan L., Yu X., Etim I.P., Ibrahim M., Yang K. Mechanical properties of magnesium alloys for medical application: A review. *Journal of the Mechanical Behavior Biomedical Materials*, 2018, vol. 87, pp. 68–79. DOI: 10.1016/j.jmbbm.2018.07.022.
2. Vinogradov A., Merson E., Myagkikh P., Linderov M., Brilevsky A., Merson D. Attaining High Functional Performance in Biodegradable Mg-Alloys: An Overview of

Challenges and Prospects for the Mg-Zn-Ca System. *Materials*, 2023, vol. 16, no. 3, article number 1324. DOI: 10.3390/ma16031324.

3. McCall C.R., Hill M.A., Lillard R.S. Crystallographic pitting in magnesium single crystals. *Corrosion Engineering Science and Technology*, 2005, vol. 40, no. 4, pp. 337–343. DOI: 10.1179/174327805X66326.
4. Shin K.S., Bian M.Z., Nam N.D. Effects of crystallographic orientation on corrosion behavior of magnesium single crystals. *JOM*, 2012, vol. 64, no. 6, pp. 664–670. DOI: 10.1007/s11837-012-0334-0.
5. Liu M., Qiu D., Zhao M.-C., Song G., Atrens A. The effect of crystallographic orientation on the active corrosion of pure magnesium. *Scripta Materialia*, 2008, vol. 58, no. 5, pp. 421–424. DOI: 10.1016/j.scriptamat.2007.10.027.
6. Bahl S., Suwas S., Chatterjee K. The control of crystallographic texture in the use of magnesium as a resorbable biomaterial. *RSC Advances*, 2014, vol. 4, no. 99, pp. 55677–55684. DOI: 10.1039/c4ra08484e.
7. Ma Y., Wang D., Li H., Yuan F., Yang C., Zhang J. Microstructure, mechanical and corrosion properties of novel quaternary biodegradable extruded Mg-1Zn-0.2Ca-xAg alloys. *Materials Research Express*, 2020, vol. 7, no. 1, article number 015414. DOI: 10.1088/2053-1591/ab6a52.
8. Parfenov E.V., Kulyasova O.B., Mukaeva V.R., Mingo B., Farrakhov R.G., Cherneikina Y.V., Erokhin A., Zheng Y.F., Valiev R.Z. Influence of ultra-fine grain structure on corrosion behaviour of biodegradable Mg-1Ca alloy. *Corrosion Science*, 2020, vol. 163, article number 108303. DOI: 10.1016/j.corsci.2019.108303.
9. Thekkepat K., Han J.-S., Choi J.-W., Lee S.-Ch., Yoon E.S., Li G., Seok H.-H., Kim Y.-Ch., Kim J.-H., Cha P.-R. Computational design of Mg alloys with minimal galvanic corrosion. *Journal of Magnesium and Alloys*, 2022, vol. 10, no. 7, pp. 1972–1980. DOI: 10.1016/j.jma.2021.06.019.
10. Song G.-L. Corrosion electrochemistry of magnesium (Mg) and its alloys. *Corrosion of Magnesium Alloys*, 2011, pp. 3–65. DOI: 10.1533/9780857091413.1.3.
11. Salahshoor M., Guo Y. Biodegradable orthopedic magnesium-calcium (MgCa) alloys, processing, and corrosion performance. *Materials*, 2012, vol. 5, no. 1, pp. 135–155. DOI: 10.3390/ma5010135.
12. Urwongse L., Sorrell C.A. The System MgO-$MgCl_2$-H_2O at 23°C. *Journal of American Ceramic Society*, 1980, vol. 63, no. 9-10, pp. 501–504. DOI: 10.1111/J.1151-2916.1980.TB10752.X.
13. Merson D., Brilevsky A., Myagkikh P., Tarkova A., Prokhorikhin A., Kretov E., Frolova T., Vinogradov A. The functional properties of Mg-Zn-X biodegradable magnesium alloys. *Materials*, 2020, vol. 13, no. 3, article number 544. DOI: 10.3390/ma13030544.
14. Merson D.L., Brilevsky A.I., Myagkikh P.N., Markushev M.V., Vinogradov A. Effect of deformation processing of the dilute Mg-1Zn-0.2Ca alloy on the mechanical properties and corrosion rate in a simulated body fluid. *Letters on Materials*, 2020, vol. 10, no. 2, pp. 217–222. DOI: 10.22226/2410-3535-2020-2-217-222.
15. Myagkikh P.N., Merson E.D., Poluyanov V.A., Merson D.L. Structure effect on the kinetics and staging of the corrosion process of biodegradable ZX10 and WZ31 magnesium alloys. *Frontier Materials & Technologies*, 2022, no. 2, pp. 63–73. DOI: 10.18323/2782-4039-2022-2-63-73.
16. McCall C.R., Hill M.A., Lillard R.S. Crystallographic pitting in magnesium single crystals. *Corrosion Engineering, Science and Technology*, 2005, vol. 40, no. 4, pp. 337–343. DOI: 10.1179/174327805X66326.
17. Zhang X., Wang Z., Yuan G., Xue Y. Improvement of mechanical properties and corrosion resistance of biodegradable Mg-Nd-Zn-Zr alloys by double extrusion. *Materials Science and Engineering: B*, 2012, vol. 177, no. 13, pp. 1113–1119. DOI: 10.1016/j.mseb.2012.05.020.
18. Ding Y., Wen C., Hodgson P., Li Y. Effects of alloying elements on the corrosion behavior and biocompatibility of biodegradable magnesium alloys: A review. *Journal of Materials Chemistry B*, 2014, vol. 2, no. 14, pp. 1912–1933. DOI: 10.1039/c3tb21746a.
19. Yang Y., He C., Dianyu E., Yang W., Qi F., Xie D., Shen L., Peng S., Shuai C. Mg bone implant: Features, developments and perspectives. *Materials and Design*, 2020, vol. 185, article number 108259. DOI: 10.1016/j.matdes.2019.108259.
20. Esmaily M., Svensson J.E., Fajardo S., Birbilis N., Frankel G.S., Virtanen S., Arrabal R., Thomas S., Johansson L.G. Fundamentals and advances in magnesium alloy corrosion. *Progress in Materials Science*, 2017, vol. 89, pp. 92–193. DOI: 10.1016/j.pmatsci.2017.04.011.

doi: 10.18323/2782-4039-2023-2-64-6

The influence of deformation at cryogenic or room temperature followed by annealing on the structure and properties of copper and its Cu–3Pd and Cu–3Pd–3Ag (at. %) alloys

Oksana S. Novikova*[1,3], PhD (Physics and Mathematics), senior researcher of the Strength Laboratory
Alina E. Kostina[1], postgraduate student, junior researcher of the Strength Laboratory
Yury A. Salamatov[1,4], PhD (Physics and Mathematics),
senior researcher of the Laboratory for Neutron-Synchrotron Research of Nanostructures
Dmitry A. Zgibnev[1,2], student, laboratory assistant of the Strength Laboratory
Aleksey Yu. Volkov[1,5], Doctor of Sciences (Engineering), Head of the Strength Laboratory
[1]*M.N. Mikheev Institute of Metal Physics of Ural Branch of RAS, Yekaterinburg (Russia)*
[2]*Ural Federal University named after the first President of Russia B.N. Yeltsin, Yekaterinburg (Russia)*

***E-mail: novikova@imp.uran.ru**

[3]ORCID: https://orcid.org/0000-0003-0474-8991
[4]ORCID: https://orcid.org/0000-0002-3857-2392
[5]ORCID: https://orcid.org/0000-0002-0636-6623

Received 14.04.2023 *Accepted 09.06.2023*

Abstract: Due to low electrical resistivity, the Cu–Pd and Cu–Pd–Ag system alloys can be used as corrosion-resistant conductors of weak electrical signals. The paper deals with a comparison of the structure and physical-mechanical properties of Cu, Cu–3Pd and Cu–3Pd–3Ag (at. %) alloys after deformation at room or cryogenic temperature followed by annealing. The authors studied specimens in different initial states: quenched, deformed at room and cryogenic temperatures. To study the processes of structure rearrangement and the evolution of properties, annealing was carried out in the temperature range from 100 to 450 °C, followed by cooling in water. The duration of heat treatments was 1 h. The dependences of the yield strength and elongation to failure on the annealing temperature showed that cryodeformation significantly increases the thermal stability of the structure of both pure copper and the Cu–3Pd–3Ag ternary alloy. According to the temperature dependence of specific electrical resistivity of the deformed Cu–3Pd–3Ag alloy during heating at a rate of 120 deg./h, it was found that the decrease in electrical resistance caused by recrystallization begins at above 300 °C. The dependences of specific electrical resistivity on true strain showed that the structure rearrangement mechanisms during deformation are different for pure copper and the Cu–3Pd–3Ag alloy. The results of mathematical processing of the peaks in the diffraction patterns established that two phases appear in the Cu–3Pd–3Ag alloy after cryodeformation and annealing, one of which is silver-enriched, and the other is depleted. The study showed that during annealing of the deformed (especially after cryodeformation) Cu–3Pd–3Ag alloy, an anomalous increase in strength properties is observed. It was identified that alloying copper with palladium and silver leads to an increase in the recrystallization temperature. Thus, copper alloys with small palladium and silver additives are obviously attractive for practical applications, since they have improved strength properties, satisfactory electrical conductivity, and a higher recrystallization temperature compared to pure copper.

Keywords: Cu; Cu–Pd; Cu–3Pd–3Ag; copper alloy with small additives of palladium and silver; copper alloying with palladium and silver; cryodeformation; anomaly of strength properties; resistometry.

Acknowledgements: The work was carried out within the state assignment, on the topic “Pressure”, state registration No. 122021000032-5. X-ray structure analysis was performed using the equipment of the “Composition of Compounds” Shared Access Center of the IHTE UB RAS.

The paper was written on the reports of the participants of the XI International School of Physical Materials Science (SPM-2023), Togliatti, September 11–15, 2023.

For citation: Novikova O.S., Kostina A.E., Salamatov Yu.A., Zgibnev D.A., Volkov A.Yu. The influence of deformation at cryogenic or room temperature followed by annealing on the structure and properties of copper and its Cu–3Pd and Cu–3Pd–3Ag (at. %) alloys. *Frontier Materials & Technologies*, 2023, no. 2. DOI: 10.18323/2782-4039-2023-2-64-6.

INTRODUCTION

The production of high-strength and corrosion-resistant electric current conductors is an important applied research task. Many foreign companies and domestic researchers pay great attention to the development of methods aimed at the improvement of the strength properties of copper alloys, without a significant decrease in their electrical conductivity and while maintaining sufficient plasticity. Alloying is one of the ways to solve this issue. For example, the introduction of beryllium, niobium, etc. into copper can significantly improve the strength properties [1; 2]. However, the toxicity and high cost of beryllium (as well as the niobium density) hinder the application of such alloys in industry. Works on copper matrix strengthening by introducing nanodispersed particles of various metals (for example, chromium) using the severe plastic deformation (SPD) methods should also be mentioned [3]. Currently, it is generally accepted that silver is an optimal alloying element to create strong copper-based conductors. As is known, silver is slightly soluble in copper; therefore, even its small additions (3–5 at. %) lead to significant hardening due to the precipitation of dispersed Ag-based particles in the copper matrix.

Previously, it was shown that alloying copper with silver leads to the production of an electrically conductive material with high strength properties [4–6]. The work [5] established that the redistribution of dissolved substances upon annealing of a cold-rolled Cu–3Ag (at. %) alloy, leads to the formation of a heterogeneous dislocation structure, where there are areas with low (due to a decrease in the content of silver atoms) and high (due to preservation of the excess silver concentration) dislocation density. Such a heterogeneous microstructure allowed improving the plasticity while maintaining the high strength of the annealed material [7].

As is known, SPD effectively refines the grain structure of metals and alloys and, therefore, is used as well to solve issues of increasing the strength properties of copper conductors [8]. However, the grinding process during SPD slows down after reaching a certain amount of accumulated strain, and the average grain size asymptotically tends to a certain minimum reachable value (which is usually in the submicrocrystalline range). Deformation at very low temperatures – the so-called cryogenic, or low-temperature, deformation can become one of the ways to solve this problem. It is established that very low deformation temperatures, firstly, prevent grain growth, and secondly, hinder the redistribution of dislocations, which contributes to an increase in their density and, as a result, leads to an increase in internal stresses. All this stimulates further microstructure refinement [8]. In the Cu–Ag alloys, the possibility of increasing the strength properties due to preliminary cryodeformation, for example, cryorolling [9–11] or cryodrawing [12; 13] is identified.

Recently, additional requirements for corrosion resistance have been imposed on conductors. For example, to solve this issue, copper conductors are coated with a thin palladium layer [14]. However, during the operation of such wires, palladium diffuses rather quickly, forming a set of ordered phases at the interface. In the work [15], the authors identified that alloying with palladium (less than 10 at. %) allows increasing the copper strength properties, due to solid solution hardening while simultaneously increasing corrosion resistance. However, under the conditions of increasing requirements for producing high-strength electric current conductors, hardening by alloying with one component is not enough. Therefore, to form high functional properties of alloys, currently, alloying with two or more elements is used to combine two hardening mechanisms (for example, solid solution and dispersion ones due to the second phase precipitation [16]) or simultaneous occurrence of several phase transformations [17]. Viewed in this way, Cu–Pd alloys can serve as a matrix for their additional hardening with silver.

Previously, we have shown that the application of cryodeformation before annealing leads to the formation of a high-strength ordered state of the Cu–47Pd (at. %) alloy with an ultrafine-grained structure and low specific electrical resistivity [18]. These results allow suggesting that preliminary cryodeformation will lead to additional grain refinement of the Cu–Pd–Ag ternary alloy, which, together with dispersion strengthening due to the precipitation of silver particles, will improve the mechanical properties. The influence of cryodeformation on the structure and properties of Cu alloys alloyed with silver and palladium has not been considered before.

The purpose of this work is to study the influence of deformation at room and cryogenic temperatures on the physical and mechanical properties of the Cu–3Pd–3Ag (at. %) copper alloy with small additions of palladium and silver.

METHODS

The Cu–3Pd–3Ag alloy (at. %) was smelted from copper, palladium, and silver with a purity of 99.98; 99.99, and 99.99 % respectively. To compare the structure and properties, samples of pure copper and Cu–3Pd alloy (at. %) were used. Smelting was carried out in a vacuum of 10^{-2} Pa with casting into a graphite crucible. The chemical composition of the alloys was checked using a JEOL JCXA-733 X-ray microanalyser. All heat treatments were performed in evacuated glass or quartz ampoules.

An ingot Ø5 mm was homogenized at a temperature of 800 °C for 3 h, quenched by cooling in water, and cut into two parts. From one part of the ingot, a wire Ø1.5 mm was produced by drawing, from which samples for mechanical tensile tests were cut. Further drawing to a diameter of 0.22 mm allowed obtaining a thin wire for resistometry. The other part of the ingot was rolled to produce plates with a thickness of 0.3 mm, which were used for phase composition assessment at various stages of processing.

The alloy cryodeformation was carried out between two stainless steel plates. This construction was placed in liquid nitrogen for about 1 min, after which rolling was performed. This operation was repeated. Part of the wires and plates deformed at room temperature were annealed at a temperature of 700 °C during 1 h and cooled in water. Thus, the authors studied samples in several initial states: quenched, deformed at room temperature, and deformed at cryogenic temperature. The value of the true deformation of the samples (e) was determined by the equation: $e=\ln(S_o/S_f)$, where S_o and S_f are the cross-section areas of the sample in the initial and final states.

To study the processes of structural rearrangement and evolution of properties, annealing was carried out in the temperature range from 100 to 450 °C (with a step of 50 °C) followed by cooling in water. The duration of heat treatments was 1 h.

To measure specific resistivity (ρ), the standard four-contact method was used (DC value is I=20 mA). To increase the accuracy in calculating the cross-section area of the sample, the wire diameter was measured by optical methods with an error of ±1 μm. When determining the conductor length, a special conductor was used with a set of contact points, the distance between which (from 120 to 150 mm) was measured with an accuracy of 0.1 mm. The specific electrical resistivity was calculated as the average value of 5 measurements between different pairs of contacts. The electrical resistivity temperature dependences were obtained by heating and cooling the samples at a rate of 120 deg/h.

Mechanical tests were carried out on a ZD 10/90 tensile testing machine at a tensile rate of 3 mm/min; the length of the working part of the samples was 30 mm. For each structural state, at least five samples were tested.

X-ray diffraction analysis (XRD) was performed using a DMAX 2200 diffractometer (Rigaku) in the shooting mode at a speed of 4 °/min, Cu-*K*α radiation was monochromatised by a graphite single crystal. The average size (D_0) of coherent scattering regions (CSR) in the studied alloys deformed to the same degree at different temperatures was estimated based on the X-ray diffraction data using the Williamson–Hall method [19]. The authors carried out mathematical processing of several peaks on X-ray diffraction patterns of copper, Cu–3Pd alloy, and Cu–3Pd–3Ag ternary alloy. It involved deconvolution, i.e., inverting the signal convolution with the broadening function of the device. This inversion was carried out by solving the convolution integral equation, using the regularisation method for inverse problems [20]. The lattice parameter corresponding to each component of the original peak was calculated for both peaks of its doublet and averaged.

RESULTS

The obtained XRD results show that the introduction of small palladium or silver additions into copper causes an increase in the fcc lattice parameter (Fig. 1, Table 1). For visual clarity, the inset in Fig. 1 shows the peaks (200) for pure copper, the Cu–3Pd binary alloy, and the investigated Cu–3Pd–3Ag ternary alloy. It is clearly seen that alloying leads to a shift of this peak towards smaller angles.

Moreover, Fig. 1 shows that the plastic deformation of the studied alloys by the same degree (*e*≈3.5) causes a different broadening of the X-ray peak. One can conclude that alloying leads to refinement of structural elements.

As we can see from Table 1, the CSR size in deformed binary and ternary alloys is several tens of nanometers. Cryorolling further refines the structure. Therefore, the studied Cu–3Pd and Cu–3Pd–3Ag alloys after deformation (*e*≈3.5) can be attributed to nanostructured materials.

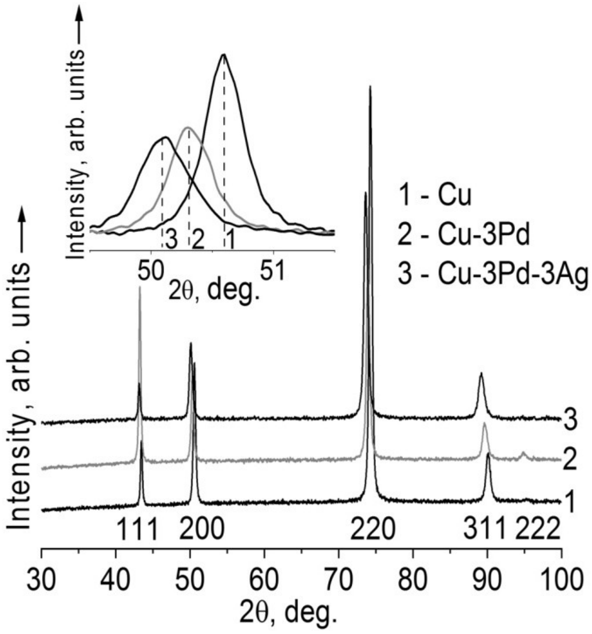

Fig. 1. Diffraction patterns of copper (1), Cu–3Pd (2) and Cu–3Pd–3Ag (3) alloys after cryodeformation (e≈3.5)

***Table 1.** Crystal lattice parameter and the average size of the areas of coherent scattering of deformed (e≈3.5) specimens of the studied alloys and copper*

Specimen	Lattice parameter *a*, nm	CSR average size D_0, nm
Cu*	0.3619	>100
Cu–3Pd	0.3627	66±7
Cu–3Pd*	0.3628	50±5
Cu–3Pd–3Ag	0.3639	58±6
Cu–3Pd–3Ag*	0.3645	40±4

** Specimens produced by cryodeformation.*

The change in yield strength ($\sigma_{0.2}$) and relative elongation to failure (δ) after exposure (for 1 h) of pre-deformed samples of Cu–3Pd and Cu–3Pd–3Ag alloys in the temperature range from 100 to 450 °C is shown in Fig. 2 a and 2 b, respectively.

It is seen (curve 1, Fig. 2 a) that to remove cold hardening in copper specimens, annealing at a temperature of 150 °C for 1 h is sufficient. The introduction of 3 at. % palladium increases the recrystallisation temperature to ~300 °C (curve 3, Fig. 2 a), and the additional introduction of 3 at. % silver increases the recrystallisation temperature by another ~50 °C (curve 4, Fig. 2 a).

Plasticity of all heavily deformed samples is low: their elongation to failure is δ≈2÷3 %. After the completion of recrystallisation processes, as a result of annealing, the plastic properties of most alloys increase significantly – up to δ≈50 %. It can be assumed that in the cryodeformed Cu–3Pd–3Ag alloy annealed at 400 °C during 1 h, the recrystallisation processes have not yet been completed (curve 5 in Fig. 2 b). Therefore, cryodeformation significantly increases the thermal stability of the structure of both pure copper (curves 1 and 2) and the Cu–3Pd–3Ag ternary alloy (curves 4 and 5).

Since the decrease in the structure defectiveness during recrystallisation leads to a drop in the electrical resistivity, the thermal stability of the deformed structure can be understood by measuring the temperature dependences of the electrical resistivity. Fig. 3 shows the dependences of the change in electrical resistivity obtained during heating and cooling of a thin wire sample of the Cu–3Pd–3Ag alloy deformed at e≈7.1. The temperature dependence of the electrical resistivity of the initially quenched alloy has a linear form, since in this case recrystallisation processes do not occur in the alloy and are not presented in the work. The dependences of the electrical resistivity during cooling are the same regardless of the initial state of the samples and are also linear (dashed line in Fig. 3).

The temperature of recrystallisation of the Cu–3Pd–3Ag alloy can be determined in Fig. 3 as the point of deviation of the electrical resistivity dependence from the linear form during heating. Here it should be noted that the recrystallisation temperature depends on the temperature-time processing conditions [21]. Therefore, one can argue that, upon heating at a rate of 120 deg/h, the decrease in the specific

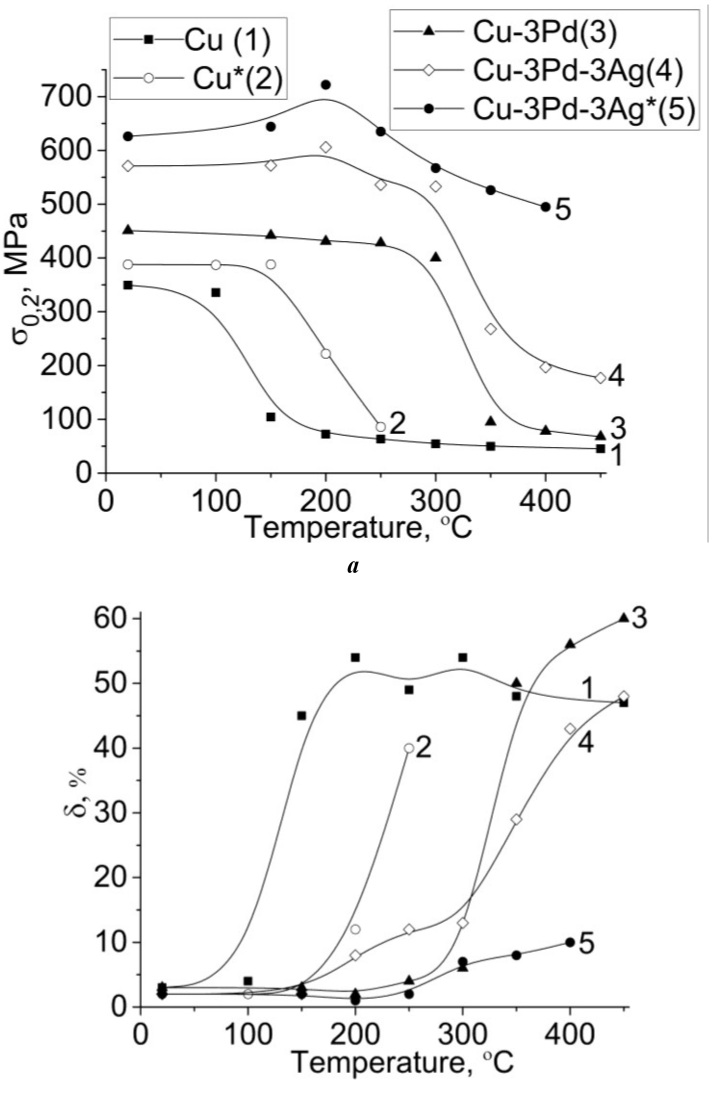

a

b

***Fig. 2.** The dependences of yield strength (**a**) and elongation to failure (**b**) on the temperature of annealing of specimens of Cu, Cu–3Pd and Cu–3Pd–3Ag alloys pre-deformed at room and cryogenic (*) temperatures (e≈2.3)*

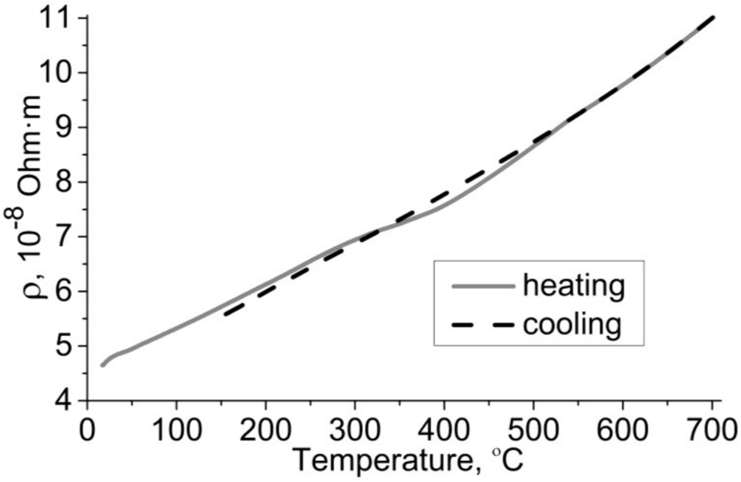

***Fig. 3.** Change in electrical resistivity at heating and cooling at a rate of 120 deg./h of the Cu–3Pd–3Ag alloy specimen drawing-deformed at room temperature (e≈7.1)*

electrical resistivity of the studied alloy caused by recrystallisation begins upon heating above 300 °C.

At room temperature, the specific electrical resistivity of the quenched Cu–3Pd–3Ag alloy is $\rho=4.5\cdot10^{-8}$ Ohm·m (i.e. the alloy electrical conductivity is 39 % IACS). The electrical resistivity of the deformed Cu–3Pd–3Ag alloy is slightly higher (this also follows from the course of the "heating – cooling" curves in Fig. 3).

The microstructure evolution under the influence of deformation is well revealed by the change in specific electrical resistivity. To compare, Fig. 4 shows the dependences of specific electrical resistivity on the true deformation of samples of pure copper and Cu–3Pd–3Ag alloy. During plastic deformation, the electrical resistivity of copper (Fig. 4, curve 1) increases by ~4 % due to an increase in the structure defectiveness; the maximum value of the electrical resistivity corresponds to the true deformation *e*≈3.5. Further deformation of copper does not lead to an increase in its electrical resistivity, since a dynamic equilibrium occurs between the generation of defects, and their annihilation due to recovery/recrystallisation processes. That is why at large deformations, the dependence of the specific electrical resistivity of copper looks like a plateau (curve 1 in Fig. 4).

Fig. 4 (curve 2) clearly demonstrates that during plastic deformation, the electrical resistivity of the Cu–3Pd–3Ag alloy increases by approximately 7 %, the maximum value of the electrical resistivity corresponds to the true deformation *e*≈4.3. Further deformation leads to a decrease in the specific electrical resistivity of the ternary alloy. Therefore, the mechanisms of structural rearrangement during deformation are different for pure copper (curve 1) and the Cu–3Pd–3Ag alloy (2).

Fig. 5 shows the diffraction patterns of the Cu–3Pd–3Ag alloy samples deformed by *e*≈3.5 at room and cryogenic temperatures and then annealed at 250 °C for 1 h.

All diffraction patterns contain the lines of only the fcc phase; no reflections of other phases were found. It is seen that a decrease in the deformation processing temperature

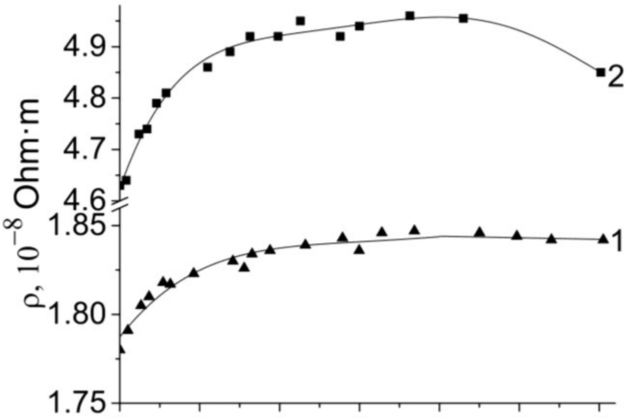

***Fig. 4.** The dependences of specific electrical resistivity on true strain of pure copper (1) and Cu–3Pd–3Ag alloy (2)*

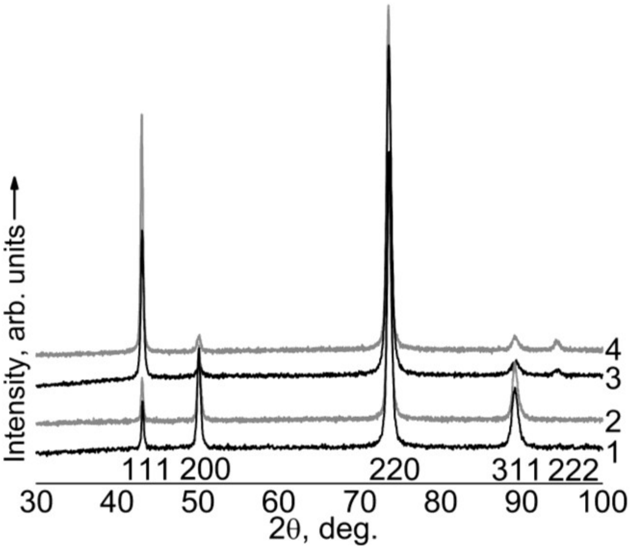

Fig. 5. *Diffraction patterns of the Cu–3Pd–3Ag alloy specimens:*
1 – deformation at room temperature (e≈3.5); 2 – treatment (1) + 250 °C, 1 h, cooling in water;
3 – cryodeformation (e≈3.5); 4 – treatment (3) + 250 °C, 1 h, cooling in water

causes an additional broadening of the X-ray peaks (diffractograms 1 and 3). Obviously, to reveal possible weak lines of the second phase, the use of methods of mathematical processing of X-ray peaks is required.

Let us present the results of such processing of one of the peaks. After the peak deconvolution (220) of the Cu–3Pd–3Ag alloy (cryodeformation (*e*≈3.5) + + 250 °C, 1 h, cooling in water), it is seen (Fig. 6) that it is clearly divided into two components, each of which is a doublet of Cu-$K\alpha_1$ and Cu-$K\alpha_2$. All other peaks in Fig. 6 are undescriptive, and are either noise or a consequence of the approximate solution of inverse problems by the regularisation method. For comparison, the authors carried out the same mathematical processing of the peak (220) of pure copper and the Cu–3Pd alloy: in contrast to the ternary alloy peak (220), after deconvolution they are divided only into a doublet Cu-$K\alpha_1$ and Cu-$K\alpha_2$, without revealing signs of the presence of the second component.

For phase 1 (left doublet, more intense), the lattice parameter was a_1=0.3646 nm. For phase 2 (right doublet, less intense), a_2=0.3632 nm. As expected, both parameters exceed the crystal lattice parameter of pure copper a=0.3619 nm.

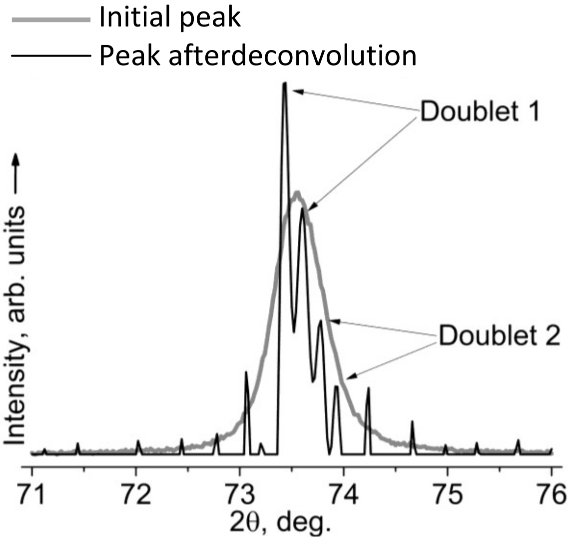

Fig. 6. *The initial peak (220) and peak after deconvolution on the diffraction pattern of the Cu–3Pd–3Ag alloy, cryodeformation (e≈3.5) + 250 °C, 1 h, cooling in water*

DISCUSSION

The most interesting result obtained during the study is the detection of a temperature anomaly in the yield strength during annealing of the Cu–3Pd–3Ag alloy. As a rule, a decrease in strength properties can be expected when annealing an initially deformed material. However, Fig. 2 a demonstrates that the annealing of the ternary alloy at a temperature of 200 °C “switches on” some additional hardening mechanism compared to the binary alloy. Indeed, in the Cu–3Pd alloy, no increase in strength occurs as a result of annealing (Fig. 2 a, curve 3 shows a plateau). In turn, the annealing of the Cu–3Pd–3Ag alloy at 200 °C after deformation at room temperature increases its yield strength by ~40 MPa, while cryodeformation increases the yield strength by ~100 MPa (compare curves 4 and 5 in Fig. 2 a). After such thermomechanical treatment, the yield strength of a low-alloyed copper-based Cu–3Pd–3Ag alloy ($\sigma_{0.2}$=720 MPa) becomes 2 times higher than the yield strength of heavily deformed pure copper ($\sigma_{0.2}$=350 MPa).

The effect of an anomalous increase in the yield strength discovered during mechanical tensile tests (Fig. 2) is observed as well when measuring the microhardness of the Cu–3Pd–3Ag alloy [22]. The ternary alloy microhardness increases after annealing at 150 °C, reaches a maximum at 250 °C, and then begins to decrease. Note that the effect of hardening as a result of annealing is more pronounced on the microhardness curves. This is probably associated with the difference in the degrees of preliminary deformation of the samples. Indeed, the pre-deformation of the plates for microhardness measurements was $e \approx 3.5$, and the true deformation of the wire for tensile tests did not exceed $e \approx 2.3$.

An anomalous increase in strength properties as a result of annealing has already been observed earlier, for example, on cryodeformed samples of Cu–Ag, Cu–Al–Zn, and Mg–Al–Zn alloys [23; 24]. This effect was explained by the segregation of atoms of the released component on various kinds of defects (dislocations, grain boundaries, etc.). Therefore, an increase in the structure defectiveness during cryodeformation should lead to a more pronounced manifestation of the temperature anomaly, which corresponds to our results obtained for the Cu–3Pd–3Ag alloy (Fig. 2).

Based on the results of mathematical processing of XRD data, one can assume that the main volume of the studied alloy is a solid solution of palladium in copper. According to [25], the change in the fcc lattice parameter when alloying copper with palladium completely satisfies the Vegard law. Thus, in full agreement with the results obtained, the crystal lattice parameter of the Cu–Pd matrix should slightly exceed the lattice parameter of pure copper.

In the Cu–5Ag alloy (wt. %), after aging at a temperature of 450 °C, a grid of silver precipitates along the grain boundaries was observed [26]. In the Cu–8Ag alloy (wt. %) after annealing at a temperature of 500 °C for 710 h, larger silver precipitates were found along the grain boundaries and at triple junctions, and fine precipitates were found inside the grains [27]. Taking into account the results of [26; 27], as well as the low solubility of Ag in Cu, one can assume that the segregation of silver atoms occurs along the grain boundaries of the Cu–Pd matrix, as well as inside them, at dislocations. Precipitation of a silver-based phase has been repeatedly observed earlier in Cu–Pd–Ag alloys with a high content of palladium and silver. For example, using the method of field ion microscopy of the Cu–50Pd–20Ag (at. %) alloy, the formation of Pd–Ag particles was observed in an atomically ordered Cu–Pd matrix [28].

In the low-alloyed Cu–3Pd–3Ag alloy studied in this work, no ordered phase is formed. Apparently, after cryodeformation and annealing at a temperature of 250 °C, two regions appear in the alloy, one of which is silver-enriched and the other is depleted. The components of the diffraction peak, which were observed after deconvolution, correspond to this two-phase state.

In further studies of Cu–Pd–Ag ternary alloys, one can follow the way of increasing the palladium content. Silver alloying of Cu–5Pd and Cu–10Pd alloys, in which the formation of nuclei of the ordered Cu_3Pd phase can be expected, will lead both to solid solution strengthening and precipitation age hardening due to the second phase precipitation, and to additional hardening due to atomic ordering processes. Probably, this will make it possible to increase noticeably the strength properties of such alloys, as was proposed for the alloyed ordered alloys based on Cu–Au and Cu–Pd in the work [29].

If to compare binary Cu–Pd and ternary Cu–Pd–Ag alloys, it should be noted that small silver additions affect slightly the electrical conductivity of Cu–Pd alloys at a simultaneous significant increase in strength properties and recrystallisation temperature. For example, the yield strength and tensile strength of the Cu–3Pd–3Ag ternary alloy are higher, and its electrical conductivity is comparable to the characteristics of the Cu–3Pd alloy.

Thus, from a practical perspective, copper alloys with small palladium and silver additions are of obvious interest, since they have increased strength properties, satisfactory electrical conductivity, and a higher recrystallisation temperature compared to pure copper.

CONCLUSIONS

1. An anomalous effect of an increase in strength properties during annealing of a deformed Cu–3Pd–3Ag alloy was identified; cryodeformation enhances significantly this effect.

2. Alloying copper alloys with a low palladium content with a small amount of silver leads to an increase in the strength properties and recrystallisation temperature, while the observed decrease in electrical conductivity is insignificant.

REFERENCES

1. Deryagina I.L., Popova E.N., Valova-Zaharevskaya E.G., Patrakov E.I. Structure and thermal stability of high-strength Cu–18Nb composite depending on the degree of deformation. *The Physics of Metals and Metallography*, 2018, vol. 119, no. 1, pp. 92–102. DOI: 10.1134/S0031918X18010088.
2. Chzhigan Ch., Tszyunvey L., Shitsyan L., Yanni S., Yuan M. Mechanisms of high-temperature deformation of the Cu-Be alloy in the high-elastic annealed state. *Fizika metallov i metallovedenie*, 2018, vol. 119, no. 1, pp. 73–80. DOI: 10.7868/S0015323018010096.
3. Valiev R.Z., Straumal B., Langdon T.G. Using severe plastic deformation to produce nanostructured materials with superior properties. *Annual Review of Materials Research*, 2022, vol. 52, pp. 357–382. DOI: 10.1146/annurev-matsci-081720-123248.

4. Zhang Zh., Ru Ya., Zuo T.T., Xue J., Wu Y., Gao Z., Liu Y., Xiao L. Achieving High Strength and High Conductivity of Cu-6 wt%Ag Sheets by Controlling the Aging Cooling Rate. *Materials*, 2023, vol. 16, no. 10, article number 3632. DOI: 10.3390/ma16103632.
5. Gubicza J., Hegedus Z., Labar J.L., Kauffmann A., Freudenberger J., Subramanya Sarma V. Solute redistribution during annealing of a cold rolled Cu–Ag alloy. *Journal of Alloys and Compounds*, 2015, vol. 623, pp. 96–103. DOI: 10.1016/j.jallcom.2014.10.093.
6. Bonvalet M., Sauvage X., Blavette D. Intragranular nucleation of tetrahedral precipitates and discontinuous precipitation in Cu-5wt%Ag. *Acta Materialia*, 2019, vol. 164, pp. 454–463. DOI: 10.1016/j.actamat.2018.10.055.
7. Sitarama Raju K., Subramanya Sarma V., Kauffmann A., Hegedus Z., Gubicza J., Peterlechner M., Freudenberger J., Wilde G. High strength and ductile ultrafine grained Cu–Ag alloy through bimodal grain size, dislocation density and solute distribution. *Acta Materialia*, 2013, vol. 61, no. 1, pp. 228–238. DOI: 10.1016/j.actamat.2012.09.053.
8. Konkova T.N., Mironov S.Y., Danilenko V.N., Korznikov A.V. Effect of low-temperature rolling on the structure of copper. *The Physics of Metals and Metallography*, 2010, vol. 110, no. 4, pp. 318–330.
9. Guo S., Liu S., Liu J., Gao Z., Liu Z. Investigation on Strength, Ductility and Electrical Conductivity of Cu-4Ag Alloy Prepared by Cryorolling and Subsequent Annealing Process. *Journal of Materials Engineering and Performance*, 2019, vol. 28, pp. 6809–6815. DOI: 10.1007/s11665-019-04448-7.
10. Wu X., Wang R., Peng C., Zeng J. Ultrafine grained Cu–3Ag-xZr (x = 0.5, 1.0 wt%) alloys with high strength and good ductility fabricated through rapid solidification and cryorolling. *Materials Science and Engineering: A*, 2020, vol. 778, article number 139095. DOI: 10.1016/j.msea.2020.139095.
11. Wang W., Chen Z.-N., Guo E.-Y., Kang H.-J., Liu Y., Zou C.-L., Li R.-G., Yin G.-M., Wang T.-W. Influence of Cryorolling on the Precipitation of Cu-Ni-Si Alloys: An In Situ X-ray Diffraction Study. *Acta Metallurgica Sinica (English Letters)*, 2018, vol. 31, pp. 1089–1097. DOI: 10.1007/s40195-018-0781-x.
12. Kauffmann A., Geissler D., Freudenberger J. Thermal stability of electrical and mechanical properties of cryo-drawn Cu and CuZr wires. *Materials Science and Engineering: A*, 2016, vol. 651, pp. 567–573. DOI: 10.1016/j.msea.2015.10.119.
13. Strzepek P., Mamala A., Zasadzinska M., Franczak K., Jurkiewicz B. Research on the drawing process of Cu and CuZn wires obtained in the cryogenic conditions. *Cryogenics*, 2019, vol. 100, pp. 11–17. DOI: 10.1016/j.cryogenics.2019.03.007.
14. Xu H., Qin I., Clauberg H., Chylak B., Acoff V.L. Behavior of palladium and its impact on intermetallic growth in palladium-coated Cu wire bonding. *Acta Materialia*, 2013, vol. 61, no. 1, pp. 79–88. DOI: 10.1016/j.actamat.2012.09.030.
15. Volkov A.Y., Novikova O.S., Kostina A.E., Antonov B.D. Effect of alloying with palladium on the electrical and mechanical properties of copper. *The Physics of Metals and Metallography*, 2016, vol. 117, no. 9, pp. 945–954. DOI: 10.1134/S0031918X16070176.
16. An B., Niu R., Xin Y., Starch W.L., Xiang Z., Su Y., Goddard R.E., Lu J., Siegrist T.M., Wang E., Han K. Suppression of discontinuous precipitation and strength improvement by Sc doping in Cu-6 wt%Ag alloys. *Journal of Materials Science and Technology*, 2022, vol. 135, pp. 80–96. DOI: 10.1016/j.jmst.2022.06.043.
17. Iwamoto C., Adachi N., Watanabe F., Koitabash R. Microstructure Evolution in Cu-Pd-Ag Alloy Wires During Heat Treatment. *Metallurgical and Materials Transactions A*, 2018, vol. 49, pp. 4947–4955. DOI: 10.1007/s11661-018-4800-3.
18. Novikova O.S., Volkova E.G., Glukhov A.V., Antonova O.V., Kostina A.E., Antonov B.D., Volkov A.Yu. Evolution of the microstructure, electrical resistivity and microhardness during atomic ordering of cryogenically deformed Cu-47at.%Pd alloy. *Journal of Alloys and Compounds*, 2020, vol. 838, article number 155591. DOI: 10.1016/j.jallcom.2020.155591.
19. Williamson G.K., Hall W.H. X-ray line broadening from filed aluminum and wolfram. *Acta Metallurgica*, 1953, vol. 1, no. 1, pp. 22–31. DOI: 10.1016/0001-6160(53)90006-6.
20. Tikhonov A.N., Arsenin V.Y. *Solution of Ill-Posed Problems*. Washington, Harper and Brace Publ., 1977. 258 p.
21. Zeldovich V.I., Frolova N.Y., Kheifets A.E., Khomskaya I.V., Shorokhov E.V. Structural transformations in copper during high-speed deformation upon the convergence of a massive cylindrical shell under implosion. *The Physics of Metals and Metallography*, 2020, vol. 121, no. 5, pp. 446–451. DOI: 10.1134/S0031918X20050154.
22. Volkova E.G., Novikova O.S., Kostina A.E., Glukhov A.V., Volkov A.Yu. Structure and properties of Cu-based alloys diluted by Pd and Ag. *IOP Conference Series: Materials Science and Engineering*, 2020, vol. 1008, pp. 12026–12030. DOI: 10.1088/1757-899X/1008/1/012026.
23. Gong Y.I., Ren S.Y., Zeng S.D., Zhy X.K. Unusual hardening behavior in heavily cryo-rolled Cu-Al-Zn alloys during annealing treatment. *Materials Science and Engineering: A*, 2016, vol. 659, pp. 165–171. DOI: 10.1016/j.msea.2016.02.060.
24. Xin Y., Zhou X., Chen H., Nie J.-F., Zhang H., Zhang Y., Liu Q. Annealing hardening in detwinning deformation of Mg–3Al–1Zn alloy. *Materials Science and Engineering: A*, 2014, vol. 594, pp. 287–291. DOI: 10.1016/j.msea.2013.11.080.
25. Subramanian P.R., Laughlin D.E. Cu-Pd (Copper-Palladium). *Journal of Phase Equilibria*, 1991, vol. 12, no. 2, pp. 231–243. DOI: 10.1007/BF02645723.
26. Gong X., Wei B., Teng J., Wang Z., Li Yu. Regulating the oxidation resistance of Cu-5Ag alloy by heat treatment. *Corrosion Science*, 2021, vol. 190, article number 109686. DOI: 10.1016/j.corsci.2021.109686.
27. Straumal B.B., Kilmametov A.R., Baretzkyet B., Kogtenkova O.A., Straumal P.B., Litynska-Dobrzynska L., Chulist R., Korneva A., Zieva P. High pressure torsion of Cu-Ag and Cu-Sn alloys: Limits for solubility and dissolution. *Acta Materialia*, 2020, vol. 195, pp. 184–198. DOI: 10.1016/j.actamat.2020.05.055.
28. Syutkin N.N., Ivchenko V.A., Telegin A.B., Volkov A.Yu. Field-ion emission microscopy of early stages of ordering and precipitation of palladium copper silver alloy. *Fizika metallov i metallovedenie*, 1986, vol. 62, no. 5, pp. 965–969.
29. Shashkov O.D., Syutkina V.I., Sukhanov V.D. Precipitating phase nucleation on periodical antiphase boundaries. *Fizika metallov i metallovedenie*, 1976, vol. 41, no. 6, pp. 1280–1287.

doi: 10.18323/2782-4039-2023-2-64-4

The study of the structure and properties of a wear-resistant gas-thermal coating containing tungsten

Aleksey Yu. Plesovskikh*, postgraduate student
Svetlana E. Krylova[1], Doctor of Sciences (Engineering), Professor
Orenburg State University, Orenburg (Russia)

***E-mail: plesovskih@tehno-oren.ru**
[1]ORCID: https://orcid.org/0000-0002-5303-9780

Received 14.02.2023 *Accepted 08.05.2023*

Abstract: The paper presents the results of reverse engineering including metallographic, mechanical, and engineering-technical studies of used rods of a compressor produced by the Dresser-Rand company (Siemens, Germany). The study established that the original product is made of AISI 4140 steel with a working coating based on tungsten carbide applied to a depth of 0.2 mm by the HVOF method. The paper contains the results of the development of an import-substituting technological process for producing a wear-resistant powder coating of the Ni–Cr–B–WC system applied by cold gas flame spraying on the surface of a critical unit of compressor equipment in the oil and gas industry. Microanalysis identified that the sprayed spherical WC particles are evenly distributed in the nickel bond without the formation of free cavities at the lamella boundary, retain the size identical to the original powder composition upon the high-speed collision with the substrate, and minimize the level of residual mechanical stresses in the surface layer. The study shows that the sprayed coating has a high microhardness (the bases – 700 $HV_{0.1}$, WC – up to 2000 $HV_{0.1}$), which ensures high wear resistance during operation of the rod in a friction pair. A comparative analysis of the tribological properties of the coatings showed that when changing the shape, particle size distribution, and percentage ratio of tungsten carbide from 20 to 70 % in the nickel matrix, the overall wear resistance of the coating equivalently increases. The authors concluded on the possibility of manufacturing an import-substituting product using the gas flame spraying technology with metallurgical powder compositions containing tungsten. The authors developed an industrial technology for applying a wear-resistant coating on the working surface of a rod made of AISI 4140 steel. The paper presents the results of the analysis of the stress state of a material with a coating produced using the developed technology in comparison with the original product. In the product obtained by the experimental technology, in the process of applying the coating and its subsequent mechanical processing, uniform residual mechanical stresses are formed that do not exceed the value of the difference in the principal mechanical stresses. The paper presents the results of the study obtained both on standard samples and on a pilot part.

Keywords: reverse engineering; compressor rod; cold gas flame spraying; wear-resistant tungsten-based coating; tribological properties; residual mechanical stresses.

For citation: Plesovskikh A.Yu., Krylova S.E. The study of the structure and properties of a wear-resistant gas-thermal coating containing tungsten. *Frontier Materials & Technologies*, 2023, no. 2. DOI: 10.18323/2782-4039-2023-2-64-4.

INTRODUCTION

Currently, most of the critical parts of pumping and compressor equipment of the chemical and oil and gas processing industries of the Russian Federation are made according to the technologies of foreign manufacturers. Taking into account the existing external economic situation, the purchase and operation of components for this equipment, in particular heavy-duty rods of compressor units, is difficult, however, the need for these parts is very significant and amounts to 800–1500 thousand pieces per year within the state. Taking into account this fact, the companies of service maintenance and repair of the oil and gas industry objects are forced to quickly solve a number of scientific and technical issues related to the manufacture of import-substituting products.

Thus, within the repairing machine-building enterprise OOO Tekhnologiya, as a research and technological groundwork, metallurgical studies and re-engineering of used compressor equipment rods from the foreign manufacturer, the German company Dresser-Rand Group (Siemens, Germany), were carried out to determine the grade of the main material, as well as the technology of its surface and volume hardening.

Based on literature data, reference documentation for the compressor equipment parts and the available experience of industrial operation of products, the technology of applying protective coatings using gas-thermal spraying processes seemed to be the most likely method of surface hardening [1]. In this regard, the determination of the chemical composition, particle size distribution and geometric shape of the initial original materials for gas-thermal spraying, as well as the necessary analysis of the properties of coatings, has become an urgent task.

The work [2] shows that HVOF-deposited coatings of the WC–12Ni system containing additives of Cr_3C_2 carbides have a lower porosity than pure WC–10Ni coatings, and their mechanical properties depend not on the deposition rate and the composition of the carrier gas but on the percentage of dispersed chromium-based phases. The grain-size ratio of fine (up to 15 μm) and coarse (100–150 μm) WC grains exerts an important influence on the impact strength and elastic modulus of WC–Cr_3C_2–12Ni coatings.

The authors of [3] consider that, despite the corrosion resistance of tungsten coatings with a cobalt binder, the latter should be replaced by nickel to protect human health and the environment, as well as for economic reasons. At the same time, as alternative coatings, the authors propose using powder mixtures based on WC as a solid phase with a metal matrix based on Fe and Ni (WC–NiMoCrFeCo, WC–FeNiCrMoCu, WC–FeCrAl), indicating the corrosion resistance of such coatings in 3.5 % NaCl solution, their low porosity and hardness values (≈1200 HV) comparable to a conventional WC–CoCr coating, which makes them suitable for industrial applications.

Sprayed tungsten-containing composite coatings can reliably protect the working surface from wear [4; 5]. Tungsten-containing composite coatings, have increased contact strength, hardness, the ability to maintain durability and mechanical properties at elevated temperatures up to 700–800 °C, resistance to corrosive environments due to the addition of molybdenum and the formation of close interatomic bonds with the metal base of cobalt or nickel [6; 7]. This is particularly true since the parts of oil and gas and power equipment are often subject to thermal cycling, abrasion, erosion, and corrosion in the presence of a wearing and corrosive environment.

It is known that a decrease in the WC grain size leads to an increase in hardness and a decrease in the crack resistance of the coating [8–10]. In the work [11], the authors compared the micro-structure and mechanical properties of the WC coating. The authors noted that reducing the WC grain size significantly increases the coating hardness due to enhanced decarburisation of the WC grains. The sources [12; 13] analyze the influence of deposition kinematic parameters on the thickness, porosity, residual stresses, and micro-hardness. It is shown, that the parameters of gas-thermal spraying change in the interrelated way, determined by the geometry: the retraction distance, the spraying angle, and the burner displacement velocity. Changes in these technological factors, in turn, affect the conditions of particle collision, which largely determines the properties of the coating.

The analysis of the literature sources showed that thermally sprayed coatings with WC are widely used in industry, since they offer an effective and economical method for protecting the base material from environmental influences and provide wear resistance without compromising other properties of the component [14]. By now, a wide range of materials for applying coatings of this type have been developed and are being produced. Modern technological equipment has been created, numerous experimental studies have been carried out to determine the modes of coating deposition, and contact interactions of the applied coatings with the surface of the part and with each other have been studied.

However, the issue of the formation of a coating with a predictable structure still has a number of implementation difficulties associated with the lack of objective control of the strength, and porosity of the coating during the technological process, which does not allow introducing appropriate adjustments to the deposition parameters. In each specific case, the proposals for the choice of a material and a spraying technology are advisory, since even within the same chemical composition, coatings differ significantly in density, porosity, applied loads, and other subjective factors.

Residual stress control is a major problem in the coating application technology [15; 16], which can be especially crucial in cases where there is a large discrepancy between the thermal, structural, and mechanical properties of layers and substrates. Therefore, the aggregate influence of the structure, and properties of the sprayed material and spraying parameters on the structure and residual stresses for each specific case requires a detailed study.

An object of the study is a compressor rod with a working surface hardened by flame spraying of a powder composition containing tungsten carbide.

A subject of the research is the modes of gas-thermal spraying of coatings, which ensure the formation of the required structure and performance characteristics of the coating surface layer.

The purpose of the study is to develop and test a rational technology for obtaining a tungsten-containing surface coating, that provides the required combination of performance properties of the import-substituting product “a compressor plant rod” of the Dresser-Rand Group company (Siemens, Germany).

METHODS

In this work, the authors used spherical tungsten carbide with a fraction of 60–80 μm mixed with a binder of the Ni–Cr–B system as a strengthening carbide phase. One of the stages of planning and implementation of flame spraying technology was the development and preparation of a powder composition with 20–80 % WC content.

Gas-thermal spraying was carried out on a CastoDyn DS 8000 processing unit with a combustible gaseous mixture of acetylene C_2H_2 and oxygen O_2 in the ratio of 1:5 with a SSM 10 installed spraying module designed for work on the restoration and hardening of parts by metal powder compositions. Flame spraying was carried out in the mode of continuous linear displacement of the burner relative to the rotating part.

The authors performed spectral analysis of the chemical composition of the tested materials on a PMI-MASTER 13L0059 spectrometer in accordance with the GOST 18895 standard.

Electron microscope investigations were performed by the SEM method using a JEOL JCM-6000 microscope equipped with wave and energy-dispersive analyzers; scanning was performed by varying the accelerating voltage in the range of 5–15 kV. The coating elemental composition was determined by X-ray microanalysis of multiple individual zones of the surface layer.

The microhardness of the deposited layer (matrix and carbide inclusions) was determined by the imprint on an HVS-1000 microhardness tester according to the GOST 9450-76 standard at a load of 0.968 N. The authors performed measurements on transverse sections with a step of 0.05 mm. The measurement error did not exceed 1–3 %. The substrate material hardness was measured on a METOLAB 601 hardness tester using the Brinell method in accordance with the GOST 9012-59 standard.

Mechanical tensile tests of the base materials were carried out using a UTS 111.2-100 testing machine at room temperature in accordance with the GOST 1497-84 standard. For impact toughness testing, the authors used a Resil 300 pendulum impact machine; tests were carried out according to the GOST 9454-78 standard on samples with a U-shaped stress concentrator.

To analyse the stressed state of the coated material, the authors evaluated the distribution of the principal mechanical stress difference (PMSD) over the sprayed surface corresponding in geometry and length to the working area of the finished product. For this purpose, the authors carried out a comparative study of samples with experimental cold flame spraying of the developed composition on AISI 4140 steel and samples obtained from the original Dresser-Rand compressor rod made of the same steel. The stress state of the finished product was assessed by the obtained diagrams of stress in the coating using the STRESSVISION mechanical stress scanner operating based on the magneto-anisotropic method.

The PMSD measurement scheme is shown in Fig. 1. According to this scheme, a template was made and attached to the surface of the rod with a sprayed coating.

Coating porosity was determined according to ASTM E2109-01 on an Eclipse MA200 metallographic microscope at a temperature of 22.1 °C and a humidity of 55 %.

The adhesive strength tests of the coatings were carried out by the adhesive method according to ASTM C633-13 on a SHIMADZU AGS-X universal tensile testing machine at a temperature of 24.1 °C and a humidity of 54 %.

For a reasoned proposal of the developed coating for operation, it was necessary to evaluate its wear resistance. The authors evaluated the wear resistance of the resulting coating in comparison with the surface layer of the original product. To determine the resistance of the coating of the Ni–Cr–B–WC system to abrasive wear, the studied samples were subjected to friction tests under dry wear conditions at a load of 50 N, a rotation speed of 500 rpm, a temperature of 22 °C, and a humidity of 63 %. The tests were carried out on a SMTs-2 friction machine without lubricant to eliminate the modifying effect on the friction surface. During testing, the authors used a disc made of 9HS tool steel with a hardness of 60 HRC as a counter-body. The contact area during testing was 50 mm^2.

RESULTS

According to the established chemical composition (Table 1), the original product "compressor rod" is made of AISI 4140 steel.

The analysis of the microstructure of the original product templates showed that the working surface of the "compressor rod" has a surface layer 150–200 µm deep that essentially differs from the base material and does not have a transition heat-affected zone (Fig. 2), which confirmed the assumption that the coating was applied using the high-speed HVOF flame spraying method.

Considering that the mechanism for obtaining the coating provides for a high-speed impact of molten particles on the prepared metal substrate (degreasing, drying, surface activation, and heating up to 120–150 °C), the surface layer structure is formed due to the formation of layered lamellae 5–7 µm thick parallel to material base. As a rule, small pores and oxides crystallise between the lamellae. Such a heterogeneous layered structure, evidently, has lower strength characteristics than the original material; however, it has advantages at friction, which ensures long-term operation of the part in the "rod – stuffing box seal" coupling pair.

Fig. 3 shows a typical fragment of the studied coverage area and the spectrum composition corresponding to the selected area. The chemical composition of the spectrum area is given in Table 2.

According to the results of X-ray micro-analysis, the working surface layer contains about 86 % of tungsten, cobalt is present as a binder and amounts 6–8 %, and the presence of carbon, vanadium, chromium, and iron allows predicting the additional influence of the carbide and intermetallide hardening mechanism in the cobalt binder.

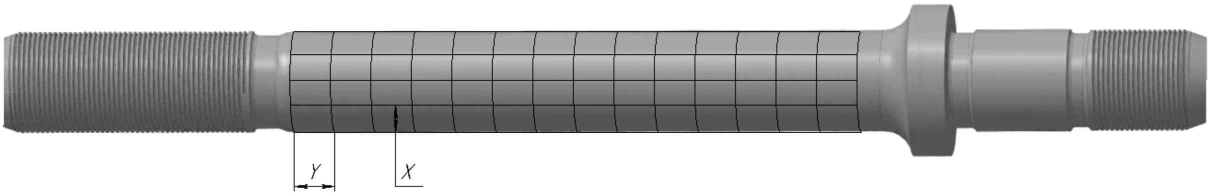

Fig. 1. *PMSD measurement diagram:*
X – measuring section length equal to 52 mm; Y – measuring section width equal to 16 mm

Table 1. *Chemical composition of the product base, % by weight*

	C	Si	Mn	Cr	Mo	Ni	Fe
Average value*	0.400	0.270	0.960	0.920	0.218	0.054	97.178
AISI 4140	0.430	0.300	1.000	1.100	0.250	–	96.920

* *The average value is obtained from the results of at least three measurements.*

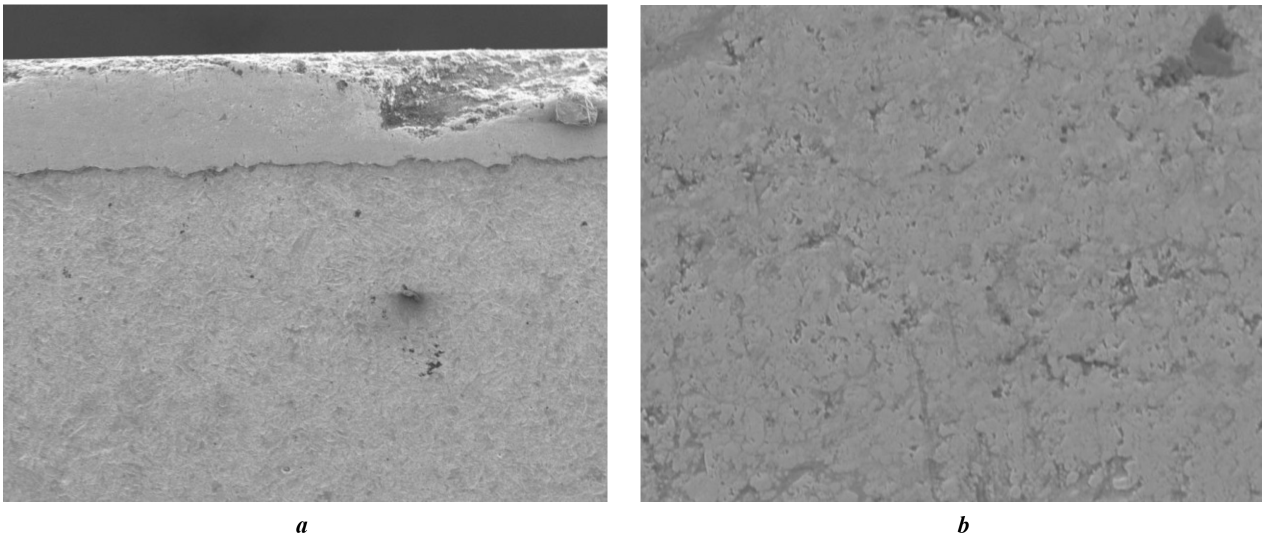

a *b*

Fig. 2. *The results of metallographic studies of the working surface:*
a *– surface general view (×100);* ***b*** *– structure type (×100)*

The porosity of the original coating is distributed uniformly and does not exceed 2.1 % (Fig. 4). The intensity of porosity manifestation along the coating thickness increases towards the base of the material.

Table 3 presents the results of comparative mechanical tests of the original rod material and the selected AISI 4140 analogue after heat treatment.

Based on the data of reverse engineering studies, the main technological principles for the production of rods, for booster compressor station by the foreign Dresser-Rand Group company were determined. The authors identified that for trouble-free operation of these products of oil and gas engineering at a contact load on the rod of 0.7 kg/mm^2, a pressure within 68 kgf/cm^2, at a working medium temperature of up to 150 °C, the composition of associated oil-containing gases: H_2S – 2 %, CO_2 – 2 %, water vapour – up to 1 %, the working coating must have a dispersed tungsten-based carbide structure and an adhesion strength of the coating of at least 50 MPa.

Fig. 5 shows the results of metallographic studies with the research of the WC dimension in the coating of a prototype, with a 20 % content of a hardening carbide phase.

The structure analysis follows that the tungsten carbide in the coating is a spherical granule with a size identical to the original powder composition. This indicates that the sprayed particles are not subjected to serious mechanical stresses during high-speed impact with the substrate, as a result of which their shape and dimensions remain unchanged; they do not prevent the free formation of lamellas of the coating viscous nickel component, they are evenly distributed in the binder without forming free cavities at the boundary of WC and Ni–Cr–B-based binder. Fig. 6 and Table 4 show the results of spectral analysis of individual WC carbide inclusions.

At the stage of adjusting the technology for deposition of a tungsten-based coating, the coating adhesion strength corresponded to the values of the original and varied within 45–55 MPa. The surface layer porosity was recorded within 6.1 % (with a permissible value of pores up to 10 %) [17], the micro-hardness of the coating base (Ni–Cr–B) was about 700 HV$_{0.1}$, and the micro-hardness of tungsten carbide inclusions was 2000 HV$_{0.1}$.

The data in Table 5 demonstrate that with an increase in the percentage ratio of tungsten carbide from 20 to 70 %, the overall wear resistance of the coating increases as well.

Based on the conducted metallographic studies and wear resistance tests, the Ni–Cr–B–WC composition with a tungsten carbide content of 70 % is the optimal composition for hardening the surface layer of the “compressor rod” item. This coating, with a lower WC content in the volume, ensures satisfactory and comparable to the original micro-hardness values, meets or exceeds the original in the wear resistance of the working surface due to the application of a combined Ni–Cr–B metal base instead of the original cobalt binder, which provides additional attractiveness of the development in economic terms.

The results of PMSD measurements obtained using the STRESSVISION mechanical stress scanner (indicator) are shown in Fig. 7.

The numerical characteristics obtained by mathematical processing of the maps of the PMSD distribution in the original rod and the prototype are summarized in Table 6.

The analysis of distribution cartograms of residual mechanical stresses showed that the cold flame spraying technique, which allows obtaining the thickness of the developed coating corresponding to the original product (in the range from 0.2 to 0.25 mm), is optimal in terms of internal stresses at the metal-coating boundary. (Fig. 6). Fig. 8 presents the numerical characteristics obtained by mathematical processing of PMSD distribution maps, which reflect the comparative distribution of maximum stresses over the zones of scanning.

The analysis of the data (Fig. 6, Fig. 7) shows that the PMSD distribution over the surface of the experimental sprayed sample is uniform and does not exceed 10 c. u. after manufacturing. Stress state analysis data were obtained from the original product at the stage of reverse engineering of the compressor rod used for 4 thousand hours. The original product has two local stress state zones: zone 8, where the PMSD maximum value is 346.84 c. u.,

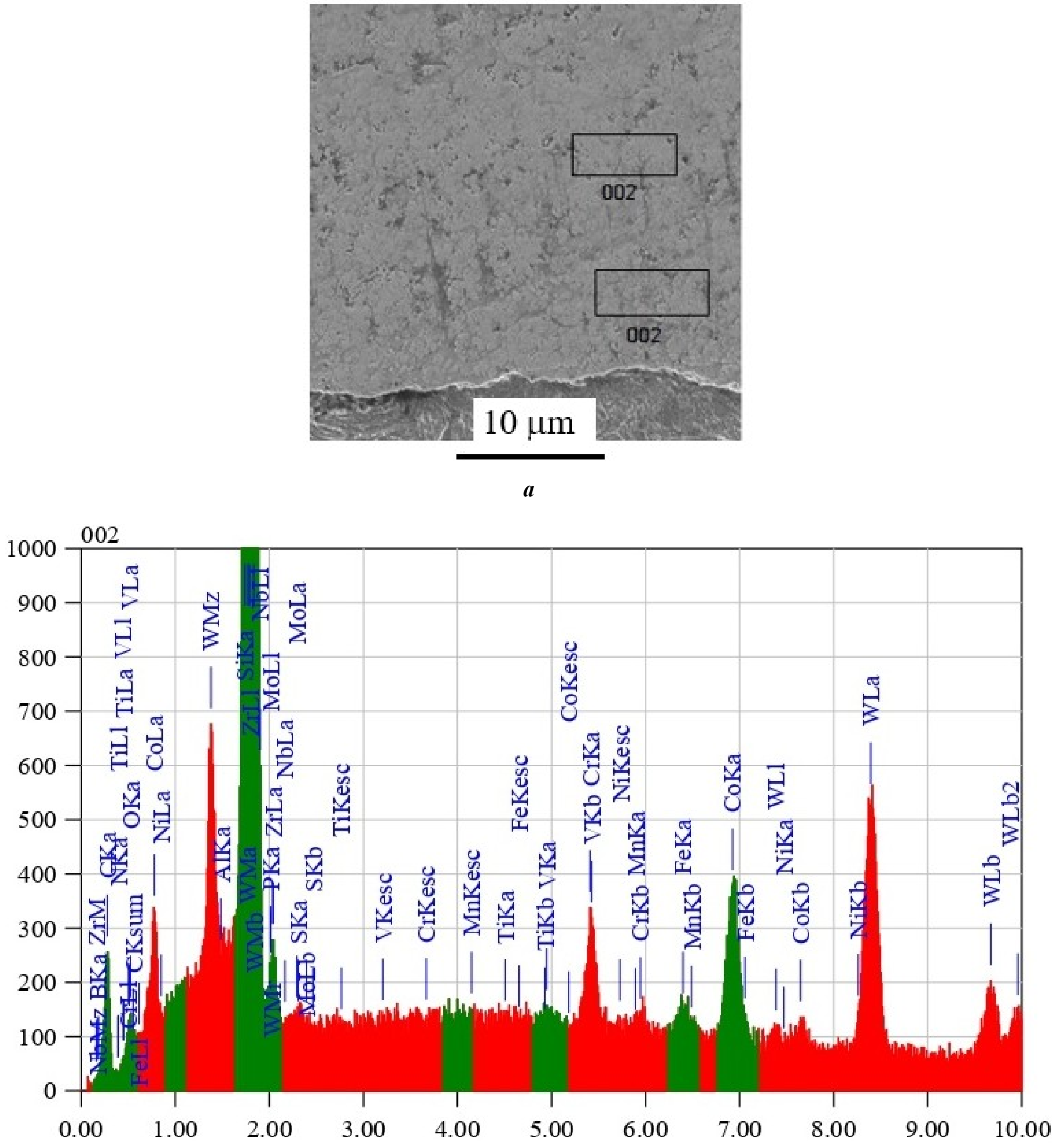

a

b

Fig. 3. *Elemental composition of the specific coating area:*
a *– an analyzed fragment of the coating (002 spectrum);* ***b*** *– a spectrogram of the respective analysis area*

Table 2. *Chemical composition of the coating in the 002 spectrum area, % by weight*

C	V	Cr	Mn	Fe	Co	W
2.27	0.06	2.81	0.03	0.92	7.82	86.09

and zone 6, where the PMSD maximum value is 225.5 c. u. However, the average background of stress distribution is also stable and lies within 10–20 c. u. The existence of zones with the increased PMSD values is explained by the cumulative effect of stresses in local friction zones during operation. The obtained data show that in the experimental sample with surface hardening by cold flame spraying, in the process of coating and its subsequent mechanical processing, insignificant uniform residual mechanical stresses are formed in the coating zone not exceeding the PMSD values compared to the foreign manufacturer technology. This makes it possible to recommend, reasonably, the developed coating composition and its application method for testing on a pilot item.

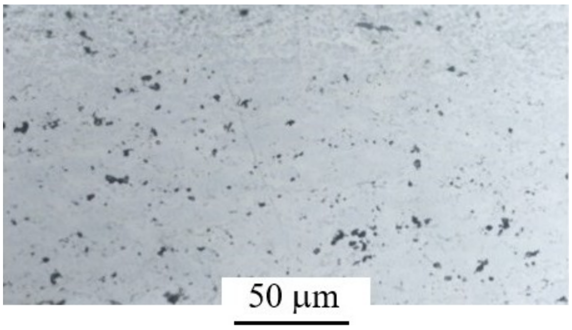

Fig. 4. *Microphotographs of the coating section when measuring porosity*

Table 3. *Mechanical properties of the base metal of the product*

Characteristics	An original	A material – AISI 4140 analogue
Yield strength $\sigma_{0.2}$, Mpa	347	563
Ultimate stress limit $\sigma_в$, MPa	728	784
Percentage elongation δ_5, %	23.2	17.1
Percentage reduction ψ, %	63.1	67.9
Impact resistance KCU^{+20}, J/sm^2	62.5	176
Hardness, HB	215	226

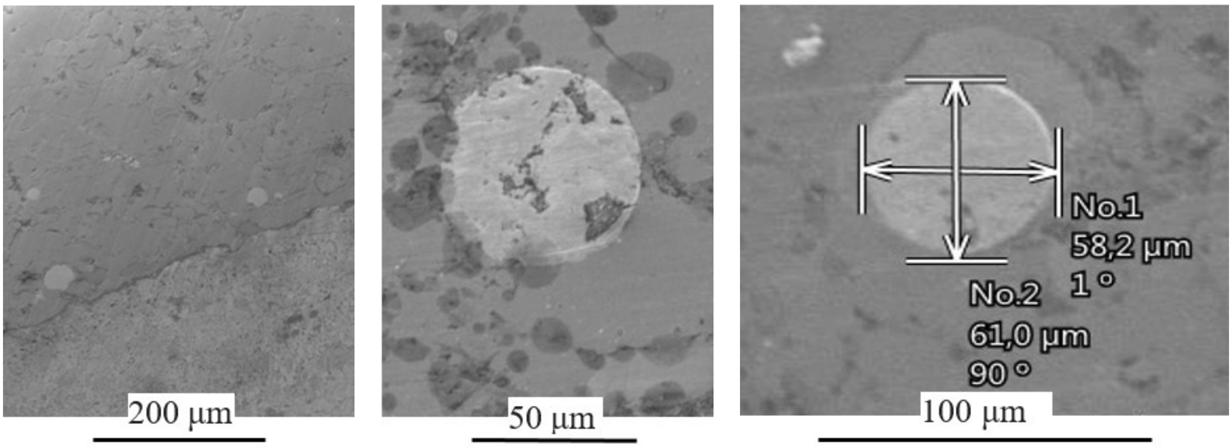

a ***b*** ***c***

Fig. 5. *The structure of the coating surface layer produced by cold gas flame spraying:*
a, b *– structure general view;* ***c*** *– dimensions and shape of the tungsten carbide particles (×500)*

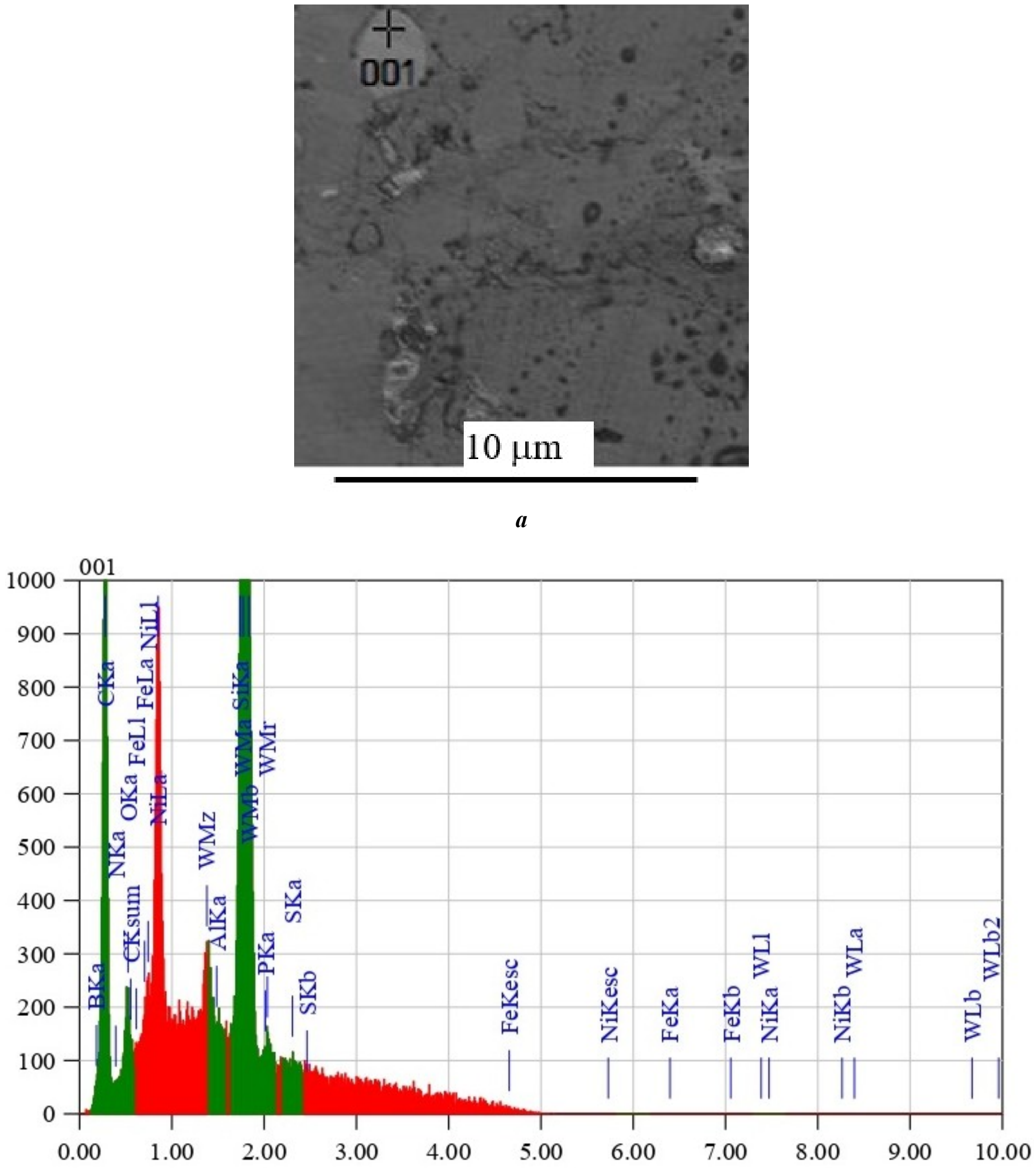

b

Fig. 6. *The results of X-ray microanalysis of spherical tungsten carbide:*
a *– an analyzed fragment of the coating (001 spectrum);* ***b*** *– a spectrogram of the analyzed fragment of the coating (001 spectrum)*

Table 4. *WC chemical composition in the 001 spectrum, % by weight*

C	B	Ni	O	W
32.23	2.54	1.05	1.40	62.78

DISCUSSION

The development of manufacturing technology for the import-substituting "compressor rod" item included: the development of the design-engineering documentation, metallographic studies, engineering and technical experiments [18; 19].

In the process of coating formation by flame spraying, at the stage of plasticisation and deformation of refractory particles during high-speed impact, typical defects and free cavities inevitably form in the zone of contact of the previously applied layers of lamellas with the surface. Their interaction with the atmosphere during the precipitation of dust fractions up to 80 μm in size, as well as the adsorption of gases on freshly formed coating layers, significantly worsen the structure and, consequently, the properties of the interlayer coating zone. Reducing the size of the sprayed particles can significantly improve the layer-by-layer filling of the coating through the formation of a more homogeneous structure,

Table 5. *The dependence of the wear value on the carbide phase amount in the coating*

Tungsten carbide amount in the coating, %	**Specimen weight, g**		**Wear, g**
	before tests	**after tests**	
Experimental spraying			
20	11.45	11.38	0.07
30	11.50	11.43	0.07
50	11.49	11.44	0.05
70	14.65	14.64	0.01
Original rod			
90	14.57	14.56	0.01

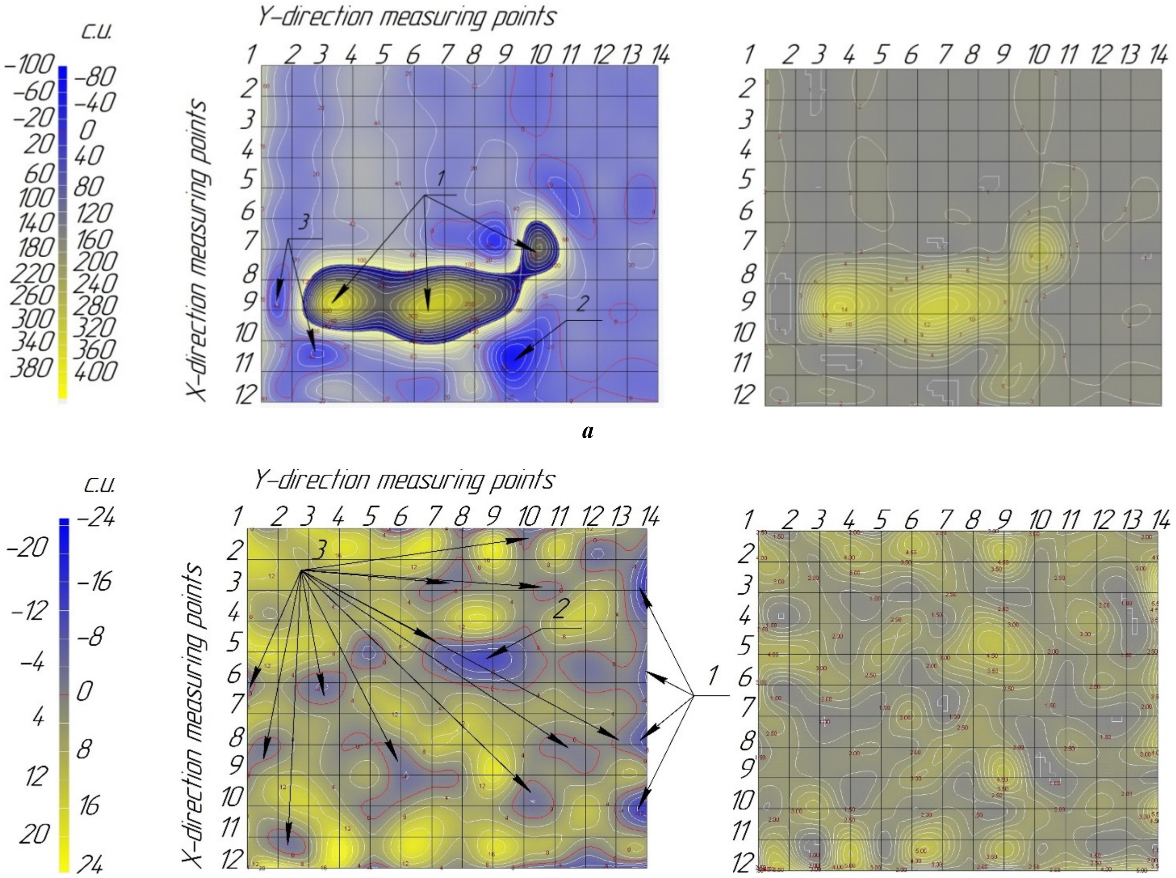

a

b

Fig. 7. *Cartograms of PMSD distribution:*
a *– of an experimental specimen;* ***b*** *– of an original compressor rod:*
1 – edge defect zone, 2 – compressive stress zone, 3 – compensation zones

increasing its density while reducing the volume of microvoids. In this regard, the choice of fractional composition and shape of powder particles takes on special significance.

Thus, powder compositions for the formation of the working layers of pumping and compressor equipment should ensure high adhesive strength (more than 50 MPa), wear resistance, and minimal coating porosity. These requirements can be fully met by spraying powder compositions, with tungsten carbide inclusions, in a working layer. In early works [18; 19], the authors paid attention to comparing the efficiency of introducing tungsten carbide particles of different morphology and granulometry into the nickel

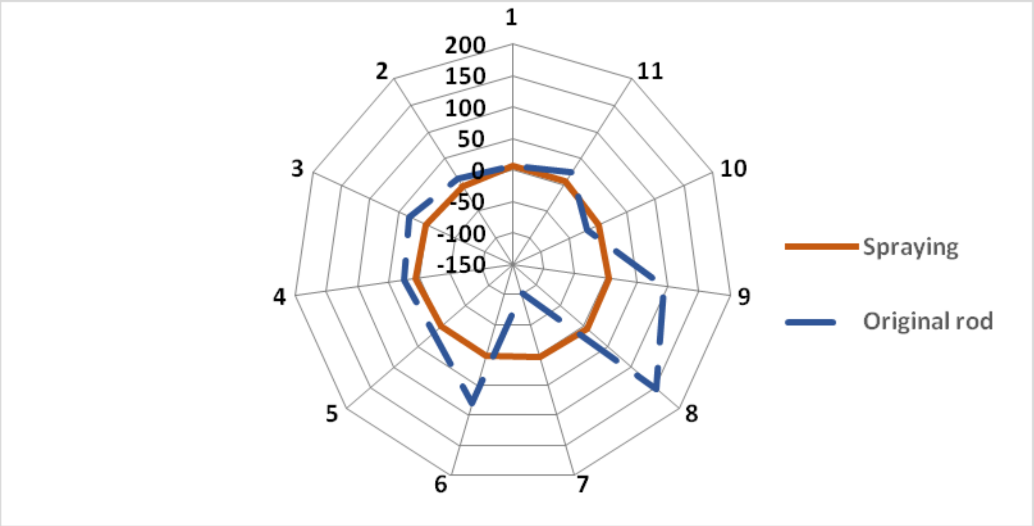

Fig. 8. *Comparative analysis of the distribution of average residual stresses in the test sample and the original product*

matrix, showed the advantage of introducing dispersed spherical particles with regard to the formation of a monolithic surface layer that excludes cracking, coarse pores, and tears under load. Based on the studies performed, it was found that particles of spherical tungsten carbide (WC) up to 50 μm in size [17–19] contained in the matrix in the range of 60–70 vol. % provide the best result of carbide hardening, which is confirmed by the present results.

The research showed that a nickel matrix existing in the form of a γ-solid solution in the deposited layer contributes to increasing the coating fracture toughness and abrasive resistance, and the presence of dispersed high-strength spherical carbide phases in the metal base provides the coating increased strength and wear resistance in the context of boundary friction and friction without lubrication. Comparative studies of wear resistance showed that due to the elastic-plastic properties of the coating composite material, the wear rate decreases by 1.2–1.3 times. The increase in wear resistance at a constant friction coefficient is associated with hardening through the structure refinement and the targeted formation of a significant number of hardening phases in the working layer.

CONCLUSIONS

1. Based on the data of the reverse engineering studies of a booster compressor station rod, the original product of the Dresser-Rand Group company (Siemens, Germany), the grade of the main material – AISI 4140 steel (chemical composition, wt. %: 0.38–0.43 C; 0.15–0.30 Si; 0.75–1.0 Mn; 0.80–1.10 Cr; 0.15–0.25 Mo; 0.04 S; 0.035 P; the rest is Fe) and technological features of the working surface manufacturing, and hardening by applying a wear-resistant tungsten-containing coating using the cold gas-thermal spraying technique were determined.

2. A composition of a wear-resistant powder coating based on the Ni–Cr–B metal system with the spherical tungsten carbide (WC) inclusions was developed. The proposed technology of its application using the cold gas-thermal spraying method allowed obtaining a surface wear-resistant layer of 0.2–0.25 mm having a base microhardness in the range of 700 $HV_{0.1}$ with a uniform distribution of strengthening carbide phases with a micro-hardness of up to 2000 $HV_{0.1}$.

3. It is established that the nickel matrix carbide hardening by the dispersed spherical tungsten carbide WC particles within 60–70 vol. % allows improving the layer-by-layer formation of coating lamellae, increasing the density and uniformity of the structure, reducing the volume of free microvoids at the "WC – binder" boundary from 10 to 6 %, according to the coating porosity analysis.

4. The proposed Ni-Cr-B-WC coating compares with the original product in wear resistance, has a certain economic attractiveness, while ensuring accurate geometric dimensions and a minimum stress state gradient not exceeding 10 MPa. These technological advantages made it possible to start implementing the technology of surface hardening of compressor equipment rods under production conditions.

REFERENCES

1. Barvinok V.A., Shitarev I.L., Bogdanovich V.I., Dokukina I.A., Karasev V.M. Wearability, wearproof and heat-shielding coverings for details of the gas path of the turbine, the compressor and the chamber of combustion of gas turbine engine. *Vestnik Samarskogo gosudarstvennogo aerokosmicheskogo universiteta im. akademika S.P. Koroleva*, 2009, no. 3-1, pp. 11–28. EDN: LADTXX.
2. Yao H.-L., Yang Ch., Yi D.-L., Zhang M.-X., Wang H.-T., Chen Q.-Yu., Bai X.-B., Ji G.-Ch. Microstructure and mechanical property of high velocity oxy-fuel sprayed WC-Cr3C2-Ni coatings. *Surface and Coatings Technology*, 2020, vol. 397, article number 126010. DOI: 10.1016/j.surfcoat.2020.126010.
3. Testa V., Morelli S., Bolelli G., Benedetti B., Puddu P., Sassatelli P., Lusvarghi L. Alternative metallic matrices for WC-based HVOF coatings. *Surface and Coatings Technology*, 2020, vol. 402, article number 126308. DOI: 10.1016/j.surfcoat.2020.126308.

4. Rakhadilov B.K., Muktanova N., Zhurerova L.G. Application of HVOF technology for WC-based wear-resistant coatings – an overview. *Vestnik NYaTs RK*, 2023, no. 1, pp. 4–14. DOI: 10.52676/1729-7885-2023-1-4-14.
5. Pereira P., Vilhena L.M., Sacramento J., Senos A.M.R., Malheiros L.F., Ramalho A. Abrasive wear resistance of WC-based composites, produced with Co or Ni-rich binders. *Wear*, 2021, vol. 482-483, article number 203924. DOI: 10.1016/j.wear.2021.203924.
6. Santos R.F., Ferro Rocha A.M., Bastos A.C., Cardoso J.P., Rodrigues F., Fernandes C.M., Sacramento J., Ferreira M.G.S., Senos A.M.R., Fonseca C., Vieira M.F., Malheiros L.F. The effect of Cr content on the corrosion resistance of WC-Ni-Cr-Mo composites. *International Journal of Refractory Metals and Hard Materials*, 2021, vol. 95, article number 105434. DOI: 10.1016/j.ijrmhm.2020.105434.
7. Santos R.F., Ferro Rocha A.M., Bastos A.C., Cardoso J.P., Rodrigues F., Fernandes C.M., Sacramento J., Ferreira M.G.S., Senos A.M.R., Fonseca C., Vieira M.F., Malheiros Luís F. Microstructural characterization and corrosion resistance of WC-Ni-Cr-Mo composite – The effect of Mo. *International Journal of Refractory Metals and Hard Materials*, 2020, vol. 86, article number 105090. DOI: 10.1016/j.ijrmhm.2019.105090.
8. Wang D., Zhang B., Jia Ch., Gao F., Yu Yu., Chu K., Zhang M., Zhao X. Influence of carbide grain size and crystal characteristics on the microstructure and mechanical properties of HVOF-sprayed WC-CoCr coatings. *International Journal of Refractory Metals and Hard Materials*, 2017, vol. 69, pp. 138–152. DOI: 10.1016/j.ijrmhm.2017.08.008.
9. Chivavibul P., Watanabe M., Kuroda S., Shinoda K. Effects of carbide size and Co content on the microstructure and mechanical properties of HVOF-sprayed WC–Co coatings. *Surface and Coatings Technology*, 2007, vol. 202, no. 3, pp. 509–521. DOI: 10.1016/j.surfcoat.2007.06.026.
10. Yuan J., Ma Ch., Yang Sh., Yu Zh., Li H. Improving the wear resistance of HVOF sprayed WC-Co coatings by adding submicron-sized WC particles at the splats' interfaces. *Surface and Coatings Technology*, 2016, vol. 285, pp. 17–23. DOI: 10.1016/j.surfcoat.2015.11.017.
11. Ma N., Guo L., Cheng Zh., Wu H., Ye F., Zhang K. Improvement on mechanical properties and wear resistance of HVOF sprayed WC-12Co coatings by optimizing feedstock structure. *Applied Surface Science*, 2014, vol. 320, pp. 364–371. DOI: 10.1016/j.apsusc.2014.09.081.
12. Katranidis V., Gu S., Allcock B., Kamnis S. Experimental study of high velocity oxy-fuel sprayed WC-17Co coatings applied on complex geometries. Part A: Influence of kinematic spray parameters on thickness, porosity, residual stresses and microhardness. *Surface and Coatings Technology*, 2017, vol. 311, pp. 206–215. DOI: 10.1016/j.surfcoat.2017.01.015.
13. La Barbera-Sosa J.G., Santana Y.Y., Moreno E., Cuadrado N., Caro J., Renault P.O., Le Bourhis E., Staia M.H., Puchi-Cabrera E.S. Effect of spraying distance on the microstructure and mechanical properties of a Colmonoy 88 alloy deposited by HVOF thermal spraying. *Surface and Coatings Technology*, 2010, vol. 205, no. 7, pp. 1799–1806. DOI: 10.1016/j.surfcoat.2010.01.017.
14. Wang Q., Zhang Sh., Cheng Y., Xiang J., Zhao X., Yang G. Wear and corrosion performance of WC-10Co4Cr coatings deposited by different HVOF and HVAF spraying processes. *Surface and Coatings Technology*, 2013, vol. 218, pp. 127–136. DOI: 10.1016/j.surfcoat.2012.12.041.
15. Varis T., Suhonen T., Jokipii M., Vuoristo P. Influence of powder properties on residual stresses formed in high-pressure liquid fuel HVOF sprayed WC-CoCr coatings. *Surface and Coatings Technology*, 2020, vol. 388, article number 125604. DOI: 10.1016/j.surfcoat.2020.125604.
16. Santana Y.Y., La Barbera-Sosa J.G., Staia M.H., Lesage J., Puchi-Cabrera E.S., Chicot D., Bemporad E. Measurement of residual stress in thermal spray coatings by the incremental hole drilling method. *Surface and Coatings Technology*, vol. 201, no. 5, pp. 2092–2098. DOI: 10.1016/j.surfcoat.2006.04.056.
17. Krylova S.E., Plesovskikh A.Yu., Kurnoskin I.A., Tavtilov I.Sh. Influence of heat treatment on the structure and properties of the tungsten-containing coating of the working part of oil and gas equipment. *Chernye metally*, 2022, no. 12, pp. 36–42. DOI: 10.17580/chm.2022.12.05.
18. Plesovskikh A.Yu., Krylova S.E., Oplesnin S.P. Import-substituting technology for manufacturing parts of the oil and gas industry with the application of wear-resistant coatings based on tungsten. *Vestnik sovremennykh tekhnologiy*, 2019, no. 2, pp. 9–14. EDN: WJOBJF.
19. Plesovskikh A.Y., Krylova S.E., Oplesnin S.P., Kurnoskin I.A. Import-substituting technology for manufacturing parts of the oil and gas industry with the application of tungsten based wear-resistant coatings. *Materials Today: Proceedings*, 2021, vol. 38, part 4, pp. 1595–1598. DOI: 10.1016/j.matpr.2020.08.161.

doi: 10.18323/2782-4039-2023-2-64-8

Cyclic regularities of the acoustic emission generation during plasma-electrolytic oxidation of an Al–Mg alloy in the bipolar mode

Igor A. Rastegaev*[1], PhD (Physics and Mathematics),
senior researcher of the Research Institute of Advanced Technologies
Marat R. Shafeev[2], junior researcher of the Research Institute of Advanced Technologies
Inna I. Rastegaeva[3], senior lecturer of Chair "Nanotechnologies, Materials Science and Mechanics"
Anton V. Polunin[4], PhD (Engineering), leading researcher of the Research Institute of Advanced Technologies
Mikhail M. Krishtal[5], Doctor of Sciences (Physics and Mathematics), Professor,
chief researcher of the Research Institute of Advanced Technologies
Togliatti State University, Togliatti (Russia)

***E-mail: RastIgAev@yandex.ru,**
I.Rastegaev@tltsu.ru

[1]ORCID: https://orcid.org/0000-0003-3807-8105
[2]ORCID: https://orcid.org/0000-0002-4490-6547
[3]ORCID: https://orcid.org/0000-0002-7634-2328
[4]ORCID: https://orcid.org/0000-0001-8484-2456
[5]ORCID: https://orcid.org/0000-0001-7189-0002

Received 03.05.2023 *Accepted 13.06.2023*

Abstract: The paper analyzes the features of the acoustic emission (AE) signal generation during plasma-electrolytic oxidation (PEO) of the AMg6 aluminum alloy in a bipolar (anode-cathode) pulsed mode within each cycle of voltage application. The authors studied the range of PEO modes that almost completely covers all standard technological modes for processing aluminum alloys by the current densities (6–18 A/dm^2) and current ratio in half-cycles (0.7–1.3), which allowed fixing and studying the AE accompanying the formation of oxide layers for various purposes. For the first time, due to AE registration, a new PEO stage was identified, in which there was no microarc breakdown to the substrate, but which was accompanied by an increase in the layer thickness, and the nature of which has not yet been determined. According to the known features of the oxidation stages, the authors systematized the repetitive forms of AE manifestation in the cycles of exposure and identified their five types and three subtypes. The study shows that the approach used to establish the PEO stages by the "acoustic emission amplitude" parameter has poor accuracy, since it does not take into account the form of signals and the half-period of their registration. Therefore, the authors developed and tested a new approach for analyzing AE frames synchronously with the cycles of change in the forming voltage during PEO, and proposed a new "acoustic-emission median" parameter, which allows identifying the main types and subtypes of signals accompanying the oxidation stages. An experimental study of the proposed AE parameter was carried out to identify these PEO stages, which confirmed the operability, high accuracy and sensitivity of the proposed parameter to the subtypes of AE signals recorded at the cathode stage of "soft sparking". The latter is of particular interest, since it is a means of studying a given oxidation stage with a resolution equal to the exposure cycle.

Keywords: aluminum alloy; plasma electrolytic oxidation; acoustic emission; microarc discharges.

Acknowledgments: This work was supported by the Russian Science Foundation (Project No. 20-79-10262, https://rscf.ru/project/20-79-10262/).

For citation: Rastegaev I.A., Shafeev M.R., Rastegaeva I.I., Polunin A.V., Krishtal M.M. Cyclic regularities of the acoustic emission generation during plasma-electrolytic oxidation of an Al–Mg alloy in the bipolar mode. *Frontier Materials & Technologies*, 2023, no. 2. DOI: 10.18323/2782-4039-2023-2-64-8.

INTRODUCTION

Today, one of the relevant issues of the technology of plasma electrolytic, or microarc, oxidation (PEO or MAO) of the surface of products made of valve group metals (Al, Mg, Ti, Zr, Nb, etc.) is to monitor the process of formation of a multifunctional oxide "coating" (oxide layer). According to [1], the multifunctionality of coatings is the possibility of their application in various fields of science, and technology under conditions that differ vastly in the main damaging factors (mechanical-chemical, chemical-thermal, mechanical-electrical, etc.). It is known [2] that the ability to resist the impact of external and internal damaging factors is provided by the physicochemical properties of oxide layers (adhesion, hardness, wear resistance, etc.), which, in turn, are determined by a complex of characteristics and factors – structural (thickness, porosity, residual strains, etc.), phase (qualitative and quantitative composition), morphology of the layer, and its defectiveness [2]. Many authors show that the uniformity of the properties of oxide layers in thickness (sublayers) depends on the PEO process parameters, more specifically, the frequency of forming pulses and current density [3], the presence of the cathode current component [4; 5], and its power ratio with the anode component [6], electrolyte composition [7] and its quality [8], which together determine the types of formed discharges and their power [9]. In particular, it was established in [3], that the application of the increased current densities (70–90 A/dm^2) in combination with high frequencies of forming pulses (up to 900 Hz) leads to a decrease in the porosity and non-uniformity of oxide layers, due to a decrease in the surface density of microdischarges. In [4; 5] the authors found that an increase in the cathode component during PEO of an aluminum alloy, and a transition to the "soft sparking" mode can lead to the occurrence of developed nanosized porosity in combination with a barrier layer densification at the "metal substrate – oxide layer" interface [4], which is also observed during the magnesium alloy PEO [6]. In [5], it was found that the cathode half-cycle (negative polarization) during the PEO of aluminum alloy leads to additional formation of aluminum hydroxide, with a decrease in the resistance to microarc breakdown of the barrier layer followed by the formation of stable Al_2O_3 modifications, as a result of $Al(OH)_3$ dehydration in the anode half-cycle, and to the barrier layer densification, which ultimately improves the uniformity and protective properties of the oxide layers. Therefore, the possibility of the PEO process in situ monitoring, recognition of its stage, microarc breakdown type, and the emerging microarc discharge (MAD) allows establishing the mechanism of surface oxidation and oxide layer formation at a time, and thus, at the stage of developing PEO modes, organizing feedback to control the energy released in the MAD breakdown channels directly in the oxidation process, i.e., controlling the quality and functional properties of the oxide layers.

Nowadays, several methods for PEO process monitoring have been proposed and tested already. They are tracking electrical parameters in the PEO circuit [10; 11], electrical impedance spectroscopy of oxide layers [12], luminosity intensity tracking using high-speed photo-video recording [13; 14], photo-EMF recording [15], optical emission spectroscopy [16], infrared thermometry [17], coating thickness monitoring using various non-contact methods [18], acoustic signals (acoustic emission (AE) in the sound and ultrasonic ranges). The sound range is rarely used compared to the ultrasonic range, since it has a significantly lower noise immunity [19], therefore, in this paper, the authors consider AE only in the ultrasonic range.

AE tracking appears to be one of the most promising methods for PEO monitoring, since elastic waves accompany the process of stored energy relaxation with a rather wide range of known physical and chemical phenomena [20]. However, as far as we know, in the studies of AE during PEO, for a moment it was possible to identify only the primary correlation of the oxidation stages, with the integral characteristics of acoustic radiation without detailing the special aspects of the AE signals recorded on them. For example, in [21; 22], the authors discuss the relationship between acoustic radiation and PEO modes in the categories of "increase" and "decrease" of its level, even without specifying the parameters for estimating AE signals. In [23], using the AE threshold method, the correlation of AE signals with the stage of development of forming discharges (sparking, microarc, and arc discharges) was shown, and [24] described the correlation of the trends in the accumulation of counts during AE and the kinetics of the growth of oxide layers on the D16 alloy. In [25], the authors showed that with an increase in the oxide layer thickness, the acoustic signal shifts to a more low-frequency and high-amplitude region, which, in their opinion, indicates the localization and increase in the power of a single MAD. In [26], the acoustic emission monitoring of the PEO process, and the criterion assessment of the change in the AE amplitude, allowed improving the quality of the oxide layers, and its reproducibility on the D16AT alloy. In [27; 28], against the background of tracking the trends in AE energy changes, an attempt was made to separate acoustic signals into pulsed and continuous (resonant) types, with their following description by their parameters: amplitude, energy, rise time, and frequency at the peak. The work [29] presents the preliminary results of recording the AE signals obtained by PEO of AMg6 samples, and, in particular, establishes the synchronism of AE signal recording with the exposure cycle and shows the correlation of their temporal position with visual observations and literature data of optical measurements, using photo-video recording and photo-EMF analysis, as well as the PEO electrical parameters. However, identifying the PEO process stages by comparing their visual features with the AE amplitude features, gives a significant error in identifying the stage, and requires a more detailed understanding of the AE manifestation within the exposure cycle.

The analysis of indicated works showed that the parametric distributions of the used main parameters of the AE assessment significantly overlap (superimposed); therefore, the construction of diagnostic signs of PEO stages, using them has a high probability of error in identifying the type of emerging MADs. Consequently, to increase the AE method sensitivity, other approaches to the evaluation of acoustic signals are required.

The aim of the work is to identify the acoustic emission special features within the cycle of bipolar pulsed electrical action on the oxidized material (using the example of the AMg6 aluminum alloy) during plasma electrolytic oxidation as the basis for developing a new method for controlling PEO, to reduce the time for selecting its optimal mode through a more accurate detection of boundaries of various stages of the oxidation process.

METHODS

The subject of research is the AE that accompanies the formation of oxide layers on the AMg6 Al–Mg alloy (foreign analogue is alloy 1560, chemical composition, wt. %: 6.2 Mg; 0.65 Mn; 0.5 Ti; 0.4 Si; 0.3 Fe; 0.18 Zn; 0.087 Cu; Al – the base) at various modes of bipolar anode-cathode pulse action.

The samples for research had overall dimensions $(140\times20\times6)$ mm^3, which were immersed in the electrolyte, not completely, in order to install the AE sensor directly on the sample. As a result, during PEO, only a part of the sample with the size of $(60\times20\times6)$ mm^3 was oxidized. The rest, part of the sample, was insulated using an electrically insulating varnish and epoxy resin, which served as a contact medium and an AE sensor holder on the sample.

PEO was carried out on an innovative research self-made plant, produced by Togliatti State University consisting of a stainless steel bath with a volume of 15 l, an external cooling system based on a liquid/liquid heat exchanger, and a circulation pump for electrolyte thermostat control; pulse inverter power unit with a peak power of 40 kW, with a computer system to control the PEO modes for current and voltage in the specialized LabVIEW software. In the work, the bipolar (anode-cathode) pulsed mode of oxide layer formation was used as the most efficient, and promising in terms of obtaining the best quality, and properties of oxide layers, which allows transferring the results of the AE analysis to the PEO anodic mode, without taking into account the cathode component.

The experimental constants for all PEO modes were the frequency of the forming current pulses – 500 Hz, i.e. the duration of the exposure cycle during PEO – 2 ms; the pulse duty cycle of the process current – 65 %; the ratio of the durations of the cathode and anode forming pulses is 55 %/45 %, respectively; pauses between the cathode and anode pulses – 50 %; electrolyte composition and temperature; PEO duration – 180 min.

During the experiment, the authors varied the root-mean-square current density *j*, A/dm^2 (6; 9; 12; 15 and 18 A/dm^2) through the sample, and the ratio of currents in the cathode and anode half-cycles *C/A* (0.70; 0.85; 1.00; 1.15 and 1.30), which were set at the PEO process initiation, and further kept constant by the plant control system. Totally, AE was recorded in 25 PEO modes, which almost completely cover the known and currently used modes of the oxide layer formation on aluminum alloys and, therefore, all PEO process stages (anodic passivation, anode sparking, anode-cathode MAO, and soft sparking modes [30]) and the MAD types (anode sparking, anode microarc and cathode microarc discharges, anode arc and cathode arc discharges, as well as discharges of A, B, and C types [31; 32]).

As an electrolyte, an aqueous solution based on KOH potassium hydroxide (3 g/l), $Na_4P_2O_7 \times 10H_2O$ sodium pyrophosphate (8 g/l), and $Na_2SiO_3 \times 5H_2O$ sodium metasilicate (12 g/l) was used. The electrolyte temperature during PEO was maintained by an external cooling system at a level of (285±3) K.

The AE was recorded directly from the sample, which determined the minimum coefficients of signal distortion and attenuation. Acoustic signals were converted into electrical ones, using the piezoeffect by a P111-(0.02-0.3) transducer (Russia) with a bandwidth of 20–800 kHz, with a main sensitivity in the frequency range up to 300 kHz. Further, the signals were amplified by a MSAE-FA010 two-stage broadband filter-amplifier (Russia), digitized, and recorded in frames with a duration of 40 ms (20 complete exposure cycles) every 1 min using an Advantech PCI-1714 12-bit A-to-D card (ADC) (Taiwan) at a sampling rate of 2 MHz, which provided the AE analysis frequency range up to 1 MHz. Therefore, in contrast to the works that used the threshold method of AE registration, the authors of this research excluded the omission in the record of AE changes, within the recorded exposure cycles. At the same time, the AE recording frame equal to the exposure cycle includes 4000 counts (4000 counts/2 MHz=2 ms). Synchronously with the acoustic signals, the same ADC recorded frames of voltage and current changes in the PEO cycles as well.

In our work [29], we described in detail the technical features and problems of obtaining an AE signal and protecting the sensor when an oxidized sample in an electrolyte.

The oxide layer thicknesses were measured, using a Konstanta K6 eddy-current thickness gauge (Russia), with a PD1 transducer, as well as on transverse metallographic sections using a Jeol JCM-6000 Neoscope II scanning electron microscope (Japan). The microhardness $HV_{0.1}$ was measured on cross sections in accordance with the GOST R 8.748-2011 standard on a Shimadzu DUH-211S dynamic microhardness tester (Japan). Wear resistance (linear wear rate) was evaluated using the ASTM G133 method on a Nanovea TRB-50N tribometer (USA). In more detail, the special aspects of measuring the thickness, hardness, and wear resistance of the obtained oxide layers using the specified techniques and the results obtained are described in [33; 34].

RESULTS

AE amplitude-time features during PEO

AE recording, together with visual tracking of the PEO process, showed that the main PEO stages have characteristics of AE signals that evolve synchronously with the observed MADs (Fig. 1). At the initial moment of time, the anode surface passivation, and the "barrier layer" formation occur as a result of chemical anodization and primary microarc breakdowns, which is accompanied by the onset and rapid increase in the AE amplitude (Fig. 1, stage I). As the barrier layer "strengthens", with the simultaneous oxide layer formation, the MADs amplify, begin to unite into cascades, and even change into separate (point) arc discharges at the stages II and III (Fig. 1), which is accompanied by AE signals of almost constant (Fig. 1, stage II) and increased (Fig. 1, stage III) amplitude. Then, for most of the studied modes, stage IV begins with a sharp drop in the AE signal amplitude, which coincides with the almost complete visual disappearance of burning MADs and the PEO process transition to the "soft sparking" mode.

In the process of comparing the sweep of the AE records and the time marks of stages I–IV (Fig. 1), obtained by visual observations of the change in the sample luminescence during PEO, the AE signs of the boundaries of the PEO stages were formed (Fig. 1). As standard visual boundaries of the PEO stages, the high-speed video recording freeze-frames given in [14], and similar to our experiment were taken. It is established that the first AE peak observed after the oxidation onset can be taken as the AE sign of the boundary of transition from stage I to stage II of PEO (Fig. 1, stage I). The beginning of the second AE peak equal to the first AE peak level or exceeding it (Fig. 1, stage II) can be taken as the sign of the boundary of the transition from stage II to stage III of PEO. The beginning of the recording section with a sharp drop in the AE amplitude (Fig. 1, stage III) can be taken as the AE sign of the boundary of the transition from stage III to stage IV of PEO. However, Fig. 1 shows that the amplitude "marks" and the PEO flow estimates have a time ambiguity and consequently, give an error during in situ monitoring of the process. In this regard, their use is unacceptable in the case when it is necessary to limit strictly the transition, from one stage to another, to achieve exactly the desired complex of functional properties of the layer.

Fig. 2 shows the results of the division of the studied PEO variants at the stage when using amplitude AE signs shown in Fig. 1.

Cyclic patterns of AE manifestation during PEO

If we synchronize the AE recording with the voltage change cycles, so that the beginning of the AE recording, frame coincides with the beginning of the anode PEO pulse half-cycle, and the length of the AE recording frame is equal to the full exposure cycle duration, then all the AE signals observed in various PEO modes can be divided into

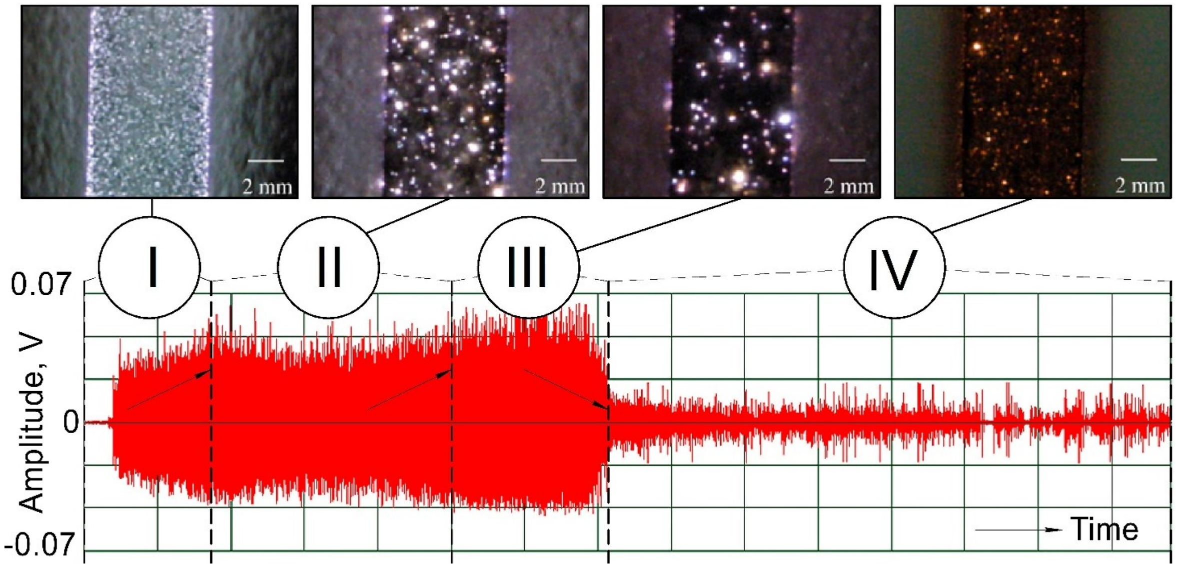

Fig. 1. *AE signs of PEO stages in the experiment and visual signs of microarc discharges on the sample during PEO under similar conditions [14]:*
I – anodic passivation and the beginning of sparking; II – PEO with the pronounced microarc discharges;
III – anode-cathode PEO stage; IV – "soft sparking" stage.
Record sweep duration along the OX (horizontal) axis – 180 minutes

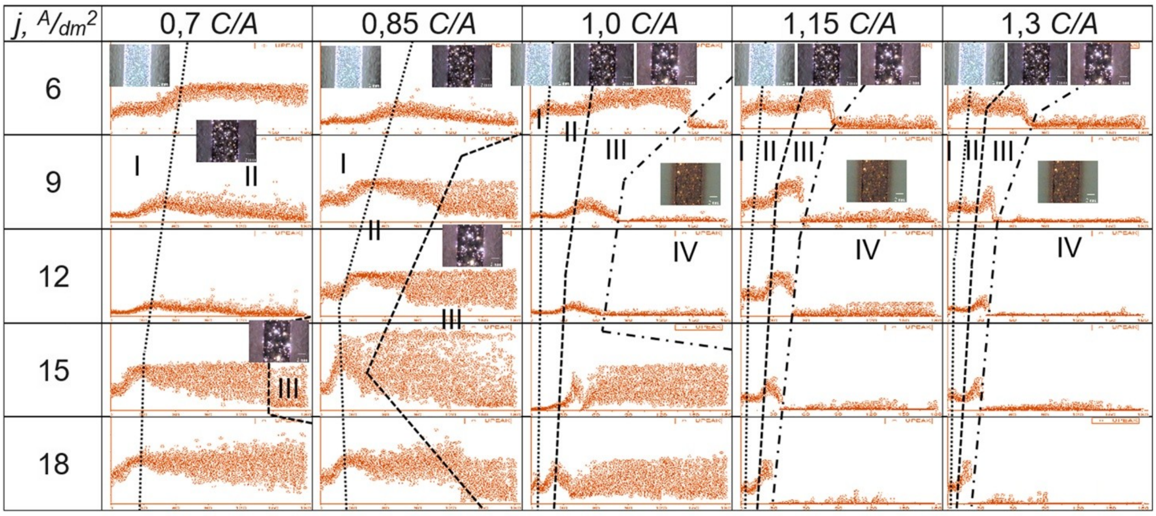

Fig. 2. *General nature of the change in the AE amplitude in 25 PEO modes, differing in current density j, A/dm^2 and the ratios of the positive to negative pulse currents C/A, at the oxidation duration of 180 minutes with a division into stages according to the visual and amplitude AE features shown in Fig. 1.*
The sizes of the axes on the graphs are fixed: along the OX (horizontal) axis – 180 minutes, along the OY (vertical) axis – 0.15 V

anode, anode-cathode, and cathode according to the location within the exposure cycle. At the same time, since the AE recording time is longer than the signal packet duration, all signals become pulsed (discrete) in form (Fig. 3). Signals of a continuous type were not observed within this approach to recording and analyzing the AE. We should note that the AE signals disappear both during the change of the forming pulse polarity and during the pulse itself (Fig. 3).

All peculiarities of the appearance of the signals recorded in the studied PEO modes can be reduced to the forms shown in Fig. 3.

We specially mention that in Fig. 3 b, the oscillations on the forming voltage curve *V(t)* (blue line) are associated with the power unit features and were not observed in the experiment, which is associated with the power unit design different from that used in [15].

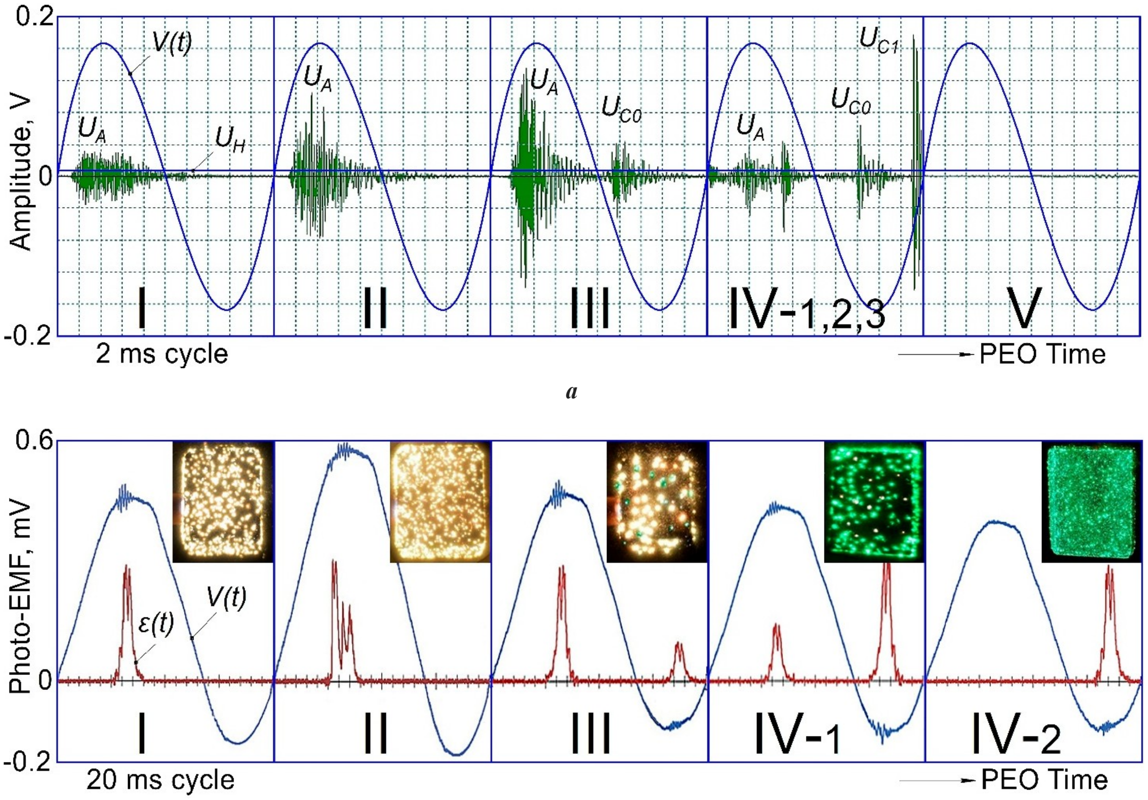

a

b

Fig. 3. *The main forms of AE signals observed at I–V PEO stages (**a**) and the comparison with the data [15] on recording photo-EMF ε(t) with video frames of PEO stages under similar conditions (**b**).*
I–V – PEO mode stages discovered by AE features;
U_A *and* U_{Ci} *– the AE signal amplitude in the anode and cathode half cycles;*
U_N *– noise RMS value;*
U_H *or the black line – RMS value of AE signals at the beginning of PEO;*
V(t) or the blue line – the voltage change curve showing the anode and cathode parts of the exposure cycle.
U_A*,* U_{Ci}*,* U_H *and* U_N *are measured in V or dB of reference 1 mkV in accordance with Russian National Standard GOST 55045-2022. In the latter case, the same magnitudes are marked as* L_{U_A}, $L_{U_{C_i}}$, L_{U_H} *and* L_{U_N}

At stage I of PEO, with visual signs of anodization, and the anode sparking onset (Fig. 1 and 2), in all the studied modes, the AE signals are recorded only in the anodic half-cycle (U_A) (Fig. 3 a). The AE signals are a burst of overlapping pulse signals, with approximately equal amplitude, dying out as the forming pulse amplitude voltage decreases (Fig. 3 a, I). The duration of the burst of AE signals of the PEO stage I, takes about 60 % of the half-cycle duration, and its beginning is shifted from the cycle beginning. The shift of the beginning, and the end of the AE signal burst from the boundaries of the anodic half-cycle, indicates the presence of the minimum voltage necessary to start the oxidation process. The gradual increase, and decrease in the amplitude at the beginning, and the end of the AE signal burst indicates a gradual increase/decrease in the scale of processes or its waviness, i.e., when several MAD "waves", or cascades, occur within one half-cycle.

AE signals of this type are summarized in Table 1 and, parametrically, in the amplitude-time domain for stage I, satisfy the condition (1) in this table. AE signs of the PEO stage I (depending on the mode) are observed up to oxide layer thicknesses of 0.4–14.0 μm, and then the process passes to stage II.

At stage II of PEO with clear visual signs of the occurrence of MADs distinguishing by greater brightness and intensity of movement along the anode compared to stage I, AE signals are also recorded only in the anodic half-cycle (U_A) (Fig. 3 a, II). In appearance, they are often close to the form of the PEO stage I signals, but have pronounced high-amplitude pulses (Fig. 3 a, II). In terms of the AE burst duration, the signals at the PEO stage II take from 60 to 100 % of the anodic half-cycle (half-period) duration, and their beginning is also shifted from the cycle beginning. In this case, high-amplitude AE pulses (emissions) are recorded in different parts of the AE signal burst. Parametrically, in the amplitude-time domain, the AE signals of the PEO stage II satisfy the condition (2) in Table 1.

At the PEO stage III (Fig. 3 a, III), the AE has detectable bursts of signals in the anode (U_A) and cathode (U_{C0}) half-periods of the exposure cycle, i.e., igniting MADs are recorded with the help of the AE in both half-periods. The main AE sign of this stage is that the total energy (power) of the signals in the anode half-cycle is higher than in the cathode one (Fig. 3 a, III), therefore, parametrically, in the amplitude-time domain, the AE signals of this type satisfy the condition (3) in Table 1. As well as in the anode

Table 1. *PEO stages and parametric conditions of AE signals in them*

PEO stage	AE type	Parametric conditions for the PEO stages identification in the AE amplitude-time area*	
I	I	$L_{U_H} > L_{U_N} + 3dB;\quad L_{U_A} < L_{U_H} + 6dB;\quad L_{U_{C0}}$ and $L_{U_{C1}} \le L_{U_N} + 3dB$	(1)
II	II	$L_{U_H} > L_{U_N} + 3dB;\quad L_{U_A} > L_{U_H} + 6dB;\quad L_{U_{C0}}$ and $L_{U_{C1}} \le L_{U_N} + 3dB$	(2)
III	III	$L_{U_A} > L_{U_N} + 3dB;\quad L_{U_{C0}} > L_{U_N} + 3dB;\quad L_{U_{C0}} < L_{U_A};\quad L_{U_{C1}} \le L_{U_N} + 3dB$	(3)
IV	IV-1	$L_{U_A} > L_{U_N} + 3dB;\quad L_{U_{C0}} > L_{U_N} + 3dB;\quad L_{U_{C0}} \ge L_{U_A};\quad L_{U_{C1}} \le L_{U_N} + 3dB$	(4)
	IV-2	$L_{U_A} \le L_{U_N} + 3dB;\quad L_{U_{C0}} > L_{U_N} + 3dB;\quad L_{U_{C1}} \le L_{U_N} + 3dB$	(5)
	IV-3	$L_{U_A} \le L_{U_N} + 3dB;\quad L_{U_{C0}} > L_{U_N} + 3dB$ or $L_{U_{C0}} \le L_{U_N} + 3dB;\quad L_{U_{C1}} > L_{U_N} + 3dB$	(6)
V	V	$L_{U_A} = L_{U_{C0}} = L_{U_{C1}} \le L_{U_N} + 3dB$	(7)

Note. L_{U_A}, $L_{U_{C0}}$ *and* $L_{U_{C1}}$, L_{U_H} *and* L_{U_N} *– the levels of* U_A, U_{C0} *and* U_{C1}, U_H *and* U_N *signals (Fig. 3), measured in dB relative to 1 mkV.*

part, in the cathode half-cycle, the AE signals (U_{C0}) do not have cyclic repeatability in time, and can occur in any part of the cathode half-cycle (pulse U_{C0} in Fig. 3). This behavior can be explained by the necessity of achieving a specified current in the cathode half-cycle, which cannot be ensured only by the process of electron flow, through the micropore channels into the sample. As a consequence, when a certain oxide layer thickness (about 20–50 µm) is reached, within the cathode half-cycle, the amplitude voltages reach 200–250 V, which is sufficient for the barrier layer breakdown, and leads to the MAD ignition with a concomitant sharp increase in the current [32]. AE signs of the PEO stage III, depending on the PEO mode in the experiment, begin to appear at coating thicknesses of 2.7–51.5 µm, which significantly refines the ignition moment of cathode MADs during aluminum alloy PEO relative to the data of [32].

The main difference of the PEO stage IV ("soft sparking" [14; 22]) from the previous ones is that the AE has the energy (power) of signals in the cathode half-cycle higher than in the anode one (Fig. 3 a, IV). Considering this general condition of type IV signals, the following subtypes were identified here: IV-1 – AE is recorded in the anode and cathode half-cycles and satisfies the condition (4) (Table 1); IV-2 – AE occurs only in the cathode half-cycle, i.e., the condition (5) is fulfilled (Table 1); IV-3 – type IV-2 AE signals are recorded, in which, except the U_{C0} cathode signals with the above described features, a U_{C1} signal is observed at the PEO stages III and IV (Fig. 3 a, IV). The physical nature of the U_{C1} signals is not yet fully understood, and requires additional research, but in time, they are always recorded at the end of the cathode half-cycle. Parametrically, in the amplitude-time domain, the type IV-3 AE signals satisfy the condition (6) (Table 1).

It is known [4; 32] that MADs in the cathode half-cycle occur at a coating thickness of more than 40–50 µm, which complies in the time of appearance of the stage IV AE signals, with our measurements of the coating thickness [29; 34], but only in the 0.7 C/A and 0.85 C/A modes at current densities of 9÷18 A/dm^2. In other modes (C/A=1.0; 1.15 and 1.3), where there is stage IV of PEO, the AE signals of this type begin to be recorded at coating thicknesses from 8.8÷36.9 µm, i.e., the stage of "soft sparking" begins to occur within them much earlier.

The PEO stage V was identified for the first time: it lacks acoustic signals distinguishing from background noise in the anode and cathode half-cycles (Fig. 3 a, V), so the condition for identifying this AE type takes the form of an expression (7) (Table 1). The PEO stage V was observed, as a rule, only in the modes with the highest current densities (12–18 A/dm^2) at C/A 1.15, and 1.30 and after observing the signs of stages I–IV, i.e., it falls on the end of the PEO process. Measurements showed that in the time interval of stage V, the layer thickness continues to increase at a low rate, and its properties change [34; 35], but visually at this stage, the MADs and their glowing on the sample are practically not recorded, and the AE signal, as noted above, does not exceed the noise one. Taken together, this does not allow speaking about full extinction of the PEO process.

Table 1 shows that under all conditions (1)–(7), the AE fold change is normalized relative to the levels L_{U_H} and L_{U_N}, which cannot be specified in absolute values. The latter occurs, because these magnitudes depend on the sensitivity of the AE preformation used; the type and amount of contact medium; the place and accuracy of the AE transducer installation, and other factors affecting the transformation and attenuation of AE waves and ambient noise. In this regard, the values of L_{U_H} and L_{U_N} should be determined before PEO in a particular mode and taking into account the features of the AE equipment and PEO plant.

AE criterion for identifying the PEO process stage

One can conclude that, based on the identified patterns of AE manifestation during the pulse exposure period, the key features of dividing the forms of the AE cyclic manifestation into types are the time position of the signals (in the cathode and/or anode part), and the power (energy) correlation between them. Therefore, their tracking will allow identifying and classifying the stage of the PEO process implementation. For this purpose, the authors proposed a new "AE median" parameter-criterion – t_{AEm} (Fig. 4). AE median is a time mark in the exposure cycle, which divides the area under the curve, describing the nature of the AE measurement for the exposure cycle (S) into two equal parts ($S=S_1+S_2$, $S_1=S_2$, Fig. 4).

In this work, the *RMS(t)* curves were obtained from the AE recording frames (Fig. 1) using a sliding window equal to 10 counts (5 µs) with a shift step of 1 count.

Fig. 5 shows the results of dividing the AE recorded when accompanying the studied PEO modes, into the described stages using the above-defined signs of changing the AE shape and conditions (1)–(7) with the display of the proposed t_{AEm} parameter in the form of pictograms.

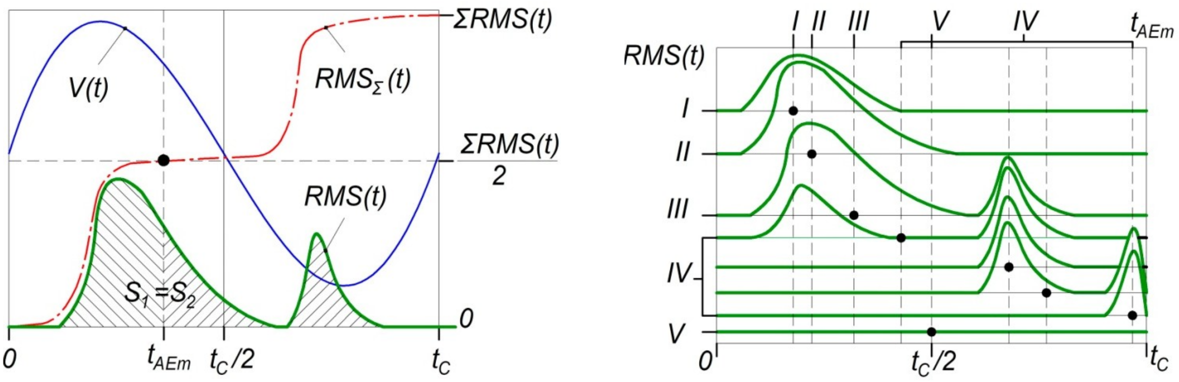

a *b*

***Fig. 4.** Explanatory diagrams for the method calculating of the t_{AEm} parameter-criterion (**a**) and the directions of its change when registering AE I–V waveforms indicated in Fig. 3 a (**b**)*

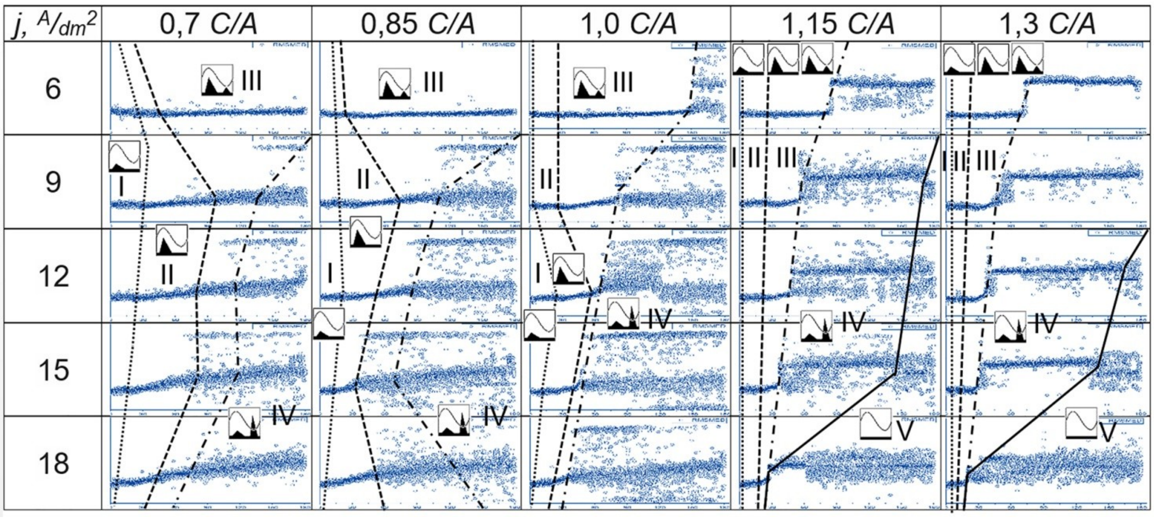

***Fig. 5.** General nature of the change in the AE median in 25 PEO modes, differing in current density j, A/dm^2 the ratios of the positive to negative pulse currents C/A, at the oxidation duration of 180 minutes, divided into stages according to the conditions (1)–(7).*
The sizes of the axes on the graphs are fixed: along the OX axis – 180 minutes, along the OY axis – 4000 readings (eq. 2 ms).
The AE signal type observed at each stage is indicated by a pictogram corresponding to the type of signal in Fig. 4 b

DISCUSSION

The analysis of Fig. 2 and 5 shows that the PEO mode division into stages according to visual signs, and AE signal amplitude (Fig. 1 and 2) allows distinguishing stages I and II, but has a high inaccuracy at stages III and IV, and does not allow identifying stage V. The proposed "AE median" parameter t_{AEm} (Fig. 4 and 5), on the contrary, has a relatively low "sensitivity" to the PEO stages I and II, but allows identifying the presence of the cathode MADs in the AE record, which makes it possible to clearly identify the process stages III–V and detail stage IV into subtypes. Conditions (1)–(7) are universal, but their use requires preliminary studies and monitoring of several of the abovementioned amplitude parameters within their time marks of manifestation in each exposure cycle, which is not a trivial task.

Therefore, the calculation of the amplitude, and AE median for exposure cycles together allows describing the main features of all stages with just two numbers, and the identification of PEO stages in their two-parameter space seems to be the most promising for application towards PEO process monitoring. Moreover, since the errors of the proposed parameters, when detecting the PEO stages are of an antibate nature, their combined use should increase the probability of detecting the PEO stages. However, if we are talking only about the identification and monitoring of the PEO stages III–V, then the "AE median" parameter is self-sufficient.

Indeed, due to the developed parameter, it was possible to establish that the PEO modes, with the highest current density of 18 A/dm^2 at a current ratio C/A of 1.15 and 1.30 pass from stage III immediately to stage V (Fig. 5), which is accompanied by some increase in the thickness (Fig. 6 a), a decrease in the hardness (Fig. 6 b), an increase in the friction ratio in a pair, and a decrease in the wear resistance of oxide layers (Fig. 6 d). The PEO transition to stage V and an increase in its duration (Fig. 5) leads to a sharp increase in the friction ratio for the "oxide layer–steel ball" pair (Fig. 6 c), which is not entirely clear at this stage and requires additional research. One can also note, that as the duration of the PEO stage IV increases (Fig. 5), a decrease in the wear intensity of the friction pair is observed (Fig. 6 d), while the appearance of stage V, and an increase in its duration leads to an increase in the wear intensity of the pair in 1.5–2.5 times.

The joint analysis of Fig. 5 and 6 shows that the appearance of the cathodic MADs, close in power to anodic microarcs or exceeding them, and the PEO transition to the process stage IV lead to a slight decrease in the thickness of the formed oxide layers (Fig. 6 a), but at the same time, their average microhardness reaches the highest values

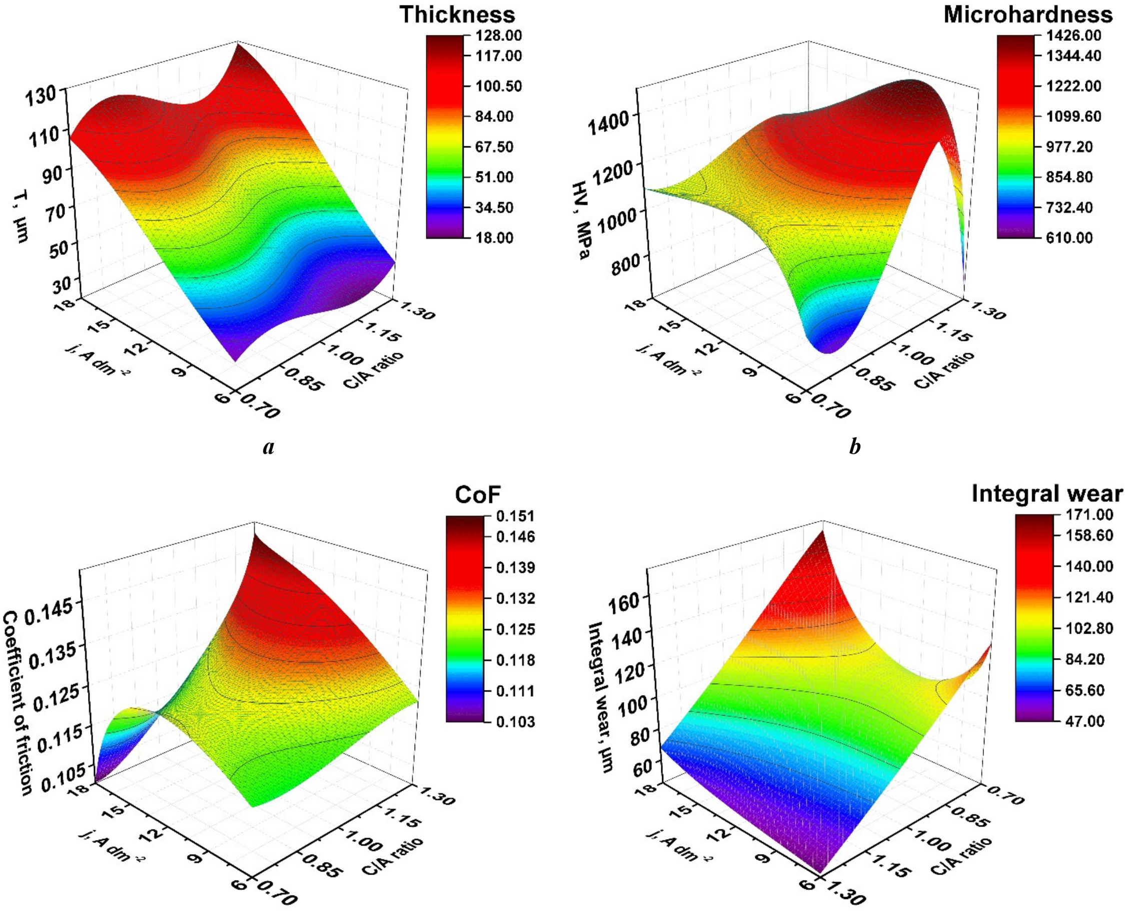

a *b*

c *d*

Fig. 6. *The dependences of the average thickness T, µm (**a**), microhardness HV 0.1, MPa (**b**), friction coefficient (**c**), and linear reduced wear (**d**) of the "oxide layer – steel ball" friction pair on the current parameters of the PEO mode*

(Fig. 6 b). Therefore, the introduced "AE median" parameter, which has an increased sensitivity to the PEO final stages, allows tracking their duration. Based on this, the transition to the oxidation process AE control is possible, by confirming reaching the specified stages in each PEO mode, and monitoring the compliance of the exposure time for each of them, which technologically should provide the required complex of coating properties. The latter is the subject for further experimental studies.

It should be noted that since the obtained data on the AE signal manifestation in the anode, and cathode half-cycles (half-periods) correlate with the light flashes during PEO [15] (Fig. 3 a and 3 b), the proposed parameter for dividing the PEO modes into stages will also be applicable when processing the results of observations during photo-video recording, and photo-EMF registration, where instead of changing the AE, for example, the glow intensity median in the anode and cathode exposure cycles can be monitored.

CONCLUSIONS

1. Possible forms of AE change within an exposure cycle during PEO of the AMg6 Al–Mg alloy in a bipolar pulse mode are established, which are reduced to five main types and three subtypes, as well as the boundaries (time points) of their change in a wide range of industrial PEO modes are identified. In this case, three subtypes of the AE change forms are of particular interest, since they refer to the "soft sparking" mode.

2. For the first time, a previously unknown stage V of the PEO process was identified, where a vapour-gas phase microarc breakdown to the metal substrate and the AE generated by it are practically missing.

3. The study shows that the approach to identifying the PEO stages using the standard "AE amplitude" parameter has a larger error, since it does not take into account the shape of the signals, and the half-period of their recording. The proposed new "acoustic-emission median" (AE median) parameter-criterion allows taking into account the indicated features, when dividing the PEO modes into stages according to AE, which makes it possible to specify the cyclic features of the AE manifestation determined in the work. It is experimentally shown, that the proposed parameter is efficient, has good accuracy and sensitivity to the subtypes of the AE signals, especially those recorded within the "soft sparking" mode.

REFERENCES

1. Mardare C.C., Hassel A.W. Review on the Versatility of Tungsten Oxide Coatings. *Physica Status Solidi A*, 2019, vol. 216, no. 12, article number 1900047. DOI: 10.1002/pssa.201900047.
2. Simchen F., Sieber M., Kopp A., Lampke T. Introduction to Plasma Electrolytic Oxidation–An Overview of the Process and Applications. *Coatings*, 2020, vol. 10, no. 7, article number 628. DOI: 10.3390/coatings10070628.
3. Martin J., Melhem A., Shchedrina I., Duchanoy T., Nominé A., Henrion G., Czerwiec T., Belmonte T. Effects of electrical parameters on plasma electrolytic oxidation of aluminium. *Surface and Coatings Technology*, 2013, vol. 221, pp. 70–76. DOI: 10.1016/j.surfcoat.2013.01.029.
4. Rogov A.B., Yerokhin A., Matthews A. The role of cathodic current in plasma electrolytic oxidation of aluminum: Phenomenological concepts of the "soft sparking" mode. *Langmuir*, 2017, vol. 33, no. 41, pp. 11059–11069. DOI: 10.1021/acs.langmuir.7b02284.
5. Rogov A.B., Matthews A., Yerokhin A. Relaxation Kinetics of Plasma Electrolytic Oxidation Coated Al Electrode: Insight into the Role of Negative Current. *The Journal of Physical Chemistry C*, 2020, vol. 124, no. 43, pp. 23784–23797. DOI: 10.1021/acs.jpcc.0c07714.
6. Rahmati M., Raeissi K., Toroghinejad M.R., Hakimizad A., Santamaria M. Effect of Pulse Current Mode on Microstructure, Composition and Corrosion Performance of the Coatings Produced by Plasma Electrolytic Oxidation on AZ31 Mg Alloy. *Coatings*, 2019, vol. 9, no. 10, article number 688. DOI: 10.3390/coatings9100688.
7. Butyagin P.I., Khokhryakov E.V., Mamaev A.I. Effect of Electrolyte Composition on the Wear Resistance of MAO Coatings. *Tekhnologiya metallov*, 2005, no. 1, pp. 36–40. EDN: KVFCPL.
8. Kuchmin I.B., Nechaev G.G., Soloveva N.D. Changes in the character of physical and chemical properties of two-silicate alkaline electrolyte for microarc oxidation over the production process. *Vestnik Saratovskogo gosudarstvennogo tekhnicheskogo universiteta*, 2013, vol. 4, no. 1, pp. 57–62. EDN: SEFXLX.
9. Hussein R.O., Northwood D.O., Nie X. Processing Microstructure Relationships in the Plasma Electrolytic Oxidation (PEO) Coating of a Magnesium Alloy. *Materials Sciences and Applications*, 2014, vol. 5, no. 3, pp. 124–139. DOI: 10.4236/msa.2014.53017.
10. Yerokhin A.L., Nie X., Leyland A., Matthews A., Dowey S.J. Plasma electrolysis for surface engineering. *Surface and Coatings Technology*, 1999, vol. 122, no. 2-3, pp. 73–93. DOI: 10.1016/S0257-8972(99)00441-7.
11. Suminov I.V., Belkin P.N., Epelfeld A.V., Lyudin V.B., Krit B.L., Borisov A.M. *Plazmenno-elektroliticheskoe modifitsirovanie poverkhnosti metallov i splavov* [Plasma-electrolytic surface modification of metals and alloys]. Moscow, Tekhnosfera Publ., 2011. Vol. 2, 512 p.
12. Golubkov P.E., Pecherskaya E.A., Kozlov G.V., Zinchenko T.O., Melnikov O.A., Shepeleva J.V. Application of impedance spectroscopy for research of the micro-arc oxidation process. *Proceedings – 2020 7th International Congress on Energy Fluxes and Radiation Effects (EFRE 2020)*. Tomsk, Publishing House of IAO SB RAS, 2020, pp. 773–777.
13. Arrabal R., Matykina E., Hashimoto T., Skeldon P., Thompson G.E. Characterization of AC PEO coatings on magnesium alloys. *Surface and Coatings Technology*, 2009, vol. 203, no. 16, pp. 2207–2220. DOI: 10.1016/j.surfcoat.2009.02.011.
14. Clyne T.W., Troughton S.Ch. A review of recent work on discharge characteristics during plasma electrolytic oxidation of various metals. *International Materials Reviews*, 2019, vol. 64, no. 3, pp. 127–162. DOI: 10.1080/09506608.2018.1466492.
15. Rakoch A.G., Gladkova A.A., Linn Z., Strekalina D.M. The evidence of cathodic micro-discharges during plasma electrolytic oxidation of light metallic alloys and micro-discharge intensity depending on pH of the electrolyte. *Surface and Coatings Technology*, 2015,

vol. 269, pp. 138–144. DOI: 10.1016/j.surfcoat.2015.02.026.

16. Wang L., Chen L., Yan Z., Fu W. Optical emission spectroscopy studies of discharge mechanism and plasma characteristics during plasma electrolytic oxidation of magnesium in different electrolytes. *Surface and Coatings Technology*, 2010, vol. 205, no. 6, pp. 1651–1658. DOI: 10.1016/j.surfcoat.2010.10.022.
17. Jin F.-Y., Wang K., Zhu M., Shen L.-R., Li J., Hong H.-H., Chu P.K. Infrared reflection by alumina films produced on aluminum alloy by plasma electrolytic oxidation. *Materials Chemistry and Physics*, 2009, vol. 114, no. 1, pp. 398–401. DOI: 10.1016/j.matchemphys.2008.09.060.
18. Golubkov P.E. Analysis of the applicability of thickness measurement methods dielectric layers in controlled synthesis protective coatings by micro-arc method oxygenating. *Izmerenie. Monitoring. Upravlenie. Kontrol*, 2020, no. 1, pp. 81–92. DOI: 10.21685/2307-5538-2020-1-11.
19. Rastegaeva I.I., Rastegaev I.A., Vikarchuk A.A., Merson D.L., Seleznev M.N., Vinogradov A.Yu. Acouctic emission-based feedback system for optimization of liquid processing in rotor devices. *Pribory i sistemy. Upravlenie, Kontrol, Diagnostika*, 2012, no. 5, pp. 25–31. EDN: SMJGQD.
20. Darband G.B., Aliofkhazraei M., Hamghalam P., Valizade N. Plasma electrolytic oxidation of magnesium and its alloys: Mechanism, properties and applications. *Journal of Magnesium and Alloys*, 2017, vol. 5, no. 1, pp. 74–132. DOI: 10.1016/j.jma.2017.02.004.
21. Tjiang F., Ye L., Huang Y.-J., Chou C.-C., Tsai D.-S. Effect of processing parameters on soft regime behavior of plasma electrolytic oxidation of magnesium. *Ceramics International*, 2017, vol. 43, no. 1, pp. S567–S572. DOI: 10.1016/j.ceramint.2017.05.179.
22. Tsai D.-S., Chou C.-C. Review of the Soft Sparking Issues in Plasma Electrolytic Oxidation. *Metals*, 2018, vol. 8, no. 2, article number 105. DOI: 10.3390/met8020105.
23. Bespalova Zh.I., Panenko I.N., Dubovskov V.V., Kozachenko P.N., Kudryavtsev Yu.D. Investigation of the formation of optical black oxide-ceramic coatings on the surface of aluminum alloy 1160. *Izvestiya vysshikh uchebnykh zavedeniy. Severo-Kavkazskiy region. Seriya: Estestvennye nauki*, 2012, no. 5, pp. 63–66. EDN: PFATGJ.
24. Mukaeva V.R., Gorbatkov M.V., Farrakhov R.G., Parfenov E.V. A study of the acoustic characteristics of plasma electrolytic oxidation of aluminum. *Elektrotekhnicheskie i informatsionnye kompleksy i sistemy*, 2018, vol. 14, no. 3, pp. 60–65. EDN: YSAZNZ.
25. Bao F., Bashkov O.V., Chzhan D., Lyuy L., Bashkova T.I. The study of the influence of micro-arc oxidation modes on the morphology and parameters of an oxide coating on the D16AT aluminum alloy. *Frontier Materials & Technologies*, 2023, no. 1, pp. 7–21. DOI: 10.18323/2782-4039-2023-1-7-21.
26. Boinet M., Verdier S., Maximovitch S., Dalard F. Plasma electrolytic oxidation of AM60 magnesium alloy: Monitoring by acoustic emission technique. Electrochemical properties of coatings. *Surface and Coatings Technology*, 2005, vol. 199, no. 2-3, pp. 141–149. DOI: 10.1016/j.surfcoat.2004.10.145.
27. Boinet M., Verdier S., Maximovitch S., Dalard F. Application of acoustic emission technique for in situ study of plasma anodizing. *NDT & E International*, 2004, vol. 37, no. 3, pp. 213–219. DOI: 10.1016/j.ndteint.2003.09.011.
28. Rastegaev I.A., Polunin A.V. Regularities and features of acoustic emission under plasma electrolytic oxidation of wrought Al-Mg alloy. *Journal of Physics: Conference Series*, 2021, vol. 2144, article number 012020. DOI: 10.1088/1742-6596/2144/1/012020.
29. Kaseem M., Fatimah S., Nashrah N., Ko Y.G. Recent progress in surface modification of metals coated by plasma electrolytic oxidation: Principle, structure, and performance. *Progress in Materials Science*, 2021, vol. 117, article number 100735. DOI: 10.1016/j.pmatsci.2020.100735.
30. Cheng Y.-L., Xue Z., Wang Q., Wu X.-Q., Matykina E., Skeldon P., Thompson G.E. New findings on properties of plasma electrolytic oxidation coatings from study of an Al–Cu–Li alloy. *Electrochimica Acta*, 2013, vol. 107, pp. 358–378. DOI: 10.1016/j.electacta.2013.06.022.
31. Troughton S.C., Clyne T.W. Cathodic discharges during high frequency plasma electrolytic oxidation. *Surface and Coatings Technology*, 2018, vol. 352, pp. 591–599. DOI: 10.1016/j.surfcoat.2018.08.049.
32. Polunin A.V., Denisova A.G., Cheretaeva A.O., Shafeev M.R., Borgardt E.D., Rastegaev I.A., Katsman A.V. The effect of process current parameters on the properties of oxide layers under plasma electrolytic oxidation of AMg6 alloy. *Journal of Physics: Conference Series*, 2021, vol. 2144, article number 012018. DOI: 10.1088/1742-6596/2144/1/012018.
33. Polunin A.V., Cheretaeva A.O., Shafeev M.R., Denisova A.G., Borgardt E.D., Rastegaev I.A., Katsman A.V., Krishtal M.M. Mechanical and anticorrosive properties of oxide layers formed by PEO on wrought 1560 Al-Mg alloy: The effect of electric current parameters. *AIP Conference Proceedings*, 2022, vol. 2533, article number 020029. DOI: 10.1063/5.0098844.

doi: 10.18323/2782-4039-2023-2-64-7

Microstructure and properties of the Zn–1%Li–2%Mg alloy subjected to severe plastic deformation

Vil D. Sitdikov*[1,2,4], Doctor of Sciences (Physics and Mathematics), expert
Elvira D. Khafizova[2,3,5], PhD (Engineering), assistant professor of Chair of Materials Science and Physics of Metals,
senior researcher at the Research Laboratory "Metals and Alloys under Extreme Impacts"
Milena V. Polenok[2,3,6], graduate student,
laboratory assistant of the Research Laboratory "Metals and Alloys under Extreme Impacts"
[1]*LLC RN-BashNIPIneft, Ufa (Russia)*
[2]*Institute of Physics of Molecules and Crystals of Ufa Research Center of the RAS, Ufa (Russia)*
[3]*Ufa University of Science and Technologies, Ufa (Russia)*

***E-mail: SitdikovVD@bnipi.rosneft.ru**

[4]ORCID: https://orcid.org/0000-0002-9948-1099
[5]ORCID: https://orcid.org/0000-0002-4618-412X
[6]ORCID: https://orcid.org/0000-0001-9774-1689

Received 29.05.2023 *Accepted 13.06.2023*

Abstract: In this paper, the authors consider the mechanisms of formation of high-strength states in the Zn–1%Li–2%Mg alloy as a result of its processing by the high pressure torsion (HPT) method. For the first time, the study showed that using HPT treatment, as a result of varying the degree of deformation at room temperature, it is possible to increase the ultimate strength of a zinc alloy from 155 to 383 MPa (with an increase in the yield stress from 149 to 306 MPa) without losing its ductility. To explain the reasons for the increase in the zinc alloy mechanical properties, its microstructure was analyzed by scanning electron microscopy (SEM), X-ray phase analysis (XPA), X-ray diffraction analysis (XRD), and small-angle X-ray scattering (SAXS). Using XPA, the authors established for the first time that $Zn_{(eutectic)}+\beta\text{-}LiZn_{4(eutectic)}\rightarrow\sim LiZn_3+Zn_{(phase)}+Zn_{(precipitation)}$ and $MgZn_2\rightarrow Mg_2Zn_{11}$ phase transformations occur in the zinc alloy during HPT treatment. SEM analysis showed that at the initial stages of HPT treatment, cylindrical Zn particles with a diameter of 330 nm and a length of up to 950 nm precipitate in β-$LiZn_3$ phase. At the same time, the SAXS method showed that needle-like $LiZn_4$ particles with a diameter of 9 nm and a length of 28 nm precipitate in the Zn phase. The study established that, only spherical Zn and $LiZn_4$ particles precipitate at high degrees of HPT treatment. Precision analysis of the zinc alloy microstructure showed that HPT treatment leads to grain refinement, an increase in the magnitude of crystal lattice microdistortion, a growth of the density of dislocations, which are predominantly of the edge type. As a result of the analysis of hardening mechanisms, the authors concluded that the increase in the zinc alloy strength characteristics mainly occurs due to grain-boundary, dislocation, and dispersion hardening.

Keywords: Zn–1%Li–2%Mg alloy; phase transformations in zinc alloy; severe plastic deformation; X-ray scattering methods; strength and plasticity; deformation mechanisms.

Acknowledgements: The research was supported by the grant of the Russian Science Foundation No. 23-29-00667, https://rscf.ru/project/23-29-00667.

The paper was written on the reports of the participants of the XI International School of Physical Materials Science (SPM-2023), Togliatti, September 11–15, 2023.

For citation: Sitdikov V.D., Khafizova E.D., Polenok M.V. Microstructure and properties of the Zn–1%Li–2%Mg alloy subjected to severe plastic deformation. *Frontier Materials & Technologies*, 2023, no. 2. DOI: 10.18323/2782-4039-2023-2-64-7.

INTRODUCTION

Currently, zinc and its alloys demonstrate a high potential for industrial applications in medicine, due to their high biocompatibility and corrosion resistance [1–3]. As is known [4], pure Zn is a quite brittle material with low strength properties (yield strength is ~29 MPa, ultimate strength is ~34 MPa, ductility is ~1 %). Therefore, it needs significant strengthening to meet the clinical requirements for biodegradable metal stents (yield strength is >200 MPa, tensile strength is >300 MPa, ductility is >15–18 %) [5]. In order to improve the physical and mechanical properties of zinc and expand its application field in medicine, it is necessary to alloy it with certain biosoluble admixtures (lithium, magnesium, calcium, etc.), and carry out thermomechanical treatment according to various schemes and modes.

Among various classes of zinc alloys, the Zn–Li–Mg system is of particular interest, since, on the one hand, it is capable of aging, and, on the other hand, it has corrosion resistance and biocompatibility values close to pure zinc [3; 6; 7]. Under traditional modes of thermomechanical treatment (rolling + annealing), hardening in the Zn–Li system alloys occurs due to the precipitation of $LiZn_4$ particles in the Zn phase, and Zn particles in the primary β-$LiZn_4$ phase of predominantly acicular morphology, which, when intertwined, form a spatial grid [3; 6; 7]. This type of two-phase precipitation of particles during warm rolling allows increasing the ultimate strength of this alloy from 230 to 360 MPa [6]. In the recent work [8], the mechanical properties of Zn–0.8%Li, Zn–0.8%Li–0.2%Mg, and Zn–0.8%Li–0.2%Ag alloys were studied. The study showed that a Zn–Li–Ag system alloy has high ductility, and a Zn–Li–Mg system alloy has the highest yield strength and tensile strength [8]. At the same time, by increasing the Mg content in the Zn–0.8%Li–0.4%Mg alloy and performing hot extrusion, the authors [1] showed that the alloy achieves a tensile strength of ~647 MPa, which is currently the maximum value.

Despite the relatively high hardness indices of the Zn–Li–Mg system alloys, an active search for new modes and schemes of thermomechanical treatment aimed at further increasing the strength properties of this alloy, is still carried out, since this issue remains very relevant. Recent studies demonstrate that an increase in strength properties in metals and alloys can be achieved by grinding the grain structure using severe plastic deformation (SPD) [9–11]. One should note that the grain structure refinement in zinc alloys has its own characteristics, since in thermally hardened zinc alloys, the aging processes are observed, which leads to the release of atypical hardening particles of the second phases [12]. This creates additional opportunities for improving the strength properties of zinc alloys; however, it requires optimization of technological modes for obtaining ultrafine-grained (UFG) samples, which simultaneously combine high biocompatibility, increased strength, and optimal corrosion rate. At the same time, new hardening mechanisms (segregations and nanoclusters) can also be involved in UFG metallic materials leading to an increase in the mechanical properties of metals and alloys. In this regard, it is important to comprehensively study the microstructure of the formed UFG Zn–Li–Mg alloys using various methods of X-ray phase analysis (XPA), X-ray diffraction analysis (XRD), electron microscopy, and small-angle X-ray scattering (SAXS).

The purpose of the study is to improve the strength characteristics of the Zn–1%Li–2%Mg zinc alloy as a result of SPD, as well as to identify possible hardening mechanisms explaining high-strength states.

METHODS

As an object of research, the biosoluble Zn–1.0 wt. % Li–2.0 wt. % Mg alloy made of high-purity components Zn (99.95 wt. %), Mg (99.95 wt. %), and Li (99.95 wt. %) was selected. To enhance strength characteristics and improve corrosion resistance, this alloy was subjected to high-pressure torsion (HPT) at room temperature with a number of revolutions equal to 0.5, 1, 2, 3, 6, 8 and 10. The pressure applied during HPT was 6 GPa, the rotation speed of the strikers was 1 rpm. Mechanical tensile tests of the alloy were carried out using a special-purpose testing machine for small samples, and the material microhardness was measured by the Vickers method on a Shimadzu HMV-G universal hardness tester with an indenter load of 100 g.

To determine the microstructure parameters using the XRD method, the authors analyzed the diffraction patterns obtained on a Bruker D8 Advance diffractometer (Bragg – Brentano scheme). The diffraction patterns were measured in the continuous shooting mode at a speed of 1.5 °/min within the scattering angle 2θ from 20° to 150° on $\mathrm{Cu}_{\mathrm{K}\alpha}$ radiation generated at a voltage of 40 kV and a current of 40 mA. The lattice constant, the size distribution of coherent scattering domains (CSD), the dislocation density, and the fraction of edge-type dislocations were determined using the PM2K program [13]. The diffraction patterns were analysed by refining such parameters as sample displacement in depth and angular position, lattice constant a, dislocation density ρ, fraction of edge-type dislocations m_{ixp}, effective dislocation radius R_e, shapes and sizes of CSD D.

Qualitative X-ray phase analysis was performed using the PDF-2 diffraction database in the EVAplus program (www.bruker.com). Quantitative X-ray phase analysis with determining the ratio of the identified phases was carried out by the Rietveld method [14] in the TOPAS v. 4.2 program (www.bruker.com). Scattering curves necessary to analysed the size and shape of precipitates were obtained on a Bruker D8 Advance diffractometer with a small-angle attachment in the parallel beam mode. Scattering curves were measured within the range of q vector from 0.0 to 1.5 nm^{-1}. The diameter of the analysed surface was ~4 mm.

The investigated alloy microstructure analysis was carried out by scanning electron microscopy (SEM) on a FEI Thermo Scientific Q250 scanning electron microscope. The main characteristics of the survey: accelerating voltage of electrons is 25 kV, beam diameter is 2 μm, focal length is 10.0 mm, pressure in the chamber is 5×10^{-4} Pa.

RESULTS

Results of measuring the mechanical properties

Table 1 shows the results of tests for measuring the zinc alloy microhardness and mechanical properties. The analysis of the results of tensile tests of samples showed that the alloy in the initial state is characterized by relatively low values of the yield strength, tensile strength and extremely low ductility, typical of the coarse-grained analogs of this alloy [3; 6]. HPT treatment leads to the expected growth of strength characteristics (Table 1). In particular, even at the initial HPT treatment stages (1–2 revolutions), the value of the yield strength increases by ~1.7 times, and the ultimate strength value increases by more than 2 times compared to the initial state. In this case, a sharp increase in ductility is observed. The increase in the alloy microhardness values is also in good agreement with the data of mechanical tests (Table 1).

When increasing the number of HPT revolutions from 3 to 6, a further, although insignificant, increase in the alloy strength characteristics is observed. The results after 10 HPT revolutions are the most interesting (Table 1). In this state, compared with the initial (as-cast) state, the microhardness value increases by more than 5 %, the ultimate strength increases by more than 2 times, and the ultimate strength increases by ~2.6 times.

Results of SEM studies

Fig. 1 shows the SEM images of the microstructure of the alloy in the initial (as-cast) state. The as-cast zinc alloy microstructure is characterized by bright and dark areas (Fig. 1 a–c), and two types of bright areas are distinguished (Fig. 1 a). The first type predominantly consists of an oval shape with an average diameter of 18 μm (Fig. 1 a). In some places, these areas merge into rather large areas. The second type of bright areas has a layered structure of different lengths (Fig. 1 b). The average layer width is 800 nm, and their length varies from one to several tens of microns. The analysis of the area of light regions showed that its surface fraction is ~88 %. As is known [3; 6], on the Li–Zn alloy phase

Table 1. *The values of microhardness and mechanical properties of the Zn–1%Li–2%Mg alloy*

State		HV	σ_T, MPa	σ_B, MPa	*e*, %
Initial		170.0±8.0	149	155	~0,4
HPT	**1 rev.**	183.8±12.8	256	383	42
	2 rev.	176.9±6.8	260	332	41
	3 rev.	176.7±12.0	264	361	44
	6 rev.	180.6±11.3	278	363	48
	8 rev.	179±12.6	301	394	51
	10 rev.	178.9±13.3	330	409	47

Note. HV – Vickers microhardness; σ_T *– yield stress;* σ_B *– ultimate strength; e – percentage of elongation.*

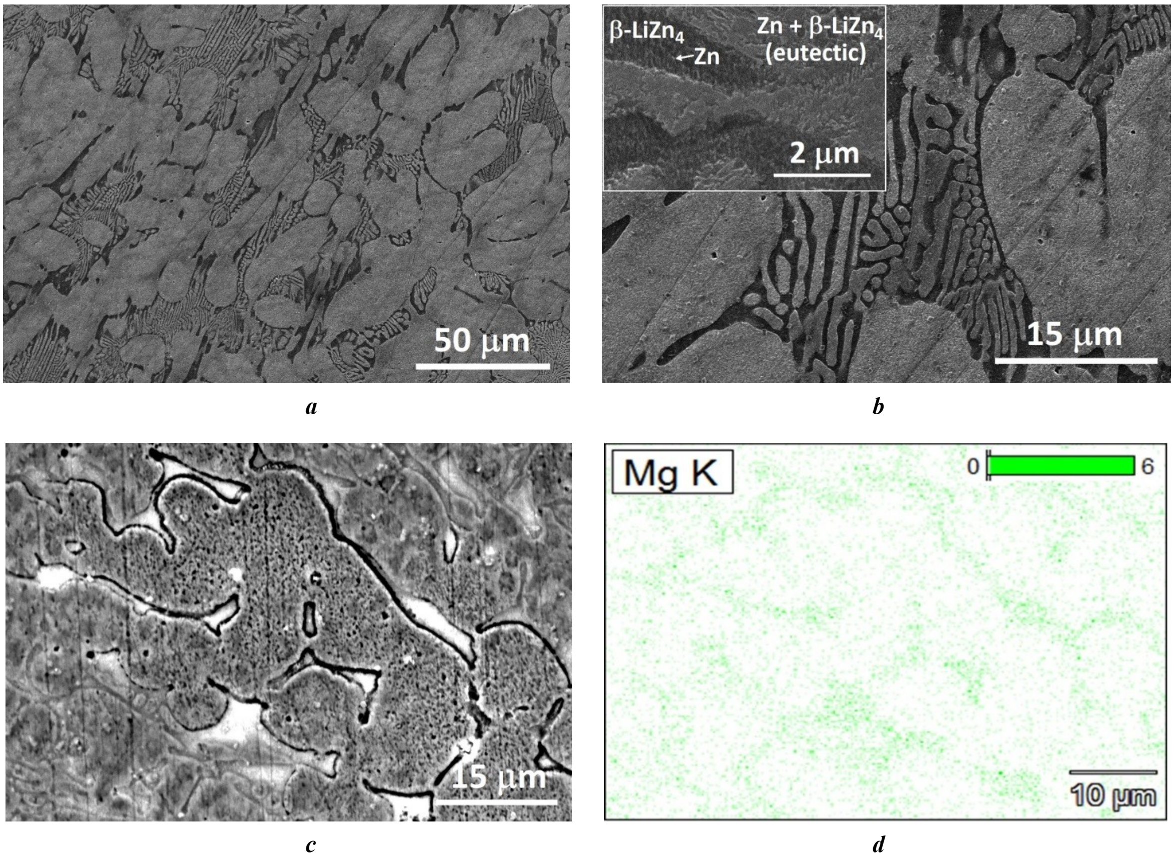

Fig. 1. *SEM images of the zinc alloy microstructure in the post-cast state at various magnifications:*
a *– ×2000;* ***b*** *– ×8000, in the insert ×80000;* ***c*** *– ×6000;* ***d*** *– distribution of Mg atoms in Fig. 1 c*

diagram at a Zn content of about 97 %, one can expect the formation of the primary β-$LiZn_4$ phase, as well as the Zn and β-$LiZn_4$ eutectic phases. According to [6], lithium atoms have a much lower retarding potential, in contrast to zinc atoms. Considering the Li–Zn system phase diagram, it can be affirmed that the light (oval + layered) regions in the SEM images should belong to the Zn+β-$LiZn_4$ eutectic phases. At the same time, dark areas with a surface fraction of ~12 % should belong to the primary β-$LiZn_4$ phase.

Fig. 1 b and the insert show the precision areas of light and dark regions at high magnifications. During microstructure detailed analysis, one can see that there are numerous fine particles of predominantly acicular shape (Fig. 1 b, insert) in the primary β-$LiZn_4$ phase (dark areas). The average particle diameter is ~80 nm, and their length varies within 60–230 nm. According to the literature data [3; 6; 7], in the primary β-$LiZn_4$ phase, when the alloy is cooled, zinc particles usually precipitate (Fig. 1 b, insert). On the other hand, the light areas belonging to the Zn+β-$LiZn_4$ phase have a lamellar structure typical of a eutectic (Fig. 1 b, insert). Since the dark areas are more subjected to etching corrosion processes, they can be identified in SEM images as β-$LiZn_4$ eutectic phases (Fig. 1 b).

Fig. 1 c shows an image atypical for the Zn–Li system alloy with many bright areas located mainly along the boundaries of the Zn+β-$LiZn_4$ eutectic and the primary β-$LiZn_4$ phase. To identify them, the authors carried out the element-by-element mapping, the result of which is shown in Fig. 1 d. A comparative analysis of the images (Fig. 1 c, 1 d) showed that the Mg atoms belonging to the $MgZn_2$ phase, as shown below by the XPA method, are concentrated in the detected bright areas.

Fig. 2 presents SEM images of the alloy after various degrees of HPT treatment. It is evident that during implementing the HPT treatment, even at the early stages of torsion (0.5 revolution), changes in the ratio of dark and bright areas are visible against the initial (as-cast) state (Fig. 2 a). It can be seen that, in the primary β-$LiZn_4$ phase (dark areas), filamentous zinc precipitates grow intensively with the formation of a peculiar network of precipitates (Fig. 2 a, insert). The analysis showed that the diameter of zinc precipitates varies from ~90 to ~785 nm, and their length varies from 110 nm to 10 μm. Moreover, at the boundary of the eutectic Zn+Mg_2Zn_{11} phase (bright areas, according to X-ray diffraction data presented below), a ~2 μm thick zinc phase is formed (Fig. 2 a, insert). The belonging of this layer to the zinc phase follows from the fact that there is no clear transition interface between this phase and zinc precipitates in the primary β-$LiZn_4$ phase. This fact confirms that these structures belong to the same phase.

When increasing the number of HPT rotations (1 revolution), a band (elongated) structure oriented perpendicular to the radius of the sample is formed (Fig. 2 b). Moreover, in the primary β-$LiZn_4$ phase, a certain orientation of zinc precipitates is visible, which sometimes merge (Fig. 2 b, insert). The images show that the thickness of the Zn+Mg_2Zn_{11} phase plates decreases even more.

It was noted that when increasing the number of HPT treatment revolutions, the proportion of dark areas increases, while the proportion of light areas decreases (Fig. 2 c, 2 d). High degrees of HPT treatment are characterised by effective grinding of the Zn+~$LiZn_3$ (~$LiZn_3$ phase is similar to β-$LiZn_4$) phase, as well as of the Zn+Mg_2Zn_{11} and Zn phases (Fig. 2 c, 2 d). In particular, it can be seen that the average grain size of the zinc phase is ~230 nm (Fig. 2 c, insert), which contain darkened areas related to $LiZn_4$ precipitates. In this case, the Zn precipitates themselves in the ~$LiZn_3$ phase precipitate in a spherical shape (Fig. 2 d, insert). The information found by the microscopy method indicates the intense phase transitions and changes that have occurred in certain phases. In particular, by increasing the proportion of dark areas and XPA results, it is possible to identify the $Zn_{(eutectic)}$+β-$LiZn_{4(eutectic)}$→~$LiZn_3$+$Zn_{(phase)}$+ +$Zn_{(precipitate)}$+Mg_2Zn_{11}+β-$LiZn_4$ phase transition.

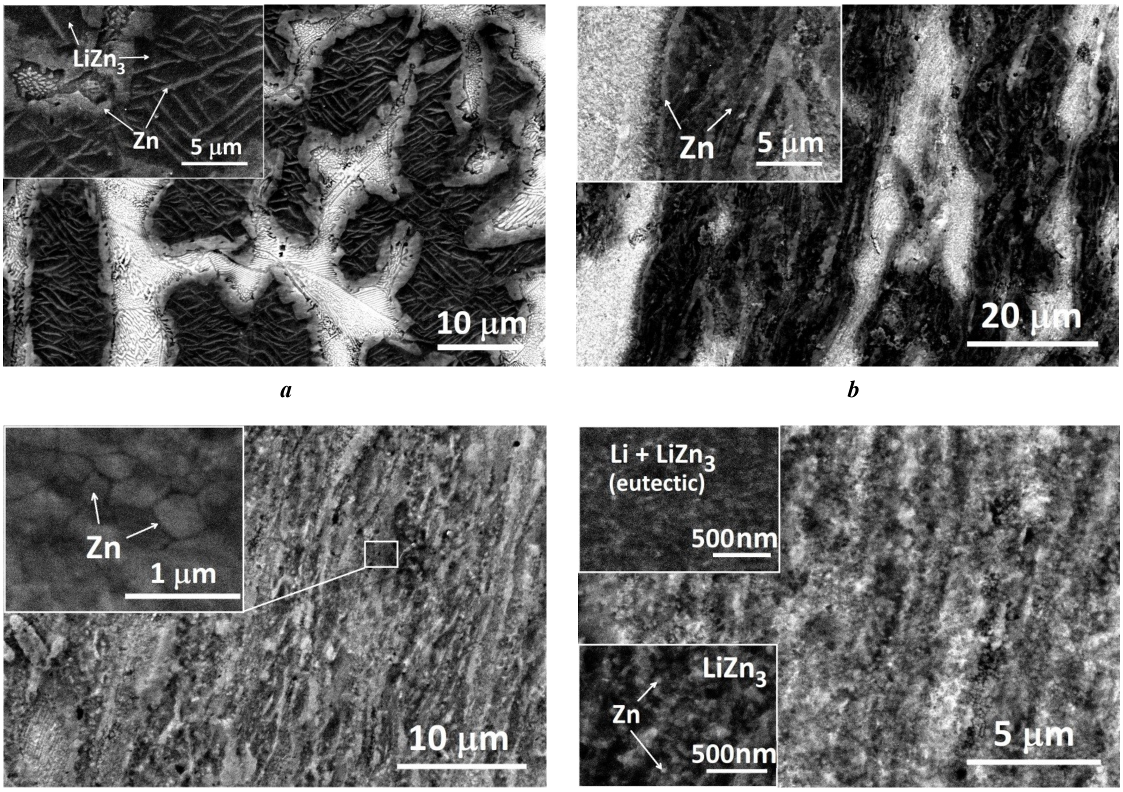

a *b*

c *d*

Fig. 2. *SEM images of the zinc alloy microstructure in the state after HPT treatment:*
a *– 0.5 revolution, in the insert – Zn particles and Zn phase;* ***b*** *– 1 revolution, in the insert – Zn particles;*
c *– 6 revolutions, in the insert – Zn grains;* ***d*** *– 10 revolutions, in the inserts – Zn particles*

Results of studies by XRD analysis

Fig. 3 shows the X-ray spectra of the studied states and an example of the processed section of the zinc alloy diffraction pattern. The analysis of the general view of the diffraction patterns showed that all zinc alloy X-ray spectra are characterised by the same set of intense peaks (Fig. 3 a). At the same time, qualitative XPA showed that the detected reflections belong to the Zn, ~$LiZn_3$, β-$LiZn_4$, $MgZn_2$, and Mg_2Zn_{11} phases (Fig. 3 b). The analysis of the diffraction patterns showed that the original alloy reflections are quite narrow, and HPT treatment leads both to a broadening of the reflections and to a quantitative change in the ratio of reflection intensities (Fig. 3).

The peculiarities found on the diffraction patterns indicate changes in the identified phases and the occurrence of various phase transitions in the studied alloy as a result of HPT treatment. To determine the quantitative characteristics of phase transitions, the authors analysed the diffraction patterns using the Rietveld method implemented in the TOPAS program. An example of processing the alloy diffraction pattern measured after HPT (1 revolution) is shown in Fig. 3 b. It should be noted that in all the studied

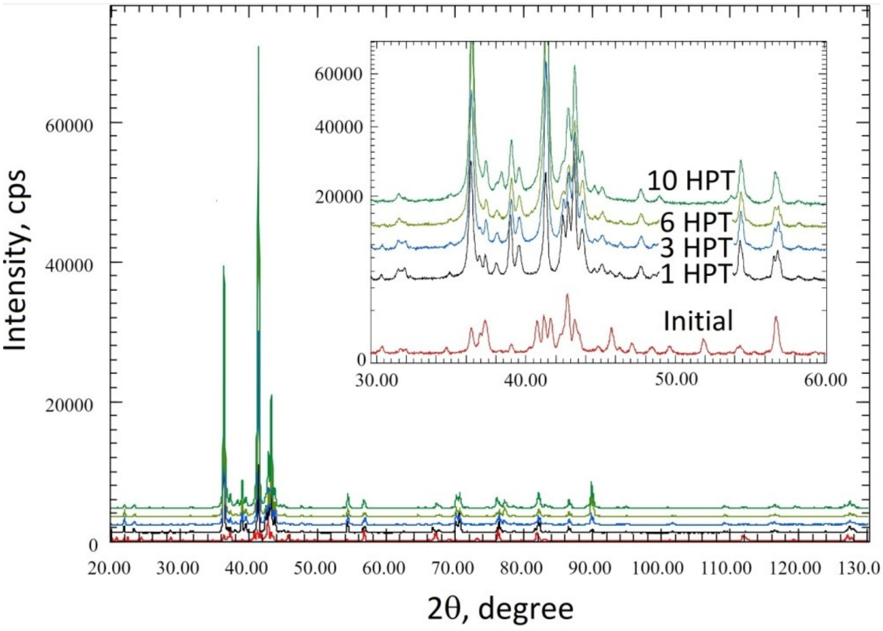

a

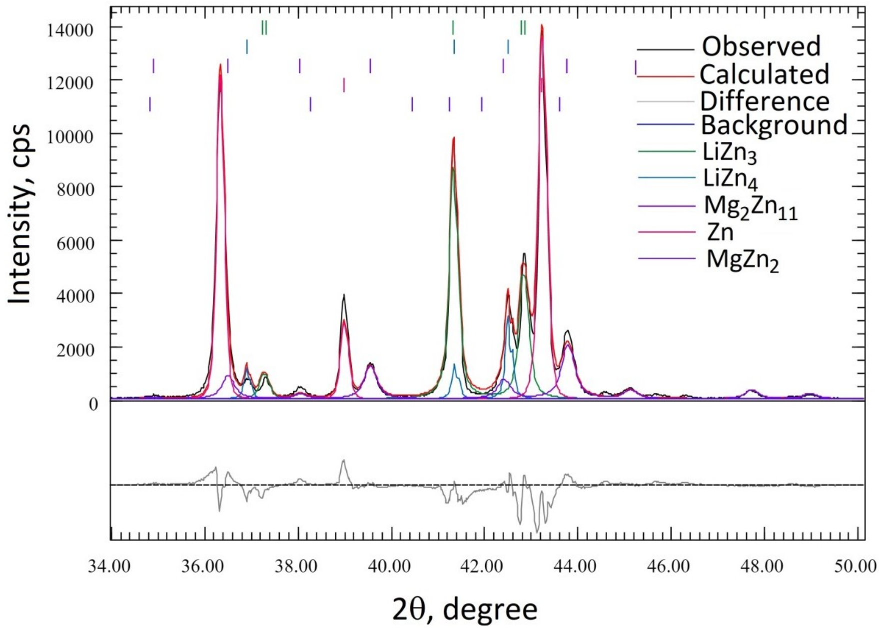

b

Fig. 3. *Diffraction patterns of the Zn–Li–Mg alloy in the initial state and after HPT treatment:*
a *– general view of diffraction patterns, in the insert – precision surveying area from 30° to 60°;*
b *– a section of the diffraction pattern processed by the Rietveld method*

states, the diffraction patterns were refined until a value of less than 5 %, and the permissible limit of the χ^2 value was set equal to 1.5 %. The results of qualitative and quantitative phase analyses for the selected states are shown in Tables 2–4.

The analysis of the zinc alloy in the initial (as-cast) state showed that the β-$LiZn_4$, ~$LiZn_3$, $MgZn_2$, and Zn phases were formed in it. Their quantitative ratio is given in Table 2. In the initial state of the alloy, the main phase includes the β-$LiZn_4$+Zn eutectic phase (~76 %), i.e., light areas detected by SEM. To assess the correctness of XPA calculations, the detected phases were first decomposed into elemental components in terms of Zn, Li, and Mg (Table 2), and then their total values were compared with the casting data (Table 1, bottom row).

The XPA obtained results are in very good agreement with the data obtained when casting the blank parts. This fact indicates the XPA correctness and obtaining correct information about the quantitative ratio of the phases. In the case of HPT treatment applied to the alloy, the mass fractions of the β-$LiZn_4$, ~$LiZn_3$, and $MgZn_2$ phases decrease, while the zinc fraction increases (Table 3). At the same time, HPT treatment leads to the formation of the Mg_2Zn_{11} phase, which is non-characteristic of the as-cast state, i.e., to the occurrence of the $MgZn_2 \rightarrow Mg_2Zn_{11}$ phase transition. An increase in the number of revolutions of the HPT treatment leads to a further regular growth of the Zn and Mg_2Zn_{11} phases (Table 3). In this case, a slight decrease in the content of the β-$LiZn_4$, ~$LiZn_3$, and $MgZn_2$ phases are observed.

A precision analysis of the diffraction patterns showed that, in contrast to the diffraction pattern of the initial state, the measured X-ray spectra of HPT samples are characterised both by a redistribution of reflection intensity and by an increased width of diffraction maxima. As a rule, an increase in the width of reflections characterises the changes occurred in the analyzed material microstructure, and, first of all, they are associated with a decrease in the CSD size, an increase in the crystal lattice microdistortions, and the density of introduced defects.

To assess these changes, the authors performed a full-profile analysis of the diffraction patterns in the PM2K program. When analysing, the main attention was paid to the Zn phase, since its content during HPT treatment is maximum. The data on the alloy microstructural characteristics obtained as a result of the XRD analysis of the diffraction patterns are shown in Table 4.

Fig. 4 shows the CSD size distributions in the phase of zinc in the initial state and in the states after HPT treatment. In the initial state, the average CSD size is typical for coarse-grained metallic materials (~380 nm). The implementation of 1 HPT revolution leads to a significant decrease in the CSD size to 86 nm (Fig. 4, Table 5). With a further increase in the number of HPT revolutions, a regular decrease in the CSD size to ~30 nm is observed (Fig. 4). At high HPT degrees, the CSD average size scarcely changes.

Results of SAXS studies

Fig. 5 shows the scattering curves measured on thin foils of the original alloy and the alloy after HPT, as well as the results of their processing. The SAXS curve of the initial state is characterised by one inflection. After HPT treatment, the scattering curves have two inflection points, one of which is concentrated in the region of small values of the scattering vector *q*, and the other is located in the region of large *q* values (Fig. 5 a). This fact indicates the presence of precipitates of one type in the initial state and two types (small and large) of precipitates after HPT, i.e., the bimodal nature of the particle distribution.

The inflection on the SAXS curve of the initial state is located in the region from 0.4 to 0.6 nm^{-1}, and the type of the intensity dependence decreases according to $I(1/q^2)$. According to [16; 17], this indicates the precipitation of cylindrical particles. After HPT treatment of zinc alloy, the general view of the SAXS curve changes (Fig. 5 a). In particular, after 1 HPT revolution, two inflection sections can be distinguished on the SAXS curve. The first inflection is concentrated in the range up to 0.15 nm^{-1}, and before the inflection, the intensity decreases according to the $I(1/q^2)$ dependence (Fig. 5 a), which indicates the precipitation of relatively large cylindrical precipitates [16; 17]. The second inflection section on the SAXS curve is in the range from 0.75 to 0.85 nm^{-1}, and the X-ray quanta intensity decreases according to the $I(1/q^4)$ dependence. Such a dependence on the SAXS curve manifests itself during intensity decreases according to the $I(1/q^4)$ dependence. Such a dependence on the SAXS curve manifests itself during the precipitation of spherical particles [16; 17]. When increasing the number of HPT treatment revolutions, the first

Table 2. *The detected phases, their weight fractions and element-by-element content of Zn, Li, and Mg atoms in each component. Initial (as-cast) state*

Phases	**Phase fraction, wt. %**	**Element content in the phase, wt. %**		
		Li	**Mg**	**Zn**
β-$LiZn_4$	11.85	2.59	0.00	97.41
β-$LiZn_4$ (eut.)	44.98	1.30	0.00	98.70
Zn	31.31	0.35	0.45	99.20
$MgZn_2$	11.86	0.00	15.67	84.33
Total	100.00	1.00	2.00	97.00

Table 3. *The detected phases, their weight fractions and element-by-element content of Zn, Li, and Mg atoms in each component. HPT treatment (1 revolution)*

Phases	**Phase fraction, wt. %**	**Element content in the phase, wt. %**		
		Li	**Mg**	**Zn**
β-LiZn$_4$	9.65	2.59	0.00	97.41
~LiZn$_3$	24.43	2.66	0.00	97.34
Mg$_2$Zn$_{11}$	16.28	0.00	6.33	93.67
Zn	47.65	0.21	1.38	98.41
MgZn$_2$	1.99	0.00	15.67	84.33
Total	100.00	1.00	1.99	97.01

Table 4. *The detected phases, their weight fractions and element-by-element content of Zn, Li, and Mg atoms in each component. HPT treatment (10 revolutions)*

Phases	**Phase fraction, wt. %**	**Element content in the phase, wt. %**		
		Li	**Mg**	**Zn**
β-LiZn$_4$	7.23	2.59	0.00	97.41
~LiZn$_3$	21.66	3.47	0.00	96.53
Mg$_2$Zn$_{11}$	18.24	0.00	6.33	93.67
Zn	52.39	0.12	1.47	98.41
MgZn$_2$	0.48	0.00	15.67	84.33
Total	100.00	1.00	1.99	97.01

and second inflection points shift towards small vector *q* values (Fig. 5 a), which is associated with the size growth of precipitates.

The analysis of the SAXS curves showed that, in the initial state, Zn precipitates in the β-LiZn$_4$ phase precipitate in an acicular shape with an average diameter of 75 nm and a length of 150 nm (Fig. 5 b). As a result of HPT treatment (1 revolution), in addition to Zn particles, β-LiZn$_4$ particles also precipitate in the alloy; however, in contrast to the initial state, they have different shapes and sizes. Large particles after 1 HPT revolution, related to Zn precipitates, have a cylindrical shape with a diameter of 330 nm and a length of up to 900 nm. At the same time, small particles belong to LiZn$_4$ precipitates and are formed in a spherical shape with a diameter of 17 nm (Fig. 5 b).

When increasing the number of HPT revolutions, regular changes in the particle size and morphology are observed. In particular, after 10 HPT revolutions, only spherical morphology is formed. In this case, the average size of small LiZn$_4$ particles is 45 nm, while larger Zn particles have an average diameter of 86 nm.

DISCUSSION

The results of tensile tests of the specimens factually demonstrated a significant increase in the zinc alloy mechanical properties during HPT treatment. In particular, the analysis of the results of mechanical tests showed that even after 1 HPT treatment revolution, the yield strength increases by ~1.7 times, and the ultimate strength increases by about 2.5 times (Table 1). With a further increase in the HPT treatment degree, a regular increase in mechanical properties occurs (Table 1). After 10 HPT revolutions implemented at room temperature, the yield stress of 330 MPa and tensile strength of 409 MPa, maximum for this alloy, were found. To explain the obtained record values of mechanical properties and to analyze possible hardening mechanisms, the alloy microstructure analysis was carried out.

The conducted studies using microscopy and X-ray diffraction analysis showed that in the Zn–1%Li–2%Mg alloy during HPT treatment, phases of the same type are formed with the precipitates identical in type (Fig. 1, 2). As known [3; 6], as the casting temperature drops to room temperature, according to the phase diagram, the solubility of Zn atoms in the β-LiZn$_4$ phase decreases, therefore,

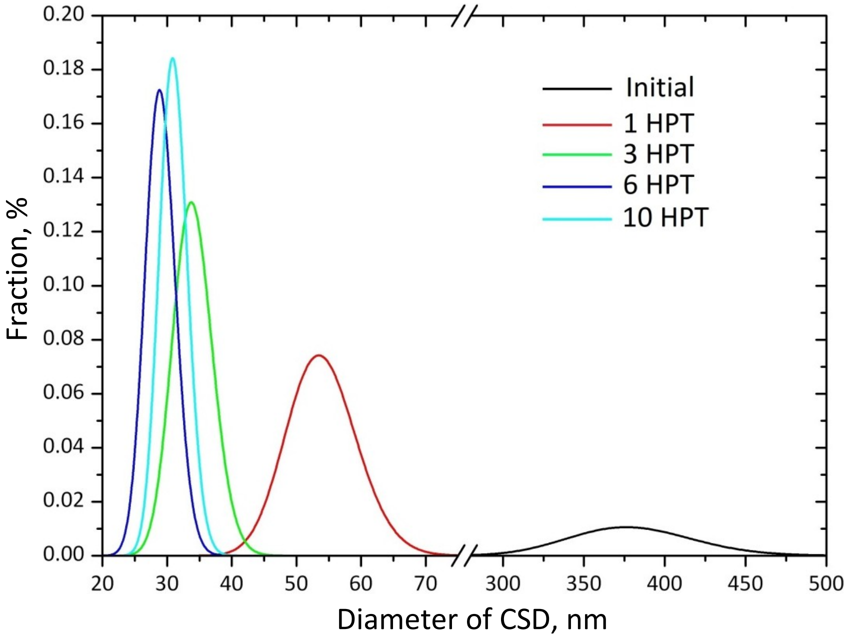

Fig. 4. *CSD distribution by sizes in the alloy in the initial state and after different HPT treatment degrees*

Table 5. *Parameters of the zinc alloy microstructure obtained by the XRD method*

State	*a/c*, nm	*D*$_{ave}$, nm	*D*$_{SEM}$, nm	ε, %	ρ, 10^{15} m^{-2}	*m*$_{ixp}$, %
Initial	0.266123 0.493885	370±80	60000	0.08±0.01	0.5±0.1	0.29±0.03
HPT, 1 rev.	0.266604 0.494040	86±4	906	0.15±0.01	2.4±0.2	0.41±0.02
HPT, 3 rev.	0.266578 0.494251	43±1	383	0.23±0.01	5.1±0.1	0.68±0.03
HPT, 6 rev.	0.266595 0.494252	29±2	246	0.26±0.01	5.4±0.1	0.79±0.02
HPT, 10 rev.	0.266588 0.494254	32±3	218	0.25±0.02	5.3±0.4	0.77±0.04

Note. a/c – lattice constant, pure zinc: a/c=0.26594/0.49368 [15];
D_{ave} – average dimension of CSD obtained by the XRD method;
D_{SEM} – grain dimension obtained by SEM;
ε – RMS crystal lattice microdistorsion;
ρ – density of dislocations;
m_{ixp} – the proportion of edge-type dislocations.

Zn particles will precipitate in the β-$LiZn_4$ phase. On the other hand, the solubility of Li atoms in the Zn phase also sharply decreases upon cooling, which leads to the formation of β-$LiZn_4$ precipitates in the Zn phase. In the initial state, the zinc alloy is characterised by the presence of a primary β-$LiZn_4$ phase, a Zn+β-$LiZn_4$ eutectic phase, and a $MgZn_2$ phase. In this case, as the analysis showed, Zn particles of cylindrical morphology precipitate in the β-$LiZn_4$ phase. For the quantitative characteristics of the detected phases, the authors analysed the diffraction patterns using the Rietveld method. To check the correctness of the quantitative XPA results, the content of each phase was decomposed into elemental components (Table 2) and compared with the data taken during alloy casting.

The comparison of the total content of Zn, Li, and Mg atoms with the data entered during the casting of blank parts showed a very good convergence between them. This fact indicates the reliability of the information obtained in the ratio of the analysed phases. In particular, XPA shows that in the initial state, the mass content of Li atoms in the primary β-$LiZn_4$ phase is 2.59 %, and the content of Zn atoms is 97.41 %, which corresponds to the equilibrium

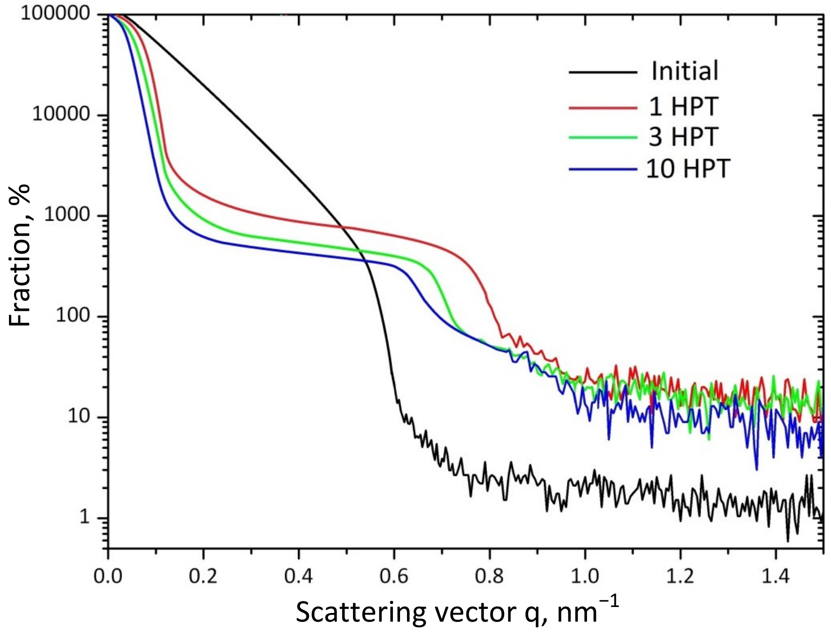

a

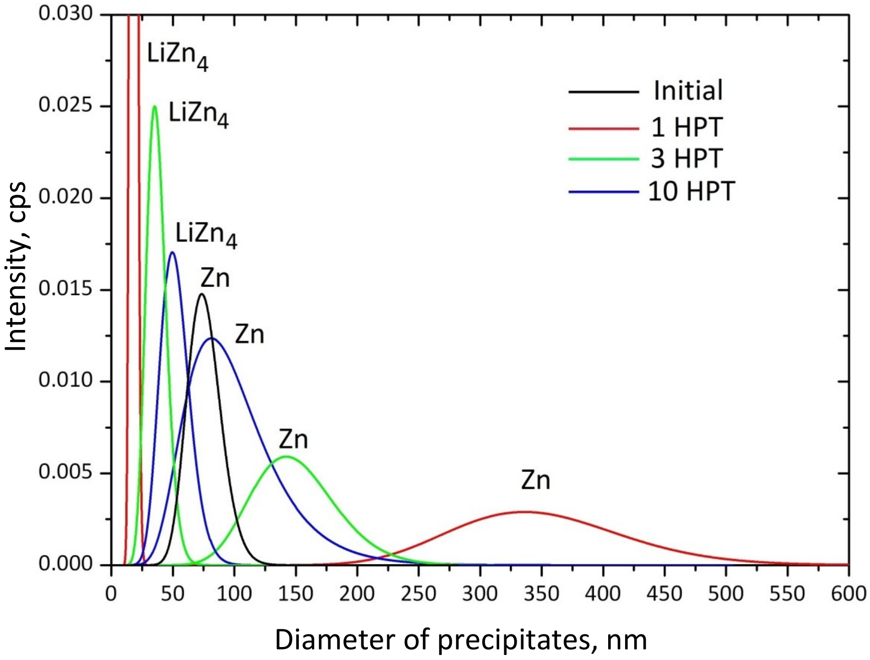

b

Fig. 5. *Data of small-angle X-ray scattering (SAXS) of the alloy in different structural states:*
a *– SAXS curves;* ***b*** *– precipitation distribution*

state of this component. At the same time, in the $LiZn_4$ eutectic phase, a reduced content of Li atoms (1.30 %) compared with the standard value of 2.59 % in the primary β-$LiZn_4$ phase was revealed (Table 2). Moreover, a small content of Li and Mg atoms was found in the pure Zn phase, the presence of which led to an increase in the Zn lattice constant both along the *a* edge and along the *c* axis of the HCP lattice basis (Table 5). The total mass content of Li, Mg, and Zn atoms over all the phases taken in the zinc alloy is 1 %, magnesium is ~2 %, and zinc is ~97 % (Table 1, bottom line), which corresponds to the data taken during casting of the alloy.

The HPT treatment leads to significant changes in the quantitative ratios of the β-$LiZn_4$, ~$LiZn_3$, $MgZn_2$, and Zn phases in the alloy. In particular, at the HPT initial stages, the content of the ~$LiZn_3$ phase sharply decreases from ~45 to ~24 %. The content of Li atoms in this phase is higher than in the primary β-$LiZn_4$ phase; therefore, the β-$LiZn_4$ phase was defined as ~$LiZn_3$ [18]. This state is characterised by an increase in the proportion of the Zn phase from ~31 to ~48 %. Along with this, the fraction of Li atoms in the Zn phase decreases, while the fraction of Mg atoms increases (Table 3). The decrease in Li atoms in the Zn phase is most likely associated with the precipitation of $LiZn_4$ particles, and an increase in the fraction of Mg atoms in the Zn phase leads to an increase in the Zn lattice constant (Table 5). As a result of HPT, the $MgZn_2\rightarrow$ $\rightarrow Mg_2Zn_{11}$ phase transition atypical for the coarse-grained state also occurs (Table 3). With a further increase in the degree of HPT treatment, on the one hand, a further decrease in the content of the β-$LiZn_4$, ~$LiZn_3$, $MgZn_2$ phases, and, on the other hand, an increase in the proportion of the Zn and Mg_2Zn_{11} phases are observed. Moreover, it was found that the content of admixture Li atoms in the ~$LiZn_3$ phase increases, while the fraction of Mg atoms in the Zn phase increases, and the fraction of Li atoms decreases. These facts seem to indicate the precipitation of Zn particles in the ~$LiZn_3$ phase and the growth of β-$LiZn_4$ precipitates in the Zn phase. An increase in the content of Mg atoms in Zn leads to a further increase in the Zn lattice distance (Table 5).

The SEM studies factually confirmed the occurrence of the detected phase transformations. In particular, in the initial state, the SEM method revealed light areas (oval + layered) belonging to the Zn+β-$LiZn_4$ eutectic phase with a surface fraction of ~88 %, and dark areas with a fraction of ~12 % identified as the primary β-$LiZn_4$ phase (Fig. 1). At high magnifications, in the primary β-$LiZn_4$ phase, numerous acicular Zn precipitates with a diameter of ~80 nm and a length from 60 to 230 nm were identified. The dimensions of these precipitates agree with the results of SAXS studies (Fig. 5 b). During HPT treatment, significant changes occur in the microstructure. The SEM images of the alloy (0.5 HPT revolution) show predominantly dark areas (Fig. 2 a). This fact is associated with an increase in the content of Li atoms in the ~$LiZn_3$ phase (Table 3) and taking into account the low retarding potential of Li (–3.04 V) compared to Zn (–0.76 V). The ~$LiZn_3$ phase is more subjected to etching, i.e., to the appearance of dark regions. At the early HPT stages (0.5 revolution), a decrease in the thickness of the bands of the Zn+Mg_2Zn_{11} phase to ~16 μm was revealed. In this case, the formation of the zinc phase around the eutectic phases was identified (Fig. 2 a). With an increase in the number of HPT revolutions to 1, the average thickness of the light plates decreases to ~11 μm, and after 10 HPT revolutions, its value decreases to 1.7 μm. Filamentous Zn precipitates generate in the $LiZn_4$ phase forming a grid of precipitates. The average diameter of Zn precipitates is 350 nm, and the average length is ~2 μm. Moreover, in this state, a band structure is formed, in which Zn precipitates are sometimes merge (Fig. 2 b, insert).

In general, with an increase in the degree of HPT treatment, an effective structure refinement occurs, and Zn precipitates have a spherical shape. The size and morphology of Zn precipitates detected by the SEM method correlate well with the results of SAXS studies (Fig. 5 b). In particular, the bimodal nature of the distribution of precipitates was established from the *I(q)* dependence of the scattering curve. In the early HPT stages, Zn precipitates have a cylindrical shape with a diameter of 330 nm and a length of up to 900 nm, while fine $LiZn_4$ particles precipitate in a spherical shape with an average diameter of 17 nm. When increasing the number of HPT revolutions to 10, the diameter of spherical $LiZn_4$ particles increases to 45 nm, and Zn precipitates have a spherical morphology and a diameter of 88 nm.

To assess the change in the microstructure parameters (CSD size, crystal lattice microdistortions, density and type of dislocations), the authors analysed the diffraction patterns using the PM2K program. The main attention was paid to the Zn phase, since it is the main phase in HPT treatment. The analysis showed that the application of HPT to the alloy leads to the CSD fragmentation (Fig. 4, Table 5). In particular, after 0.5 revolution, the average CSD size decreases from 410 to 86 nm. At the same time, lattice microdistortions and dislocation density sharply increase (Table 5). An increase in the degree of HPT treatment leads to further CSD refinement, an increase in microdistortions and defect density (Table 5). The analysis showed that dislocations at high degrees of HPT treatment are predominantly of the edge type, since the value of m_{ixp} is close to unity (Table 5).

The conducted studies of the alloy microstructure make it possible to assess qualitatively the main mechanisms responsible for its hardening. As possible hardening mechanisms, the authors considered grain boundary strengthening, solid solution strengthening, precipitation strengthening, and dislocation strengthening. In particular, the grain structure refinement (i.e., a decrease in the CSD) causes grain boundary strengthening σ_{gb} of the alloy, which can be determined by the Hall – Petch–type relationship [19]. The solid solution strengthening σ_{ss} of a supersaturated alloy solid solution will be determined by the excess content of Zn, Mg, and Li elements in the identified phases [20]. Precipitation strengthening σ_{pp} [21] is determined by the presence of precipitates and their proportions and is determined by the Ashby – Orowan relation, and the value of dislocation strengthening σ_d is directly proportional to $\sqrt{\rho}$ [22].

The obtained qualitative results of theoretical strength calculations are shown in Table 6, and give a visual representation of the expected contribution of each of the hardening mechanisms to the resulting strength of the alloy. It is obvious that in the initial state, the alloy strength is mainly provided by the mechanisms of dislocation and solid solution hardening (Table 6).

Table 6. *Contribution of different mechanisms to the alloy hardening*

State	σ_o	σ_{gb}	σ_{pp}	σ_d	σ_{ss}
Initial	+	+	+	++	++
After HPT	+	+++	+++	+++	+

In this case, the role of grain boundary and precipitation strengthening is low, which is explained by the rather large grain size (about 60 μm) and a small fraction of dispersed particles in the alloy structure. In the case of the HPT treatment implementation, the role of the grain boundary and dislocation strengthening mechanisms increases significantly, and the mechanisms of precipitation strengthening are also activated (Table 6). Thus, grain refinement, an increase in the density of introduced defects, and an increase in the proportion of particles of secondary phases (Zn, $LiZn_4$) contributed significantly to the increase in the strength characteristics of the zinc alloy. At the same time, the increase in the alloy ductility during HPT is explained by the formation of a unique microstructure consisting of Zn and ~$LiZn_3$ phases, in which precipitates of different types and shapes simultaneously occur [3; 6].

CONCLUSIONS

As a result of processing by severe plastic deformation by torsion in the Zn–1%Li–2%Mg alloy, a high-strength state was obtained, characterised by a yield strength of 330 MPa and a tensile strength of 409 MPa. For the first time, the XPA method identified the occurrence of phase transformations during HPT: $Zn_{(eutectic)}+\beta\text{-}LiZn_{4(eutectic)}\rightarrow\rightarrow{\sim}LiZn_3+Zn_{(phase)}+Zn_{(precipitate)}+\beta\text{-}LiZn_4$ and $MgZn_2\rightarrow\rightarrow Mg_2Zn_{11}$. The study shows that HPT treatment leads to the formation of Zn precipitates in the ~$LiZn_3$ phase, as well as to the formation of β-$LiZn_4$ precipitates in the Zn phase. According to the results of SAXS studies, it was found that large Zn precipitates at the initial stages of HPT precipitate in a cylindrical shape, while small ones precipitate in a spherical shape. When increasing the degree of HPT treatment, zinc and $LiZn_4$ particles precipitate only in a spherical shape. Based on the analysis of diffraction patterns, it was found that HPT treatment leads to refinement of coherent scattering domains (grains), an increase in the crystal lattice microdistortions, and an increase in the density of dislocations, predominantly of the edge type. An increase in the alloy strength characteristics occurs due to grain refinement, an increase in the density of introduced defects, as well as an increase in the proportion of Zn and $LiZn_4$ precipitates.

REFERENCES

1. Yang H., Jia B., Zhang Z., Qu X., Li G., Lin W., Zhu D., Dai K., Zheng Yu. Alloying design of biodegradable zinc as promising bone implants for load-bearing applications. *Nature Communications*, 2020, vol. 11, no. 1, article number 401. DOI: 10.1038/s41467-019-14153-7.
2. Jia B., Yang H., Han Yu., Zhang Z., Qu X., Zhuang Y., Wu Q., Zheng Yu., Dai K. In vitro and in vivo studies of Zn-Mn biodegradable metals designed for orthopedic applications. *Acta Biomaterialia*, 2020, vol. 108, pp. 358–372. DOI: 10.1016/j.actbio.2020.03.009.
3. Li Z., Shi Z.-Z., Hao Y., Li H.-F., Liu X.-F., Volinsky A.A., Zhang H.-J., Wang L.-N. High-performance hot-warm rolled Zn-0.8Li alloy with nano-sized metastable precipitates and sub-micron grains for biodegradable stents. *Journal of Materials Science and Technology*, 2019, vol. 35, no. 11, pp. 2618–2624. DOI: 10.1016/j.jmst.2019.06.009.
4. Tong X., Zhang D., Zhang X. et al. Microstructure, mechanical properties, biocompatibility, and in vitro corrosion and degradation behavior of a new Zn–5Ge alloy for biodegradable implant materials. *Acta Biomaterialia*, 2018, vol. 82, pp. 197–204. DOI: 10.1016/j.actbio.2018.10.015.
5. Bowen P.K., Drelich J., Goldman J. Zinc Exhibits Ideal Physiological Corrosion Behavior for Bioabsorbable Stents. *Advanced materials*, 2013, vol. 25, pp. 2577–2582. DOI: 10.1002/adma.201300226.
6. Li Z., Shi Z.-Z., Hao Y., Li H.-H., Zhang H.-J., Liu X.-F., Wang L.-N. Insight into role and mechanism of Li on the key aspects of biodegradable Zn-Li alloys: Microstructure evolution, mechanical properties, corrosion behavior and cytotoxicity. *Materials Science and Engineering C*, 2020, vol. 114, article number 111049. DOI: 10.1016/j.msec.2020.111049.
7. Sitdikov V.D., Kulyasova O.B., Sitdikova G.F., Islamgaliev R.K., Yufeng Zh. Structural-phase transformations in the Zn-Li-Mg alloy exposed to the severe plastic torsion deformation. *Frontier Materials & Technologies*, 2022, vol. 3-2, pp. 44–55. DOI: 10.18323/2782-4039-2022-3-2-44-55.
8. Zhang Y., Yan Y., Xu X., Lu Y., Chen L., Li D., Dai Y., Kang Y., Yu K. Investigation on the microstructure, mechanical properties, in vitro degradation behavior and biocompatibility of newly developed Zn-0.8%Li-(Mg, Ag) alloys for guided bone regeneration. *Materials Science and Engineering: C*, 2019, vol. 99, pp. 1021–1034. DOI: 10.1016/j.msec.2019.01.120.
9. Martynenko N., Anisimova N., Rybalchenko O. et al. Structure, Biodegradation, and In Vitro Bioactivity of Zn–1%Mg Alloy Strengthened by High-Pressure Torsion. *Materials*, 2022, vol. 15, article number 9073. DOI: 10.3390/ ma15249073.
10. Mollaei N., Fatemi S.M., Abootalebi M., Razavi H. Zinc based bioalloys processed by severe plastic deformation - A review. *Journal Ultrafine Grained Nanostructure Materials*, 2020, vol. 53, pp. 39–47. DOI: 10.22059/JUFGNSM.2020.01.06.
11. Ye L., Liu H., Sun C., Zhuo X., Ju J., Xue F., Bai J., Jiang J., Xin Y. Achieving high strength, excellent ductility, and suitable biodegradability in a Zn-0.1Mg alloy using room-temperature ECAP. *Journal of Alloys Compounds*, 2022, vol. 926, article number 166906. DOI: 10.1016/j.jallcom.2022.166906.
12. Chen C., Fan S., Niu J., Huang H., Jin Z., Kong L., Zhu D., Yuan G. Alloying design strategy for biodegradable zinc alloys based on first-principles study of solid solution strengthening. *Materials & Design*, 2021, vol. 204, article number 109676. DOI: 10.1016/j.matdes.2021.109676.
13. Leoni M., Confente T., Scardi P. PM2K: A flexible program implementing Whole Powder Pattern Modelling. *Zeitschrift für Kristallographie, Supplement*, 2006, vol. 1, no. 23, pp. 249–254. DOI: 10.1524/9783486992526-043.
14. Rietveld H.M. A profile refinement method for nuclear and magnetic structures. *Journal of Applied Crystallography*, 1969, vol. 2, no. 2, pp. 65–71. DOI: 10.1107/S0021889869006558.
15. Jette E.R., Foote F. Precision determination of lattice constants Locality: synthetic Sample: at T = 25 C Note: lattice parameter is average of three samples. *Journal of Chemical Physics*, 1935, vol. 3, pp. 605–616. DOI: 10.1063/1.1749562.
16. Boldon L., Laliberte F., Liu L. Review of the fundamental theories behind small angle X-ray scattering, molecular dynamics simulations, and relevant integrated application. *Nano Review*, 2015, vol. 6, article number 25661. DOI: 10.3402/nano.v6.25661.
17. Pedersen J.S. Analysis of small-angle scattering data from colloids and polymer solutions: modeling and

least-squares fitting. *Advances in Colloid and Interface Science*, 1997, vol. 70, pp. 171–210. DOI: 10.1016/s0001-8686(97)00312-6.

18. Pavlyuk V., Chumak I., Akselrud L., Lidin S., Ehrenberg H. $LiZn_{4-x}$ (x=0.825) as a (3+1)-dimensional modulated derivative of hexagonal close packing. *Acta Crystallographica*, 2014, vol. 70, pp. 212–217. DOI: 10.1107/S2052520613030709.
19. Bednarczyk W., Wątroba M., Kawałko J., Bała, P. Can zinc alloys be strengthened by grain refinement? A critical evaluation of the processing of low-alloyed binary zinc alloys using ECAP. *Materials Science and Engineering: A*, 2019, vol. 748, pp. 357–366. DOI: 10.1016/j.msea.2019.01.117.
20. Bednarczyk W., Wątroba M., Jain M., Mech K., Bazarnik P., Bała P., Michler J., Wieczerzak K. Determination of critical resolved shear stresses associated with <a> slips in pure Zn and Zn-Ag alloys via micro-pillar compression. *Materials & Design*, 2023, vol. 229, article number 111897. DOI: 10.1016/j.matdes.2023.111897.
21. Lee J.D., Niessen P. Superplasticity in a new dispersion strengthened zinc alloy. *Metallurgical Transactions*, 1973, vol. 4, pp. 949–957. DOI: 10.1007/BF02645595.
22. Zhao C., Chen X., Pan F., Wang J., Gao S., Tu T., Liu C., Yao J., Atrens A. Strain hardening of as-extruded Mg-xZn (x = 1, 2, 3 and 4 wt%) alloy. *Journal of Materials Science & Technology*, 2019, vol. 35, no. 1, pp. 142–150. DOI: 10.1016/j.jmst.2018.09.015.

doi: 10.18323/2782-4039-2023-2-64-5

Electrically conductive nanocomposite bituminous binders containing carbon nanotubes and multilayer graphene

Dmitry V. Tarov[1], PhD (Engineering), leading researcher
Daniil A. Evlakhin, student
Andrey D. Zelenin[2], junior researcher
Roman A. Stolyarov[3], PhD (Engineering), senior researcher
Viktor S. Yagubov*[4], PhD (Engineering), senior researcher
Nariman R. Memetov[5], PhD (Engineering), leading researcher
Anastasiya E. Memetova[6], PhD (Engineering), assistant professor
of Chair "Technology and Methods of Nanoproducts Manufacturing"
Nikolay A. Chapaksov[7], junior researcher of Chair "Nanotechnology Engineering"
Alena V. Gerasimova [8], PhD (Engineering), senior lecturer
of Chair "Technology and Methods of Nanoproducts Manufacturing"
Tambov State Technical University, Tambov (Russia)

***E-mail: yagubov.vs@mail.tstu.ru,**
vitya-y@mail.ru

[1]ORCID: https://orcid.org/0000-0002-8067-9548
[2]ORCID: https://orcid.org/0000-0002-2399-9510
[3]ORCID: https://orcid.org/0000-0001-8495-3316
[4]ORCID: https://orcid.org/0000-0003-4855-0530
[5]ORCID: https://orcid.org/0000-0002-7449-5208
[6]ORCID: https://orcid.org/0000-0002-1036-7389
[7]ORCID: https://orcid.org/0000-0001-9076-9400
[8]ORCID: https://orcid.org/0000-0003-1912-6642

Received 17.05.2023 *Accepted 09.06.2023*

Abstract: In the modern literature, there is practically no data on the electrical characteristics of bituminous binders modified with carbon nanotubes and graphene nanoplates, while they are necessary for the design and development of innovative asphalt pavement compositions, sensitive to the super-high-frequency microwave radiation. Contemporary bituminous binders are multi-component systems, that may contain polymers, rubbers, synthetic or natural resins, inorganic salts, and even fragrances. As a result of the application of modifying additives, bitumen acquires high performance characteristics. A special class of modifiers are micro- and nano-sized electrically conductive fibers and particles (steel wool, carbon fibers, carbon black, carbon nanotubes, graphene nanoplates). The use of which makes it possible to ensure the sensibility of bituminous binders to super-high-frequency microwave radiation and the implementation of the process of healing cracks in an asphalt pavement with its subsequent regeneration. As part of the study, the authors developed an original technique to produce bituminous binders modified with carbon nanotubes and multilayer graphene. Modified bituminous compositions in the concentration range from 0.2 to 6 and from 0.2 to 11 wt. % for multi-walled carbon nanotubes (MWCNT) and multilayer graphene nanoplates (MG), respectively were experimentally obtained. For the first time, the dependence of the specific volume electrical conductivity of bitumen-based nanocomposites on the concentration of nanostructured carbon filler (MWCNT and MG) was researched. The maximum values of electrical conductivity were 4.76×10^{-4} S/cm and 3.5×10^{-4} S/cm for nanocomposites containing 6 wt. % MWCNT and 11 wt. % MG, respectively. The study determined the filler volume fractions at the percolation threshold for nanocomposites containing MWCNT and MG. They amounted to 0.22 and 2.18, respectively. The formation of a percolation contour in nanocomposites containing MWCNT occurs at significantly lower filler concentrations compared to bituminous compositions containing MG.

Keywords: bituminous binders; electrically conductive nanocomposites; carbon nanotubes; multilayer graphene; graphene nanoplates; percolation threshold.

Acknowledgments: The study was financially supported by the Department of Education and Science of the Tambov Region and the Coordinating Council for Higher Education and Science within the scientific project No. MU2022-02/18 "Grant to support applied research of young scientists in 2022".

For citation: Tarov D.V., Evlakhin D.A., Zelenin A.D., Stolyarov R.A., Yagubov V.S., Memetov N.R., Memetova A.E., Chapaksov N.A., Gerasimova A.V. Electrically conductive nanocomposite bituminous binders containing carbon nanotubes and multilayer graphene. *Frontier Materials & Technologies*, 2023, no. 2. DOI: 10.18323/2782-4039-2023-2-64-5.

INTRODUCTION

To meet the high contemporary requirements for the performance characteristics of road surfaces, it is necessary to introduce modifying additives into the composition of bituminous binders, the main of which are polymers and rubbers [1; 2]. The application of modifying additives improves the performance characteristics of bitumen, such as heat, frost resistance, load resistance, elasticity, and durability [1; 2].

Over the last years, due to the intensive development of nanotechnologies, it became possible to consider nanomaterials as modifying additives for bituminous binders used in asphalt pavements [3]. It is proved that the application of modifying additives of nanosilica, nanoclay, and Fe_2O_3 nanoparticles, improves the mechanical characteristics (plastic strain value, elasticity modulus, and tensile strength) of asphalt pavements [4]. However, the high cost of nanomaterials and the short service life of modified asphalt pavements have led to low economic efficiency of the use of nanosilica, nanoclay, and Fe_2O_3 nanoparticles as bituminous binder modifiers [4].

The most promising modifiers for bituminous binders are carbon nanotubes and graphene nanoplates, which have excellent mechanical characteristics [5]. In the work [6], for the samples of asphalt concrete mixture, modified with carbon nanotubes (at a CNT concentration of 1 wt. %), an increase in tensile strength, elastic modulus, and fatigue strength by 17, 55, and 270 %, respectively, was shown. Due to adding graphene nanoplates to the asphalt mix with a concentration of 3 wt. %, the tensile strength of the modified samples increased by 150 % compared to the control one [7].

The effective use of carbon nanomaterials as bituminous binder modifiers allows applying an innovative approach to healing cracks in an asphalt pavement by exposure to microwave radiation followed by regeneration of this pavement [3]. In [8], ordinary bitumen was modified with carbon nanotubes and graphene nanoplates, and the efficiency of microwave radiation absorption in the obtained compositions was studied. The concentrations of MWCNTs (multi-walled carbon nanotubes) and graphene were 10 % of the bitumen volume. The results of the study showed that both additives increase the heating rate of bitumen under the action of microwave radiation, but the heating rate of samples modified with CNTs is 24 % higher than that of bitumen modified with graphene. The authors of [9] analysed the characteristics of microwave heating of an asphalt mix containing graphene nanoplates at a concentration of 1 and 2 wt. %. The study results showed, that the addition of 2 wt. % of graphene to the asphalt mix doubles the sample heating rate and, therefore, increases the energy efficiency of the sample regeneration process under the action of microwave radiation. Similar results were obtained by adding 9 wt. % of slag to the asphalt mix.

The application of MWCNTs, and other microwave-susceptible carbon nanostructures as modifiers, leads to an improvement of the performance properties of bituminous binders at significantly lower concentrations compared to metal fiber [3; 10]. Moreover, metal fiber has a rather high cost, and the selection and manufacture of modified bitumen compositions are complicated by the shape of the filler particles and reduced adhesion of bitumen to stainless steel [3; 10]. Therefore, the use of carbon nanomaterials as modifiers in asphalt mixes will both improve the service characteristics of these mixtures, and intensify the process of heating the road surface with electromagnetic microwaves.

To study the mechanisms occurring under the action of microwave irradiation in nanocomposite bitumen systems containing carbon nanostructures, the information on the electrical characteristics of these systems (specific electrical conductivity, the volume fraction of the filler at the percolation threshold, and the critical electrical conductivity index) is required. Unfortunately, in the contemporary literature, there is only one work on the study of the electrical conductivity of bitumen compositions modified with graphene nanoplates, and the data are given for only two concentrations – 1 and 2 wt. % [9]. Studies of the electrical conductivity of nanomodified bitumen are entirely absent.

Therefore, in the current study, the most widespread, industrially produced and sensitive to electromagnetic radiation carbon nanostructures, such as multi-walled carbon nanotubes [11; 12] and graphene nanoplates [12–14] were selected as a filler for bitumen matrix.

The aim of the study is to develop the techniques of obtaining and studying the electrical characteristics of nanocomposites based on bitumen containing multi-walled carbon nanotubes (MWCNTs) and multilayer graphene nanoplates (MGs).

METHODS

Road bitumen of the BND 60/90 grade (OOO Ural Bitumen Plant, Yekaterinburg, Russia) was used as the base for the composites.

Bitumen was modified by "Taunite-M" MWCNT and "Taunite-GM" MG (OOO NanoTechCenter, Tambov, Russia). "Taunite-M" MWCNT are filamentary structures consisting of graphene layers with an internal channel. Their synthesis is carried out by chemical gas deposition. "Taunite-GM" MG is a two-dimensional graphene plates in the form of an aqueous paste. The dry residue content in the paste is 5–7 %. The parameters of "Taunite-M" MWCNT and "Taunite-GM" MG are given in Tables 1 and 2.

To eliminate aggregation and remove adsorbed water, MWCNTs were preliminarily dried in a vacuum furnace at 150 °C for 4 h. After drying, MWCNTs were mechanically activated in a WF-20B blade mill for 3 min at a rotation speed of a grinding body of 25000 rpm. This was done to reduce the size of agglomerates and improve the process of their dispersion in the polymer matrix, as was shown in [11].

MG in its original form was a water paste, which prevented its combination with bitumen. In this regard, MG was freeze-dried in a Scientz-10N dryer (Scientz, China) in two stages. At the first stage, the MG sample was frozen for 20 h to a temperature below −30 °C. Freezing was carried out until the temperature of the freezing chamber and the frozen sample equalized. At the second stage, the frozen sample was vacuum-treated for 20 h. After freeze-drying, MG was mechanically activated under the same conditions as MWCNTs.

To produce composite mixtures based on bitumen with MWCNTs (BCNT) and bitumen with MG (BMG), the following procedure was developed. Initially, the modifier was mixed with Nefras S2-80/120 gasoline (NK Rosneft, Russia) using a HT-120DX vertical rotary mixer (Daihan, Korea) and processed with I-10 ultrasound (Ultrasonic Technique – INLAB, Russia) within 30 min. Gasoline heated to 110 °C and lump bitumen were placed in a separate metal container. In such a way, bitumen co-melt and co-solution were obtained. The previously prepared dispersion of the modifier in gasoline was introduced into the resulting melt.

As part of the work, the authors designed a measuring cell to study the specific volume electrical resistivity of modified bitumen compositions (Fig. 1). Fig. 1 a shows the general view of the assembled measuring cell.

The cell (Fig. 1 b) consisted of measuring electrodes (1 and 2) made of foil fiberglass plastic, between which a fluoroplastic matrix (3) was installed. In the center of the matrix, there was a hole with a diameter of 6 mm.

The measurements were carried out as follows. At the first stage, the lower measuring electrode (2) was fastened to the matrix (3). The molten composite (4) was placed into the matrix hole, then, the upper measuring electrode (1) was installed on the assembly with the composite. The cell was tightened with screws and finger nuts, thereby forming a sample for measurement, which was a cylinder with a diameter of 6 mm and a height of 2 mm. The resistance of the samples was measured by connecting the upper and lower measuring electrodes to an E6-13A teraohmmeter (PunaneRet, Estonia) with an upper range limit of 10^{14} Ohm. The electrical conductivity was calculated according to the formula [15]:

$$\sigma = \frac{4h}{\pi d^2 R},$$

where h – studied sample height (cm);
d – studied sample diameter (cm);
R – electrical resistance (Ohm).

RESULTS

The electrical conductivity of the nanocomposites increased with increasing MWCNT mass content. The maximum electrical conductivity of 4.76×10^{-4} S/cm was achieved at 6 wt. % content of MWCNT in BCN, which is 3 orders of magnitude higher than the electrical conductivity of BMG nanocomposites containing 6 wt. % of MG (8.12×10^{-6} S/cm). In the case of using MG, the maximum electrical conductivity of 3.5×10^{-4} S/cm was observed in the BMG nanocomposite containing 11 wt. % (Fig. 2).

The results presented in Fig. 2 demonstrate that the dependence of the electrical conductivity of nanocomposites on the mass content has a percolation nature and is described by the expression [16]:

Table 1. *Characteristics of "Taunite-M" MWCNT and "Taunite-GM" MG [16]*

Characteristics	Taunite-M	Taunite-GM
Outer diameter, nm	10–30	–
Inner diameter, nm	5–15	–
Length, μm	≥2	–
Specific surface area, m^2/g	≥270	–
Pour density, g/cm^3	0.025–0.06	–
Number of graphene layers	–	15–25
Thickness of nanoplates, nm	–	6– 8
In-plane dimension of nanoplates, μm	–	2–10
Content of nanoplates, wt. %	–	4–7
Specific absorption rate, lm/(g·cm)	–	30–33

Note. Data of the company "NanoTechCenter" Ltd[1,2].

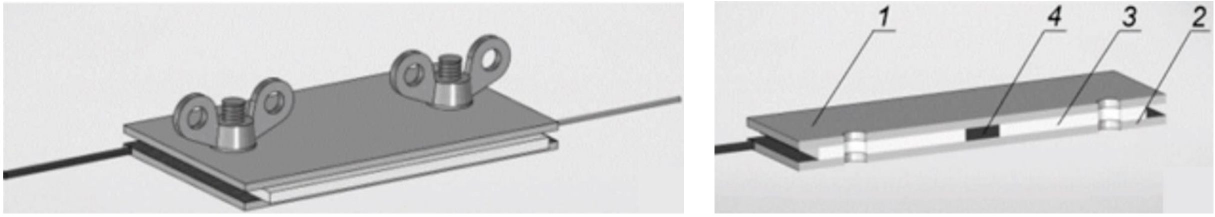

a ***b***

Fig. 1. *A cell for measuring specific volume resistivity:* ***a*** *– cell general view;* ***b*** *– cell in section.*
1, 2 – measuring electrodes; 3 – matrix; 4 – composite

---

[1] *CNT of "Taunite" series // NanoTechCenter. URL:* http://www.nanotc.ru/producrions/87-cnm-taunit.

[2] *Taunite GM" graphene // NanoTechCenter. URL:* http://www.nanotc.ru/producrions/176-cnm-taunit-5.

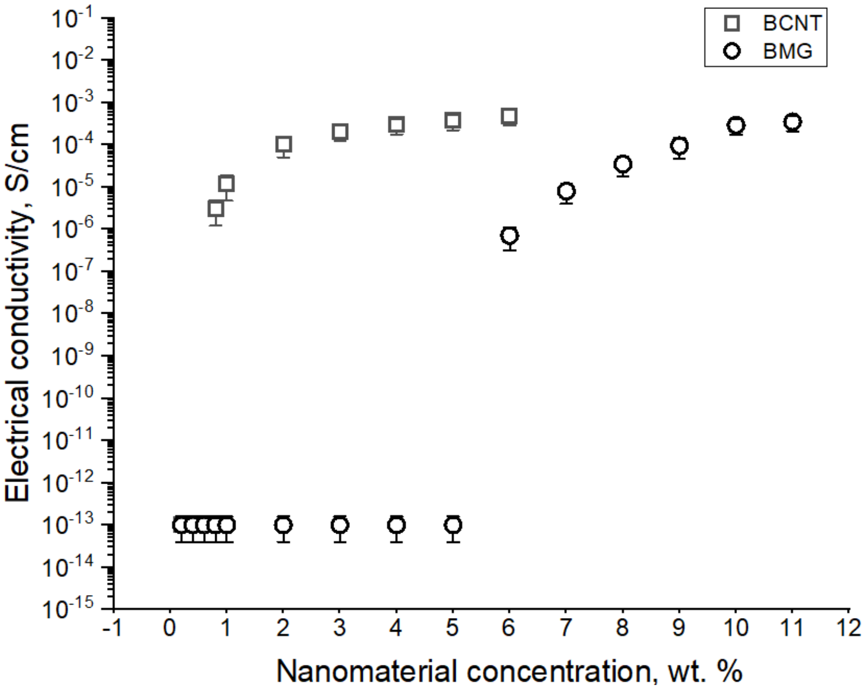

Fig. 2. *The dependences of specific volume electrical conductivity of bitumen-based nanocomposites on the carbon nanomaterial concentration*

$$\sigma = \sigma_f \left(\varphi - \varphi_c\right)^t , \qquad (1)$$

where σ_f – MWCNT electrical conductivity;
φ_c – filler volume fraction corresponding to percolation threshold;
t – electrical conductivity critical value.

The obtained experimental electrical conductivity data are in good agreement with the theoretical values obtained according to formula (1) (Fig. 3). The correlation coefficients of the experimental and estimated curves for BCNT and BMG composites are equal to 0.99. The MWCNT volume fractions at the percolation threshold φ_c and electrical conductivity critical values t were determined using a linear regression of the $log(\sigma)$ versus $log(\varphi - \varphi c)$ plot. For BCNT, φ_c and t were equal to 0.22 and 2.18, respectively (Fig. 3 a). For BMG, φ_c and t were equal to 0.63 and 3.20, respectively (Fig. 3 b). To form a percolation grid in a bitumen matrix, the MWCNT volume concentration of 2.8 times less than that of MG is required.

DISCUSSION

The values of the filler volume fraction at the percolation threshold, and the critical electrical conductivity values of the BCNT and BMG nanocomposites obtained, based on experimental data, create the prerequisites for the design and production of optimized bituminous compositions, with a given volume electrical conductivity, as well as those sensitive to microwave radiation.

Table 2 presents characteristics of fillers, variants of their distribution in the polymer matrix, and electrical conductivity parameters of nanocomposites obtained in this work and in other studies.

Composite materials modified with graphene nanoplatelets / epoxy resin and BMG with the same random filler distribution have higher values of the critical electrical conductivity (3.7 and 3.20, respectively) compared to MWCNT-based composites (Table 2). The filler volume fractions at the percolation threshold for the studied nanocomposites differ greatly from each other (3.2 and 0.63 vol. %, respectively). This is probably related to the fact that the graphene nanoplates used by the authors of [13] have a larger lateral size than the graphene from the present work. However, in the case of nanotubes, an opposite effect can be observed (Table 2). When using longer MWCNTs (10000–30000 µm), which were applied by the authors of [12] to create a polyethylene-based composition, the filler volume fraction at the percolation threshold is 4 times less than the value obtained in the study [15] for nanocomposites with short nanotubes (~2 µm). In all the cases considered, the formation of an infinite conducting cluster (percolation contour) in a polymer matrix requires a smaller amount of carbon nanotubes compared to graphene nanoplates, regardless of their structural characteristics and distribution pattern in the polymer matrix, as evidenced by the φ_c values (Table 2).

Thus, the electrical conductivity parameters (filler volume fraction at the percolation threshold, and the critical electrical conductivity value) are determined by the filler structural and morphological characteristics (filler particle size, filler particle type, etc.), as well as by the spatial distribution of particles in the polymer matrix.

The results of this study can become the basis for the birth of new ideas for the MWCNT and MG application as bitumen modifiers, focused on imparting electrically conductive properties to it. This, in turn, will contribute to expanding the range of its practical application as the main component for antistatic materials, conductive adhesive compositions, various repair and restoration compositions, road surfaces sensitive to microwave radiation. At the same

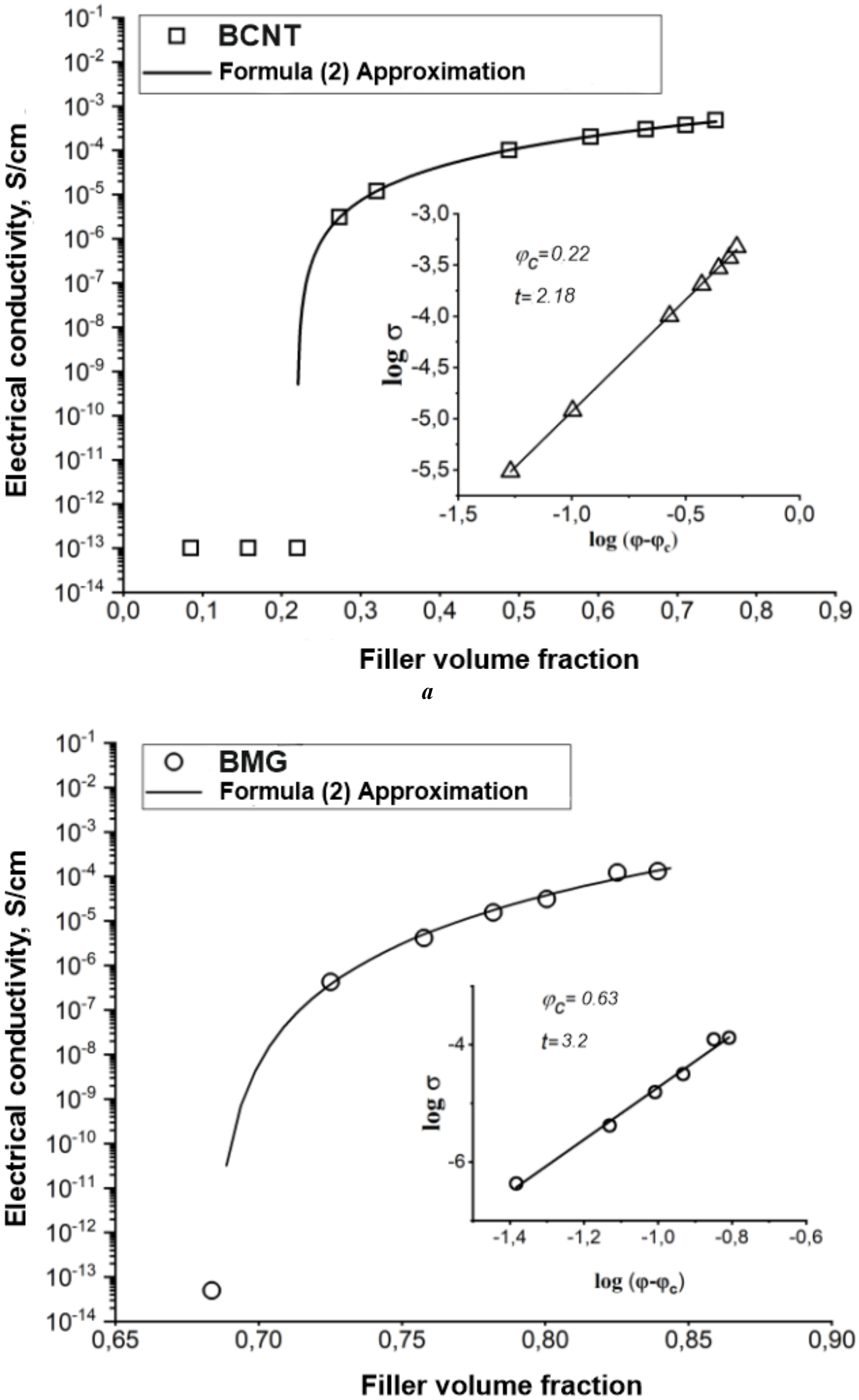

a

b

Fig. 3. *The dependence of specific volume electrical conductivity of nanocomposites on the filler concentration:*
a *– BCNT;* ***b*** *– BMG.*
The inserts show the dependences of the electrical conductivity logarithm on the logarithm of the difference between the filler volume fraction and the filler volume fraction at the percolation threshold

Table 2. *Characteristics of fillers and polymeric nanocomposites on their base*

Filler type and its distribution pattern	Polymer matrix	Diameter, nm	Thickness, nm	Length, µm	φ_c, vol. %	t	Reference to work
Graphene nanoplates, over the boundaries of polymer particles	Polyethylene	200–30000	5–65	–	0.99	2.3	[12]
Carbon nanotubes, over the boundaries of polymer particles	Polyethylene	10–30	–	10000–30000	0.09	2.0	[12]
Graphene nanoplates, random distribution	Epoxy resin	200–30000	5–65	–	3.2	3.7	[13]
Carbon nanotubes, over the boundaries of polymer particles	Polymethyl-methacrylate	10–30	–	≥2	0.372	2.4	[15]
Carbon nanotubes, random distribution	Chloroprene rubber	10–30	–	≥2	0.232	2.16	[11]
Carbon nanotubes, random distribution	BND 60/90 grade bitumen	10–30	–	≥2	0.22	2.18	The results of this study
Graphene nanoplates, random distribution	BND 60/90 grade bitumen	2000–10000	6–8	–	0.63	3.20	The results of this study

time, the cumulative socio-economic effect of their use will exceed by orders the magnitude of a possible rise in the cost of these materials compared to conventional ones. For example, an increase in the inter-maintenance period of a road surface by 30 % gives a total effect that is 3 times higher than the entire cost of the materials used and the work. This occurs due to savings caused by reducing the work in complicated conditions, reducing the number of accidents, reducing the period of traffic restrictions and, as a result, leads to a decrease in the social tension level.

CONCLUSIONS

A technique for obtaining electrically conductive composites based on bitumen containing multi-walled carbon nanotubes, and multilayer graphene nanoplates was developed. Experimental conditions were created, and a technique was developed for measuring the specific volume resistivity of bitumen-based electrically conductive nanocomposites, containing multi-walled carbon nanotubes and multilayer graphene nanoplates. The information on the electrical characteristics of nanocomposites (specific electrical conductivity, volume fraction of the filler at the percolation threshold, electrical conductivity critical value) was obtained from the experimental dependences of the electrical conductivity of nanocomposites. The study established that the formation of a percolation grid in a bitumen matrix occurs at a lower volume content of MWCNTs compared to MG.

Thus, the application of electrically conductive BCNT and BMG nanocomposites with self-healing properties in special road surfaces, units, structures, and facilities will allow improving their reliability and inter-maintenance periods, which cannot be achieved by traditional methods without affecting all phase levels of the composite material.

REFERENCES

1. Zhu J., Birgisson B., Kringos N. Polymer modification of bitumen: Advances and challenges. *European Polymer Journal*, 2014, vol. 54, pp. 18–38. DOI: 10.1016/j.eurpolymj.2014.02.005.
2. Presti D.L. Recycled Tyre Rubber Modified Bitumens for road asphalt mixtures: A literature review. *Construction and Building Materials*, 2013, vol. 49, pp. 863–881. DOI: 10.1016/j.conbuildmat.2013.09.007.
3. Gulisano F., Gallego J. Microwave heating of asphalt paving materials: Principles, current status and next steps. *Construction and Building Materials*, 2021, vol. 278, article number 121993. DOI: 10.1016/j.conbuildmat.2020.121993.
4. Crucho J., Picado-Santos L., Neves J., Capitão S. A Review of Nanomaterials' Effecton Mechanical Performance and Aging of Asphalt Mixtures. *Applied Sciences*, 2019, vol. 9, no. 19, article number 3657. DOI: 10.3390/app9183657.
5. Wu Sh., Tahri O. State-of-art carbon and graphene family nanomaterials for asphalt modification. *Road Materials and Pavement Design*, 2019, vol. 22, no. 5, pp. 1–22. DOI: 10.1080/14680629.2019.1642946.
6. Latifi H., Hayati P. Evaluating the effects of the wet and simple processes for including carbon Nanotube modifier in hot mix asphalt. *Construction and Building Materials*, 2018, vol. 164, pp. 326–336. DOI: 10.1016/j.conbuildmat.2017.12.237.
7. Le J.L., Marasteanu M.O., Turos M. Mechanical and compaction properties of graphite nanoplatelet-modified asphalt binders and mixtures. *Road Materials and Pavement Design*, 2020, vol. 21, no. 5, pp. 1799–1814. DOI: 10.1080/14680629.2019.1567376.
8. Li C., Wu S., Chen Z., Tao G., Xiao Y. Improved microwave heating and healing properties of bitumen by using nanometer microwave-absorbers. *Construction*

and Building Materials, 2018, vol. 189, pp. 757–767. DOI: 10.1016/j.conbuildmat.2018.09.050.

9. Gulisano F., Crucho J., Gallego J., Picado-Santos L. Microwave healing performance of asphalt mixture containing electric arc furnace (EAF) slag and graphene nanoplatelets (GNPs). *Applied Sciences*, 2020, vol. 10, no. 4, article number 1428. DOI: 10.3390/app10041428.
10. Xu S., García A., Su J.-F., Liu Q., Tabaković A., Schlangen E. Self-Healing Asphalt Review: From Idea to Practice. *Advanced Materials Interfaces*, 2018, vol. 5, article number 1800536. DOI: 10.1002/admi.201800536.
11. Stolyarov R.A., Yagubov V.S., Memetova A.E., Memetov N.R., Tkachev A.G., Chapaksov N.A. Electrically conductive nanocomposites based on chloroprene rubber, containing multi-walled carbon nanotubes Taunit and Taunit-M. *Materialovedenie*, 2022, no. 5, pp. 41–48. EDN: DNHSIL.
12. Vovchenko L., Matzui L., Oliynyk V., Launets V., Mamunya Ye., Maruzhenko O. Nanocarbon/polyethylene composites with segregated conductive network for electromagnetic interference shielding. *Molecular Crystals and Liquid Crystals*, 2018, vol. 672, no. 1, pp. 186–198. DOI: 10.1080/15421406.2018.1555349.
13. Vovchenko L., Matzui L., Oliynyk V., Launetz V., Zagorodnii V., Lazarenko O. Chapter 2. Electrical and shielding properties of nanocarbon-epoxy composites. *Conductive Materials and Composites*. New York, Nova Science Publ., 2016, pp. 29–91.
14. Memetov N.R., Gerasimova A.V., Stolyarov R.A., Tkachev A.G., Melezhik A.V., Chapaksov N.A., Osipkov A.S., Mikhalev P.A., Provatorov A.S. Composite Materials Based on Foam Polyurethane and Graphene Nanoplates Effectively Screening Electromagnetic Radiation. *Advanced Materials and Technologies*, 2020, no. 17, pp. 68–73. DOI: 10.17277/amt.2020.01.pp.068-073.
15. Blokhin A., Stolyarov R., Burmistrov I. et al. Increasing electrical conductivity of PMMA-MWCNT composites by gas phase iodination. *Composites Science and Technology*, 2021, vol. 214, article number 108972. DOI: 10.1016/j.compscitech.2021.108972.
16. Mamunya E.P., Davidenko V.V., Lebedev E.V. Percolation conductivity of polymer composites filled with dispersed conductive filler. *Polymer composites*, 1995, vol. 16, no. 4, pp. 319–324. DOI: 10.1002/pc.750160409.

OUR AUTHORS

Amosov Aleksandr Petrovich, Doctor of Sciences (Physics and Mathematics), Professor,
Head of Chair “Metals Science, Powder Metallurgy, Nanomaterials”.
Address: Samara State Technical University,
443100, Russia, Samara, Molodogvardeyskaya Street, 244.
E-mail: mvm@samgtu.ru, egundor@yandex.ru

Chapaksov Nikolay Andreevich, junior researcher of Chair “Nanotechnology Engineering”.
Address: Tambov State Technical University,
392000, Russia, Tambov, Sovetskaya Street, 106/5.
E-mail: tchapaxov.nikolaj@yandex.ru

Evlakhin Daniil Andreevich, student.
Address: Tambov State Technical University,
392000, Russia, Tambov, Sovetskaya Street, 106/5.
E-mail: evlahin.daniil2002@yandex.ru

Gerasimova Alena Vladimirovna, PhD (Engineering),
senior lecturer of Chair “Technology and Methods of Nanoproducts Manufacturing”.
Address: Tambov State Technical University,
392000, Russia, Tambov, Sovetskaya Street, 106/5.
E-mail: alyona_gerasimova_92@mail.ru

Ilyushkin Maksim Valeryevich, PhD (Engineering), Deputy Director.
Address: Ulyanovsk Research Institute of Aviation Technology and Production Organization,
432010, Russia, Ulyanovsk, Vracha Mikhailova Street, 34.
E-mail: fzbm@mail.ru

Ivanov Vladimir Petrovich, Doctor of Sciences (Engineering), Professor.
Address: Euphrosyne Polotskaya State University of Polotsk,
211440, the Republic of Belarus, Novopolotsk, Blokhin Street, 29.
E-mail: v.ivanov@psu.by

Kachkin Egor Maksimovich, student.
Address: Samara State Technical University,
443100, Russia, Samara, Molodogvardeyskaya Street, 244.
E-mail: adidaslock@bk.ru

Khafizova Elvira Dinifovna, PhD (Engineering),
assistant professor of Chair of Materials Science and Physics of Metals,
senior researcher at the Research Laboratory “Metals and Alloys under Extreme Impacts”.
Address 1: Institute of Physics of Molecules and Crystals of Ufa Research Center of RAS,
450054, Russia, Ufa, Prospekt Oktyabrya, 71.
Address 2: Ufa University of Science and Technologies,
450076, Russia, Ufa, Zaki Validi Street, 32.
E-mail: ela.90@mail.ru

Kiselev Evgeny Stepanovich, Doctor of Sciences (Engineering), Professor.
Address: Ulyanovsk State Technical University,
432027, Russia, Ulyanovsk, Severny Venets Street, 32.
E-mail: kec.ulstu@mail.ru

Kostina Alina Evgenyevna, postgraduate student,
junior researcher of the Strength Laboratory.
Address: M.N. Mikheev Institute of Metal Physics of Ural Branch of RAS,
620108, Russia, Yekaterinburg, S. Kovalevskaya Street, 18.
E-mail: kostina_a@imp.uran.ru

Krishtal Mikhail Mikhailovich, Doctor of Sciences (Physics and Mathematics), Professor,
chief researcher of the Research Institute of Advanced Technologies.
Address: Togliatti State University,
445020, Russia, Togliatti, Belorusskaya Street, 14.
E-mail: krishtal@tltsu.ru

Krylova Svetlana Evgenyevna, Doctor of Sciences (Engineering), Professor.
Address: Orenburg State University,
460018, Russia, Orenburg, Prospekt Pobedy, 13.
E-mail: krilova27@yandex.ru

Kryukov Nikita Alekseevich, student.
Address: Samara State Technical University,
443100, Russia, Samara, Molodogvardeyskaya Street, 244.
E-mail: n.kryukkov@mail.ru

Memetov Nariman Rustemovich, PhD (Engineering), leading researcher.
Address: Tambov State Technical University,
392000, Russia, Tambov, Sovetskaya Street, 106/5.
E-mail: memetov.nr@mail.tstu.ru

Memetova Anastasiya Evgenievna, PhD (Engineering),
assistant professor of Chair “Technology and Methods of Nanoproducts Manufacturing”.
Address: Tambov State Technical University,
392000, Russia, Tambov, Sovetskaya Street, 106/5.
E-mail: anastasia.90k@mail.ru

Merson Dmitry Lvovich, Doctor of Sciences (Physics and Mathematics), Professor,
Director of the Research Institute of Advanced Technologies.
Address: Togliatti State University,
445020, Russia, Togliatti, Belorusskaya Street, 14.
E-mail: D.Merson@tltsu.ru

Merson Evgeny Dmitrievich, PhD (Physics and Mathematics),
senior researcher of the Research Institute of Advanced Technologies.
Address: Togliatti State University,
445020, Russia, Togliatti, Belorusskaya Street, 14.
E-mail: mersoned@gmail.com

Myagkikh Pavel Nikolaevich, junior researcher of the Research Institute of Advanced Technologies.
Address: Togliatti State University,
445020, Russia, Togliatti, Belorusskaya Street, 14.
E-mail: feanorhao@gmail.com

Novikov Vladislav Aleksandrovich, PhD (Engineering),
assistant professor of Chair “Metals Science, Powder Metallurgy, Nanomaterials”.
Address: Samara State Technical University,
443100, Russia, Samara, Molodogvardeyskaya Street, 244.
E-mail: vladislav_novyi@mail.ru

Novikova Oksana Sergeevna, PhD (Physics and Mathematics),
senior researcher of the Strength Laboratory.
Address: M.N. Mikheev Institute of Metal Physics of Ural Branch of RAS,
620108, Russia, Yekaterinburg, S. Kovalevskaya Street, 18.
E-mail: novikova@imp.uran.ru

Pilipenko Stanislav Vladimirovich, PhD (Engineering), Associate Professor.
Address: Euphrosyne Polotskaya State University of Polotsk,
211440, the Republic of Belarus, Novopolotsk, Blokhin Street, 29.
E-mail: s.pilipenko@psu.by, 44-08@mail.ru

Plesovskikh Aleksey Yuryevich, postgraduate student.
Address: Orenburg State University,
460018, Russia, Orenburg, Prospekt Pobedy, 13.
E-mail: plesovskih@tehno-oren.ru

Polenok Milena Vladimirovna, graduate student,
laboratory assistant of the Research Laboratory “Metals and Alloys under Extreme Impacts”.
Address 1: Institute of Physics of Molecules and Crystals of Ufa Research Center of RAS,
450054, Russia, Ufa, Prospekt Oktyabrya, 71.
Address 2: Ufa University of Science and Technologies,
450076, Russia, Ufa, Zaki Validi Street, 32.
E-mail: renaweiwei.179@mail.ru

Polunin Anton Viktorovich, PhD (Engineering),
leading researcher of the Research Institute of Advanced Technologies.
Address: Togliatti State University,
445020, Russia, Togliatti, Belorusskaya Street, 14.
E-mail: Anpol86@gmail.com

Poluyanov Vitaly Aleksandrovich, PhD (Engineering),
junior researcher of the Research Institute of Advanced Technologies.
Address: Togliatti State University,
445020, Russia, Togliatti, Belorusskaya Street, 14.
E-mail: vitaliy.poluyanov@gmail.com

Rastegaev Igor Anatolyevich, PhD (Physics and Mathematics),
senior researcher of the Research Institute of Advanced Technologies.
Address: Togliatti State University,
445020, Russia, Togliatti, Belorusskaya Street, 14.
E-mail: RastIgAev@yandex.ru

Rastegaeva Inna Ivanovna, senior lecturer
of Chair “Nanotechnologies, Materials Science and Mechanics”.
Address: Togliatti State University,
445020, Russia, Togliatti, Belorusskaya Street, 14.
E-mail: I.Rastegaeva@tltsu.ru

Salamatov Yury Aleksandrovich, PhD (Physics and Mathematics),
senior researcher of the Laboratory for Neutron-Synchrotron Research of Nanostructures.
Address: M.N. Mikheev Institute of Metal Physics of Ural Branch of RAS,
620108, Russia, Yekaterinburg, S. Kovalevskaya Street, 18.
E-mail: salamatov@imp.uran.ru

Shafeev Marat Ravilovich, junior researcher
of the Research Institute of Advanced Technologies.
Address: Togliatti State University,
445020, Russia, Togliatti, Belorusskaya Street, 14.
E-mail: shelf-tlt@yandex.ru

Shtempel Oleg Petrovich, PhD (Engineering), Associate Professor.
Address: Euphrosyne Polotskaya State University of Polotsk,
211440, the Republic of Belarus, Novopolotsk, Blokhin Street, 29.
E-mail: o.shtempel@psu.by

Sitdikov Vil Dayanovich, Doctor of Sciences (Physics and Mathematics), expert.
Address 1: OOO RN-BashNIPIneft,
450006, Russia, Ufa, Lenin Street, 86/1.
Address 2: Institute of Physics of Molecules and Crystals of Ufa Research Center of RAS,
450054, Russia, Ufa, Prospekt Oktyabrya, 71.
E-mail: SitdikovVD@bnipi.rosneft.ru

Sosnin Ilya Mikhailovich, junior researcher at the Research Institute of Advanced Technologies.
Address: Togliatti State University,
445020, Russia, Togliatti, Belorusskaya Street, 14.
E-mail: sim.nanosci@gmail.com

Stolyarov Roman Aleksandrovich, PhD (Engineering), senior researcher.
Address: Tambov State Technical University,
392000, Russia, Tambov, Sovetskaya Street, 106/5.
E-mail: stolyarovra@mail.ru

Tarov Dmitry Vladimirovich, PhD (Engineering), leading researcher.
Address: Tambov State Technical University,
392000, Russia, Tambov, Sovetskaya Street, 106/5.
E-mail: d_tarov@mail.ru

Titov Aleksandr Andreevich, student.
Address: Samara State Technical University,
443100, Russia, Samara, Molodogvardeyskaya Street, 244.
E-mail: wgwot2019@mail.ru

Vigerina Tatyana Vladimirovna, PhD (Engineering), Associate Professor.
Address: Euphrosyne Polotskaya State University of Polotsk,
211440, the Republic of Belarus, Novopolotsk, Blokhin Street, 29.
E-mail: t.vigerina@psu.by

Volkov Aleksey Yuryevich, Doctor of Sciences (Engineering),
Head of the Strength Laboratory.
Address: M.N. Mikheev Institute of Metal Physics of Ural Branch of RAS,
620108, Russia, Yekaterinburg, S. Kovalevskaya Street, 18.
E-mail: volkov@imp.uran.ru

Yagubov Viktor Sakhibovich, PhD (Engineering), senior researcher.
Address: Tambov State Technical University,
392000, Russia, Tambov, Sovetskaya Street, 106/5.
E-mail: yagubov.vs@mail.tstu.ru, vitya-y@mail.ru

Zelenin Andrey Dmitrievich, junior researcher.
Address: Tambov State Technical University,
392000, Russia, Tambov, Sovetskaya Street, 106/5.
E-mail: zeleandrey@yandex.ru

Zgibnev Dmitry Aleksandrovich, student,
laboratory assistant of the Strength Laboratory.
Address 1: M.N. Mikheev Institute of Metal Physics of Ural Branch of RAS,
620108, Russia, Yekaterinburg, S. Kovalevskaya Street, 18.
Address 2: Ural Federal University named after the first President of Russia B.N. Yeltsin,
620002, Russia, Yekaterinburg, Mira Street, 19.
E-mail: ske4study@gmail.com

On the cover: The microstructure of the product of combustion of a mixture of zinc nitrate with glycine during the synthesis of highly dispersed zinc oxide powder (5000-fold magnification on a scanning electron microscope). Author of the photo: V.A. Novikov, PhD (Engineering), assistant professor (Chair of Metals Science, Powder Metallurgy, Nanomaterials, Samara State Technical University, Samara, Russia).